UNIVERSITY OF SOUTHAMPTON

# Germanium Mid-Infrared Photonic Integrated Circuits

by

Ahmed Osman

A thesis submitted in partial fulfillment for the degree of Doctor of Philosophy

in the

Faculty of Engineering and Physical Sciences

Optoelectronics Research Centre

November 2021

UNIVERSITY OF SOUTHAMPTON

ABSTRACT

FACULTY OF ENGINEERING AND PHYSICAL SCIENCES
OPTOELECTRONICS RESEARCH CENTRE

Doctor of Philosophy

by Ahmed Osman

Group-IV photonics has been an emerging topic of research over the last decade, which focuses on the development of photonic devices that operate in the Near-Infrared (NIR) and the Mid-Infrared (MIR) wavelength ranges. The work presented in this thesis focuses on the development of devices for the MIR. These devices are suitable for numerous applications including chemical, biological and environmental sensing, security, communications, as well as astronomy. Silicon (Si) does not emit light efficiently, therefore the integration of other light-emitting materials is highly demanded for Silicon Photonic Integrated Circuits (SPICs). The main subject, which this project addresses is the integration of light sources, in particular Quantum Cascade Lasers (QCLs) emitting light in the 3-5 $\mu$m wavelength region, that are waveguide-coupled on-chip using flip-chip boning. This thesis presents the progress made towards this aim. This includes the development of various components for the MIR wavelength range. Firstly, waveguides based on the suspended Germanium (Ge) platform were designed, fabricated and characterised. The main aim of investigating this platform is the fact that Ge is transparent in the whole MIR wavelength range, unlike all the other group-IV platforms demonstrated to date. Suspended Ge waveguides have been simulated, fabricated and characterised using Germanium-on-Silicon-on-Insulator (Ge-on-SOI) as the initial platform for wavelengths of 3.8 and 7.67 $\mu$m. The lowest measured propagation loss values were 2.82 and 2.65 dB/cm respectively. Simulations have also been carried for the wavelength of 9.5 $\mu$m.

Lastly, the integration of QCLs with waveguides based on the the Germanium-on-Silicon (GOS) platform using flip-chip bonding was demonstrated. In this approach QCLs operating at a wavelength of 5.5 $\mu$m were flip-chip bonded on a 3 $\mu$m processed GOS wafer. Light was then butt-coupled to rib waveguides and subsequently to an optical fibre using grating couplers. The light sources were in a form of bars, each one containing 24 lasers and were provided by the University of Sheffield. Simulations have been carried out to evaluate the effect of lateral and vertical misalignment on the coupling efficiency and the performance of the grating couplers. Laser-bars where characterised prior to bonding. The voltage of the laser-bar was measured at 15 °C, whereas the optical power was measured at temperatures raising from 8 °C to room temperature ∼20 °C. The laser turn-on current was between 200 and 225 mA. The emitted optical power was ranging from a minimum of ∼25 to a maximum of ∼35 mW. Laser-bars of the same material were characterised once they were flip-chip bonded. The measured coupling loss was 25 dB at the point where the maximum coupled optical power was obtained, which corresponded to a laser current of ∼300 mA. This coupling loss is attributed to various mechanisms discussed in this thesis.

# Contents

# List of Figures

# List of Tables

# Declaration of Authorship

I, Ahmed Osman , declare that the thesis entitled *Germanium Mid-Infrared Integrated Photonic Circuits* and the work presented in the thesis are both my own, and have been generated by me as the result of my own original research. I confirm that:

- this work was done wholly or mainly while in candidature for a research degree at this University;
- where any part of this thesis has previously been submitted for a degree or any other qualification at this University or any other institution, this has been clearly stated;
- where I have consulted the published work of others, this is always clearly attributed;
- where I have quoted from the work of others, the source is always given. With the exception of such quotations, this thesis is entirely my own work;
- I have acknowledged all main sources of help;
- where the thesis is based on work done by myself jointly with others, I have made clear exactly what was done by others and what I have contributed myself;
- parts of this work has been published before submission

Signed:.....

Date:.....

# Journal Papers


[1] **A. Osman**, M. Nedeljkovic, J. Soler Penadés, Y. Wu, Z. Qu, A. Z. Khokhar, K. Debnath, and G. Z. Mashanovich, "Suspended low-loss germanium waveguides for the longwave infrared," Optics Letters, vol. 43, no. 24, pp. 5997-6000, 2018.

[2] B. Troia, J. Soler Penadés, Z. Qu, A. Z. Khokhar, **A. Osman**, Y. Wu, C. Stirling, M. Nedeljkovic, V. M. Passaro, and G. Z. Mashanovich, "Silicon ring resonator-coupled Mach–Zehnder interferometers for the Fano resonance in the mid-IR," Applied Optics, vol. 56, no. 31, pp. 8769–8776, 2017.

[3] A. Sánchez-Postigo, J. G. Wangüemert-Pérez, J. Soler Penadés, A. Ortega-Moñux, M. Nedeljkovic, R. Halir, F. E. M. Mimun, Y. X. Cheng, Z. Qu, A. Z. Khokhar, **A. Osman**, W Cao, C. G. Littlejohns, P. Cheben, G. Z. Mashanovich, I. Molina-Fernández, "Mid-infrared suspended waveguide platform and building blocks," IETOptoelectronics, vol. 13, no. 2, pp. 55–61, 2018.

[4] G. Z. Mashanovich, M. Nedeljkovic, J. Soler Penadés, Z. Qu, W. Cao, **A. Osman**, Y. Wu, C. J. Stirling, Y. Qi, Y. Cheng, L. Reid, C. G. Littlejohns, J. Kang, Z. Zhao, M. Takenaka, T. Li, Z. Zhou, F. Y. Gardes, D. J. Thomson, and G. T. Reed, "Group IV mid-infrared photonics," Optical Materials Express, vol. 8, no. 8, pp. 2276–2286, 2018.

[5] J. Soler Penadés, A. Sánchez-Postigo, M. Nedeljkovic, A. Ortega-Moñux, J. G. Wangüemert-Pérez, Y. Xu, R. Halir, Z. Qu, A. Z. Khokhar, **A. Osman**, W. Cao, C. G. Littlejohns, P. Cheben, I. Molina-Fernández, and G. Z. Mashanovich, "Suspended silicon waveguides for long-wave infrared wavelengths," Optics Letters, vol. 43, no. 4, pp. 795–798, 2018.

[6] Y. Wu, Z. Qu, **A. Osman**, W. Cao, A. Z. Khokhar, J. Soler Penadés, O. L. Muskens, G. Z. Mashanovich, and M. Nedeljkovic, "Mid-infrared nanometallic antenna assisted silicon waveguide based bolometers," ACS Photonics, vol. 6, no. 12, pp.3253–3260, 2019.

[7] Y. Wu, Z. Qu, **A. Osman**, C. Wei, W. Cao, A. Tarazona, S. Oo, H. M. H. Chong, O. L. Muskens, G. Z. Mashanovich and M. Nedeljkovic, "Nanometallic antenna-assisted amorphous silicon waveguide integrated bolometer for mid-infrared," Optics Letters, vol. 46, no. 3, pp. 677-680, 2021

[8] A. Sánchez-Postigo, A. Ortega-Moñux, J. Soler Penadés, **A. Osman**, M. Nedeljkovic, Z. Qu, Y. Wu, I. Molina-Fernández, P. Cheben, G. Z. Mashanovich and J. Gonzalo Wangüemert-Pérez, "Suspended germanium waveguides with subwavelength-grating metamaterial cladding for the mid-infrared band," Optics Express, vol. 29, no. 11, pp. 16867-16878, 2021.

# Conference Papers

[1] **A. Osman**, M. Nedeljkovic, J. Soler Penadés, Y. Wu, Z. Qu, A. Z. Khokhar, and G. Z. Mashanovich, "Suspended low-loss germanium waveguides for the longwave-infrared," Proc. SPIE 10923, 1092308 (2019).

[2] **A. Osman**, J. Soler-Penadés, A. Sánchez-Postigo, Y. Wu, Z. Qu, J. G. Wangüemert-Pérez, A. Ortega-Moñux, R. Halir, P. Cheben, I. Molina-Fernández, M. Nedeljkovic, and G. Z. Mashanovich, "Silicon and germanium suspended waveguides for the mid-infrared," in "2018 IEEE Photonics Society Summer Topical Meeting Series (SUM)," (2018), pp. 181–182.

[3] Z. Qu, M. Nedeljkovic, J. Soler Penadés, A. Z. Khokhar, W. Cao, Y. Wu, **A. Osman**, Y. Qi, N. K. Aspiotis, K. A. Morgan, C. C. Huang, and G. Z. Mashanovich, "Waveguide integrated mid-infrared graphene photodetector," Photonics West 2018, San Francisco, 27 January – 1 February 2018.

[4] G. Z. Mashanovich, J. S. Penadés, W. Cao, Z. Qu, **A. Osman**, Y. Wu, A. Z. Khokhar, C. J. Littlejohns, S. Stankovic, S. Reynolds, V. Mittal, G. S. Murugan, J. S. Wilkinson, Y. Qi, F. Y. Gardes, D. J. Thomson, and M. Nedeljkovic, "Group IV mid-infrared devices and circuits," Proc. SPIE 10535, 1053512 (2018).

[5] M. Nedeljkovic, J. S. Penadés, A. S.-Postigo, J. G. W. Pérez, A. Ortega-Moñux, R. Halir, P. Cheben, I. Molina-Fernández, V. Mittal, G. S. Murugan, A. Z. Khokhar, C. Littlejohns, Y. Xu, Z. Qu, **A. Osman**, W. Cao, L. G. Carpenter, C. Gawith, J. S. Wilkinson, and G. Z. Mashanovich, "Silicon and Germanium based Waveguide Platforms for the Long Wave Infrared," in OSA Conference on Lasers and Electro-Optics, paper STh1I.3, 15th May 2018. (invited).

[6] D. J. Rowe, Y. Qi, V. Mittal, **A. Osman**, Z. Qu, Y. Wu, M. Banakar, J. Soler Penadés, A. Sánchez-Postigo, J. G. Wangüemert-Pérez, A. Ortega-Moñux, R. Halir, I. Molina-Fernández J. S. Wilkinson, M. Nedeljkovic, and G. Z. Mashanovich, "Silicon photonics for mid-infrared sensing," SENSORDEVICES 2018, The Ninth International Conference on Sensor Device Technologies and Applications, Venice, Italy, 16-20 September 2018. (invited).

[7] J. G. Wangüemert-Pérez, A. Sánchez-Postigo, J. Soler Penadés, A. Ortega-Moñux, M. Nedeljkovic, R. Halir, F. El Mokhtari Mimun, Y. X. Cheng, Z. Qu, A. Z. Khokhar,

**A. Osman**, W. Cao, C. G. Littlejohns, P. Cheben, G. Z. Mashanovich, and I. Molina-Fernández, "Mid-infrared suspended waveguide platform and building blocks," ECIO 2018, Valencia, Spain, 30 May – 1 June 2018. (invited).

[8] M. Nedeljkovic, J. Soler Penadés, **A. Osman**, Y. Qi, D. Rowe, Z. Qu, Y. Wu, W. Cao, V. Mittal, G. Senthil Murugan, A. Z. Khokhar, A. Sánchez-Postigo, J. G. Wangüemert-Pérez, A. Ortega-Moñux, R. Halir, I. Molina-Fernández, P. Cheben, J. S. Wilkinson, and G. Z. Mashanovich "Group-IV material waveguide devices for mid-infrared absorption spectroscopy", EOSAM 2018, Delft, Netherlands, 08-12 October 2018 (invited).

[9] G. Z. Mashanovich, Y. Wu, **A. Osman**, Z. Qu, A. Sánchez-Postigo, J. Soler Penadés, M. Nezhad, P. Cheben, A. Ortega-Moñux, D. Pereira-Martin, I. Molina-Fernández, R. Halir, J. G. Wangüemert-Pérez, and M. Nedeljkovic "Mid-infrared suspended group IV photonics," ICTON 2020, Bari, Italy, 19-23 July 2020. (invited).

[10] J. Soler Penadés, A. Sánchez-Postigo, M. Nedeljkovic, J. G. Wangüemert-Pérez, A. Ortega-Moñux, R. Halir, A. Z. Khokhar, **A. Osman**, I. Molina-Fernández, and G. Z. Mashanovich, "Suspended germanium waveguide for infrared wavelengths," 21st International Conference on Transparent Optical Networks, ICTON 2019, Angers, France, 9-13 July 2019. (invited).

[11] A. Sánchez-Postigo, J. G. Wangüemert-Pérez, J. Soler Penadés, A. Ortega-Moñux, M. Nedeljkovic, R. Halir, F. El Mokhtari Mimum, Z. Qu, A. Z. Khokhar, **A. Osman**, W. Cao, C. G. Littlejohns, G. Z. Mashanovich, P. Cheben, and I. Molina-Fernández, "Suspended silicon integrated platform for the long-wavelength mid-infrared band," 21st International Conference on Transparent Optical Networks, ICTON 2019, Angers, France, 9-13 July 2019. (invited).

[12] G. Z. Mashanovich, J. Soler Penadés, Y. Wu, V. Mittal, **A. Osman**. W. Cao, Z. Qu, Y. Qi, C. Stirling, M. Milosevic, L. Reid, D. J. Rowe, D. J. Thomson, and M. Nedeljkovic, "Mid-IR silicon and germanium photonic circuits for communications and sensing," IEEE Summer Topicals Meeting, Ft. Lauderdale, FL, USA, 8-10 July 2019. (invited).

[13] G. Z. Mashanovich, J. Soler Penadés, **A. Osman**, A. Sánchez-Postigo, Z. Qu, Y. Wu, C. J. Stirling, D. P. Cheben, A. Ortega-Moñux, J. G. Wangüemert-Pérez, I. Molina-Fernández, and M. Nedeljkovic, "Silicon and germanium-based mid-infrared platforms," PIERS 2019, Rome, Italy, 17-20 June 2019. (invited).

[14] G. Z. Mashanovich, W. Cao, Z. Qu, **A. Osman**, Y. Wu, D. Hagan, A. P. Knights, T. Li, Z. Zhou, J. Soler Penadés, F. Y. Gardes, K. Li, D. J. Thomson, and M. Nedeljkovic, "Silicon and germanium active devices for the mid-infrared," PIERS 2019, Rome, Italy, 17-20 June 2019. (invited).

[15] M. Nedeljkovic, Y. Qi, V. Mittal, D. J. Rowe, Z. Qu, Y. Wu, **A. Osman**, Z. Zheng, C. Wei, James S. Wilkinson, and G. Z. Mashanovich, "Absorption spectroscopy in the mid-infrared using silicon and germanium waveguides," PIERS 2019, Rome, Italy, 17-20 June 2019. (invited).

[16] G. Z. Mashanovich, W. Cao, **A. Osman**, Y. Wu, J. Soler Penadés, and M. Nedeljkovic, "Modelling of group IV photonic devices," Photonics North, Quebec City, Canada, 21-23 May 2019. (invited).

[17] M. Nedeljkovic, J. Soler Penadés, **A. Osman**, Y. Chang, Z. Qu, W. Cao, A. Z. Khokhar, V. Mittal, G. Senthil Murugan, J. S. Wilkinson, A. Sánchez-Postigo, J. G. Wangüemert-Pérez, A. Ortega-Moñux, R. Halir, P. Cheben, I. Molina-Fernández, and G. Z. Mashanovich, "Group-IV material waveguide platforms for the long wave infrared," OSA Advanced Photonics Congress, 2-5 July 2018, Zurich, Switzerland. (invited).

[18] G. Z. Mashanovich, W. Cao, Z. Qu, **A. Osman**, Y. Wu, T. Li, J. Soler Penadés, S. Stankovic, R. Slavik, F. Y. Gardes, V. Mittal, G. S. Murugan, J. S. Wilkinson, D. J. Thomson, C. G. Littlejohns, and M. Nedeljkovic, "Mid-infrared integrated photonics in silicon and germanium," ECIO 2017, Eindhoven, Netherlands, 3-5 April 2017. (invited).

[19] Y. Wu, Z. Qu, **A. Osman**, W. Cao, A. Z. Khokhar, J. Soler Penadés, O. L. Muskens, G. Z. Mashanovich, and M. Nedeljkovic, "Mid-Infrared silicon waveguide-based bolometer," GFP 2019.

[20] M. M. Milosevic, W. Zhou, H. K. Tsang, **A. Osman**, S. Stankovic, Y. Qi, M. Nedeljkovic, Z. Qu, X. Yan1, A. Z. Khokhar, G. T. Reed, and G. Z. Mashanovich, "Hyperuniform disordered polarisers for the mid-infrared," CLEO 2019, San Jose, CA, USA, 5-10 May 2019.

[21] J. Soler Penadés, **A. Osman**, A. Sánchez-Postigo, Z. Qu, Y. Wu, C. J. Stirling, D. P. Cheben, A. Ortega-Moñux, J. G. Wangüemert-Pérez, M. Nedeljkovic, and G. Z. Mashanovich, "Silicon and germanium mid-infrared platforms," SIOE 2019, Cardiff, Wales, 16-18 April 2019.

# List of Acronyms

**AFM** Atomic Force Microscopy

**Al** Aluminium

**$Al_2O_3$** Aluminium Oxide

**AlN** Aluminium Nitride

**AMMI** Angled Multi-Mode Interferometer

**ANOI** Aluminium Nitride-on-Insulator

**As** Arsenic

**$As_2Se_3$** Arsenic Triselenide

**ASE** Amplified Spontaneous Emission

**Au** Gold

**AuGeNi** Gold Germanium Nickel

**AuSn** Gold Tin

**AWG** Arrayed Waveguide Grating

**BCB** Benzocyclobutene

**BOX** Buried Oxide

**$C_4F_8$** Octafluorocyclobutane

**$CF_4$** Tetrafluoromethane

**$CH_4$** Methane

**ChGs** Chalcogenide glasses

**CMOS** Complementary Metal-Oxide Semiconductor

**CMP** Chemical Mechanical Polishing

**$CO_2$** Carbon Dioxide

**Cr** Chromium

**CROW** Coupled-Resonator Optical-Waveguide

**CRR** Coupled Racetrack Resonator

**CVD** Chemical Vapor Deposition

**CW** Continuous Wave

**CZ** Czhochralski

**DBR** Distributed *Bragg* Reflector

**DEMUX** De-Multiplexer

**DFB** Distributed Feedback Laser

**DI** Deionised water

**DoE** Design of Experiments

**DVS-BCB** Divinylsiloxane-Bis-Benzocyclobutene

**e-beam** Electron-beam

**EHP** Electron-Hole Pair

**EME** Eigenmode Expansion

**$F^-$** Fluoride

**FDE** Finite Difference Eigenmode

**FDTD** Finite-Difference Time-Domain

**$FeCl_3$** Iron Trichloride

**FIB** Focused Ion Beam

**FMM** Film Mode Matching

**FP** Fabry-Pèrot

**FSR** Free Spectral Range

**FTIR** Fourier Transform Infrared Spectroscopy

**FWM** Four Wave Mixing

**FZ** Float zone

**GaAs** Gallium Arsenide

**GaSb** Gallium Antimonide

**Ge** Germanium

**Ge-on-SOI** Germanium-on-Silicon-on-Insulator

**$GeH_4$** Germane

**$GeO_2$** Germanium Dioxide

**GeSn** Germanium-Tin

**GOI** Germanium-on-Insulator

**GOS** Germanium-on-Silicon

**GOSN** Germanium-on-Silicon Nitride

**GPIB** General Purpose Interface Bus

**H** Hydrogen

**$H_2$** Hydrogen

**$H_2O$** Water

**$H_2SiCl_2$** Dichlorosilane

**HCPB** Hollow-Core Photonic Bandgap

**HF** Hydrofluoric Acid

**HgCdTe** Mercury Cadmium Telluride

**IC** Integrated Circuit

**ICL** Interband Cascade Laser

**ICP** Inductively Coupled Plasma

**In** Indium

**InAlAs** Indium Aluminium Arsenide

**InAsSb** Indium Arsenide Antimonide

**$InF_3$** Indium Fluoride

**InGaAs** Indium Gallium Arsenide

**InGaAsP** Indium Gallium Arsenide Phosphide

**InP** Indium Phosphide

**InSb** Indium Antimonide

**IPA** Isopropyl Alcohol

**IR** Infrared

**IR-TDLAS** Infrared Tunable Diode-Laser Absorption Spectroscopy

**LED** Light Emitting Diode

**LEPECVD** Low Energy Plasma Enhanced Chemical Vapor Deposition

**LIDAR** Light Detection and Ranging

**$LiNbO_3$** Lithium Niobate

**LOD** Limits of Detection

**LPCVD** Low-Pressure Chemical Vapor Deposition

**LWIR** Long-Wave Infrared

**MEMS** Micro-Electomechanical System

**MIR** Mid-Infrared

**MMI** Multi-Mode Interferometer

**Mo** Molybdenum

**MOCVD** Metalorganic Chemical Vapor Deposition

**MOSFET** Metal-Oxide-Semiconductor Field-Effect

**MRR** Microring Resonator

**MUX** Multiplexer

**MZI** Mach-Zehnder Interferometer

**NEP** Noise Equivalent Power

**$NH_3$** Ammonia

**NIR** Near-Infrared

**NLSE** Non-Linear Schröringer Equations

**NOI** Nitride-on-Insulator

**$O_2$** Oxygen

**OEIC** Optoelectronic Integrated Circuit

**OH** Hydroxyl

**OPO** Optical Parametric Oscillator

**ORC** Optoelectronics Research Centre

**OTP** One-Time Programmable

**PbSn** Tin Lead

**PCG** Planar Concave Grating

**PDMS** Polydimethylsiloxane

**PECVD** Plasma-Enhanced Chemical Vapor Deposition

**PIC** Photonic Integrated Circuit

**PMGI** Polydimethylglutarimide

**PML** Perfectly Matched Layer

**PSi** Porous Silicon

**Pt** Platinum

**PVDF** Polyvinylidene fluoride

**QCL** Quantum Cascade Laser

**QW** Quantum Well

**RF** Radio Frequency

**RIE** Reactive Ion Etcher

**RIU** Refractive Index Unit

**RPCVD** Reduced Pressure Chemical Vapor Deposition

**RTA** Rapid Thermal Annealing

**S** Sulfur

**SBD** Solder Ball Deposition

**Se** Selenium

**SEM** Scanning Electron Microscope

**$SF_6$** Sulfur hexafluoride

**SGOS** Silicon-Germanium alloy-on-Silicon

**Si** Silicon

**SiGe** Silicon-Germanium

**SiGeSn** Silicon-Germanium-Tin

**SIMS** Secondary Ion Mass Spectroscopy

**SiN** Silicon Nitride

**$SiO_2$** Silicon Dioxide

**SiPSi** Silicon-on-Porous-Silicon

**SMC** Single-Mode Condition

**SMF** Single-Mode Fibre

**SMSR** Side Mode Suppression Ratio

**SMW** Suspended Membrane Waveguide

**Sn** Tin

**SNC** Southampton Nanofabrication Centre

**SNR** Signal-to-Noise Ratio

**SOA** Semiconductor Optical Amplifier

**SOG** spin-on-glass

**SOI** Silicon on Insulator

**SONOI** Silicon-on-Nitride-on-Insulator

**SOS** Silicon-on-Sapphire

**SOSN** Silicon-on-Silicon Nitride

**SPIC** Silicon Photonic Integrated Circuit

**SPWAS** Silicon Photonic Waveguide Absorption Spectrometer

**SWG** Sub-Wavelength Grating

**TDD** Threading Dislocation Density

**TDFA** Thulium-Doped Fibre Amplifier

**TDH** Time Dependent Haze

**TDLAS** Tunable Diode-Laser Absorption Spectroscopy

**TE** Transverse Electric

**TEC** Thermoelectric Cooler

**TEM** Transmission Electron Microscopy

**Ti** Titanium

**TM** Transverse Magnetic

**TMAH** Tetramethylammonium Hydroxide

**TPA** Two-Photon Absorption

**UHV-CVD** Ultra-High Vacuum Chemical Vapour Deposition

**varFDTD** Variational Finite-Difference Time-Domain

**VCSEL** Vertical Cavity Surface Emitting Laser

**WDM** Wavelength Division Multiplexer

**WPE** Wall-Plug Efficiency

**$Y_2O_3$** Yttrium Oxide

**ZnSe** Zinc Selenide

# Acknowledgements

Firstly, I would like to thank Prof. Graham Reed for introducing me to the field of Silicon Photonics back in the days when I was attending the MSc in Optical Fibre Technologies. I would like to express my gratitude to my primary supervisor Prof. Goran Mashanovich who have guided this research and offered his insight in the general field of silicon photonics and specifically the research of mid-infrared silicon photonics. I would like to thank him for the support throughout my whole PhD. I would also like to thank all the members of the Photonics Systems Circuits and Sensors (PSCS) group who have kindly helped me during my PhD, especially Dr. Milos Nedeljkovic who has offered me valuable training and technical support on simulation techniques, fabrication processes as well as measuring and data processing. Special thanks to Dr. Colin Mitchell for answering my endless questions and offering his valuable support on the laser integration part of this work regarding the design, fabrication and characterisation of the devices. Also, for all of our discussions about device fabrication which provided numerous insights and made solving numerous issues easier. I would also like to thank Dr. Jordi Soler Penadés for showing me how to design grating couplers as well as introducing me to the suspended devices. Many thanks to Dr. Ali Khokhar and Dr. Kian Kiang and all the staff at the Southampton Nanofabrication Centre (SNC) for all their help with sample fabrication. The part of the work related to the laser integration was carried out in collaboration with colleagues from other universities. Working with the University of Sheffield staff, especially with Prof. Jon Heffernan and Dr. Kristian Groom, has been a pleasant and constructive experience. I am grateful to the UK Engineering and Physical Sciences Research Council (EPSRC) for providing me the studentship without which this work would have not been possible. Above all, I would like to thank my parents Mohsen and Afaf for all her unconditional love and valuable psychological support through hard times.

# Chapter 1

# Introduction

## 1.1 Silicon photonics and applications

Silicon photonics is a wide-ranging field that involves the development of Photonic Integrated Circuits (PICs) for numerous applications ranging from high-speed optical communications to ultrafast signal processing, optoelectronic integration and biological and chemical sensing. All these technologies converge in silicon photonics taking advantage of semiconductor wafer manufacturing scalability to reduce costs.

The constantly increasing demand for high speed telecommunications due to the enormous growth of social networking and data sharing, via the cloud and smart mobile handsets, has been the main driver for the development of optical interconnects. Optical interconnection has attracted high interest in the development of energy efficient communication systems, overcoming the I/O bandwidth limitations of the electrical data communication, also known as the I/O bottleneck [1].

Over the past decades, silicon photonics has been exploited to evolve telecommunication technology for the transfer of vast amounts of data around the world, enabling vital services such as the internet and reforming the very nature of telecommunications. Compared to conventional electrical interconnects that suffer from energy budget due to the high power consumption, as well as increased latency and decreased bandwidth, silicon photonic interconnects achieve ultra-high-speed due to the use of a different signal propagation mechanism thus preventing signal interference (crosstalk) [2]. As a result, silicon photonics has become a promising solution towards compact, high-bandwidth and low power-consumption communications with applications in datacom [3], optical access networks [4] and computer systems based on silicon photonic interconnects [5]. More importantly, these devices can be fabricated using the already well-developed Complementary Metal-Oxide Semiconductor (CMOS) fabrication infrastructure. This results in high yield and production of devices in high volume at a cost that is scalable

TABLE 1.1: Cost of different interconnect solutions [6].

| Technology | Cost of energy | Power consumption for 10 Gbps link | Power per Tbps |
|---|---|---|---|
| Copper | 3500$ per year | 10 W | 1 kW |
| Traditional optical interconnect | 700$ per year | 2 W (10 Km) | 200 W |
| VCSEL or Silicon Photonics | 70$ per year | 0.2 W | 20 W |

with large numbers. Table 1.1 shows cost and energy consumption figures of different interconnect solutions.

Even though III-V-based photonics is the most mature integration technology due to the fact that high-performance active devices can be developed using this platform, it still needs to overcome the main issue of its incompatibility with the well-established CMOS fabrication technology exploited for decades in electronics by various foundries. Therefore, silicon photonics is the most promising next-generation technology that offers the potential of development of photonic devices with a dramatically lower power consumption, while keeping development costs low by taking advantage the currently available CMOS high volume manufacturing capabilities. Furthermore, silicon photonics enables the minimisation of time-to-market for the development of innovative and disruptive photonic and opto-electronic devices, while maximising the industrial return on investment.

The development of most silicon photonic devices is demonstrated using the CMOS-compatible SOI platform (a few hundred nanometers of single crystal silicon layer on top of a few micron thick BOX layer), due to the fact that this platform offers the ability of integrating both electronic and photonic components on the same chip. This has mainly been driven by the high index contrast between the silicon core ($n_{Si} \sim 3.47$) and the cladding material whether it is air or $SiO_2$ ($n_{SiO_2} \sim 1.45$) which allows for high confinement of the optical mode in the waveguide core. Moreover, their optical transparency in the 1.55 $\mu$m wavelength window enables the development of ultra-compact passive PICs of dimensions in the submicron scale, allowing for high density integration on a chip. One of the first device demonstrations using this platform was waveguides in 1985 [7] which was commercialised later in 1989 by Bookham Technology Ltd. [8]. The advancement in data communications technology lead to the realisation of SOI-waveguide p-i-n junction modulators [9] and Ge-, Silicon-Germanium (SiGe)-based photodetectors [10], and modulators [11]. However, the integration of light sources on Si-based platforms still remains a challenge. Several advancements towards obtaining an on-chip light source for the development of integrated PICs have been made as discussed in 2.3.

Other devices demonstrated based on the SOI platform include ring resonators [12], Wavelength Division Multiplexers (WDMs) [13], photonic crystals [14], Angled Multi-Mode Interferometers (AMMIs) [15], grating couplers [16], optical power and polarisation splitters [17, 18], etc.

Apart from common short-reach applications such as data communications in data centres, silicon photonics is also used for long-reach high-bandwidth digital communication applications. In this case, complex modulation schemes and coherent communications are required. Numerous other novel applications are also being investigated in both academia and industry using this technology including biosensing [19] and nonlinear optics [20]. Moreover, silicon photonics has enabled the development of chip-scale solid-state Light Detection and Ranging (LIDAR) systems which require the dense integration of multiple optical components including lasers, amplifiers, phase and amplitude control low-noise photodetectors, mode converters, and optical waveguides. Silicon photonics also enables the integration of these components in a compact form factor that can be manufactured in high volume. [21].

In a nutshell, the fact that the development of commercial electronic devices make use of the same material is the main advantage of silicon photonics in enabling the integration of both optical and electronic devices on a single platform thus reducing product size and development cost.

## 1.2 Mid-infrared silicon photonics and applications

MIR silicon photonics is a topic of research that focuses on the development and integration of compact, low cost and energy efficient photonic devices in the wavelength region of 2-15 $\mu$m. This region of the electromagnetic spectrum has appeared to be attractive for the development of various devices for gas, chemical and biological sensing [22] as well as spectroscopic applications [23]. That is because the vibrational transition energies of numerous molecules fall in the wavelength range of 2-20 $\mu$m. This spectral region includes absorption bands for various molecules.

Detection and measurement of gases is of crucial importance in modern life. For example, it can determine whether the air we breathe or the water we drink is clean or polluted. For example, volatile organic compounds, such as monochlorobenzene and chloroform, are contaminants in drinking water and have absorption peaks near 13 $\mu$m [24]. In addition, emission and immission measurements of, e.g., car exhaust and greenhouse gases that are responsible for global warming, are required to help legislation and politics to establish efficient ways to ensure our common health and future. In medicine, the measurement of exhaled gases can be employed for the diagnosis of numerous diseases. Many other gases that may be highly toxic or combustible, are hazardous. Therefore, gas-sensing systems are required to ensure a safe working environment especially in an

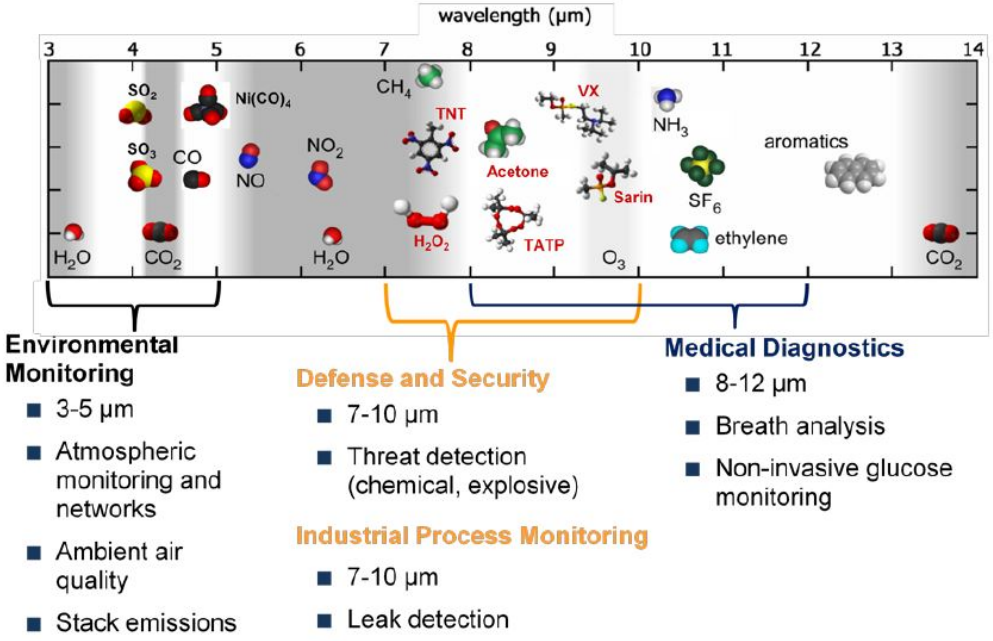


FIGURE 1.1: Graphical representation of the location of strong absorptions of molecules of interest [26].

industrial environment. For example, sulfur dioxide, which is produced as a by-product of the burning of fossil fuels contaminated with sulfur compounds, has strong absorption near 7.6 $\mu$m [25]. Natural gas is still one of the most important energy sources worldwide and the basis for a huge number of products. But mixtures of air and natural gas can be highly explosive. Therefore, leaks at gas wells, gas distribution infrastructure, power plants as well as private residencies must be detected in a very short time. Finally, many industries are producing and using special gases in their production processes. Gas detection and concentration measurement systems down to trace-level concentrations are essential for the operation of these plants. Additionally, gas sensing is important to ensure safe operation in areas where explosive gases may exist. Apart from the aforementioned substances, other molecules such as $H_2O$, $CH_4$, $CO_2$, CO, NOx, SOx, $NH_3$, and many other chemicals and gases also have strong absorption lines in the MIR as shown in Figure 1.1. And because of the fact that the MIR "fingerprint" of different gas molecules can be spectrally separated, a high degree of selectivity can be achieved.

The real-time monitoring of these gases in the environment and during industrial processes demands low cost and compact sensors. Due to the fact that most of the sensors and analysers are used to ensure safety, they have to comply with many regulations. Therefore, some important specifications must be fulfilled:

- fail-safe operation
- limit of detection (LOD) significantly below lower explosive limit of gas mixtures
- no signal failure or saturation at high concentrations

- preferably linear response
- self-testing and indication of malfunction or inoperability
- long-term autonomous operation
- low cross-interferences, no false alarms
- fast response time

Silicon photonics appears to be a promising candidate because it can enable the development of an integrated solution, at a low cost and with high compactness. Detection of an analyte is based on its interaction with the evanescent field of the optical mode in a waveguide. By appropriately designing the cross-section of the waveguide, this mode overlap is maximised. This overlap results in light absorption at a specific wavelength range, detected by measuring the transmission at the output of the waveguide, which can consequently be translated into analyte concentration. A recent demonstration of such a PIC is described in the next paragraph.

Among other gases that are important for trace-gas detection applications such as air-quality monitoring and medical diagnostics, methane detection has attracted a lot of interest over the past decade. A recent demonstration of such a system was presented by IBM where silicon photonics technology was leveraged to develop a Tunable Diode-Laser Absorption Spectroscopy (TDLAS) sensor that was CMOS-compatible [27]. The demonstrated device (Figure 1.2) uses NIR (1650 nm) light from a DFB laser and an uncooled InGaAs detector, to detect ambient $CH_4$ using its interaction with the evanescent optical field of a high-index contrast nanoscale silicon waveguide. The resulting minimum detectable concentration is sub-100 ppm, which is limited by the Gaussian noise.

However, $CH_4$ has a much stronger absorption line in the 7-8 $\mu$m wavelength region than in the NIR as shown in Figure 1.3. Therefore, a MIR sensor with the same characterstics (i.e. laser power, detector Noise Equivalent Power (NEP), passive circuit loss, etc.) would have a greater sensitivity than the NIR one.

An equally important gas to monitor is Carbon Dioxide ($CO_2$) as it is vital for life on Earth. In addition, it is a waste product of human activities and is widely used in agriculture and industry. Moreover, it is important for monitoring the climate change. Therefore, developing systems for sensing it accurately sensing is of great interest. A recent demonstration presents absorption spectroscopy of $CO_2$ using a suspended waveguide based on the SOI platform at 4.24 $\mu$m [29]. The resulting performance is optical sensing of $CO_2$ concentrations down to 0.1%. Using this type of waveguide, an optical mode field overlap ($\Gamma$) of 44% that of free-space sensing, is achieved.

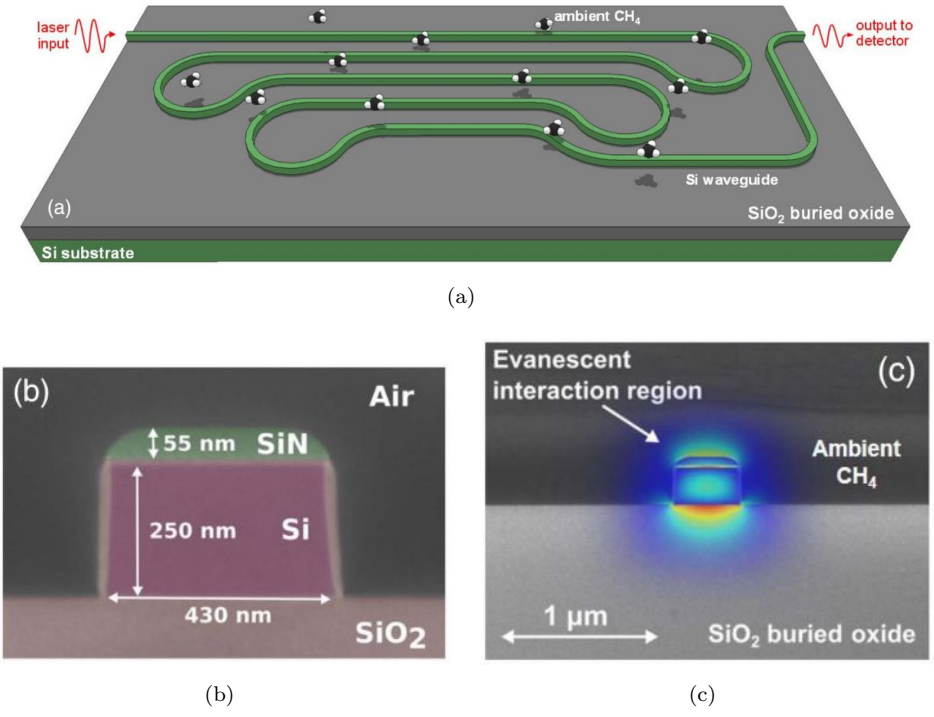


FIGURE 1.2: (a) Schematic representation of the SPWAS. The evanescent field of the guided mode of a 10 cm SOI waveguide probes ambient $CH_4$ via IR-TDLAS. To minimise the size of the device the waveguide is designed in a "paperclip" layout reducing the area to 16 $mm^2$. (b) False-colour cross section of the silicon waveguide. In order to maximise the overlap of the optical mode field $\Gamma$ with the ambient analyte the waveguide dimensions are designed for operation near the cutoff frequency. (c) $E_y$ field profile of the waveguide's fundamental TM mode. [27]

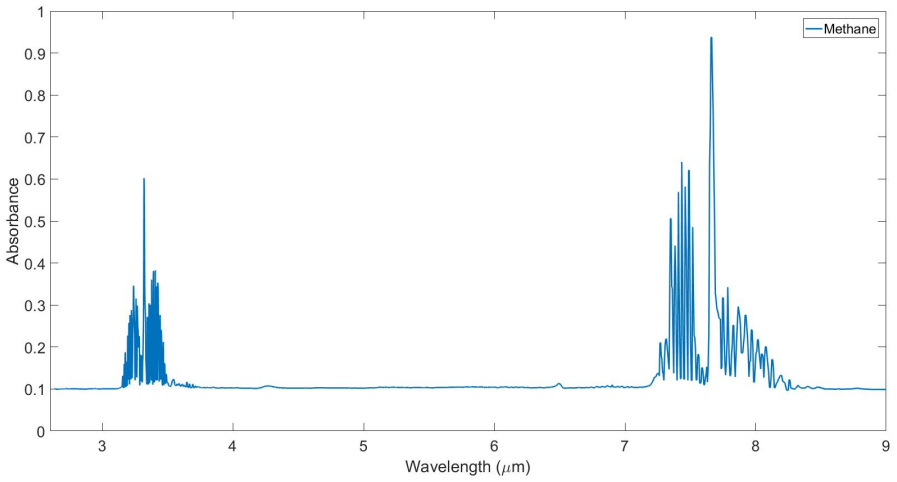


FIGURE 1.3: Methane absorption in the MIR spectrum for a path length of 5 cm [28].

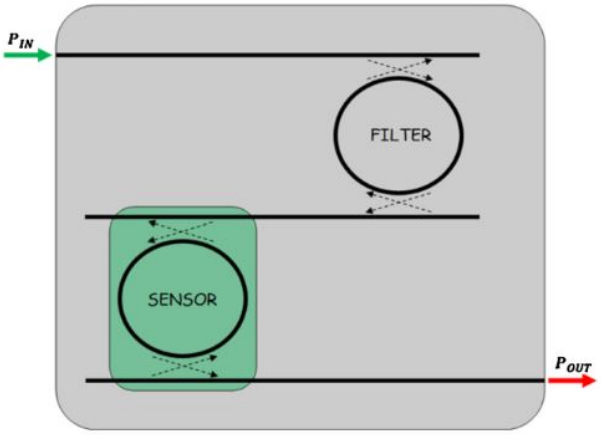


FIGURE 1.4: Schematic of an optical sensor using the *Vernier* effect.

To improve the sensitivity, the effective interaction of the optical mode field with the desired material for detection needs to be enhanced which can be achieved by utilising Microring Resonators (MRRs) (Figure 1.5). In these devices light propagates around the ring several times which increases the effective length of the sensing waveguide while reducing the footprint of the device at the same time. MRRs based on the SOI platform have been demonstrated for the MIR in the 3–5 $\mu$m wavelength region [30, 31]. However, the main disadvantage of MRR devices is that tunable laser needs to be employed in order to excite the cavity resonance. This issue can be overcome by using a Coupled-Resonator Optical-Waveguide (CROW) (Figure 1.5(c)) as proposed in [32], where only a fixed wavelength is required to excite the CROW. The sensing scheme of a sensor using CROW is based on measurements in the spatial domain in which case a fixed wavelength is required to excite the CROW for imaging the out-of-plane elastic light-scattering intensity patterns.

An alternative solution to the MRR sensor is to use resonant disks [33] as shown in Figure 1.5(d). In this approach, detection of the analyte is achieved by monitoring the change in the transfer characteristics of the resonator disc when the analytes interact with the active area. Compared to the MRRs, micro-disk resonators demonstrate higher sensitivities due to the increased number of times that the optical mode interacts with each analyte due to the resonance recirculation within the the micro-disc.

To further improve the performance of the sensor the *Vernier* effect is utilised. In this case, the optical sensor is based on two cascaded rings with different Free Spectral Ranges (FSRs) that is due to a slight difference in the radii of the two rings. One of them acting as a filter and the other one acting as a sensor as shown in Figure 1.4.

In order to avoid any interaction of the analyte to be detected with the optical mode field in the filter ring resonator, a cladding medium is used to cover it. On the other hand, the sensing ring resonator is directly exposed to the analyte, resulting in a variation of the optical mode effective index which in turn causes a wavelength shift $\Delta\lambda_{sensor}$

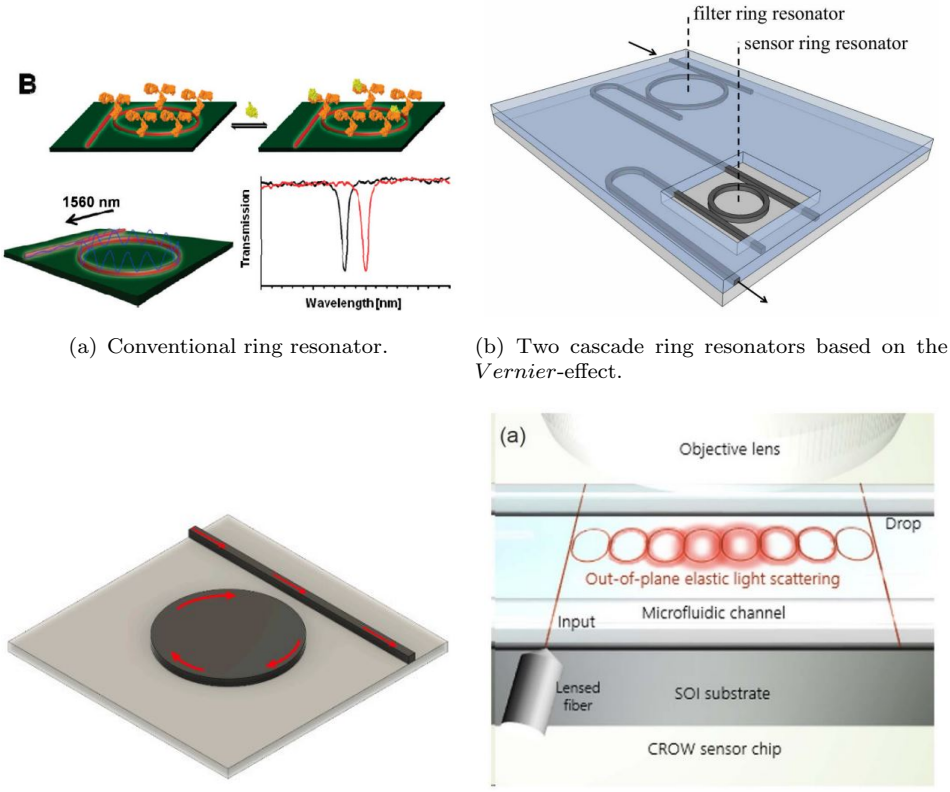


(a) Conventional ring resonator.

(b) Two cascade ring resonators based on the *Vernier*-effect.

(c) Micro-disk resonator.

(d) CROW.

FIGURE 1.5: Various ring resonator biosensors using different ring geometries.

of the transmission peak. This wavelength shift is then translated into the change in concentration of the substance to be detected as described in [34].

In this way, sensitivity of an optical sensor is enhanced many times compared to that of a single-ring sensor. This has been demonstrated in the NIR [35, 36, 37] and in the MIR based on the SOI [38] and the GOS platform [39].

To further increase the sensitivity of a gas sensor, suspended waveguides have been used to realise an optical sensor. This type of waveguides exhibit a higher external evanescent field confinement factor $\Gamma$ resulting in higher interaction of the optical mode with the analyte. In [40] the authors report the first demonstration of suspended InGaAs membrane waveguides in the InGaAs-InP platform at such a long wavelength with gas sensing results. Fully suspended InGaAs waveguide devices with a SWG cladding were designed and fabricated for mid-infrared sensing at $\lambda = 6.15$ $\mu$m in the low-index contrast InGaAs-InP platform exhibiting a propagation loss of 4.1 dB/cm. The authors experimentally detect 5 ppm Ammonia ($NH_3$) using a 3 mm long suspended waveguide. A schematic illustration of the proposed device is shown in

Another field in which MIR spectroscopy has been applied to is healthcare. Applications such as drug detection and glucose monitoring have benefited from the ability to develop small, low-cost and mass-producible detectors. For example, cocaine detection in human

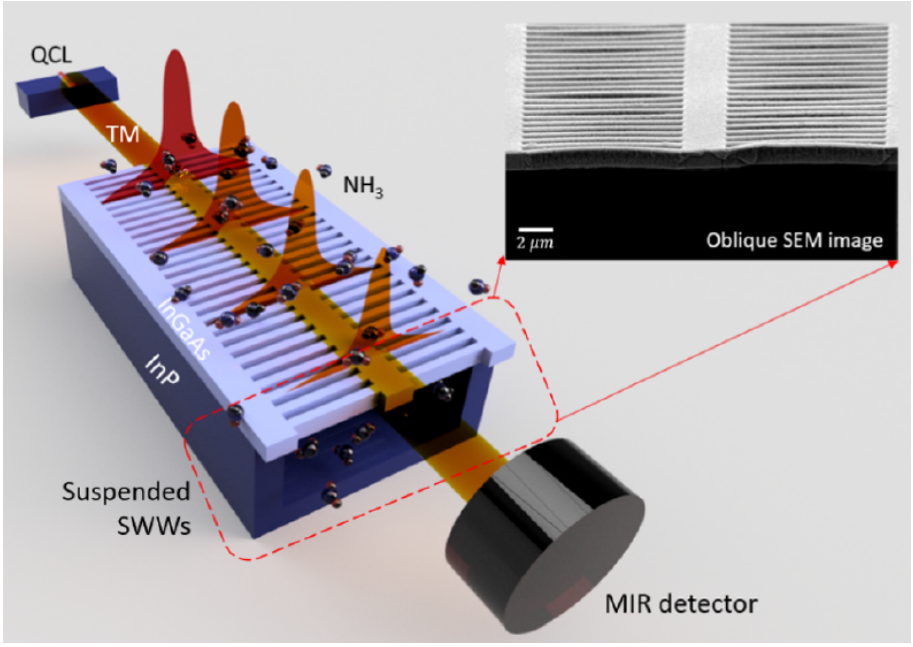


FIGURE 1.6: Schematic illustration of a suspended InGaAs membrane waveguide with a SWG cladding [40].

saliva has been demonstrated using GOS waveguides operating at 5.3 $\mu$m [41] and 5.8 $\mu$m [42].

In addition to the sensing applications, the high atmospheric transmission windows in the 3-5 $\mu$m and 8–13 $\mu$m ranges enables the development of applications in longer distances such as remote explosive detection [43], thermal imaging [44], and free-space communications [45]. Figure 1.7 shows these high transmission atmospheric windows in the electromagnetic spectrum from the visible (400-700 nm) through the MIR. This could be beneficial for atmospheric communications and for LIDAR systems as the larger waveguide dimensions that are used in for the MIR compared to the NIR, make the system more tolerant to fabrication errors. This in turn helps improve the phase array performance as well as reducing the phase error induced by the sidewall roughness. Furthermore, MIR light penetration in the cornea and skin tissues is lower, making MIR lasers safer for humans [46].

Moreover, the threshold for Two-Photon Absorption (TPA) to occur in Si is ~2.2 $\mu$m, enabling higher-power density transmission in the MIR than at telecom wavelengths. As a result, the MIR range has attracted great interest for the development of nonlinear optical devices operating at high power. The resulting higher power density in the waveguides enables nonlinear phenomena utilised in applications such as wavelength conversion [48], parametric amplification [49], and frequency comb generation [50].

The most popular platform for developing PICs has been SOI due to its CMOS compatibility. Over the past few years, several research groups have demonstrated low-propagation-loss MIR waveguides in the wavelength range of 2-4 $\mu$m [51, 52, 53, 54, 55].

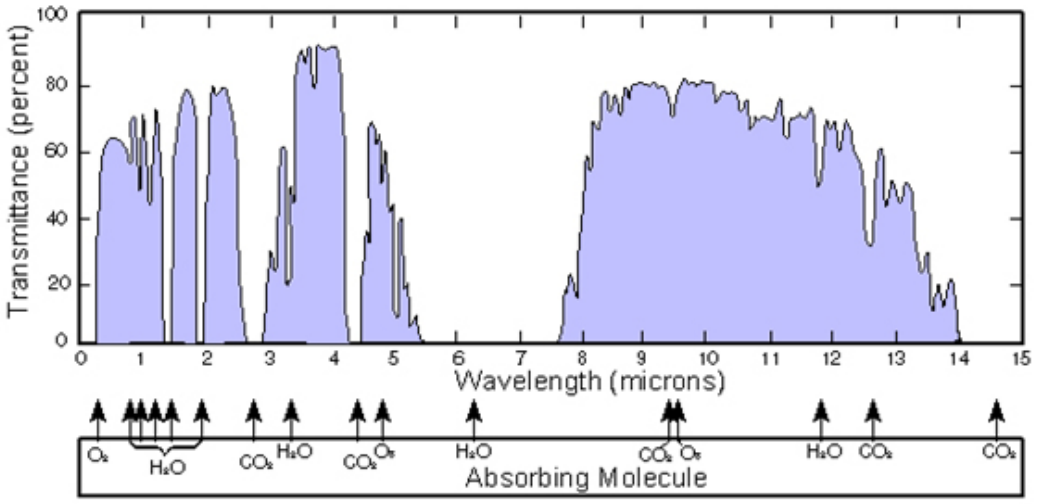


FIGURE 1.7: Earth's atmospheric transmittance over 1 nautical mile sea level path from the visible to the MIR. The sources of the major absorptions are also indicated [47].

However, this platform becomes unsuitable for applications using wavelengths beyond 4 $\mu$m as explained in 1.3. Therefore, alternative material platforms need to be investigated which are studied in detail in 2.2.1.

Apart from Si- and Ge-based CMOS-compatible platforms, various alternative platforms have been investigated due to their remarkable properties. Chalcogenide glasses (ChGs) are well-known for their high infrared transparency (2-20 $\mu$m) and amenability to fabrication in thin film form which makes them attractive candidates for MIR optical sensors. Chalcogenide on-chip waveguides have been demonstrated exhibiting low propagation losses (up to 0.84 dB/cm at 5.2 $\mu$m for a $Ge_{0.115}$Arsenic $(As)_{0.24}$Selenium $(Se)_{0.645}$ on $Ge_{0.115}As_{0.24}$Sulfur $(S)_{0.645}$ platform [56] and 0.6 dB/cm in the 2.5–3.7 $\mu$m wavelength range for a Zinc Selenide (ZnSe) on $SiO_2$ platform) [57]. However, there are a variety of properties associated with chalcogenide glasses that can complicate the utility of these materials in traditional applications, including low thermal stability, low chemical durability and photosensitivity, as compared to oxide materials. Traditional fabrication techniques such as thermal evaporation and photo-lithography have been shown to be viable for large-scale production of planar optical devices, but can suffer from drawbacks, such as poor compositional fidelity and high post-fabrication surface roughness which can lead to increased optical loss. As a result, the detection limit and sensitivity of the final sensor system are affected.

III–V-based platforms such as InGaAs are very promising because of the wide transparency range and low propagation losses [40]. Moreover, they exhibit large second-order nonlinear coefficients making them suitable for nonlinear applications in the MIR. However, there are drawbacks associated with III-V-based platforms. One of them them

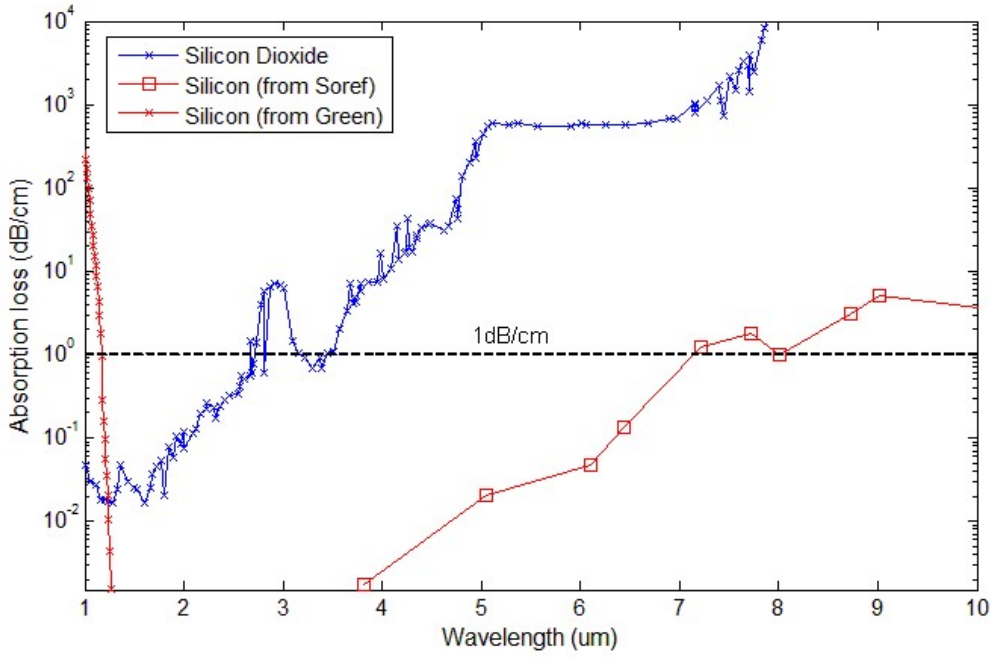


FIGURE 1.8: Absorption spectra of Si (red lines) and $SiO_2$ (blue line) for $\lambda$ = 1-10 $\mu$m, $SiO_2$ data imported from [58], Si data imported from [59] and [60]. It is worth noting that $SiO_2$, from which the loss in the graph was measured, is not high-purity silica that is used for the production of optical fibres, but a high in water impurities $SiO_2$ layer that was formed by thermal oxidation. Graph reproduced from [61]

is the low refractive index contrast ($\Delta$n ~0.3) between the waveguide core and the substrate, resulting in larger passives.

As a result, for large-scale integration Si- and Ge-based platforms are the most attractive, even if their losses are still higher than chalcogenide-based platforms. In particular, in appellations requiring large volumes and functionalities such as routing or multiplexing sources, Si- and Ge-based platforms are probably the most suitable where a moderate insertion loss of a few dB can generally be tolerated.

## 1.3 Main vision and thesis outline

The MIR spectral region promises to enable potentially transformative technologies. However, due to the high absorption of $SiO_2$ above 3.6 $\mu$m (i.e., higher than $2.5\times10^3$ dB/cm at 7.6 $\mu$m, rising to ~$2.5\times10^4$ dB/cm at 8.0 $\mu$m) [58] and Si above 8.5 $\mu$m (Figure 1.8), in order to develop devices which will operate at even longer wavelengths, alternative material platforms to SOI are investigated.

More specifically, Ge is a promising material of high interest for building photonic devices because its transparency range (2-14 $\mu$m) is larger than that of Si (1.2-8 $\mu$m) as well as other photonic materials such as Sapphire (150 nm - 4.5 $\mu$m) and Silicon Nitride (SiN) (150 nm - 6.5 $\mu$m) as shown in Figure 1.9.

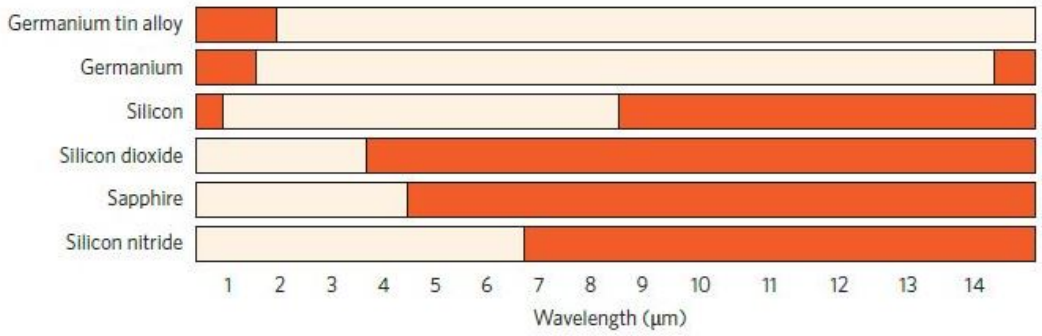


FIGURE 1.9: IR wavelength range over which waveguide propagation loss is less than 2 dB/cm. The white areas represent optical transparency; the red areas signify high loss [62].

In addition, its refractive index is high (4.02 at 3.8 $\mu$m) meaning higher refractive index contrast to air than that of Si to $SiO_2$. Furthermore, optical modulation, non-linear effects and carrier mobility are larger in Ge compared to Si. The work carried out in this thesis focuses on developing Ge low loss waveguides in order to be integrated with light sources in the future. The platform used for this purpose is Ge-on-SOI at 3.8 $\mu$m wavelength. However, the main aim is to operate at wavelengths longer than 4 $\mu$m, therefore due to the limitations in terms of absorption of $SiO_2$, alternative platforms such as suspended Si [63] have also been investigated.

As already mentioned Silicon Photonics offers a great opportunity for the development of low-cost, mass-manufactured, miniaturised, optical sensor systems. Vibrational spectroscopy based systems in particular are where chip-scale integrated systems are attractive. SOI has been the main platform for such systems due to its transparency range (1.2-4 $\mu$m) [64], given that suitable integrated light sources and photodetectors are available. Si and Ge, the two main materials that are broadly used in silicon photonics, would be the ideal candidates for the monolithic development of PICs. However, these two materials have an indirect bandgap, rendering monolithic laser integration onto PICs infeasible at the moment. Although recent developments have shown that light sources can be realised using strained Ge [65], the technology is not yet mature. On the other hand, high performance semiconductor lasers have been realised in III-V semiconductors. Therefore, in order to achieve the development of comprehensive PICs, there is an apparent need for the heterogeneous integration of III-V semiconductor light sources on PICs. This integration can be realised in numerous ways which are thoroughly discussed in 2.3.

The intention of the work included in this thesis is to demonstrate a range of devices operating in the MIR that constitute the building blocks required for the development of systems that sensing applications will benefit from. In particular, most of the effort has been driven towards the integration of QCLs operating in the MIR, which have been developed at the university of Sheffield, onto a GOS platform. The other point

of interest in this thesis is the development of group-IV material platforms that can support a much wider wavelength range extending their functionality beyond what has been utilised to date. This thesis consists of the following chapters:

- Chapter 2 contains the literature review including recent results for various MIR waveguide platforms as well as their benefits and drawbacks. It also includes an extensive overview of the various photonic integration approaches and analyses their advantages and disadvantages.
- Chapter 3 details the work carried out on suspended Ge. The chapter starts with the waveguides developed for $\lambda = 3.8$ $\mu$m and then for $\lambda = 7.67$ $\mu$m and lastly for the longer wavelength of $\lambda = 9.5$ $\mu$m. The simulation tools, fabrication process and characterisation techniques are also presented in this chapter.
- Chapter 4 describes the development of the QCL integration with GOS waveguides using flip-chip bonding. This includes the detailed discussion on the simulations carried out for the various components comprising the whole device (angled waveguide facets, waveguide bends, grating couplers, etc.), the fabrication process and measurement setup used to characterise the final device.
- Chapter 5 discusses the conclusions for this thesis and describes possible future work.

# Chapter 2

# Literature review

In this chapter the literature review including recent results for various MIR waveguide platforms as well as their benefits and drawbacks is provided. Furthermore, an extensive overview of the various photonic integration approaches as well as a discussion on their advantages and disadvantages is also included.

## 2.1 Fundamental theory of waveguides

Waveguides are the main building block of every PIC. This section firstly presents the basic theory of the underlying principles of planar waveguides. Next, an extensive overview of the currently ongoing research for MIR photonics is provided by firstly describing various material platforms used and then by providing an extensive overview on the state-of-the-art device demonstrations.

To understand the operation of the waveguides presented in this thesis, a short description of the main types of waveguide geometries is provided. Next, Maxwell's equations will be used to provide an analysis of the planar waveguide.

The function of optical waveguides is to guide a light beam from one point to another. They are the fundamental building blocks of optical integrated systems. Their basic structure is comprised of a high-index core, through which the guided wave is propagated, and a low-index cladding surrounding the core. In general, the waveguide cross-section dimensions are of the same order of magnitude as of the the wavelength used.

There are several types of waveguides used in silicon photonics depending on the application including rib, strip, buried and slot waveguides, the first two being the most common types. The strip waveguide (Figure 2.1(b)) is mostly used for routing as it offers the ability to use tight bending due to the high mode confinement in the waveguide core. Rib waveguides (Figure 2.1(a)) are used in active devices such as modulators

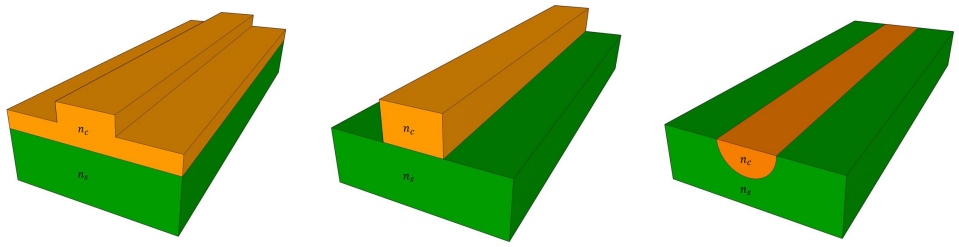

(a) Strip waveguide (b) Rib waveguide (c) Buried waveguide

FIGURE 2.1: Three main types of channel waveguides (a) strip, (b) strip and (c) diffused.

where electrical connections need to be made. Diffused (also known as buried) waveguides (Figure 2.1(c)) are formed by creating a high-index region in a substrate through diffusion of dopants, such as a Lithium Niobate ($LiNbO_3$) waveguide with a core formed by Titanium (Ti) diffusion. The sidewalls of this type of waveguides are not sharply defined due to the diffusion process. The thickness and width of the waveguide core are defined by the diffusion depth and distribution of the dopant respectively. The diffused dopants cause a change in refractive index that is approximately proportional to their concentration. Alternatively, materials can also be implanted using ion implantation. However, this process causes damages to the lattice and is therefore followed by annealing. Diffused waveguides have the advantage of low propagation loss (0.05 dB/cm [66]). This type of waveguides is used in integrated optics, for light modulation as it provides light guidance in small devices while controlling its flux. In this context, $LiNbO_3$ has always played a prominent role in the development of modulators due to its electro-optical properties [67]. Alternatively, buried waveguides can be realised using ion-implantation as well. In [68] integrated sub-micron erasable waveguides were realised for the first time on an SOI platform. The waveguides were formed by ion implantation induced damage, which can be subsequently processed with a localised laser treatment step to repair the crystalline structure. By employing such implanted waveguides, erasable directional couplers have been demonstrated with high coupling efficiency, which form the basic building block of an One-Time Programmable (OTP) photonic circuit. As a proof-of-principle demonstration, 1×4 and 2×OTP switching circuits have been successfully realised.

Oxide cladding is used for the protection of the devices and to allow placement of metal interconnects without increasing propagation loss due to the metal absorption. However, oxide cladding cannot be used at wavelengths higher than 4 $\mu$m due to the increasing absorption as explained in 1.3.

In order to implement a theoretical analysis based on Maxwell's equations the simplest optical waveguide structure, which is the step-index planar waveguide, is used. A planar waveguide consists of a high-index dielectric layer with thickness $h$ surrounded by a

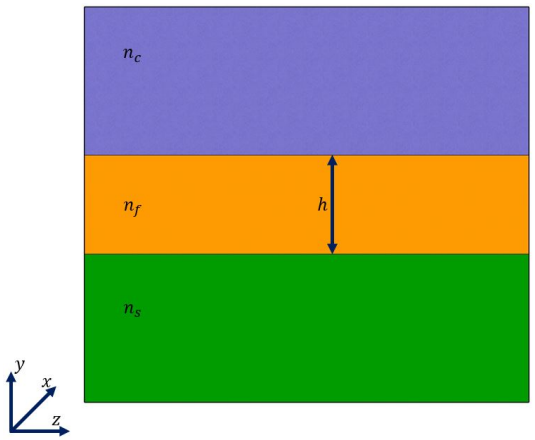


FIGURE 2.2: Schematic of an asymmetrical planar waveguide showing the three different layers and their respective refractive indices. From top: Cladding ($n_c$), guiding film ($n_f$) and substrate ($n_s$).

lower-index top cladding and bottom substrate, as shown in Figure 2.2, where the refractive index of the film $n_f$ is higher than the one of the substrate $n_s$ and upper cladding $n_c$. In addition, it is assumed that $n_s > n_c$, which forms an *asymmetric* waveguide.

Light is propagated along the $z$ axis, with its electric and magnetic field perpendicular to each other and both being perpendicular to the propagation direction ($z$). In a region of constant refractive index, the following wave equations for TE (2.1) and TM field (2.2) can be derived from Maxwell's equations. These describe the electric and magnetic field distribution in the waveguide [69]:

$$\frac{d^2E_x(y)}{dy^2} + [k_0^2 n^2(y) - \beta^2]E_x(y) = 0 \tag{2.1}$$

$$\frac{d^2H_x(y)}{dy^2} + [k_0^2 n^2(y) - \beta^2]H_x(y) = 0 \tag{2.2}$$

where $E$ and $H$ are the electric field and magnetic field, respectively. $k_0$ is the wavenumber and $\beta$ is the propagation constant and are given by:

$$k_0^2 = \left(\frac{2\pi}{\lambda_0}\right)^2 = \mu_0\epsilon_0\omega^2 \tag{2.3}$$

$$\beta = k_0 N \tag{2.4}$$

where $\lambda_0$, $\mu_0$ $\epsilon_0$, $\omega_0$ and $N$ are the free space wavelength, free space permeability, free space permitivity, angular frequency and effective refractive index of the mode, respectively.

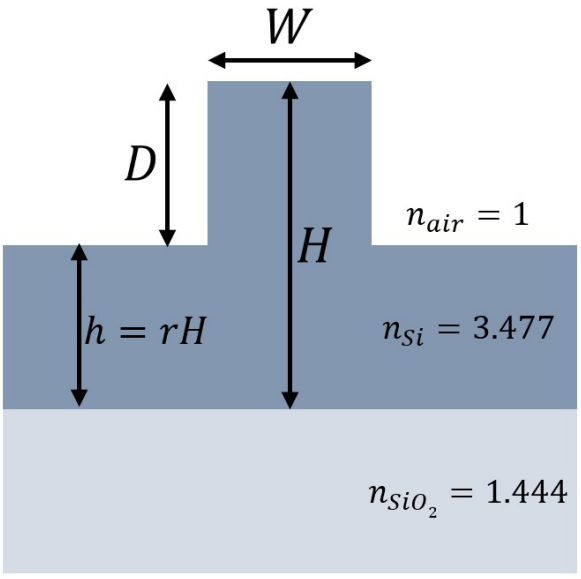


FIGURE 2.3: Schematic of the cross-section of an SOI rib waveguide.

Each of the equations 2.1 and 2.2 corresponds to the one of the two different orthogonal polarisations of the mode. The first one is the TE mode where, the electric field is polarised in y-direction (normal to the propagation direction ($z$)) in which $E = E_x$, $E_y = E_z = 0$, $H_x = 0$. The second one is the TM mode, where the magnetic field is polarised in y-direction in which $H = H_x$, $H_y = H_z = 0$, $E_x = 0$. These equations are second-order differential equations, and to solve them, additional conditions must be imposed. The solution to equations 2.1 and 2.2 can be found in [69]. It is worth noting that the result consists of a sinusoidal electric (and magnetic) field in the core ($n_f$) and exponentially decaying (evanescent) fields in the cladding ($n_c$) and the substrate ($n_s$). The field inside the core can be considered as transverse standing wave for which only discrete field distributions are possible, which are referred to as guided modes. A waveguide is considered as single-mode or multi-mode depending on the number of modes that can be supported in it. The number of modes that a waveguide can support depends on its geometry as well as the refractive indices of the core and the cladding layers. A simple expression for the Single-Mode Condition (SMC) for large rib waveguides (Figure 2.3) was first proposed by Soref et al. [70]:

$$\frac{W}{H} \leq 0.3 + \frac{r}{\sqrt{1 - r^2}} \tag{2.5}$$

(for $0.5 \leq r < 1$), where $r$ is the ratio of slab height to overall rib height, and $W/H$ is the ratio of waveguide width to overall rib height as shown in Figure 2.3. The analysis carried out was limited to shallow etched ribs ($r > 0.5$) and the waveguide dimensions were assumed to be larger than the operating wavelength.

## 2.2 Review of research for mid-infrared photonics

In this section, silicon photonics for MIR applications will be comprehensively reviewed, with regard to the state-of-the-art achievements from various device demonstrations using alternative material platforms by various groups in the field. In addition, an assessment of the outlook of potential future research topics and engineering challenges along with opportunities are provided.

### 2.2.1 Material platforms and waveguides

Silicon photonics has been mainly connected with the development of PICs operating in the NIR wavelength region. This technology has attracted great research interest in the past decade due to the increasing demands for high data transmission capacity in telecommunication applications and data centres. The key driving force that renders silicon photonics a strong candidate is its fabrication compatibility with the well-developed CMOS technology, which combines low-cost and high volume of production. However, the NIR is not the only main point of interest. The MIR has attracted great research over the past decade, research has been driven by the need to enable potential applications described in 1.2. However, many substances have strong absorption lines at wavelengths longer than 4 $\mu$m making the SOI platform not suitable for such applications. For example, as already mentioned, $CH_4$ has a stronger absorption line in the 7-8 $\mu$m wavelength region. Therefore, alternative material platforms, which will enable the exploitation of a wider range of the MIR, need to be investigated.

Low propagation loss in optical waveguides is the main requirement that should be met towards the development of PICs. In pursuit of this goal, various material platforms and geometric structures have been demonstrated.

- **Silicon-on-Insulator (SOI)**

  In the last decade, SOI has been the most attractive material platform for the development of PICs and this is due to a number of reasons. Firstly, crystalline Si is an exceptionally good optical material that exhibits low absorption in the 1.2-8 $\mu$m wavelength region which makes Si the most suitable candidate for telecom applications at 1310 and 1500 nm. Moreover, the high refractive index contrast ($\Delta$n) of 2.02 at 1550 nm between Si and $SiO_2$ results in high optical mode confinement in a waveguide cross-section of sub-wavelength dimensions. This reduces the component's size enabling the integration of compact photonic components on a chip. Lastly, SOI is compatible with the mature and well-developed CMOS manufacturing processes. SOI-based waveguides that exhibit low propagation loss down to 0.6-0.7 dB/cm for both TE and TM polarisations have been demonstrated at 3.39 $\mu$m using a 2 $\mu$m thick Si layer [71]. In 2012 and 2013, other developments report

propagation losses in the 3-5 dB/cm rage at 3.8 $\mu$m using 500 nm and 400 nm thick strip SOI waveguides [53, 54]. Other demonstrations have been reported for wavelengths up to 4 $\mu$m by several research groups by optimising the cross-section design of the waveguides [30, 51, 52, 55, 72]. In terms of fabrication compatibility, this is the most commonly chosen platform for wavelengths <4 $\mu$m). At longer wavelengths, mode sizes become bigger meaning that mode confinement is reduced which results in leakage of the optical mode into the substrate. To minimise it, the thickness of the BOX has to be taken into account. Commercially available SOI wafers are provided with either 2 or 3 $\mu$m of BOX. The first is suitable for operating wavelengths around 2 $\mu$m, while at higher wavelengths around 3.75 $\mu$m a thicker BOX is required.

- **Suspended silicon membrane**

  A novel solution to extend the operation of SOI and exploit the full transparency range of Si is to remove the lossy BOX by several techniques thus creating a suspended Si membrane. There are several advantages of using suspended structures. Firstly, they can be fabricated using commercially available SOI wafers using the existing well-developed CMOS fabrication processes available. In addition, by accurately controlling the structure's dimensions, its optical properties such as dispersion, can be engineered. The first demonstration of such structure for the MIR was reported by Cheng et al. in 2012 [73]. In this work the BOX in a typical SOI wafer is locally removed using HF to create a SMW where access to the BOX is provided by an array of periodic holes alongside the waveguide. The initial platform comprised a 340 nm thick Si layer on a 2 $\mu$m thick BOX. Rib waveguides were defined by a combination of Electron-beam (e-beam) lithography and ICP etching steps. The dimensions of the waveguides were: Width (W) = 1 $\mu$m and etch depth (ED) = 240 nm. The influence of the periodical holes on the optical mode, the *Bragg* grating coupler coefficient ($\kappa$). From simulations, the minimum distance between the holes and the waveguide (W1) at which $\kappa$ is negligible, was 2 $\mu$m. To take into account a margin for error, this distance was selected to be 2.5 $\mu$m. The holes had a distance between them of (L1) = 2 $\mu$m while each one had a width of (W2) = 0.5 $\mu$m and a length of (L2) = 1 $\mu$m. For these dimensions, the corresponding wet etching time for the complete removal of the BOX was 80 minutes. Figure 2.4 shows an SEM image of the cross-section of a fabricated SMW. The waveguides were characterised at $\lambda$ = 2.75 $\mu$m and the resulting propagation loss was 3±0.7 dB/cm.

  However, the described approach involved 2 dry etch steps, one to define the rib waveguide and a second one to define access holes. Furthermore, the mechanical stability of the structure was limited due to the large distance of the waveguide core from the fully etched holes required to reduce reflections resulting in wide and thin Si membranes. An alternative design was proposed by Penades et al.

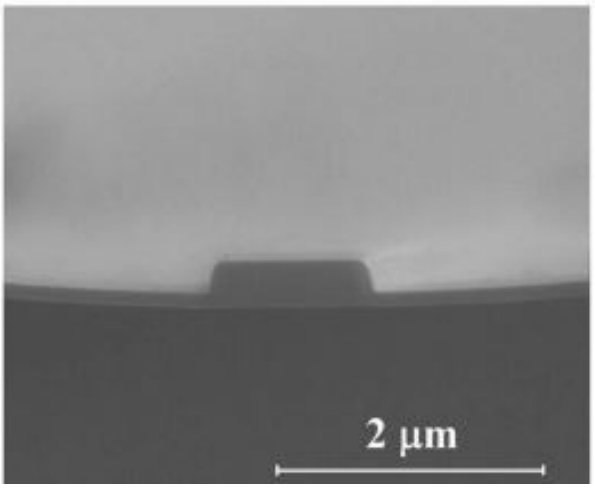


FIGURE 2.4: Cross-sectional SEM image of the SMW showing the complete removal of the underlying BOX [73].

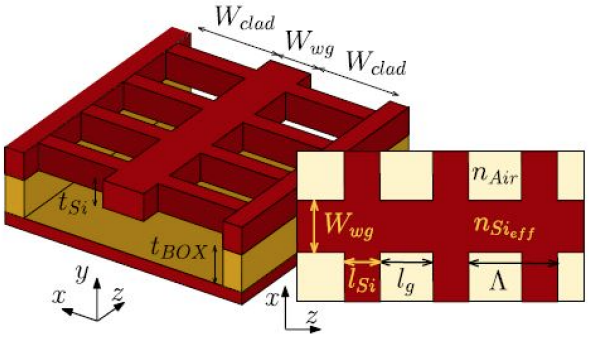


FIGURE 2.5: Schematic of the suspended waveguide with SWG lateral cladding [74].

in 2014 [74] where a new concept was introduced. The main is idea is to have a sub-wavelength lattice of holes that will act as both a lateral waveguide cladding as well as access to the BOX allowing for its subsequent removal using HF as shown in Figure 2.5. The advantage of such a design is that only 1 dry etch step is required. Moreover, an improvement of the the mechanical stability of the structure is achieved as the waveguide core remains unetched unlike in [73]. The dimensions of the waveguide core and the SWG cladding are determined using Bloch–Floquet mode calculations. The propagation loss achieved using this approach was 3.4 dB/cm at 3.8 $\mu$m.

The same approach was used by the same group upon optimising the waveguide geometry and fabrication process [75] to develop 1.3 $\mu$m wide suspended strip waveguides using a 500 nm thick Si layer on a 3 $\mu$m thick BOX achieving a remarkably low propagation loss of 0.82 dB/cm at 3.8 $\mu$m. However, the potential of this structure was not fully exploited until 2018 when the same group demonstrated suspended Si waveguides at $\lambda = 7.67$ $\mu$m. The propagation loss was measured before and after the BOX removal to be 62.3±9.6 and 3.1±0.3 dB/cm respectively.

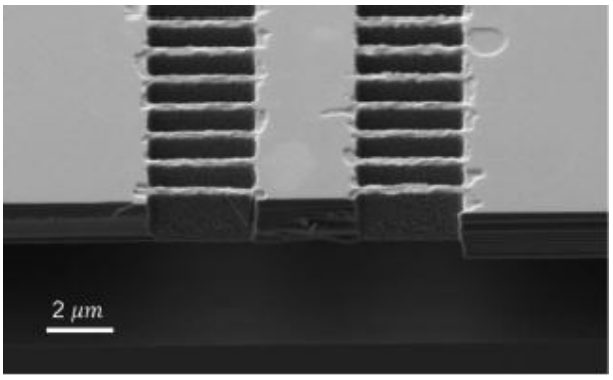


FIGURE 2.6: SEM image of the cross-section of a cleaved suspended waveguide. It can be seen that the underlying BOX has been completely removed. The roughness at the etched parts of the waveguide caused by the HF etching is also apparent [63].

The authors attribute the loss to multiple sources. The material loss and substrate leakage contributed by ∼2.2/dB/cm in total according to simulations while the remaining 0.9 dB/cm emanated from scattering caused by the HF etching as observed from the SEM image shown in Figure 2.6.

Nonlinear applications are where suspended structures have attracted interest. This is due to the fact that this type of waveguide offers sub-wavelength mode confinement with effective modal area of ∼1 $\mu m^2$. This results in a significant enhancement of the nonlinear optical interactions which enables efficient wavelength conversion using low pulse energies. This enables the development of nonlinear optical systems that exhibit small size, low complexity, and reduced power consumption. In a recent demonstration, suspended Si waveguides with a SWG cladding were used for frequency comb generation across a bandwidth of 2.0–8.8 $\mu$m [76].

- **Silicon Nitride (SiN)**

  SOI has some drawbacks that make it unsuitable for some emerging applications of silicon photonics. For example, Si is not transparent in the visible wavelength range (±400-700 nm). SiN is an alternative material platform that has high index contrast with Si ($\Delta n = 1.44$ at 1550 nm), and similarly to SOI, it is CMOS compatible. SiN is typically deposited by either Low-Pressure Chemical Vapor Deposition (LPCVD) at high temperature (>700 °C) or by Plasma-Enhanced Chemical Vapor Deposition (PECVD) at low temperature (<400 °C). Low loss waveguides have been demonstrated using this material in the MIR. In [77] SOSN, the authors report propagation loss as low as 0.16 dB/cm at $\lambda = 2.65$ $\mu$m. Apart from the guiding material, SiN is acting as a bottom cladding material in SOSN waveguides replacing the BOX, thus extending the transparency range beyond 4 $\mu$m of wavelength. Waveguides with propagation loss of 5.2 and 5.1 dB/cm for TE and TM respectively at $\lambda = 3.39$ $\mu$m have been demonstrated [78]. Fabrication of the SOSN platform is achieved by bonding. Firstly, An SOI sample is coated with a low-stress SiN layer by PECVD. Then the SiN is directly bonded to a Si handling

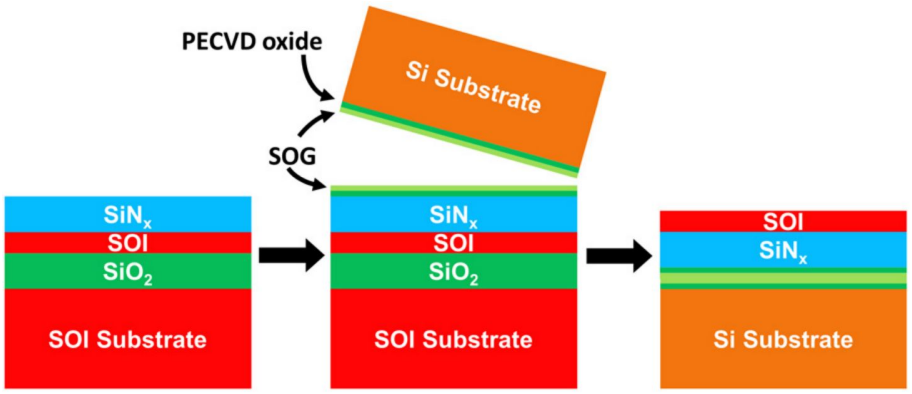


FIGURE 2.7: Schematic of SOSN fabrication process [78].

sample after planarising the surface using spin-on-glass (SOG). The fabrication process is depicted in Figure 2.7. To complete the process, the final structure is annealed at 450 °C in a nitrogen environment. To remove the back Si a combination of lapping and wet etching using Tetramethylammonium Hydroxide (TMAH) is carried out. Finally, the BOX layer is removed using diluted HF acid solution exposing the thin Si film to process the waveguide. The authors note that bonding is carried out in vacuum as opposed to at atmospheric pressure in order to avoid the formation of undesired bubbles. This is crucial for achieving low propagation loss as these bubbles can act as a source of loss since they could cause dislocations in the silicon layer resulting in scattering.

- **Silicon-on-Sapphire (SOS)**

  Another alternative to SOI that has been investigated is SOS. This platform was firstly used in the electronics industry as an alternative to bulk Si [79] due to sapphire's high insulating capability as a substrate resulting in low parasitic capacitance and lower power consumption compared to bulk Si [80]. This platform has attracted research interest since it is commercially available, it provides a high refractive index contrast between the core and the bottom sapphire cladding of $\Delta$n $\sim$1.7 resulting in high optical mode confinement, and it is suitable for operation in the MIR since sapphire is transparent up to 5.5 $\mu$m. Researchers have reported waveguides based on the SOS platform for the MIR. In [81], the authors report 1.8×0.6 $\mu$m waveguides operating at 4.5 $\mu$m with a propagation loss of 4.3 $\pm$ 0.6 dB/cm. 100 mm diameter wafers were used where the Si layer was epitaxially grown on a sapphire substrate. The waveguides were defined by a combination of e-beam lithography and dry etching using Tetrafluoromethane ($CF_4$) plasma. Next, a wet resist removal was used to strip the resist. However, it was not completely removed leaving residue on the waveguide surface. The chip was then cleaned using a piranha etch, which resulted in a considerable waveguide loss improvement. An SEM image of the fabricated SOS waveguide is shown in Figure 2.8.

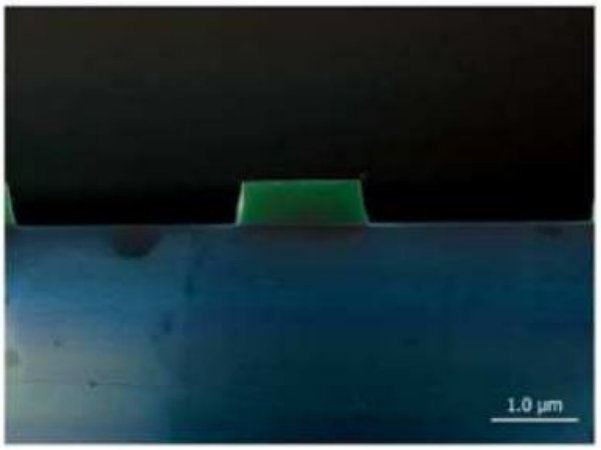


FIGURE 2.8: False-colour SEM image of the cleaved end-facet of an SOS waveguide. Silicon is depicted in green while sapphire in blue [81].

However, compared to what has been achieved using other platforms, the propagation loss achieved was fairly high. Another demonstration reports propagation losses below 1.4 dB/cm near $\lambda = 2.08$ $\mu$m and less than 2 dB/cm at $\lambda = 5.18$ $\mu$m [82]. The results achieved at the longer wavelength in particular, represent a significant reduction over the best previously published results in this wavelength range. In this work, the low loss is attributed to the epitaxial growth process used to fabricate the SOS material stack, resulting in a dramatic reduction of defect density. In this work, the waveguides were defined using an I-line stepper mask aligner that can achieve a resolution of ~400 nm. This contributed to minimising the sidewall roughness, thus reducing scattering losses.

Although there are promising results achieved using SOS, there are not substantial advantages over other material platforms, in terms of the low loss range given the fabrication difficulty of sapphire due to its hardness. In addition SOS wafers suffer from high dislocation defect densities at the Si–sapphire interface [83]. Therefore, the Si layer has to have a minimum thickness of 600 nm to achieve low propagation losses. Moreover, the sapphire substrate exhibits high loss beyond 6 $\mu$m and typical SOS wafers involve more complicated fabrication processes, and are more expensive than commercially available SOI wafers.

- **Silicon-on-Porous-Silicon (SiPSi)**

  An additional proposed platform for MIR devices is the SiPSi in which the bottom cladding consists of a Porous Silicon (PSi) layer, formed in the same Si wafer using high-energy proton beam irradiation and electrochemical etching. In [52] the authors demonstrate 4×2 $\mu$m strip waveguides at 1.55 and 3.39 $\mu$m. Figure 2.9 shows an SEM image of the proposed waveguide structure.

  The resulting propagation losses were 2.1 ± 0.2 dB/cm at 1.55 $\mu$m and 3.9 ± 0.2 dB/cm at 3.39 $\mu$m. In the same report, SOI waveguides of the same dimensions were also fabricated with a propagation loss of 0.6-0.7 dB/cm at 3.39 $\mu$m. The loss

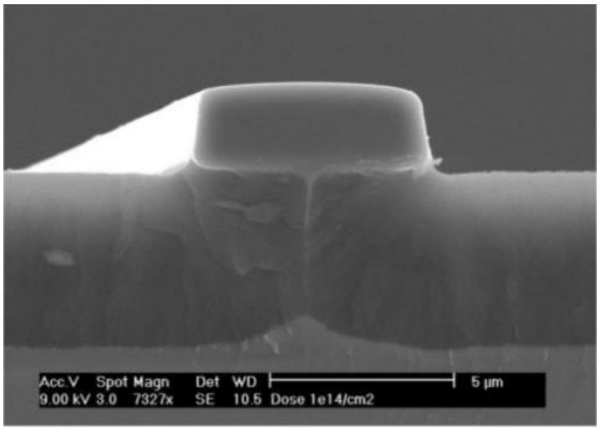


FIGURE 2.9: Cross section of a SiPSi waveguide [52].

figures of the SiPSi are noticeably higher than than those of SOI waveguide, mainly due to the the high-energy irradiation which has resulted in material damage and therefore scattering loss. Despite the higher propagation loss, SiPSi exhibits the highest mechanical stability among all waveguide types fabricated on a standard Si wafer, however, accurate control of the high-energy irradiation is needed in order to to avoid damaging the guiding region which will lead to an increased propagation loss.

- **Germanium-on-Silicon (GOS)**

  As discussed in the previous sections, Si based platforms have been widely used for photonic integrated circuits in the MIR, However, the intrinsic absorption of Si at wavelengths longer than 7.7 $\mu$m (i.e., 2.14 dB/cm at 7.67 $\mu$m, increasing to 4.6 dB/cm at 9 $\mu$m and 9.3 dB/cm at 11 $\mu$m [84]) renders Si-based MIR integrated devices unable to operate in the long-wave infrared fingerprint spectral region (8–15 $\mu$m). Ge has become a material of high interest for MIR integrated photonics due to its CMOS compatibility, wide spectral transparency window (2–15 $\mu$m) [62], high refractive index (n = 4 at 7.67 $\mu$m), and high third-order nonlinear susceptibility ($\sim 10^{-18}$ $m^2/V^2$) [62]. These features enable the exploitation of a wider wavelength range in the MIR, as well as the development of small-footprint and high-efficiency nonlinear devices. The first demonstrated work where Ge was used as guiding material in the mid infrared was in [85]. The authors reported single TM mode strip waveguides fabricated using GOS at 5.8 $\mu$m with a propagation loss of 2.5 dB/cm measured using the *Fabry–Perot* resonance method. This loss value is attributed to the sidewall roughness since Ge has low intrinsic absorption in the MIR. Moreover, due to the 4.2% lattice mismatch between Si and Ge, dislocations form in the first few hundred nanometers in the interface between them. These defects cause scattering contributing to the propagation loss. GOS waveguides have also been demonstrated at higher wavelengths. In [86] the authors report waveguides for the 7.5-8.5 $\mu$m wavelength range, with a minimum propagation

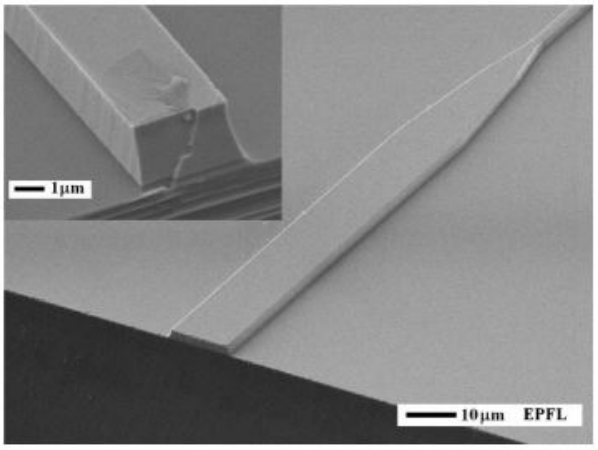


FIGURE 2.10: SEM image of the 2 $\mu$m GOS waveguide [86].

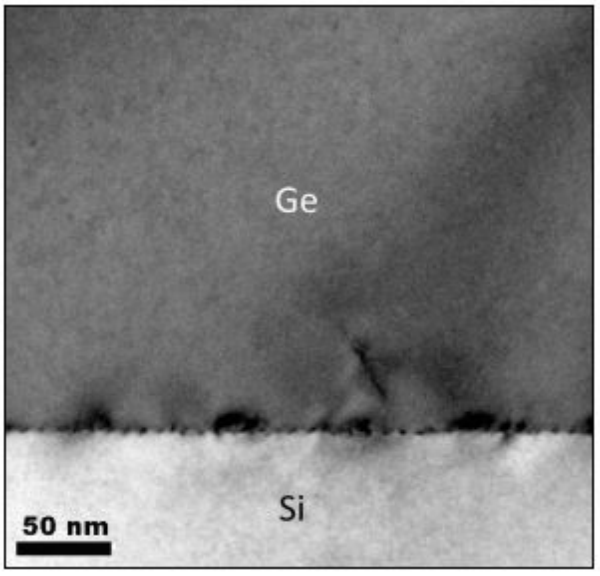


FIGURE 2.11: TEM images of the Ge/Si interface showing that the defects are mainly accumulated at the interface [87].

loss of 2.5 dB/cm at 7.575 $\mu$m. The loss sources are investigated however there is not one being the dominant. Figure 2.10 shows an SEM image of the proposed GOS waveguide.

However, the lowest propagation loss ever reported was in 2015 from the same group [87]. In this work 2.9×2.7 rib waveguides with an etch depth of 1.7 $\mu$m were demonstrated exhibiting a propagation loss of 0.58±0.12dB/cm at a wavelength of $\lambda = 3.8$ $\mu$m. The use of a thick Ge layer resulted in a lower optical mode interaction with the defects at the Ge/Si interface. Moreover, TEM images of this interface reveal that the threading dislocations are accumulated at the interface and not propagated along the Ge layer as shown in Figure 2.11.

In addition, the use of a combination of high-resolution e-beam lithography and ICP etching, resulted in vertical etching profile with low roughness which helped

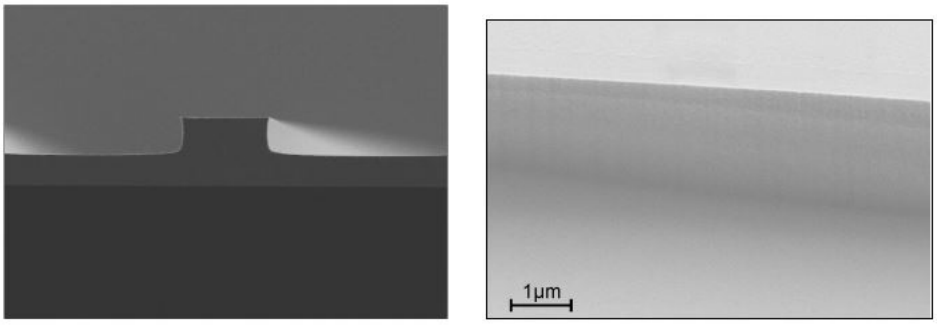


(a) Cleaved waveguide cross-section (b) Etched waveguide sidewall

FIGURE 2.12: SEM images of the proposed GOS waveguide structure proposed in [87]

reduce scattering and in turn the propagation loss as seen from the SEM images in Figure 2.12

The achieved loss is considerably lower what was reported in [85] which is due to the thinner Ge layer (2 $\mu$m) that was used and the longer wavelength (5.8 $\mu$m), resulting in lower optical mode confinement in the waveguide, hence, higher interaction with the defects.

Recently, advances towards the exploitation of the full transmission window of the GOS platform have been made. In [88] the authors demonstrate 4×2 $\mu$m rib waveguides with an etch depth of 1 $\mu$m at wavelengths ranging from 7.5 to 11 $\mu$m. The resulting propagation losses were measured with the $Fabry - Perot$ cavity method to be lower than 5 dB/cm for both TE and TM polarisation across the full wavelength range. More importantly, in the wavelength range from 10 to 11 $\mu$m the losses for TE polarisation are as low as ∼1 dB/cm, which is the propagation loss value reported at such long wavelengths.

- **Germanium-on-Silicon-on-Insulator (Ge-on-SOI)**

  GOS has been extensively utilised in developments in MIR photonics. However, it has been noted that Ge-on-SOI exhibits better performance in terms of thermal stability and electrical isolation due to the underlying $SiO_2$ buffer layer [89]. On the other hand, this raises the concern of optical absorption in the BOX, which limits the transparency range of this platform to wavelengths <4 $\mu$m. Though, this can be avoided by having a thick Si layer thus reducing the optical mode interaction with the lossy BOX. In [90] Ge-on-SOI strip waveguides with a minimum loss of ∼8 dB/cm at 3.682 $\mu$m are reported. Ge of thickness of 0.85 and 2 $\mu$m was used with a 220 nm thick Si layer on top of a 2 $\mu$m thick BOX. The top Ge layer was epitaxially grown using a Ultra-High Vacuum Chemical Vapour Deposition (UHV-CVD) system. Figure 2.13 shows TEM images of the fabricated waveguides showing large dislocation defects which have reached the Ge core overlapping with the optical mode thus increasing scattering, which in turn increases the propagation loss.

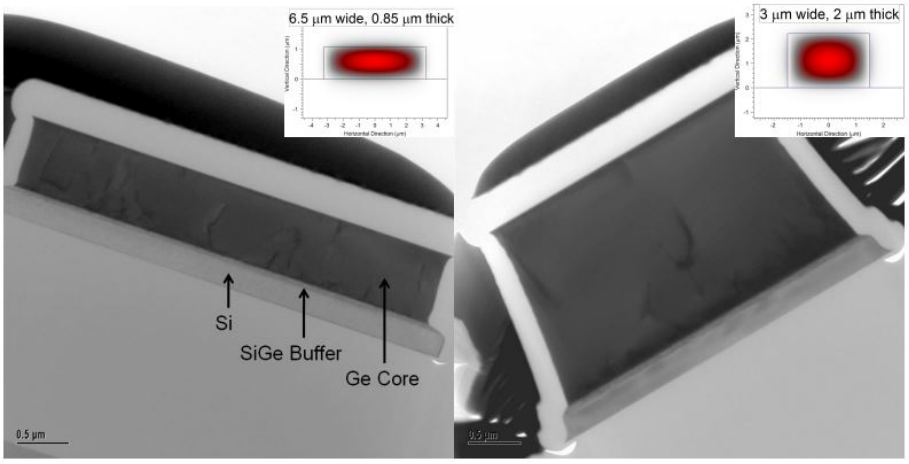


FIGURE 2.13: TEM images of the fabricated waveguide cross-section with 0.85 $\mu$m (left) and 2 $\mu$m (right) Ge core thickness. The simulated mode profiles are shown in the the corresponding image [90].

According to the authors, a high temperature anneal should follow the Ge growth to decrease the Threading Dislocation Density (TDD) thus obtaining a high quality Ge film. However, this on its own is not sufficient to dramatically reduce the propagation loss. In [89] the authors perform an annealing step at 800 °C to reduce the TDD, in a 2 $\mu$m thick Ge layer grown on a 3 $\mu$m thick SOI wafer. The measured propagation loss was 7 dB/cm showing that the annealing step is of low importance in reducing the propagation loss. Alternatively, Rapid Thermal Annealing (RTA) can be performed to cause the threading dislocations to be diffused out of the waveguide core, thus reduce scattering. Apart from the threading dislocations, the refractive index contrast between Ge ($n = 4.1$) and Si ($n = 3.4$) at $\lambda = 3.8$ $\mu$m [91] is considerably less than that of SOI ($\Delta n = 2.01$). This results in a large device footprint due to the low mode-confinement. Moreover, due to the large thermal-coefficient of Si in both GOS and Ge-on-SOI platforms, the device's sensitivity to thermal fluctuations is increased.

- **Germanium-on-Insulator (GOI)**

  An alternative material platform eliminating the issues of Si mentioned previously, is GOI. This platform was firstly demonstrated in [92] where a Ge layer of a few hundred nanometers of thickness stands on a thick BOX layer. Fabrication of the GOI wafer starts by depositing a $SiO_2$ capping layer a bulk Ge wafer to protect the latter's surface followed by implantation of $H^+$ ions under the Ge surface. The protective $SiO_2$ layer is then removed and a 10 nm Aluminium Oxide ($Al_2O_3$) layer is deposited in its place. Then, the implanted Ge wafer is bonded to a Si substrate which has a 2 $\mu$m $SiO_2$ layer on it which will compose the BOX. Finally, the wafer is annealed to cause splitting along the implanted $H^+$ ions and the top Ge surface undergoes a Chemical Mechanical Polishing (CMP) process to reduce surface roughness and obtain the final GOI wafer. The whole fabrication process

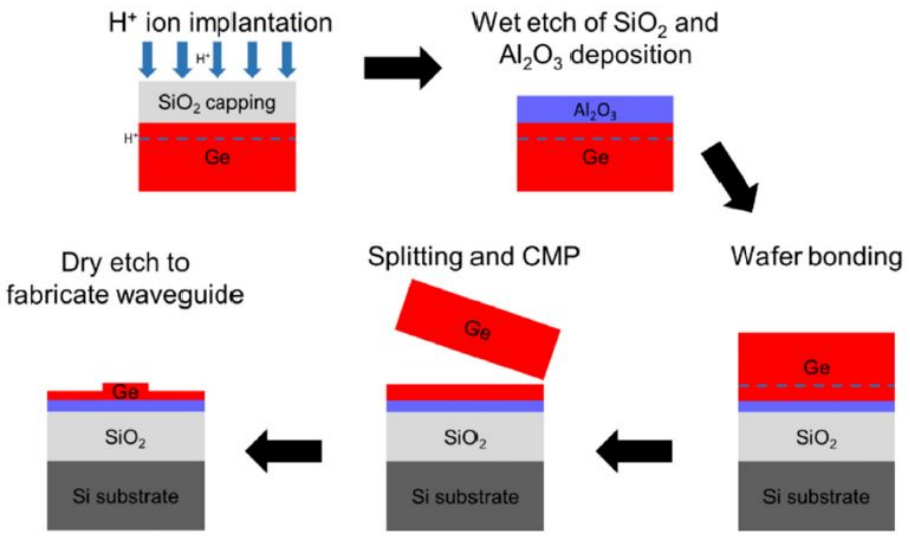


FIGURE 2.14: Fabrication process of the GOI platform using wafer bonding and layer splitting by annealing implanted $H^+$ ions [92].

is depicted in Figure 2.14. The advantage of this method overcomes the issue of the defect formation in the Si/Ge interface induced by epitaxial growth due to the lattice mismatch of the two materials in GOS and Ge-on-SOI.

In this work, a 400 nm thick Ge layer was used to fabricate 2 $\mu$m wide rib waveguides with an etch depth of 300 nm. The measured propagation loss was 14 dB/cm at a wavelength of 2 $\mu$m. The reason for obtaining such a high propagation loss (compared to what has been achieved in other Ge-based platforms) is not clearly stated. Presumably, surface roughness was the main source of loss as the waveguide dimensions were small thus increasing optical mode interaction with roughness. GOI fabricated using the same method but with a higher Ge thickness (515 nm) was used in [93]. In this report 1.1 $\mu$m wide rib waveguides with an etch depth of 265 nm were characterised exhibiting a propagation loss of 4.5±0.5 dB/cm at 3.8 $\mu$m.

However, the insulator used in the previous demonstrations was $SiO_2$ which limits the operation wavelength of the device. In order to overcome this limit, the BOX layer can be made of chalcogenide glass with a broader transmission range for operation in the MIR. In [94] the authors demonstrate the fabrication concept of a GOI platform with an Yttrium Oxide ($Y_2O_3$) BOX layer using a commercial GOI substrate with a $SiO_2$ BOX. The proposed platform enables operation at wavelengths up to at least 13 $\mu$m. The fabrication process started with the preparation of a commercial GOI substrate that had a 100 nm thick Ge layer and a 140 nm thick $SiO_2$ BOX. Next the $Y_2O_3$ is deposited on both the GOI and Si substrates by sputtering, upon removing the native oxide using diluted HF. The BOX that was deposited had a thickness of 2 $\mu$m. The ability to deposit a thick BOX enables the development of a platform with reduced loss due to substrate

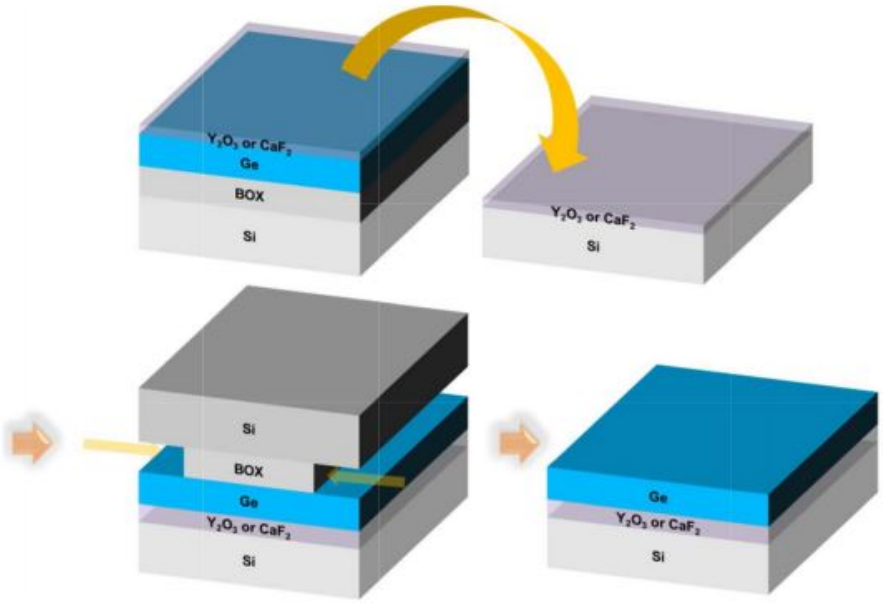


FIGURE 2.15: Fabrication process of the GOI platform using wafer bonding and layer splitting by selective etching of $SiO_2$ from commercial GOI substrate [94].

leakage loss. A CMP step followed to ensure low surface roughness before direct wafer bonding. The bonding quality is improved by treating the surface using $O_2$ plasma irradiation. The final platform is obtained upon separation from the donor wafer by selective etching of the $SiO_2$ layer. Figure 2.15 depicts the fabrication process flow.

- **Germanium-on-Silicon Nitride (GOSN)**

  As already mentioned, the relatively small refractive index contrast between Ge and Si compared to that of SOI results in larger bend radii in GOS and Ge-on-SOI meaning larger footprint of devices. Therefore, replacing the Si cladding with a material of a lower refractive index and high transparency in the MIR is essential. In addition to GOI, GOSN provides large refractive index contrast between the core and the cladding as well as a broad transparency range in the MIR as SiN is transparent at wavelengths up to ~7 $\mu$m. In [95], the authors report the development of a GOSN platform for the MIR. In this work, wafer bonding and layer transfer are used in order to realise the final platform. This technique was preferred over the direct growth of the Ge layer on SiN in which the quality of the deposited layer is poor with a high defect density at the Ge=SiN interface due to the later being amorphous resulting in high loss due to scattering. Fabrication of the structure begins with the growth of a 1.5 $\mu$m thick single crystal Ge on Si donor wafer using Reduced Pressure Chemical Vapor Deposition (RPCVD). This is then followed by coating of the deposited layer with SiN and finally transferred to another Si substrate to obtain the GOSN wafer. A 300 nm thick $SiO_2$ layer deposited using PECVD is used to assist bonding with the Si handle wafer. In this

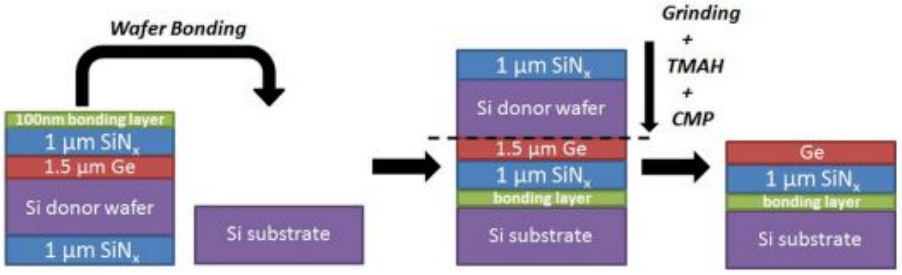


FIGURE 2.16: Fabrication of the GOSN platform using bonding and Layer transfer process. The bonding layer shown in the diagram is $SiO_2$ [95].

work, a hydrophilic type of bonding is used, resulting in the formation of water molecules during the bonding reaction. Therefore, $SiO_2$ is chosen as the bonding layer due to its ability to absorb these water molecules resulting in high bonding quality. The whole process is depicted in Figure 2.16.

The refractive index of the deposited SiN layer was measured by ellipsometry to be 1.9 at 3.8 $\mu$m meaning a refractive index contrast with Ge of $\Delta n = 2.2$. Based on the fabricated platform, waveguides were realised and characterised at 3.8 $\mu$m. Patterning the Ge layer was carried out using standard optical lithography which was then followed by Reactive Ion Etcher (RIE) to form strip waveguides with a width and height of 1 and 2 $\mu$m respectively as shown in Figure 2.17(a). As seen from this SEM, the waveguide sidewalls are not completely vertical which is attributed to the etching quality. Another SEM image taken from a different angle (Figure 2.17(b)) shows low sidewall surface quality also due to the etching. The measured propagation loss of the GOSN waveguides was 3.35 $\pm$ 0.5 dB/cm while the bend loss for a bend radius of 5 $\mu$m was 0.14 $\pm$ 0.01 dB/bend. The propagation loss achieved is higher than what has been demonstrated in GOS ([87]) but could be further reduced by engineering the surface quality of the waveguide sidewalls using alternative lithography and etching techniques such as e-beam and ICP respectively. For comparison, waveguides of the same dimensions were realised using GOS wafers where the Ge layer was grown in a similar manner. The propagation loss and bend loss measured were 8.18 $\pm$ 0.6 dB/cm and 3.35 $\pm$ 0.5 dB/cm respectively. The obtained results render GOSN a strong candidate for the development of PICs for MIR sensing applications, that exhibit small footprint and low power consumption.

- **Silicon-Germanium alloy-on-Silicon (SGOS)**

  Another platform that has attracted research interest is Silicon-Germanium alloy-on-Silicon (SGOS). $Si_{1-x}Ge_x$ alloys have been initially studied for microelectronic applications since the late 1950s. There are reasons for which it started to be studied as a material for the development of PICs for both NIR and MIR applications. First, The Si/Ge hetero-waveguide broadens the transparency range of Si to 1.9-16.7 $\mu$m assuming minimal mode overlap with the Si bottom cladding [96].

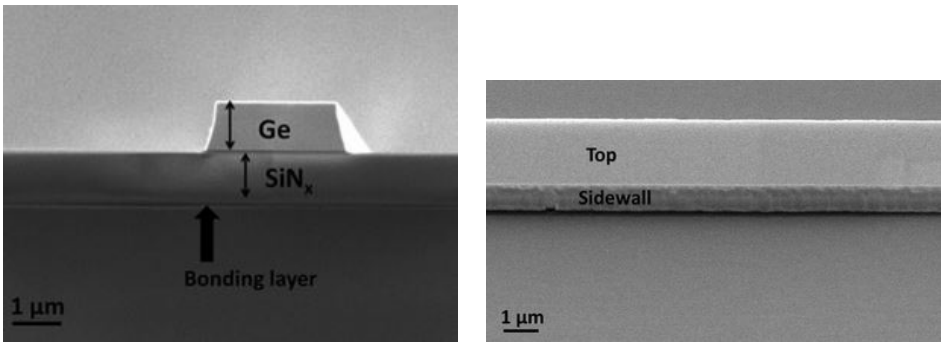


(a) Cross-section (b) Angled top view

FIGURE 2.17: SEM images of the fabricated GOSN waveguide [95].

Second, it provides the ability to accurately tune its optical properties including refractive index and bandgap, by precisely controlling the Ge concentration in the alloy [97]. Finally, its superior superior non-linear properties [98] enable non-linear applications such as Four Wave Mixing (FWM) [99]. Novel deposition techniques for the epitaxial growth of Si/Ge on Si substrates at temperatures as low as 700 °C have been reported since the early nineties [100].

Several groups have used the SGOS platform to demonstrate waveguides for the MIR. In [101], the design, fabrication and characterisation of SGOS based graded index waveguides and photonic integrated devices at wavelengths up to 7.4 $\mu$m. A 3 $\mu$m thick Si/Ge layer with a linearly varied Ge concentration (from 0-40%) was grown on a Si substrate using RPCVD. The Ge concentration was determined by gradual variation in the ratio between Germane ($GeH_4$) and Dichlorosilane ($H_2SiCl_2$) during growth. Strip waveguides of 3.3 and 7 $\mu$m width for single TM mode operation at $\lambda = 4.5$ and 7.4 $\mu$m that exhibited propagation losses of 1 and 2 dB/cm respectively.

A more recent demonstration reports three different waveguide structures with three different Ge-rich epilayer with different vertical index profiles and Ge concentrations that reaches 100% as opposed to [101]. The Si/Ge layers were deposited on commercial Si substrates using Low Energy Plasma Enhanced Chemical Vapor Deposition (LEPECVD). Different Ge concentration profiles have been defined along the growth direction. Figure 2.18(a) shows a cross-section view of the corresponding simulated TE mode of each epilayer along with the respective refractive index profile in Figure 2.18(b). All waveguide designs have a width of 4 $\mu$m and an etching depth of 4 $\mu$m.

For the 6 $\mu$m thick Si/Ge layer the measured propagation loss was as low as 2-3 dB/cm over a wavelength span from $\lambda = 5.5$ to 8.5 $\mu$m. The propagation loss spectral characteristic is obtained for all three waveguide designs over the same wavelength range for both polarisations where black and red lines correspond to quasi-TE quasi-TM polarisation respectively, as shown in Figure 2.19.

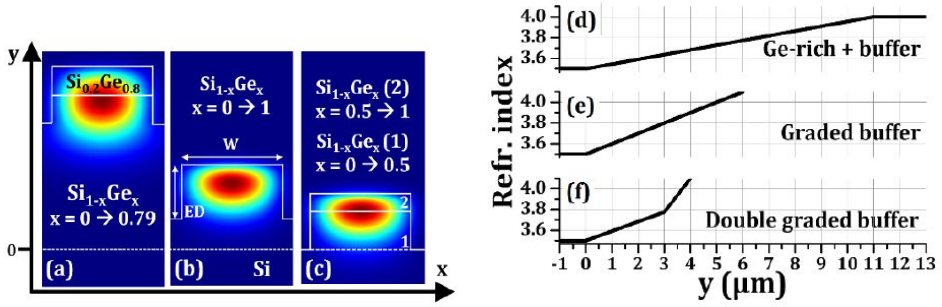


(a) Cross-section of the fundamental TE mode at $\lambda = 7.5$ $\mu$m showing the Si/Ge ratio in each direction (b) Corresponding refractive index profiles along the vertical graph. The horizontal dotted line marks the y-axis origin

FIGURE 2.18: Simulation data for corresponding to three Ge concentration profiles [102].

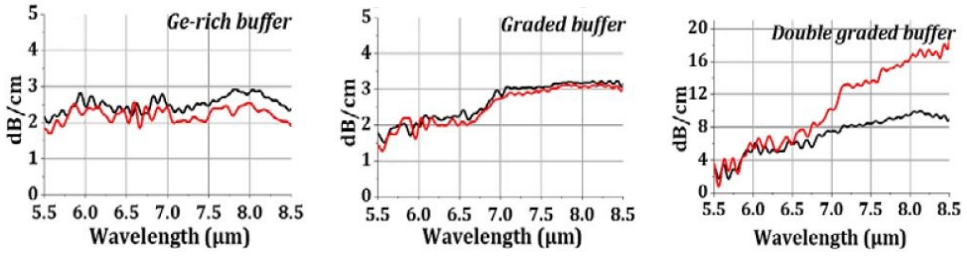


(a) (b) (c)

FIGURE 2.19: Propagation loss measured in the 5.5 - 8.5 $\mu$m wavelength range for the three investigated platforms. [102].

From the results, it can be seen that reducing the fraction of the guided mode that overlaps with the Si substrate leads to a flat low loss characteristic over a wide wavelength span.

Another recent demonstration at higher wavelength was presented by Montesinos-Ballester et al. [103]. In this work, ultra-broadband waveguides were experimentally demonstrated operating in the 5 to 11 $\mu$m wavelength range. Propagation losses from 0.5 to 1.2 dB/cm were obtained between 5.1 and 8 $\mu$m, while values below 3 dB/cm were measured between 9.5 to 11.2 $\mu$m. An increase of propagation losses was observed between 8 and 9.5 $\mu$m, but the values do not exceed 4.6 dB/cm in the whole wavelength range.

The advantage of the SGOS platform is that the formation of defects at the Ge-Si interface (in platforms where Ge is directly grown on Si substrates) is eliminated, reducing propagation loss due to scattering. However, its main issue is that the thickness of the graded waveguides is relatively large compared to other platforms which results in lower optical mode confinement making it difficult to realise tight bends. In [101] to obtain theoretical bending losses lower than 0.1 dB/cm, the

calculated bend radius for S-bends was 550 $\mu$m for $\lambda = 4.5$ $\mu$m and 1350 $\mu$m for $\lambda = 7.4$ $\mu$m.

A summary of the demonstrated waveguides along with their details is provided in Table 2.1.

### 2.2.2 Passive devices

In this section the fundamental principles of operation as well as recent results of the passive devices used in this thesis are provided.

#### 2.2.2.1 Suspended germanium waveguides

One of the main objectives of the work included in this thesis was to extend the operation of PICs to longer wavelengths, to reach the fingerprint wavelength region where sensing applications are the main point of interest. As discussed in section 2.2.1, several approaches have been investigated to achieve this, each one exhibiting its benefits and drawbacks. Specifically, Ge-based platforms seem to be the most promising ones mainly due to the transparency range of Ge as well as its CMOS compatibility. However, the main drawback of the Ge-based material platforms discussed is that the Si substrate starts to become very lossy beyond 8.5 $\mu$m. Using suspended Ge has the principal advantage of avoiding these material losses from any claddings so that Ge's entire transparency range can be exploited. A further advantage of suspended Ge compared to the GOS platform is that it has a high and symmetrical refractive index contrast between the core and upper and lower air claddings. In the case of GOS, there is a high index contrast between the Ge core ($\Delta$n $\approx$ 3.0 at 7.67 $\mu$m) and upper air cladding, but low contrast with the Si lower cladding ($\Delta$n $\approx$ 0.6 at 7.67 $\mu$m). This results in the need for thicker rib waveguides, which in turn will result in a weak mode overlap of the evanescent field with the upper air cladding. Therefore, suspended Ge enables the development of thinner waveguides that exhibit a larger evanescent field. This is a great advantage for sensing applications, in terms of sensitivity, where high mode overlap with an analyte surrounding the waveguide is desirable.

The first demonstration of a suspended Ge device for the MIR was reported by Kang et al. in 2017 [108]. In this work, the authors present a focusing SWG for light coupling into a suspended Ge-based PICs at $\lambda$=2.37 $\mu$m. The initial material stack used was the GOI where a 600 nm thick Ge layer was bonded with a 2 $\mu$m thick BOX (including the thickness of the $Al_2O_3$ bonding agent), obtained using the same fabrication process flow described in [92]. The thickness of the BOX was optimised to minimise substrate leakage as well as to achieve constructive interference between the diffracted light from the SWG and the light reflected from the air/substrate. Suspension of the Ge layer

TABLE 2.1: MIR waveguides demonstrated in various material platforms.

| No. | Platform | Structure type | Cross-Section Size ($\mu$m×$\mu$m) | Working Wavelength ($\mu$m) | Loss (dB/cm) | Pol | Year | Ref. |
|---|---|---|---|---|---|---|---|---|
| 1 | SOI | Strip | 0.9×0.22 | 2.1 | 0.6 | TE | 2012 | [72] |
| 2 | SOI | Rib | 0.9×0.34 ($H_{slab}$=0.1) | 2 | 1 | TE | 2016 | [51] |
| 3 | SOI | Rib | 2×2 ($H_{slab}$=0.8) | 3.39 | 0.6-0.7 | TE/TM | 2011 | [52] |
| 4 | | Rib | 2×2 ($H_{Slab}$=0.8) | 3.73 | 1.5±0.2 | | | |
| 5 | SOI | Rib | 2×2 ($H_{slab}$=0.8) | 3.8 | 1.8±0.3 | TE | 2012 | [53] |
| 6 | | Strip | 1×0.5 | 3.74 | 4.6±1.1 | | | |
| 7 | SOI | Rib | 1.35×0.38 ($H_{slab}$=0.22) | 3.76 | 5.3 | TE | 2013 | [54] |
| 8 | | Strip | 1.35×0.34 | | 3.1 | | | |
| 9 | SOI | Strip | 4×2.3 | 3-4 | <1 | TE | 2017 | [30] |
| 10 | SOI | Strip | 1.2×0.4 | 3.75 | 2.65 ±0.08 | TE | 2017 | [104] |
| 11 | | Rib | 1.2×0.4 ($H_{slab}$=0.16) | | 1.75 ±0.22 | | | |
| 12 | SOI | Suspended rib | 2×0.34 | 2.75 | 3±0.7 | TE | 2012 | [73] |
| 13 | SOI | Suspended strip | 1.1×0.5 | 3.8 | 3.4 | TE | 2014 | [74] |
| 14 | SOI | Suspended strip | 1.3×0.5 | 3.8 | 0.82 | TE | 2016 | [75] |
| 15 | SOI | Suspended strip | 2.6×1.4 | 7.67 | 3.1±0.3 | TE | 2018 | [63] |
| 16 | Ge-on-SOI | Suspended strip | 2.7×1 | 7.7 | 5.3±1 | TE | 2021 | [105] |
| 17 | SiN | Strip | 4×2.5 | 3.7 | 2.1 | TE | 2013 | [106] |
| 18 | SiN | Strip | 4×2.5 | 2.65 | 0.16 | TE | 2013 | [77] |
| 19 | SOSN | Rib | 2×2 ($H_{slab}$=0.8) | 3.39 | 5.1-5.2±0.6 | TE/TM | 2013 | [78] |
| 20 | SOS | Rib | 2×2 ($H_{slab}$=0.8) | 4.5 | 4.3±0.6 | TE/TM | 2013 | [81] |
| 21 | SOS | Strip | 1×0.29 | 5.18 | 1.92 | TE | 2011 | [82] |
| 22 | GOS | Rib | 3×4.3 ($H_{slab}$=1.2) | 7.575 | 2.5 | TE | 2017 | [86] |
| 23 | GOS | Strip | 2.9×2 | 5.8 | 2.5 | TM | 2012 | [85] |
| 24 | GOS | Rib | 2.7×2.9 ($H_{slab}$=1.2) | 3.8 | 0.6 | TE | 2015 | [87] |
| 25 | Ge-on-SOI | Strip | 6.5×0.85 | 3.682 | ∼8 | TE/TM | 2016 | [90] |
| 26 | Ge-on-SOI | Strip | 5.5×0.85 | 3.682 | ∼10 | TE/TM | 2016 | [107] |
| 27 | GOI | Rib | 0.6×0.22 ($H_{slab}$=0.05) | 2 | 14 | TE | 2016 | [92] |
| 28 | GOSN | Strip | 2×1 | 3.8 | 3.35±0.5 | TE | 2016 | [95] |
| 29 | SGOS | Strip | 3.3×3 | 4.5 | 1 | TM | 2014 | [101] |
| 30 | | | 7×3 | 7.4 | 2 | | | |
| 31 | SGOS | Rib | 13×6.2 ($H_{slab}$=6.9) | 5.1-8/9.5-11.2 | 0.5-1.2/<3 | TE/TM | 2020 | [103] |

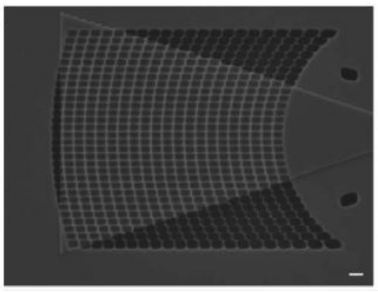

(a) Focusing SWG

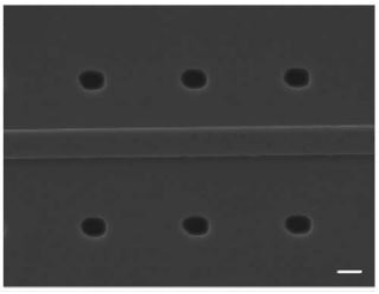

(b) Top view of the suspended Ge waveguide showing the etched periodical array of holes alongside the waveguide

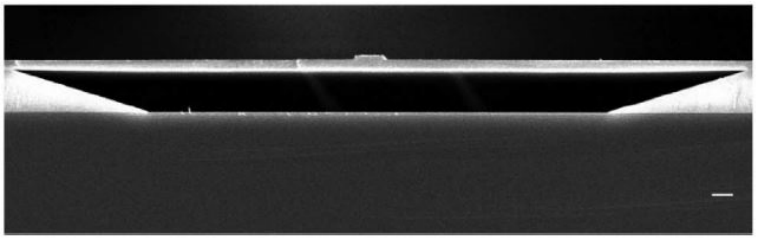

(c) Cross section of the suspended Ge waveguide showing the complete removal of the underlying BOX along a width of 30 $\mu$m while still maintaining structural rigidity

FIGURE 2.20: SEM images of the fabricated devices [108]

was carried out in the same fashion as in [73] where two dry etch steps where involved: one for the definition of the rib waveguide and one to form holes, placed far away from the waveguide core, through which access to the BOX for its subsequent removal is provided. The second etch step in this work defined the SWGs as well. 1.5 $\mu$m $\times$ 600 nm waveguides with an etch depth of 150 nm were fabricated SEM images of which are shown in Figure 2.20. However, the waveguides in this report had not been characterised thus the propagation loss that these type of waveguides are able to reach is unknown.

Shortly later, the same group demonstrated a MIR photonic crystal cavity at $\lambda$=2.35 $\mu$m using the same platform with a thinner Ge layer (300 nm) [109]. However, the waveguides were not characterised in this work either. The authors stated that the propagation loss of the suspended Ge waveguides connecting the input and output focusing SWGs was negligible. Though, this was not experimentally supported as these sections were only of 200 $\mu$m length and no dedicated propagation loss measurement was undertaken.

The propagation loss of waveguides fabricated using this approach was only experimentally measured by the same group a year later [110]. In this report the authors demonstrate MRRs using a 300 nm thick Ge layer at $\lambda = 2.15$ $\mu$m. Rib waveguides with a width of 900 nm and an etch depth of 150 nm were also fabricated and characterised achieving a propagation loss of 5.4 dB/cm which is considerably lower than what was demonstrated in [92].

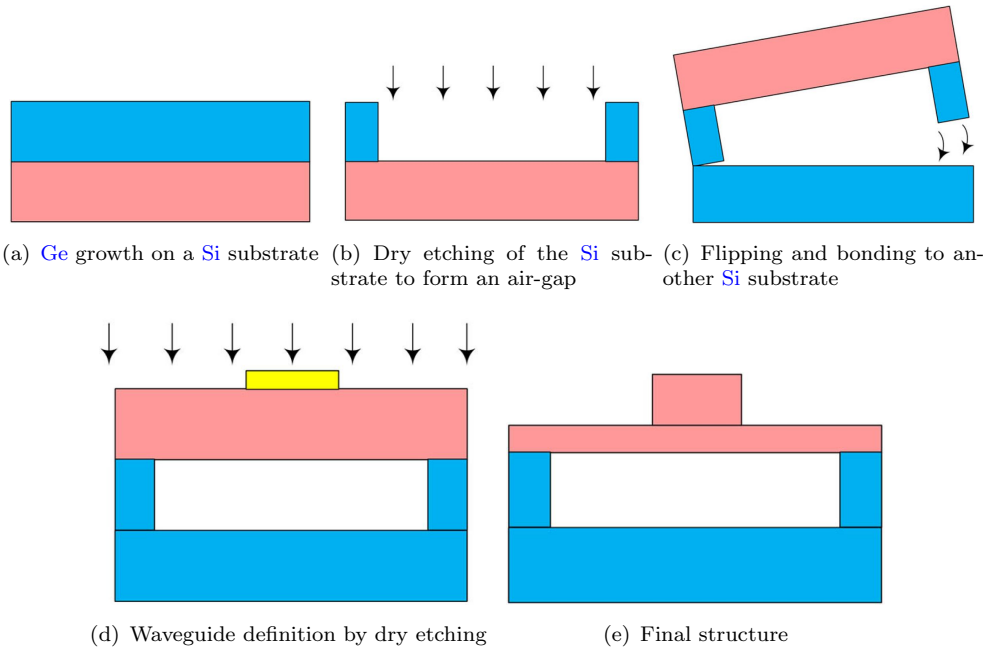

(a) Ge growth on a Si substrate (b) Dry etching of the Si substrate to form an air-gap (c) Flipping and bonding to another Si substrate

(d) Waveguide definition by dry etching (e) Final structure

FIGURE 2.21: A alternative fabrication process flow for obtaining a suspended Ge platform [111]

An alternative approach for suspending the Ge layer is proposed in [111]. Using this method, the Ge layer is firstly grown on a Si substrate using Chemical Vapor Deposition (CVD) techniques. The air-gap is then formed using RIE in the Si substrate. The etched die is then flipped and directly bonded onto another Si. Finally, the waveguide is defined using a combination of optical lithography with a metal mask, and dry etching. Using this approach the additional fabrication step of defining holes alongside the waveguide and wet etching of the BOX is avoided.

#### 2.2.2.2 Grating couplers

Light can be coupled from a fibre into a waveguide mode and vice versa by various methods as shown in Figure 2.22: prism coupling, grating coupling, butt coupling and lens coupling.

The prism coupling method uses a high-index prism to excite an incident wave to a guided mode as shown in Figure 2.22(a). It is particularly well adapted for planar waveguides. The implied surface of the prism has to be well polished and of good quality (i.e. without scattering defects). The major advantages of this method include: non-destructive, allows changing the position of the coupling point around the sample, easy manipulation and high efficiency, about 80% for input and output couplings and ability to selectively excite any guided modes by adjusting the angle of the incident light. However, it is difficult to align.

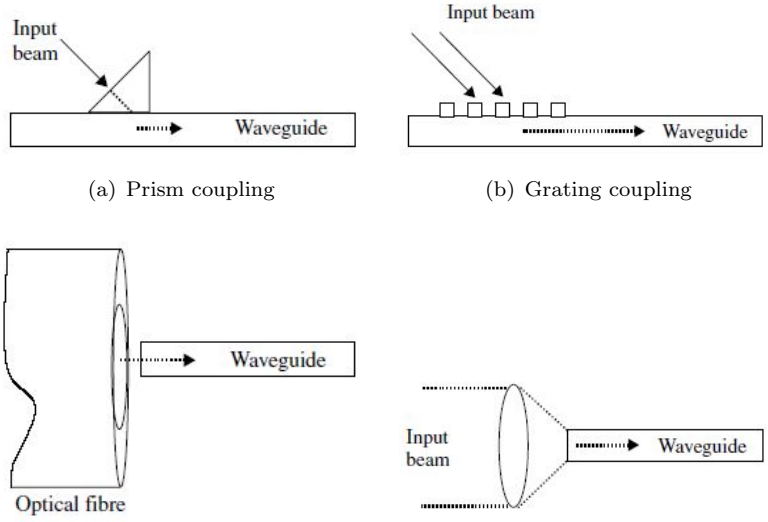


(a) Prism coupling (b) Grating coupling

(c) Butt coupling (d) Lens coupling

FIGURE 2.22: Four techniques for coupling light to optical waveguides [112].

The butt-coupling technique is the simplest method to excite a guided wave. A light wave with a profile similar to the guided mode is directly launched into an end-face normal to guided-wave propagation as shown in Figure 2.22(c). In order to obtain a high efficiency, the incident-wave profile must be as close as possible to the profile of the guided wave. The coupling end facet must exhibit extremely high optical quality and be without defects which can be prepared by polishing or cleaving treatments. End-facet flatness and the alignment accuracy are strictly required. The main disadvantage of this method is that it excites all of the guided modes simultaneously with different efficiencies thus making it difficult to select a particular excited mode when analysing a multi-mode waveguide. Furthermore, the mode field mismatch is another factor that affects coupling efficiency. In addition, in the case of Ge, due to its high refractive index, high Fresnel reflections occur at the air-waveguide interface.

The grating coupling technique relies on a periodic grating structure on the surface of the waveguide as shown in Figure 2.22(b). The grating coupling method is permanent and allows selection of a guided mode but the implementation requires a certain degree of delicate skill. The coupling efficiency depends on the grating structure, such as grating period ($\Lambda$) and grating etch depth ($\Delta$h). The grating coupler shows moderate tolerance to alignment. However, the efficiency is sensitive to the lateral beam position on the grating for a focused input beam. The fibre position has to be within approximately <1 mm above the grating to achieve the highest efficiency. Grating couplers are useful for coupling to waveguide layers of a wide range of thicknesses. However, the fact that the input beam must be introduced at a specific angle makes grating couplers not sufficiently robust for commercial devices. Nevertheless, they can be used using proper packaging. The input fibres can even be positioned so they can bend, so that external to the device the fibres come in parallel to the chip surface.

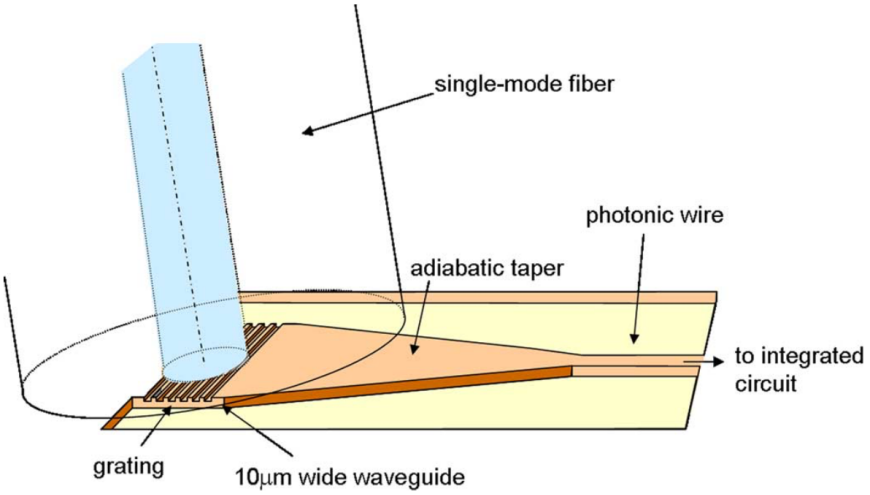


FIGURE 2.23: Coupling principle between fibre and waveguide using a grating coupler [113].

Finally, the lens coupling technique is similar to butt-coupling but it uses a microscope objective lens in order to focus light in one end of the waveguide.

In this work, coupling was carried out using grating couplers as shown Figure 2.23. The main advantages for which gratings couplers are chosen over other coupling techniques are compactness, low insertion loss and large alignment tolerance. Moreover, using grating couplers eliminates the need for a cleaved facet, which makes it possible for the light to be coupled in and out everywhere on the chip. However, grating couplers are not easy to fabricate. In addition, they can have reflections which are difficult to suppress.

In order to couple light into a waveguide mode, as depicted in Figure 2.22(a) or Figure 2.22(b), the components of the phase velocities in the direction of propagation (z direction) must be the same. This is referred to as the phase-match condition i.e., the propagation constants in the z direction of the input beam and the mode we want to couple light into must be the same. Consider first a beam (or ray) incident upon the surface of the waveguide at an angle $\theta_\alpha$, as shown in Figure 2.24.

The ray will propagate in medium $n_3$ with a propagation constant $k_0 n_3$. Therefore, the propagation constant in z-direction in medium $n_3$ will be:

$$k_z = k_0 n_3 \sin\theta_\alpha \tag{2.6}$$

The propagation constant in the z direction is of particular interest as it indicates the rate at which the wave propagates in the z direction which in this case is the direction of the waveguide. $k_z$ is often replaced in many texts by the variable $\beta$.

Therefore, the phase-match condition will be:

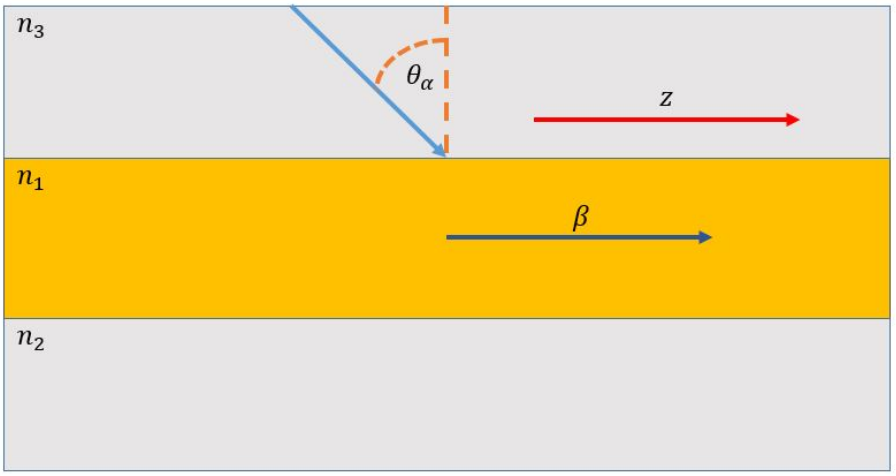


FIGURE 2.24: Light incident upon the surface of a waveguide.

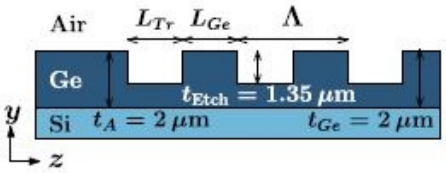


FIGURE 2.25: Schematic of the GOS grating coupler reported in [114] where $\Lambda$ is the grating period, $L_{tr}$ and $L_{Ge}$ are the lengths of the etched and unetched parts respectively and $t_{Etch}$ and $t_{Ge}$ are the etch depth and Ge thickness respectively.

$$\beta = k_z = k_0 n_3 \sin\theta_\alpha \tag{2.7}$$

Equation 2.8 is used to determine the period of the waveguide grating $\Lambda$ for a desired input angle in air for coupling to the mode with propagation constant $\beta_W$.

$$\Lambda = \frac{\lambda}{N - \sin\theta_\alpha} \tag{2.8}$$

where $\lambda$ is the wavelength of the coupled light, N is the effective index of the waveguide and $\theta_\alpha$ is the angle of the incident beam.

Various reports have demonstrated grating couplers for the MIR. In [114] a single-etch GOS grating coupler with an inversely tapered access stage, operating at 3.8 $\mu$m is reported for the first time. A coupling efficiency of -11 dB (7.9%) is achieved which is the highest value reported for a mid-infrared GOS grating coupler, exhibiting a reflectivity below -15 dB (3.2%). The structure of this grating coupler is shown in Figure 2.25

However, GOS grating couplers suffer from high back-reflection, low directionality, and low coupling efficiency, due to the high refractive index of Ge (~4.0) and the relatively low refractive index contrast between Ge and the Si substrate. An improved SWG

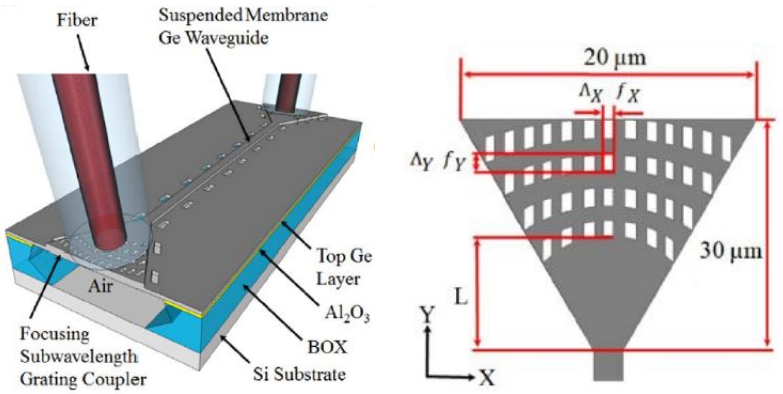


(a) 3D view of the waveguide and focusing SWG couplers

(b) Top view of the focusing SWG coupler

FIGURE 2.26: Schematic of the SWG coupler based on the suspended Ge platform proposed in [108]

coupler based on the suspended Ge platform operating at a wavelength of 2.37 $\mu$m is reported [108]. In this demonstration, instead of a conventional grating coupler structure, a focusing grating is implemented. Focusing grating couplers use curving lines' focusing character to obviate the need for a long adiabatic transition. This has the advantage of decreasing the taper's length resulting in a higher degree of integration due to the device's compactness. The resulting performance was a maximum coupling efficiency of -11 dB with the 1-dB bandwidth of ∼58 nm at a centre wavelength of 2.37 $\mu$m. Figure 2.26 shows a schematic of the proposed SWG coupler.

Another novel approach has been recently presented based on the suspended platform. In [115], a broadband all-dielectric micro-antenna operating at 7.67 $\mu$m is demonstrated. The proposed design is comprised of only two or three diffractive elements. The achieved simulated coupling efficiency is of $\sim$ 40% with a 1-dB bandwidth broader than 430 nm, which is almost twice compared to the typical fractional bandwidth (BW/$\lambda$) of a conventional grating coupler. Moreover, the proposed design is tolerant to fibre angle misalignments of $\pm 10°$. Figure 2.27 shows schematics of the proposed structure.

In order to obtain an efficient coupling between the wide region of the grating coupler and the waveguide, adiabatic tapers are used as spot-size converters. Normally, the function of the taper is to change the size and the shape of the optical mode to achieve a high coupling efficiency between two waveguides with different cross-sections. To achieve this, the taper must operate adiabatically; that is, the local first-order mode of the waveguide should propagate through the taper while undergoing relatively little mode conversion to higher-order modes or radiation modes. This adiabatic operation can be realised in the taper design by increasing/decreasing the size of the taper cross-section very slowly. There are various designs of adiabatic tapers that have been demonstrated in the SOI platform, including linear [116], exponential [117], parabolic [118] and Gaussian expansion types [119] but for simplicity a linear taper is used.

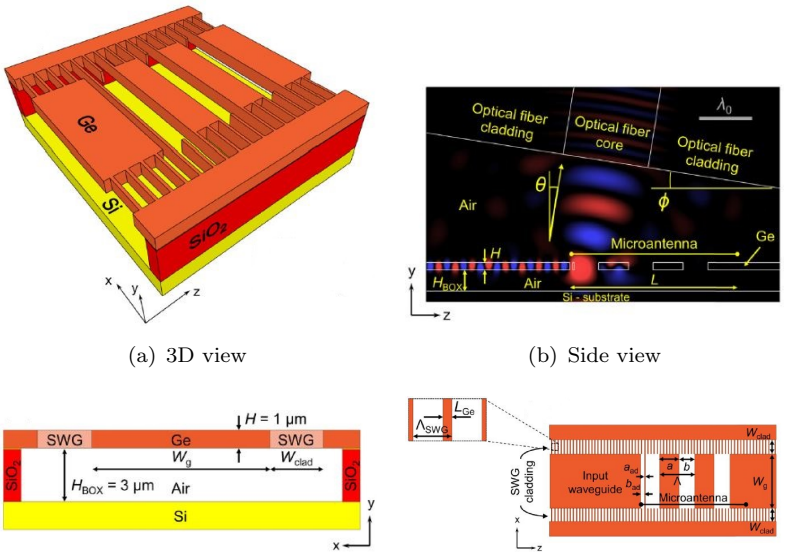


(a) 3D view (b) Side view

(c) Front view (d) top view

FIGURE 2.27: Schematics of the SWG-cladding micro-antenna fibre-chip coupler based on the suspended Ge platform presented in [115]

In a linear adiabatic taper, the lowest-order optical mode is well confined by side walls. The taper should be designed to conform with the equation 2.9 [120].

$$\theta < \frac{\lambda_0}{2W n_{eff}} \tag{2.9}$$

where $\theta$ is the local half angle of the taper at the point $z$, $\lambda_0$ is the wavelength in vacuum, $n_{eff}$ is the effective index of the mode, and $W$ is the local full width of the taper at point $z$ as shown in Figure 2.28. The rule requires that the spreading of the waveguide sidewalls be slower than the diffraction spreading of the lowest-order (first-order) mode. Accordingly, the first-order mode will be confined in the taper without mode conversion to higher-order modes or radiation modes.

## 2.3 Integration of active devices

III–V semiconductors (such as Gallium Arsenide (GaAs) or InP) have been widely used since the 1970s for the development of light emitters used in optical telecommunications and other photonic devices. At the beginning of the 21st century, research groups realised that electronic–photonic integration will enable a large variety of applications, such as biosensing, light harvesting, defence, information processing and others. Ever since, this field has attracted a lot of research interest from both industry and academia who are currently investigating the co-integration of optical functions with the electronic functions of Si and other materials. Photonics is the main building block of

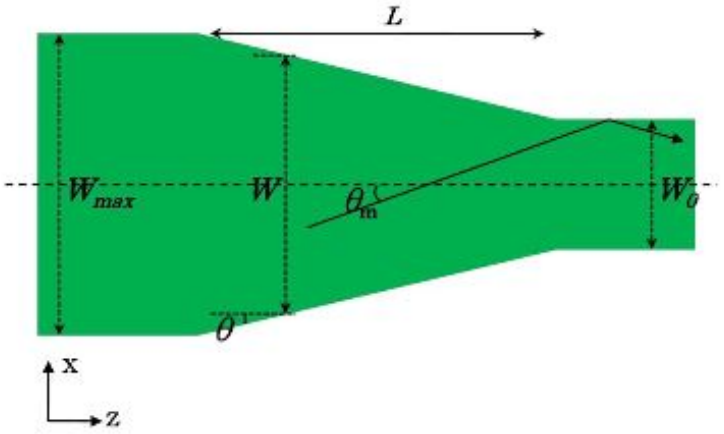


FIGURE 2.28: Top view of the structure of a linear waveguide taper. $W_0$ is the width of the single-mode waveguide, $W_max$ is the maximum taper width, $L$ is the length of the taper, $\theta$ is the local half angle of the taper at point $z$, and $\theta_m$ is the projection of the ray angle of the first-order mode of the taper [120].

today's communication networks, however, increasing signal speeds, decreasing power consumption, miniaturisation and reducing overall costs still remain as challenges. The ultimate solution addressing these challenges is using PICs, and more specifically on-chip optical interconnects. In this approach, a photonic layer would be responsible for the information routing and processing in a microprocessor resulting in reduction in energy consumption, faster data transmission and processing. This approach has already been investigated by IBM, Intel and various companies in the field of semiconductors. However, while elemental building blocks (waveguides, detectors, modulators, sources) of excellent performance have already been demonstrated, the development of an integrated laser source on Si to feed the PICs with light still remains a serious challenge. In this section, the advances that have been achieved toward the development of an ideal integrated laser source on silicon as well as the benefits and drawbacks of each approach are presented.

### 2.3.1 Ideal performances of the integrated laser

In this section the specific aspects that an integrated laser should exhibit are presented.

- Electrical injection: An integrated laser should be electrically driven so it can be driven by CMOS electronics.
- Continuous wave operation: In order to avoid any capacitive transient process, an integrated laser should operate under a Continuous Wave (CW) regime.
- Room temperature: An integrated laser should be able to operate under the same temperatures a microprocessor works under which is between 30 to 150°C.

- Emission wavelength: The emission wavelength of an integrated laser should be carefully selected according to the desired application. For this reason, QCLs are perfect candidates for MIR applications since their emission wavelength can be tailored.

- Geometric emission properties: Regardless of the integration approach, the laser cavity should emit in-plane to ease coupling into the photonic circuitry; as opposed to vertical emitting devices such as VCSELs where specific optical reflectors have to be designed to fold the direction emission in the plane. In addition, optical coupling raises alignment issues because the distance between the active area and the photonic circuitry should not exceed 300 nm.

- Footprint: An integrated laser should be as compact as possible to enable scalability. This also affects the power consumption of the device.

- Power and threshold considerations: A general requirement for an integrated laser is to exhibit the best energy yield (wall-plug efficiency). However, the output power and threshold current of an integrated laser are dependant on the photonic circuit design and it is determined by the following factors:

  - optically efficient active area (direct bandgap, good quantum confinement, high gain)
  - efficient carrier injection through contacts and adapted band engineering;
  - low optical losses in the resonant cavity (especially through photons absorption)
  - low non-radiative recombination probability (low crystal defects density, and limited Auger recombination)

  Nevertheless, in the case where a separate laser bar is bonded onto a chip, and the light is butt coupled into the waveguide, these factors are independent of the PIC design.

### 2.3.2 Quantum Cascade Lasers

QCLs are semiconductor injection lasers whose active core implements a multiple quantum well structure. Their light emission mechanism is based on intersubband transitions in semiconductor quantum wells. Photons are generated when electrons transported into the active regions from the preceding injector regions undergo radiative transitions between the upper and lower laser levels and are subsequently extracted into the next downstream injector regions. The electron transport from an injector region into the next active region occurs by means of resonant tunnelling between the injector ground level and the upper laser level as shown in Figure 2.29. The tunnelling rate, as well as many other performance related parameters, can be engineered through quantum

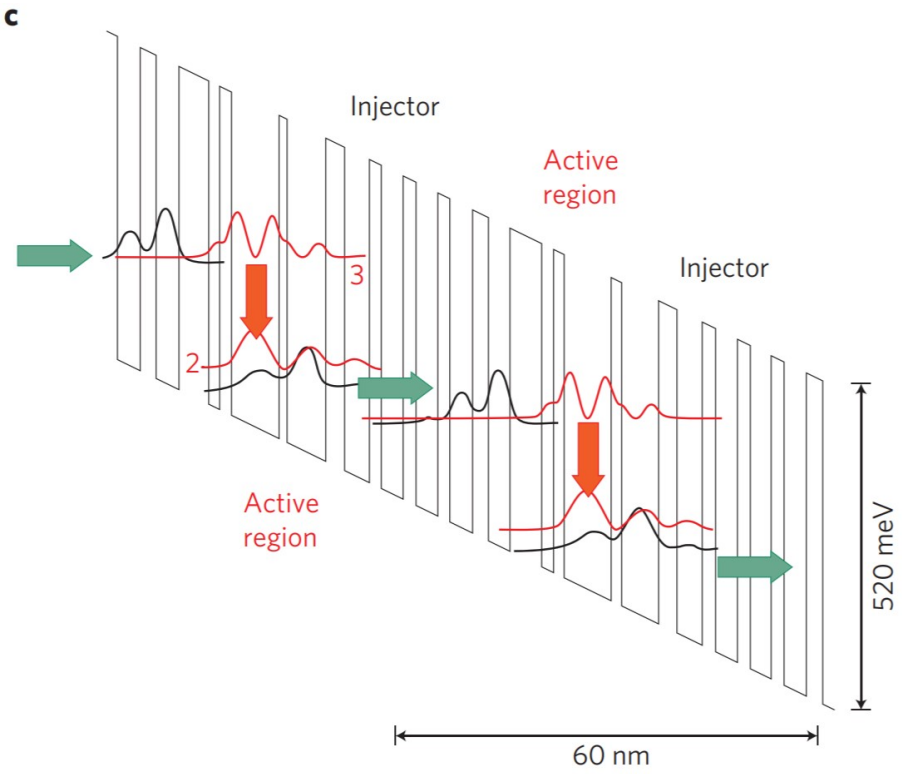


FIGURE 2.29: Simplified schematic of the conduction band structure for a basic QCL, where the laser transition is between sub-bands 3 and 2 [121].

design, for example, through the design of the coupling strength, which is defined as half of the energy splitting between the injector ground level and the upper laser level when they are in full resonance. The faster the tunnelling rate, the higher the maximum operating current density that can be supported, and therefore the higher the current efficiency (that is, how far above threshold the laser is operated), which is an important factor of Wall-Plug Efficiency (WPE). Relying on a designed staircase of intersubband transitions allows free choice of emission wavelength and, in contrast with diode lasers, a low transparency point that is similar to a classical, atomic four-level laser system.

The intersubband nature of the optical transition has several key advantages. First, the emission wavelength is primarily a function of the Quantum Well (QW) thickness. This characteristic allows choosing well-understood and reliable semiconductors for the generation of light in a wavelength range unrelated to the material's energy bandgap. Second, the cascade process in which multiple-often several tens of-photons are generated per electron becomes feasible, as the electron remains inside the conduction band throughout its traversal of the active region. As a result of this cascade process, QCLs exhibit intrinsic high-power capabilities.

In recent years, this design flexibility has expanded the achievable wavelength range of QCLs to ∼3-25 $\mu$m and the THz regime, and provided exemplary improvements in overall performance. The commercially available InP-based QCL technologies provide

promising potential for extending heterogeneous integration to wavelengths throughout the MIR and Long-Wave Infrared (LWIR) spectral bands. QCLs operate from 3 $\mu$m to the terahertz regime and can emit watts of CW output power [121, 122]. The InP-based material system in QCLs is especially favourable for the complex fabrication processing necessary for heterogeneous silicon integration. QCLs are rapidly becoming practical MIR light sources for several applications such as trace-chemical sensing and health monitoring.

In this thesis, QCLs were chosen to be integrated over other type of laser due to their flexibility of wavelength selection as well as their high emission power in the MIR. However, efficient heat extraction out of the active region is necessary for operation at room temperatures. As a result, thick metal contacts are used for heat dissipation which is a major constraint on the design of the PIC. In addition, reflected light that is returned from the waveguide facet into the QCL is another constraint on the laser performance, as it destabilises both the transverse spatial mode and the output power, thus leading to significant temporal fluctuations. Therefore, the implementation of anti-reflective coating becomes necessary for efficient coupling.

### 2.3.3 Group-IV lasers

In this section, the various advances made towards realising a light emitter using group-IV semiconductors are presented. The main interest of this type of lasers is that they are intrinsically compatible with photonic integration from the material point of view.

As opposed to most III-V semiconductors, Si and Ge are semiconductors with a indirect bandgap (X-like fundamental transition for the Si and an L-like fundamental transition for Ge), having different bandgap energies (1.12 eV for Si and 0.66 eV for Ge). This means that light emission is a phonon-mediated process with a low probability where spontaneous recombination lifetimes are in the ms range, as shown in Figure 2.30. As a result, most of the generated electron-hole pairs in Si and Ge recombine nonradiatively. This results in a very low internal quantum efficiency which is the ratio between the number of photons generated and the charge carriers injected.

Nevertheless, researchers have investigated light emission from Si by trying to reduce the influence of non-radiative centres using various strategies. The first demonstration was presented in [124] where a standard p-n Si structure was used for light emission. In this work, they proposed reducing the non-radiative centres, the non-radiative recombination rate, surface recombination and doping-induced recombinations to the maximum resulting in lowering the non-radiative recombination rate. As a result, electroluminescence at room temperature is achieved with a maximum around 1.1 $\mu$m. In addition, a power efficiency of 1% is observed. However, this approach is not suitable for reaching

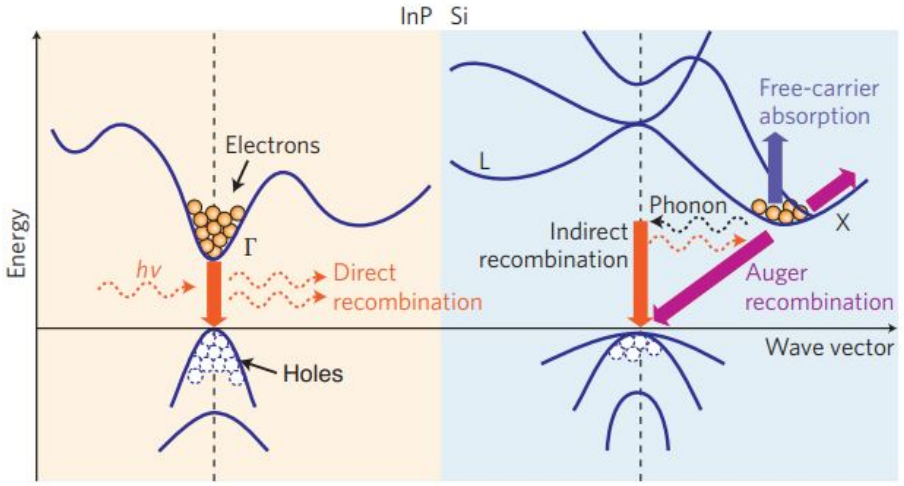


FIGURE 2.30: Energy band diagrams and major carrier transition processes in InP and Si crystals [123]. In a direct bandgap material (such as InP, left), electron-hole recombination almost always results in photon emission as opposed to an indirect bandgap material (such as Si, right), where free carrier absorption, Auger recombination and indirect recombination coexist, resulting in an inefficient photon emission accompanied by a strong phonon emission which is transformed to heat.

lasing conditions (population inversion) as the decay-time of the indirect band-to-band recombination is very long compared to the fast free carrier absorption.

An alternative approach to achieve stimulated emission in Si is using quantum confinement. By using Si nanostructures in an air or $SiO_2$ environment offers many benefits compared to using bulk Si. Confining the charge carriers spatially prevents them from reaching non-radiative recombination centres. This approach was firstly proposed in [125] where Si was partially etched forming a structure consisting of small nanowires emitting a luminescence in the visible range.

Another promising solution to achieve efficient laser emission on Si is to modify the bandstructure of group-IV semiconductors by alloying Si with either Ge or Tin (Sn) in order to obtain a direct bandgap alloy. However, this approach implies challenges due to the lattice mismatch that Ge and Sn have with Si (4.2% and 19.5% respectively). This causes both roughening of the layers due to strain release and formation of dislocations. These in turn act as non-radiative recombination centres, which is very crucial for laser operation. Nevertheless, several approaches have been presented for the development of a SiGe(Sn) laser on Si.

- **Silicon-Germanium (SiGe) lasers**

  As already stated, Ge is an indirect bandgap material with its minimum of energy located in the L-valley, which causes the long radiative lifetime, hence, preventing bulk Ge from efficient lasing. However, the energy separation between its Γ and L transitions is as small as 136 meV [126]. In addition, it is known that mechanical

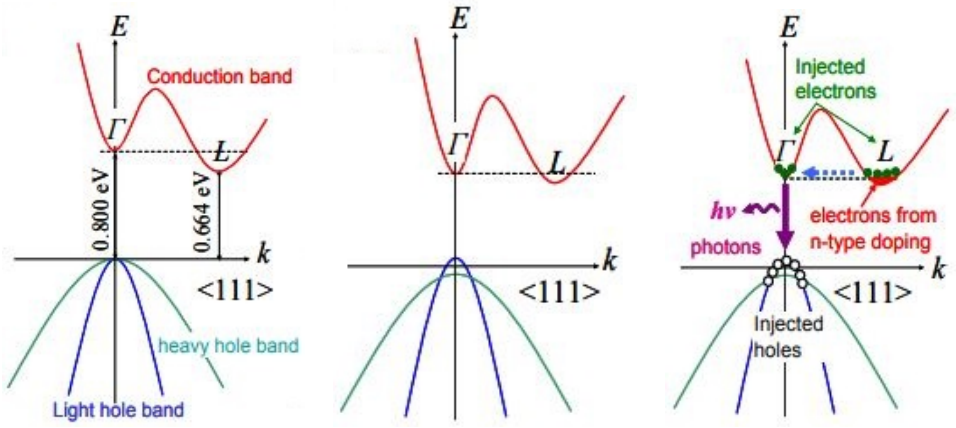


(a) Bulk Ge (b) Tensile strained intrinsic Ge (c) Tensile strained $n^+$ Ge

FIGURE 2.31: (a) Schematic of the band structure of Ge showing a 136 meV difference between the direct and the indirect bandgap. (b) Reduction of the difference between the direct and the indirect bandgap by applying tensile strain. (c) Compensation of difference between the direct and the indirect bandgap by using n-type doping to fill electrons into the L-valley. [126].

strain modifies the band structure of semiconductors by relocating the energy positions of the various valleys (X, Γ, L). The main idea is to reduce the bandgap of Ge by applying tensile strain which will cause the move of the Γ-band minimum closer to the L-band one as shown in Figure 2.31,thus transforming Ge into a potential direct bandgap emitter. In order to achieve a crossover and transform Ge into a direct bandgap material, a tensile strain of 2% has to be applied.

Various designs have been proposed to increase the level of tensile strain imposed to the Ge layers such as using the thermal mismatch between Ge and Si [10], using buffer layers (e.g., Germanium-Tin (GeSn)) [127] and using Micro-Electomechanical Systems (MEMSs) to externally control the strain state of the Ge up to 1% of biaxial strain [128]. The highest value of strain achieved was in [129] where a uniaxial strain of 5.7% was demonstrated, paving the way for direct bandgap emission.

Very recently, efficient light emission was achieved from direct-bandgap hexagonal Ge and SiGe alloys [130]. The achieved emission yield was similar to that of direct bandgap group-III–V semiconductors. It is also shown that by controlling the composition of the hexagonal SiGe alloy, the ability to continuously tune the emission wavelength over a broad range (from 3.5 $\mu$m (0.353 eV) at low temperature towards 4.4 $\mu$m (0.28 eV) at room temperature), while preserving the direct bandgap.

- **Silicon-Germanium-Tin (SiGeSn) lasers**

  Another way to obtain a direct bandgap material is to diffuse Sn atoms into a Ge or SiGe. This technique is expected to reduce the gap at the Γ-point faster than

that at the L- or X-point. A recent demonstration has shown experimentally that the $Ge_{0.9}Sn_{0.1}$ alloy with a tiny compressive strain of 1% exhibits direct bandgap behaviour [131]. However, due to the the large lattice mismatch between Ge and $\alpha$-Sn (15%) is challenging for such integration. Therefore, obtaining partially and fully relaxed GeSn layers is crucial. In this technique, a thick Ge layer is deposited on Si which helps to relax a large part of the mismatch. This causes most of the crystal defects (especially threading dislocations) to be buried and allows control of the partial relaxation of GeSn on Ge [132]. Using this approach, an optically pumped GeSn laser was demonstrated with a ridge geometry, operating below 90 K, with an emission wavelength at 2.25 $\mu$m ($\sim$55 eV) [133]. This result is very promising towards the integration of silicon photonic and electronic devices. However, in order for this type of laser to be used in practical applications several issues still have to be addressed. Initially, lasing has only so far been demonstrated using pulsed optical pumping. In addition, the laser has to be electrically driven in order for it to become useful. To do this, doping has to be improved technology such that a degenerate p- and n-type doping can be obtained to enable electrically achieved population inversion. Moreover, in order for the laser to be used in practical applications, it has to operate at in CW mode and at well above room-temperature. The authors have proposed ways to raise the temperature of operation by improving material quality to eliminate competing recombination and introducing carrier confinement with heterostructures.

### 2.3.4 III-V lasers bonded on silicon

The various advances presented in 2.3.3 that were made towards the development of a laser made of group-IV laser materials, were attractive from the integration point of view. Their CMOS compatibility is key for their integration with group-IV material platforms. However, none of these strategies has led to the development of an efficient light emitter yet. As already stated, the fundamental reason for this is the inherent limitation of Si and Ge being indirect bandgap which prevents them from emitting light efficiently. On the other hand, III-V compounds based on InP and GaAs, are direct bandgap semiconductors that are widely used in developing commercial light emitters for more than 50 years. The approaches of integrating III-V lasers on a Si substrate have been following two paths: the monolithic approach, in which III-V materials are directly grown on Si, and the bonding approach, where III-V materials are bonded on Si substrates.

In this section, the different heterogeneous integration approaches are presented along with the benefits, technological issues as well as the integration constraints associated with each approach.

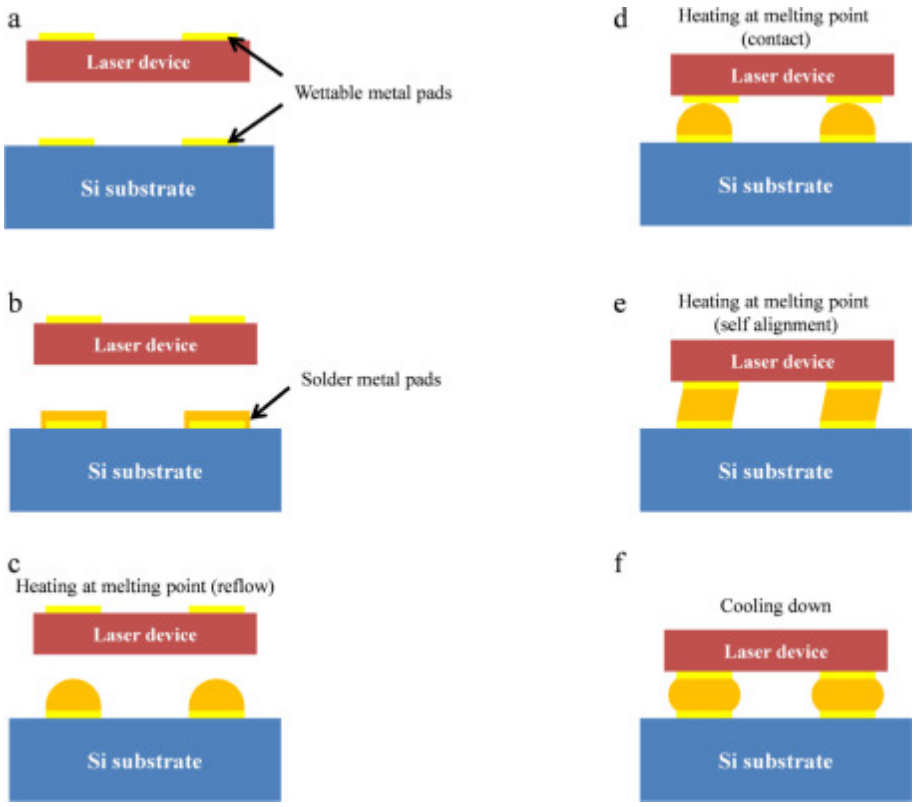


FIGURE 2.32: Flip-chip bonding fabrication process flow [137].

#### 2.3.4.1 Flip-chip bonding

The idea of heterogeneously integrating optoelectronic devices on a foreign substrate by bonding has existed since the early 90s. Flip-chip bonding was developed by IBM and it was used in the heterogeneous assembly of electronics [134]. Since then, efforts have been carried out to improve the flip-chip bonding technique [135, 136]. In this technique both host substrate (Si or any other) and the device to be flip-chipped (laser) are first patterned with wettable metallic pads such as Chromium (Cr), Ti, Platinum (Pt) or Au, deposited on a non-wettable material (dielectric) using lithography techniques. Then, a solder material such as AuSn or Tin Lead (PbSn) is deposited on the metal pad and reflowed above the melting temperature to form bumps. The integrated device and the substrate are then put in contact with a rough alignment. Both parts will be self-aligned due to tension forces. Finally, the bonded structure is cooled down to form an electrical and thermal contact that is mechanically robust. The whole fabrication process flow of flip-chip bonding is shown in Figure 2.32.

A crucial aspect of flip-chip bonding is alignment, as good coupling between lasers and waveguides is essential to minimise optical losses. Alignment of $\pm$ 500 nm has been achieved ([138]), however, sub-1 $\mu$m tolerance in preferred. Novel designs for solder pads for self-aligned flip-chip assembly have been demonstrated offering robust chip alignment [139].The advantage of flip-chip integration is that growth and fabrication of the devices

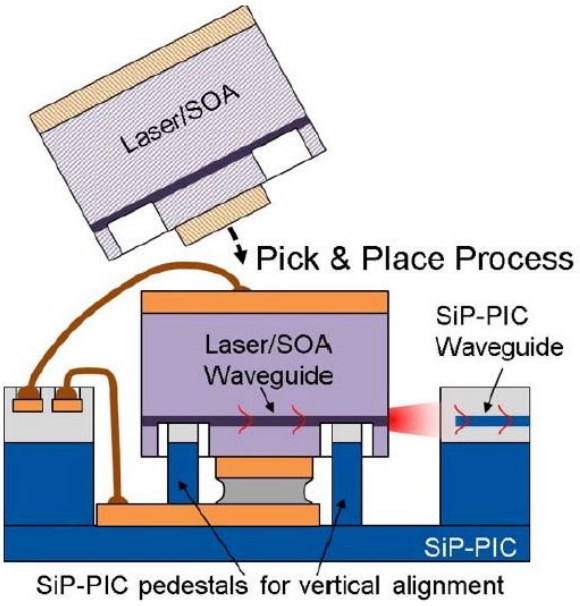


FIGURE 2.33: Schematic of the bonded laser using flip-chip bonding [141].

is carried out on their native substrate. Moreover, it allows for independent fabrication and test of both the laser and the passive components, reducing constraints on the semiconductor manufacturing process flow and allowing for the pre-selection of known good dies, hence increasing the yield. However, it also requires very high placement accuracy, as the beam size at the interface between the moving parts (i.e., between the laser and the waveguide) is very small.

Lasers have been integrated using flip-chip bonding since the late 90s. One of the first demonstrations included the mounting of high-frequency DFB lasers on a Si substrates [140]. In this work the lasers were passively aligned to single mode fibres in V-grooves using the self-aligning solder bump technique. The laser-to-fibre coupling efficiency achieved was of 2.3%, which corresponded to a coupled power of approximately 0.25 mW. A big part of the low coupling efficiency was due to the distance between the fibre and the laser which was ~20 $\mu$m, restricted by the low quality facet of the V-groove caused by the saw cut.

Instead of coupling light to a fibre, coupling to a waveguide has also been demonstrated. In [141] a Semiconductor Optical Amplifier (SOA) is integrated on Si substrate using flip-chip bonding, and subsequently coupled to a waveguide as shown in Figure 2.33.

In this work, a flip-chip integration process was developed, in which the vertical alignment was controlled by a mechanical contact between pedestals defined in a recess etched into the substrate and the SOA. Using this technique, the vertical alignment accuracy achieved was below ±10 nm not taking into account bending of the chips due to excessive stress. The measured optical power coupled to the waveguide was above 3 mW which was 3.5 dB below what was expected assuming perfect alignment according to simulations and 7 dB below the laser output power. In addition, another source of coupling

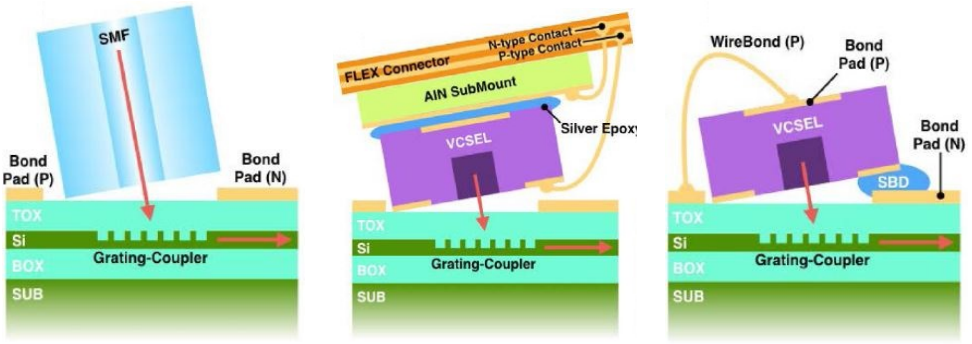


(a) Testing of the grating coupler using light launched from an SMF, showing the near-normal angle-of-incidence of approximately 10°

(b) Sample used to actively align the VCSEL with the grating coupler. Translating and tiling the sample is achieved using an electrical FLEX connector via which power to the VCSEL is also provided

(c) Tilted VCSEL flip-chip bonded above a grating-coupler, showing the SBD and the wire-bonds used to facilitate the n- and p-type electrical connections to the contact pads and tracks on the PIC

FIGURE 2.34: Schematic of the flip-chip bonded VCSEL [142].

loss was the mode mismatch between the laser and the waveguide chip that could be improved by matching of the edge couplers on either side of the interface. According to the authors, the insertion loss could be improved by 1 dB, due to a better mode matching, by tapering down the laser stripe to a 500 nm width.

Butt coupling light from the laser directly to the waveguide however, induces the issue of having back reflections from the waveguide facet back to the laser. For a laser that is sensitive to back-reflections this is crucial for its performance. A way to overcome this it to mount the laser at an angle with respect to the waveguide in which case light coupling is carried out using grating couplers as presented in [142]. In this work VCSELs emitting at ∼1550 nm, are passively aligned and flip-chip bonded to a PIC, at an angle that has been optimised for maximum coupling into standard grating couplers. The tilt angle is determined by controlling the reflow of the Solder Ball Deposition (SBD) used for the electrical connection as well as the mechanical bonding of the VCSEL with the PIC. The achieved VCSEL-to-PIC insertion loss was -11.8 dB, which was 5.9 dB lower compared to fibre-to-PIC coupling due to the mode mismatch between the VCSEL and the grating coupler. At roll-over, the maximum optical power injected into the PIC was 138 $\mu$W = -8.6 dBm. A schematic presentation of the fabricated device is shown in Figure 2.34.

Apart from NIR, MIR light sources have also been integrated. In [143] the first demonstration of a QCL on Si, integrated with SONOI waveguides. Fabrication starts with preparing the SONOI waveguide platform which is constructed by transferring the device layer from a SOI wafer onto a Nitride-on-Insulator (NOI) wafer by direct wafer bonding. Once the SONOI waveguides are processed, the QCL material is then bonded to it via flip-chip bonding. The QCL material is subsequently processed to finally obtain the light source as depicted in Figure 2.35.

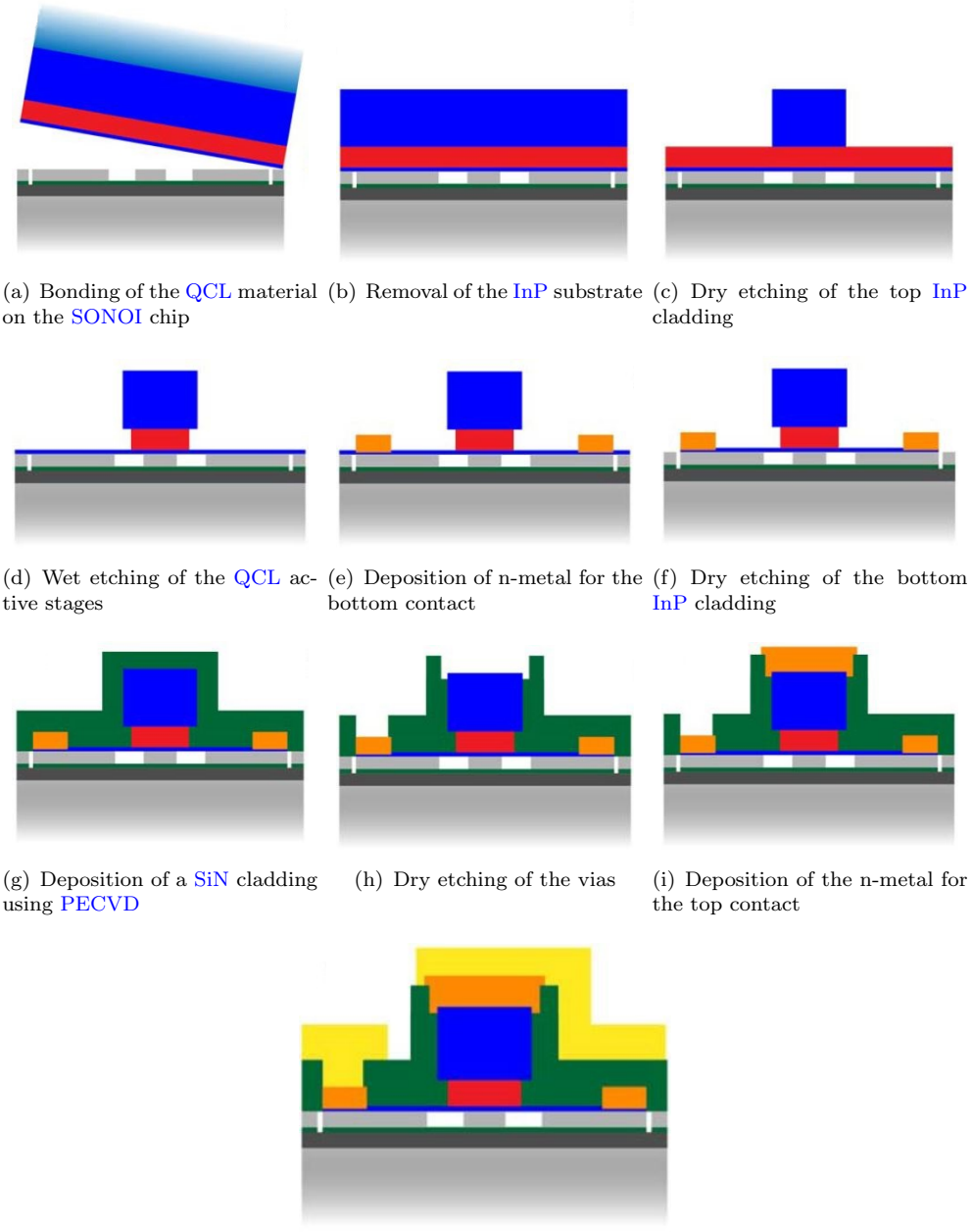

(a) Bonding of the QCL material on the SONOI chip

(b) Removal of the InP substrate

(c) Dry etching of the top InP cladding

(d) Wet etching of the QCL active stages

(e) Deposition of n-metal for the bottom contact

(f) Dry etching of the bottom InP cladding

(g) Deposition of a SiN cladding using PECVD

(h) Dry etching of the vias

(i) Deposition of the n-metal for the top contact

(j) Deposition of the probe metal

FIGURE 2.35: Fabrication process of bonding the QCL on the SONOI chip [143].

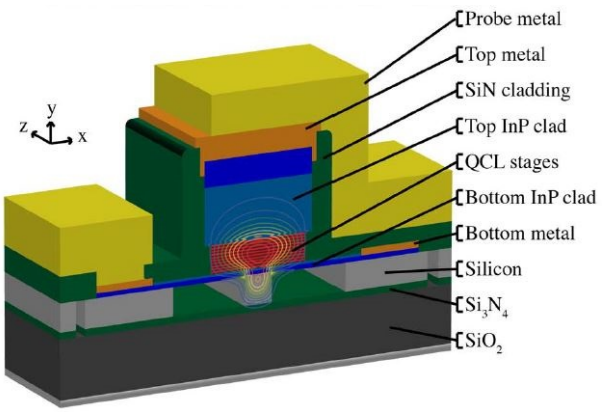


FIGURE 2.36: Schematic of the cross-section of the hybrid Si-QCL active region. A contour plot of the electric field component, $|E_y|$, of the simulated fundamental TM optical mode is overlaid [143].

The optical mode in this type of structure is so-called hybrid, meaning that it propagates in both the active region and the passive waveguide as shown in the cross-sectional schematic of the Si-QCL region (Figure 2.36).

The fabricated laser is emitting at 4.8 $\mu$m in pulsed mode, at 20 °C. Threshold currents as low as 387 mA and single-sided output powers as high as 31 mW. The observed characteristics imply that in order to achieve CW operation in the MIR, the heat dissipation should be improved. This could be achieved by using a platform without a BOX such as GOS where heat dissipation to the substrate would be better due to Si having a significantly higher thermal conductivity than $SiO_2$ (i.e, 149 W/(m·K) for Si and 1.1-1.2 W/(m·K) for $SiO_2$).

#### 2.3.4.2 Wafer bonding

Despite the fact that flip-chip bonded devices tend to self-align on the metal solder bump, precise alignment of each individual device is still a challenge. An alternative approach to alleviate the need for the precise pre-alignment, is to bond full wafers or dies of III-V material and then post-process them after bonding as depicted in Figure 2.37. Following this approach, the alignment precision is then determined by the lithographic tools.

In this technique, two mirror-polished surfaces of two different wafers are contracted to create covalent bonds between them. Several approaches have been investigated but only the three main ones that relate to the development of III-V light sources on Si are discussed in this section.

- **Molecular bonding**

  The fabrication steps of this approach are shown in 2.38.

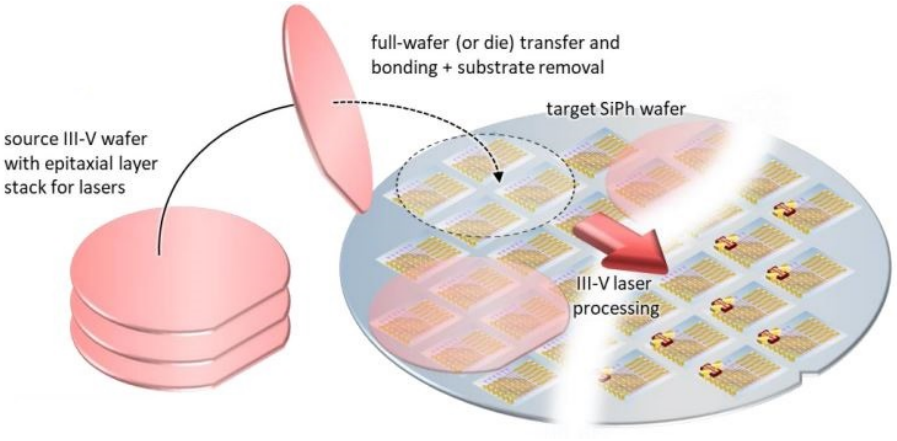


FIGURE 2.37: Schematic representation of III-V/Si wafer bonding.

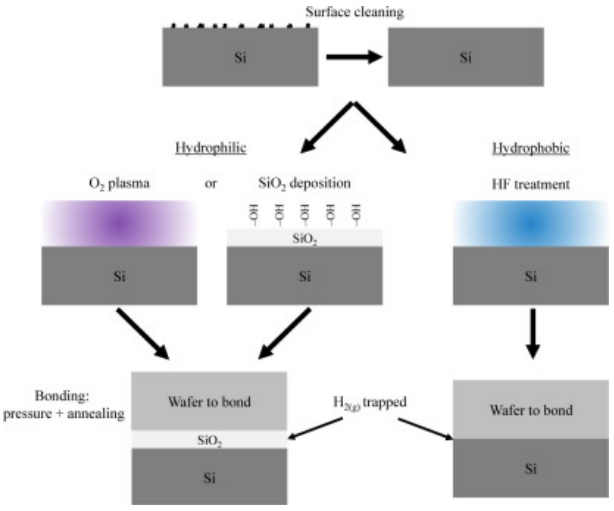


FIGURE 2.38: Fabrication process of the molecular bonding, describing the tree main approaches ($O_2$ plasma-assisted bonding, $SiO_2$-assisted bonding and bonding of hydrophobic surfaces) [137].

The two wafers are initially cleaned to minimise the number of particles on their surfaces that could degrade the bonding quality. This is carried out using a combination of solvents and acids. The surfaces are then treated to be either hydrophobic or hydrophilic. In the hydrophobic treatment, the wafer surface is terminated by -Hydrogen (H) bonds whereas in the hydrophilic treatment, the surface is terminated by -Hydroxyl (OH) bonds. Then the two wafers are contacted and bonded first through weak Van der Waals forces. In the case of the hydrophilic bonding, OH groups start bridging forming a thin layer of Water ($H_2O$) in between the two surfaces, whereas in the hydrophobic case, bonding is achieved through by bridging the hydrogen bonds. In both cases, Hydrogen ($H_2$) gas is formed at the interface causing bubbles. These are removed by annealing which causes the H to diffuse into the Si which increases the bonding strength.

However, when this approach is to be followed to bond III-V to Si wafers, different annealing temperature have to be used. High temperature annealing is not suitable

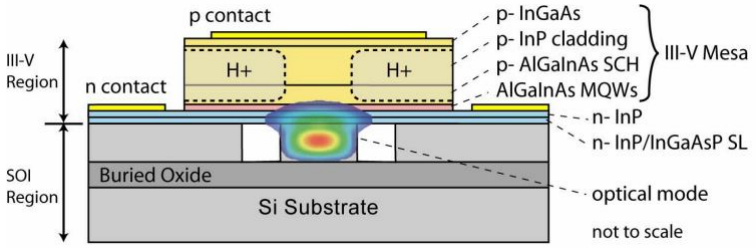


FIGURE 2.39: Schematic representation of the hybrid laser structure showing the optical mode superimposed [144].

for these wafers as GaAs or InP would desorb at 1000 °C. In addition, due to the thermal expansion coefficient mismatch between III-V materials and Si, annealing would result in wafer cracks. Strategies have been proposed by several research groups but this topic does not fall within the scope of this thesis.

The first demonstrated laser using this approach was by the group of UCSB using their hybrid III-V/Si platform where III-V layers were bonded using $O_2$ plasma-assisted molecular bonding SOI waveguides that had been pre-patterned [144]. Both active and passive region are designed such that the mode propagated in both regions as shown in Figure 2.39.

The laser cavity was a $Fabry - Perot$ cavity formed by dicing the laser and polishing the facets. The demonstrated device exhibited a threshold current of 65 mA (at 15 °C) in CW pumping, a maximum output power of 1.8 mW, an overall differential quantum efficiency of 12.7 % and a maximum lasing temperature of 40 °C.

An alternative to avoid forming the laser cavity by dicing the laser facet is to use grating-based cavities instead. The first demonstrated hybrid III-V/Si laser using DBRs to form the laser cavity was in 2008 by Fang et al. [145]. In this demonstration the cavity was defined by two $Bragg$ mirrors in the Si waveguide defined before bonding as shown in Figure 2.40.

To minimise the coupling losses between the III-V gain region and the Si waveguide, the width of the III-V waveguide is linearly tapered. The fabricated device demonstrated lasing at a single-wavelength of 1596 nm (Side Mode Suppression Ratio (SMSR) of 50 dB), with a threshold current of 65 mA at 15 °C, a maximum output power of 11 mW and a maximum lasing temperature of 45 °C.

Using the same type of structure, the same group demonstrated an improved device that reached a low threshold current of 8.8 mA for a 200 $\mu$m cavity at 20 °C [146]. The maximum CW output power was 3.75 mW from both waveguide facets. A 3 dB bandwidth of 9.5 GHz as well as 12.5 Gb/s direct modulation of the DFB laser diode was achieved on the hybrid silicon platform for the first time. A schematic of the demonstrated device is shown in Figure 2.41.

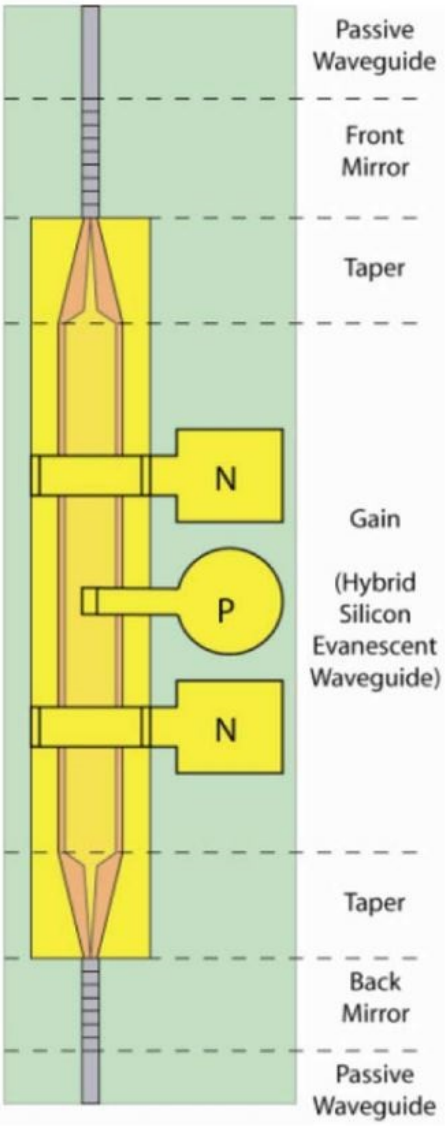


FIGURE 2.40: Top view of the DBR hybrid III-V laser demonstrated in [145].

Lasers used in ultrashort distance optical interconnects have to exhibit low-energy consumption and small footprint. To achieve this, microrings have been utilised. This type of sources has been demonstrated using the hybrid III-V/Si platform [147]. In this type of structure, after bonding the III-V layers on the SOI wafer, both the III-V and the Si top layer are patterned to obtain a III-V microring self-aligned on a Si microdisk as shown in Figure 2.42.

The disk is typically 15-50 $\mu$m in diameter and similarly to the previously described structures, the optical mode is hybrid, meaning that it propagates in both the III-V gain region, which in this case is the ring, and the Si disk. Light is extracted from the disk to a Si bus waveguide located close to the disk. Using this design, threshold current lower than 4 mA and 10 °C, maximum output power of 3.5 mW and maximum lasing temperature of 65 °C has been demonstrated [147].

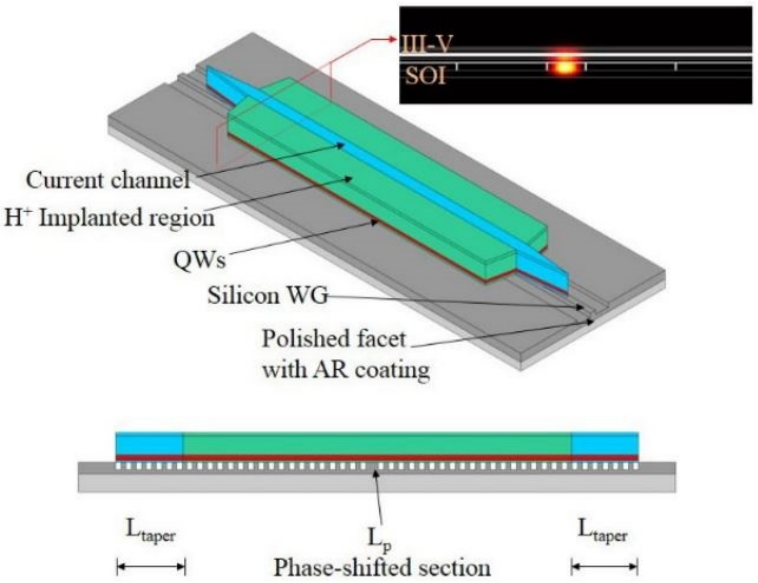


FIGURE 2.41: Schematic of the DFB hybrid III-V/Si laser demonstrated in [146].

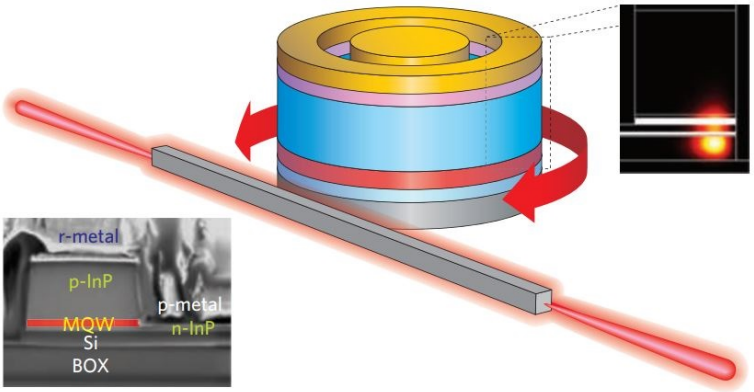


FIGURE 2.42: Schematic of the hybrid III-V/Si microring laser demonstrated in [147].

- **Polymer-assisted bonding**

  An alternative technique for bonding III-V wafers to Si is the polymer-assisted bonding. In this technique, which was developed by a group at Ghent university in Belgium, a layer of Divinylsiloxane-Bis-Benzocyclobutene (DVS-BCB) is utilised to bond the wafers.

  BCB is a thermosetting polymer widely used in applications such as bonding or passivation. In a BCB-assisted bonding process (depicted in Figure 2.43), the wafer surfaces are initially cleaned to remove any particles that could result in unbonded areas. Then, the Si or SOI wafer is spin-coated with BCB upon spin coating the wafer with an adhesion that will strengthen the adhesion of the BCB and the wafer. Next a soft baking typically at 150 °C is carried out to evaporate the solvent and remove any bubbles. While still at baking temperature, the two wafers are brought into contact and a uniform pressure is applied. Then, the following step is the curing (polymerisation) of the BCB for 1 hour in an $O_2$-free

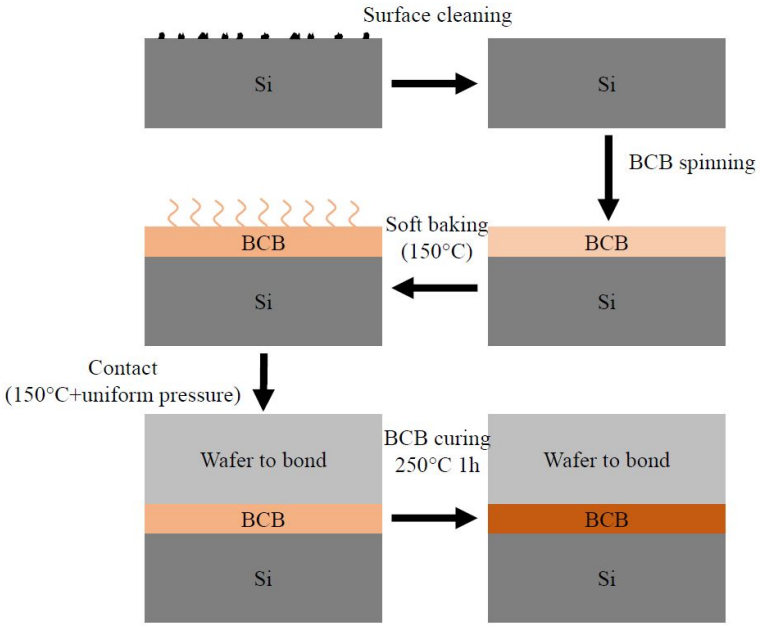


FIGURE 2.43: Fabrication process for the BCB-assisted wafer bonding technique [137].

environment, at 250 °C to transform it from liquid to solid phase. Finally the two wafers are cooled down and form a solid stack ready for further processing.

An advantage of BCB-assisted wafer bonding technique is that there are not gas by-products produced during the curing of BCB thus the bonded interface is void-free without having to carry out complex processing steps as in the molecular bonding method. In addition, BCB planarises easily after spin-coating and baking rendering bonding patterned wafers less complex. Moreover, BCB is compatible with most of the standard III–V fabrication processes (annealing, wet etching).

However, BCB-assisted bonding suffers from major drawbacks. First, the very low thermal conductivity (0.29 $W{\cdot}K^{-1}{\cdot}m^{-1}$), compared to that of $SiO_2$ (1.4 $W{\cdot}K^{-1}{\cdot}m^{-1}$), results in a lower thermal dissipation in laser devices. In addition, the refractive index of BCB is slightly higher than that of $SiO_2$ (1.54 and 1.45 at 1.55 $\mu$m respectively), resulting in a higher optical reflection at the semiconductor–BCB interface. The effect of these drawbacks can be limited by reducing the BCB thickness to tens of nanometers [148]. However, this decreases the tolerance to surface imperfections.

Integrated lasers have been developed using BCB-assisted wafer bonding. The first device was demonstrated by the group at Ghent university in 2006 [149]. In this work, laser emission from an InP/Indium Gallium Arsenide Phosphide (InGaAsP) thin film epitaxial layer bonded to an SOI waveguide circuit was observed using a *Fabry–Perot* cavity. Bonding the InP/InGaAsP epitaxial layers onto the SOI waveguide circuit was achieved by adhesive bonding using DVS-BCB.

The BCB layer used was very thick (300 nm) to allow for direct evanescent coupling between the III–V layer and the SOI waveguide. Therefore, an inverted adiabatic

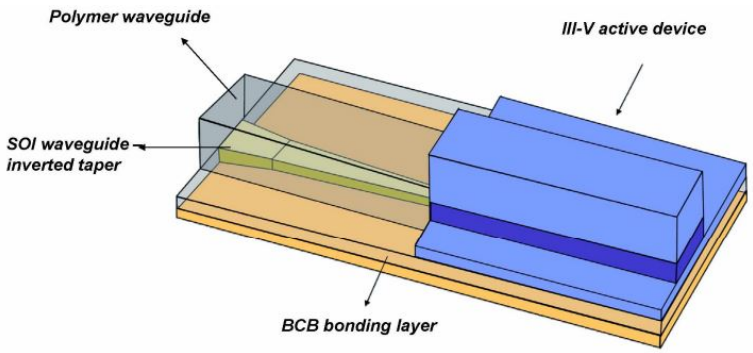


FIGURE 2.44: Schematic of the III–V/Si *Fabry–Perot* laser coupled to SOI waveguide demonstrated in [148].

taper was used to achieve efficient mode coupling between the InP/InGaAsP active layer and the SOI waveguide circuit as shown in Figure 2.44. The inverted taper adiabatically transforms the SOI waveguide mode to the fundamental mode of a polymer waveguide, which lies on top of the inverted taper and is butt coupled to the InP/InGaAsP active layer. The laser cavity was 500 $\mu$m long and the optical power coupled into the SOI waveguide was 0.9 mW in pulsed mode (at 20 °C). However, the threshold current was high (150 mA) which was caused by the bad quality of the facets and the thick BCB layer leading to a very high thermal resistance. In this work the same structure was used as a photodetector as well. The length of the devices was 50 $\mu$m and the resulting responsivity was 0.23 A/W.

Since this demonstration, work has been carried out to improve this technique by reducing the thickness of the BCB layer below 50 nm. Stankovic et al. have demonstrated both *Fabry–Perot* [150] and DFB [151] lasers. The minimum threshold current reached was down to 45 mA under CW operation for the *Fabry–Perot* cavity and 25 mA for the DFB laser, while output powers of several mW (5.2 mW for *Fabry–Perot* cavity, 2.85 mW for DFB) with sidemode suppression of 45 dB for the DFB laser. These lasers operated at 1.3 $\mu$m whereas the ones demonstrated by UCSB operated at 1.55 $\mu$m.

- **Metal-assisted bonding**

  As already described in 2.3.4.1 metallic solder bumps have been used to bond III–V lasers onto Si substrates. However, this is associated with high cost due to the demanding alignment between the light sources and the passive waveguides. Similarly to the adhesive BCB-assisted bonding technique, thin metal layers can be used as an alternative bonding interface to bond III–V dies or wafers to Si or SOI wafers. In the metal-assisted bonding method, a metal alloy is deposited on one or on both wafers . After bringing the two wafers into contact and heating them above the eutectic temperature of the metal alloy, the metal melts and spreads uniformly, filling the gaps between the wafers. By cooling back down, the metal solidifies creating a strong form.

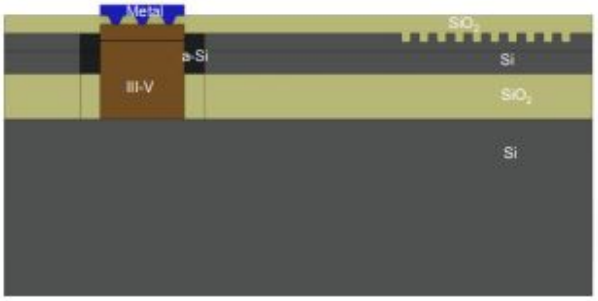


FIGURE 2.45: Cross-sectional schematic InP-based laser integrated with an SOI platform [148].

Choosing the suitable alloy is dependant on its eutectic point. If this at a very high temperature, this causes wafer cracks due to the thermal expansion mismatch between III–V and Si. If it is very low, this results in limitation of the thermal budget available for the post-bonding processing steps. A possible alloy is Gold Germanium Nickel (AuGeNi) (80:10:10), used by Tanabe et al. to bond a GaAs laser on a Si substrate [152]. In this work,a AuGeNi alloy was deposited on both wafers and bonding was carried out at 300 °C (for a eutectic point of 280 °C).

The metal-assisted bonding technique exhibits the same advantages with the solder flip-chip bonding: Apart from providing a strong bond, an electrical contact and a heat sink is also provided. In addition, it is more intolerant to surface cleanliness prior to bonding compared to molecular bonding. However, this technique has various issues: standard metal alloys contain metals such as Au that are contaminants for Si devices as they easily diffuse at bonding temperatures. More importantly, a few nanometers thick metal layers absorbs light, making light coupling more complicated. However, solutions to this issue have been demonstrated by several research groups. For example, in [153] Creazzo et al. reported bonding an InP-based laser structure into SOI wafer in which light from the III–V laser was butt coupled to the Si/$SiO_2$ waveguide as shown in Figure 2.45.

An alternative solution has been demonstrated by by Hong et al. [154]. In this work instead of depositing metal across the whole wafer surface, they were deposited selectively on areas away from the waveguides, therefore, enabling evanescent light coupling between the III–V laser and the underlying Si waveguide. The metal alloy deposited consisted of AuGeNi(100 nm)/Indium (In)(680 nm)/Sn(20 nm). AuGeNi was used to form a good ohmic contact to n-type InGaAsP and ensure strong bonding with the $SiO_2$ layer of the SOI wafer. In was selected as the main bonding medium due to its low melting point, good viscosity, and low stress accumulation. A thin Sn film above the In layer is deposited to prevent In from oxidation. The fabricated laser had a threshold current density of 1.7 kA/$cm^2$ under pulsed-wave operation. Room-temperature CW lasing with a maximum output power of 0.45 mW was realised.

TABLE 2.2: Cost of different interconnect solutions.

| **Bonding technique** | **Tolerance to surface defects** | **Light coupling with possible underlying waveguide** | **Thermal resistance** | **Cross-bonding electric drive** |
|---|---|---|---|---|
| Molecular ($O_2$-plasma assisted) | Low | Yes | Medium to low | No |
| Molecular ($SiO_2$-assisted) | Medium for large $SiO_2$ thickness | Yes for thin $SiO_2$ thickness | High for large $SiO_2$ thickness | No |
| Molecular (hydrophobic surfaces) | Very low (OK only for die bonding) | Yes | Low | Yes |
| Polymer-assisted | High for large BCB thickness | Yes for thin BCB thickness | Very high for large BCB thickness | No |
| Metal-assisted ($SiO_2$-assisted) | High | Complicated | Very low | Yes |

More recently, an alternative metal alloy was used to bond III-V material with a Si substrate [155]. In this work the integration of an InGaAs/InP quantum well infrared photodetector onto a Si substrate was demonstrated via metal-assisted wafer bonding using Molybdenum (Mo) as the diffusion barrier of metal-assisted wafer bonding.

The main advantages and drawbacks of the different bonding techniques are summarised in 2.2.

Wafer bonding provides the ability of fabricating multiple III-V light sources on a substrate simultaneously, therefore, it is ideal for mass production. However, there are drawbacks related to this technique.

- Nowadays, the size of commercial Si or SOI wafers used in CMOS foundries is 300 mm which will increase to 450 mm in the future. InP and GaAs wafers on the other hand, are fabricated with a smaller diameter (generally 100 mm for InP and 150 mm for GaAs) due to the limitation induced by their high brittleness. This size mismatch results in a loss of material whether it is Si or SOI. In addition, the cost of InP and GaAs epilayers is much higher that that of Si, hence, bonding several III-V wafers on a single Si wafer increases the cost dramatically.

- Bonding an entire costly III-V wafer results in an inefficient use of the III-V material. This is due to the fact that the III-V substrate is removed in order to access the III–V epilayer and to process the laser structure. This is generally achieved using a combination of mechanical grinding and selective wet etching. Therefore, the III-V substrate is wasted during the removal. The technique is thus quite costly due to the waste of the expensive III–V material.

- Wafer bonding requires both wafers to be perfectly clean in order to avoid defects such as bubbles in between the wafers, compromising the performance of the fabricated devices. The tolerance is very low as even a particle with a diameter of 1 $\mu$m can form a bubble with a lateral diameter of several millimetres.

- Another issue that has to be taken into account when bonding whole wafers is wafer bowing. This is caused by the strained multi-quantum wells required to develop an efficient light source.

#### 2.3.4.3 Heterogeneous III–V/Si lasers

A drawback of the previously mentioned hybrid platforms is that the overlap of the optical mode with the III–V active gain region is small. This results in increased cavity lengths to achieve sufficient gain which in turn leads to significantly high threshold currents. An approach to overcome this issue was firstly presented by the group of CEA Leti in France [156]. In this structure the optical mode is directed from the passive Si waveguide to the active III-V region and vise-versa by using two tapered rib-waveguides (mode transformers) located at the edges of the gain region as shown in Figure 2.46. The so-called supermodes of this hybrid structure are controlled by designing the tapers appropriately. By using such design, the confinement of almost the entire field in the in the middle part of the III-V active region in achieved resulting in maximum gain. The demonstrated device operated under quasi-CW regime with a threshold current of 100 mA at room temperature and the fibre-coupled output power was ∼7 mW.

This approach has been implemented with both bonding techniques, $SiO_2$-assisted [158] and BCB-assisted [157]. In the first demonstration the laser demonstrated was a single-wavelength DBR (with ring filters) while in the second was it was a DFB design. The resulted performance was similar in both demonstrations. The threshold current was 35–38 mA (at 20 °C), the maximum output power was 10–14 mW, the maximum lasing temperature was 60 °C and the sidemode suppression ratio was 45–50 dB. Another demonstration presented the same approach but using a resonant mirror fabricated in the Si waveguide [159]. Using this design the complex fabrication of tapers in the III–V materials is avoided. The laser operated under pulsed mode, however, the very low threshold current of 4 mA of this structure makes it promising for low power consumption PIC.

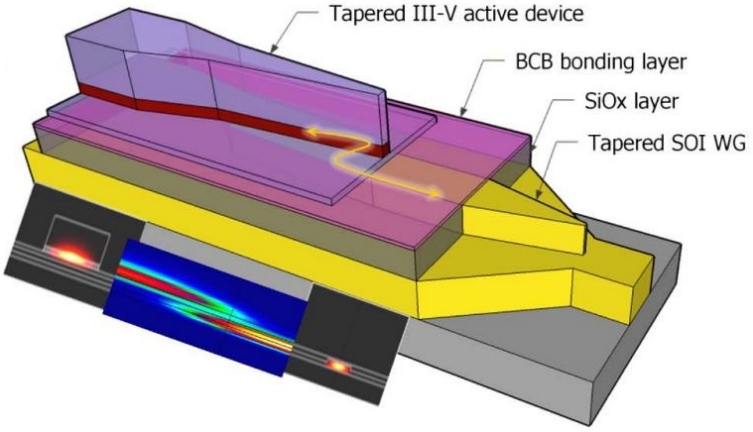


FIGURE 2.46: Schematic of the heterogeneously integrated III-V/Si DFB laser with a spot-size converter [157].

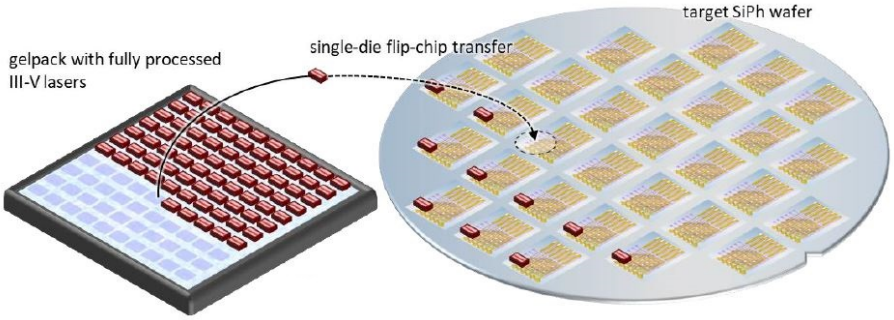


FIGURE 2.47: Schematic representation of bonding individual III-V dies to a Si wafer.

#### 2.3.4.4 Transfer printing

To avoid the drawbacks of bonding whole III-V wafers as mentioned earlier, small III-V dies can be diced and bonded individually at specific locations on the Si wafer, as shown in Figure 2.47. This approach alleviates the wafer size restriction and allows for a more efficient exploitation of both III-V and Si material. In addition, it is less susceptible to III-V wafer bowing due to the smaller surface of the the III-V die. This approach also enables the bonding of different epilayers to the same Si substrate. Moreover, by bonding dies instead of full wafers, the effect of a single defect is dramatically minimised, resulting in high yield. However, dicing the dies could cause small debris to be left at the sample edge, thus compromising bonding quality. A technique to bond III-V dies onto a Si substrate is the transfer printing method which is described in 2.3.4.4.

A novel alternative bonding technique that avoids the issues of the techniques previously discussed is transfer printing. In this method, thin film components are transferred from a source to a target substrate providing a scalable approach for device integration making efficient use of the source material.

In transfer printing, a soft elastomeric Polydimethylsiloxane (PDMS) stamp picks up a thin-film material stack or device (also referred to as coupon) from a source substrate

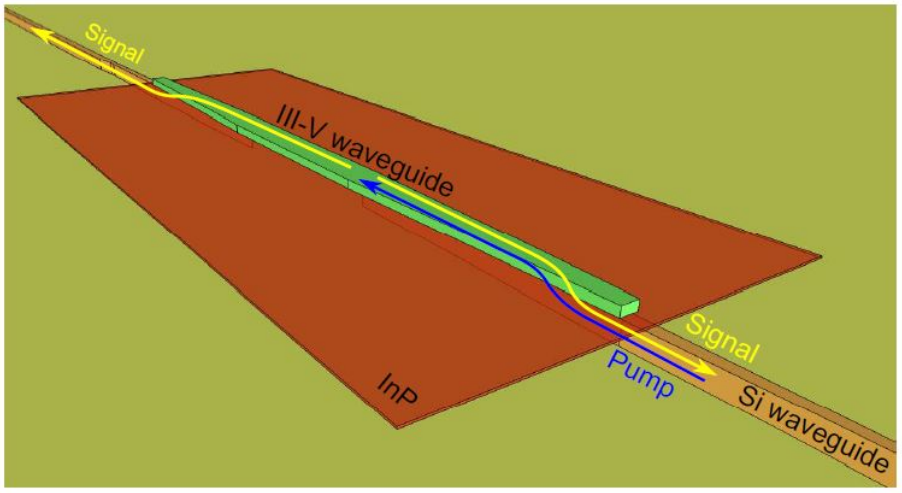


FIGURE 2.48: Illustration of the optically pumped transfer printed LED [161].

and then places it on a target substrate. As described in [160] the adhesion of the elastomeric stamp depends on the velocity of the stamp. Picking the coupon from its native substrate is carried out by moving the stamp rapidly (in order to apply a force greater than the adhesion to the native substrate). Then the coupon is printed to an SOI chip by releasing the stamp slowly. The main advantage of this method over other bonding techniques is that coupons can be transfer printed in a parallel way, by picking up and placing down large arrays of coupons simultaneously.

The first demonstration of transfer printing of III-V opto-electronic components on a silicon photonic integrated circuit was in 2016 by De Groote et al. [161]. Thin InP based membranes are transferred on and coupled to an SOI waveguide circuit, after which a single-spatial-mode broadband light source is fabricated. The LED used is pumped externally by a 1310 nm laser through the underlying single mode Si waveguide, which is subsequently coupled to III-V membrane. The generated spontaneous emission is then captured and coupled to the same SOI waveguide as Figure 2.48 shows.

The transfer-printed III-V membrane consisted of two 60 nm thick InP layers, with an InGaAsP multi-quantum-well layer stack in between, resulting in a total membrane thickness of 200 nm. The target substrate was SOI on which a 50 nm thick DVS-BCB layer was spin-coated that served the bonding agent for the transfer printed coupons. The membrane layer was grown on the InP wafer. In between, a 1 $\mu$m thick InGaAs sacrificial layer was grown. An InGaAs(100 nm) / InP(1 $\mu$m) sacrificial layer pair was grown on top of the membrane LED stack and was removed after transfer printing. This offered mechanical stability to the coupon preventing its buckling when on stamp. The next step was to define anchoring locations for the coupon by etching through the InGaAs release layer into the substrate. Finally, in order to protect all epitaxial layers above the sacrificial InGaAs layer, a photoresist coating was applied and patterned. At the same time the tethers anchoring the coupon to the substrate were defined.

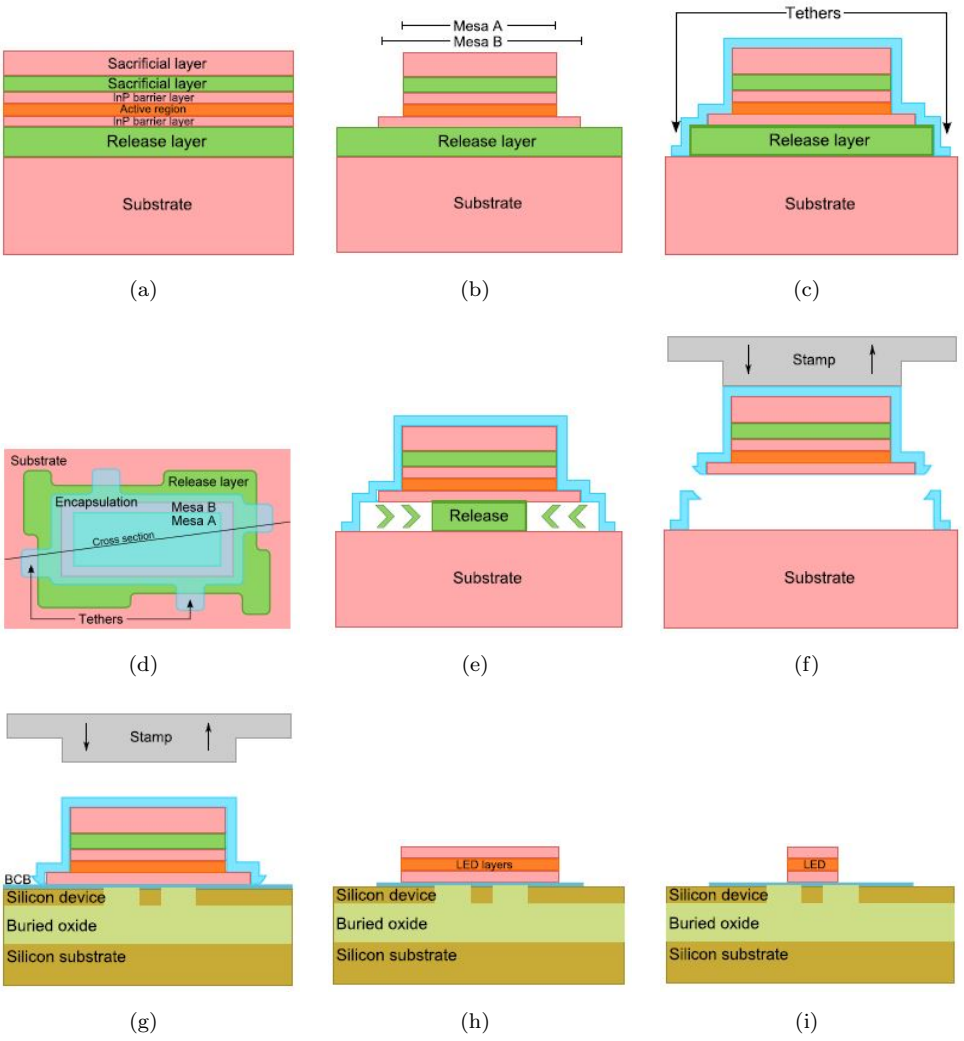


FIGURE 2.49: Process flow of transfer printed, optically pumped LED [160]. (a) InP starting layer stack, (b) Coupon patterning, (c) Encapsulation and tether definition, (d) Top view after encapsulation and tether definition. The cross section of the other figures is indicated, (e) Release etch, (f) Pick-up of the III-V coupon from the InP source substrate, (g) Printing of the III-V coupon to the SOI target substrate, (h) Removal of encapsulation and of sacrificial layers, (i) Definition of LED.

The InGaAs release layer was etched using aqueous Iron Trichloride ($FeCl_3$) preparing the coupons for the next step. Upon placing the patterned PDMS stamp on the coupon, the stamp was rapidly retracted from the InP substrate and then the coupons were transferred to the DVS-BCB coated SOI target wafer by attaching the coupons and releasing the stamp slowly. Once the coupon was placed, the photoresist encapsulation and the InP/InGaAs sacrificial layer pair were removed using $O_2$ plasma and wet etching respectively, before the membrane was further processed and aligned to the target SOI waveguide circuit using lithography. The process flow is illustrated in Figure 2.49.

Similar to wafer bonding, several interfaces between III–V and Si can be used. Alternatively, III–V can be directly printed on Si, however, surface smoothness is a crucial requirement [162]. Using BCB-assisted printing on the other hand, alleviates the need

for clean surfaces but at the expense of thermal issues [163]. To overcome the heating issues, a metal-based interface layer can be used to provide an efficient heat sinking without compromising device performance [163]. Several lasers structures on Si have been demonstrated using this approach including ridge waveguide lasers with etched facets [164, 163, 165] and surface-emitting lasers with Si photonic crystals mirrors [162].

### 2.3.5 Monolithic III-V epitaxy

Instead of integrating III–V lasers with Si by bonding approaches, an alternative approach is the monolithic integration which includes the direct crystal growth of III–V semiconductor lasers on Si. Using this mature approach, a low cost and reliable integration is enabled theoretically [166]. Some of the advantages of this approach are low cost, due to the elimination of costly III-V substrates, optimal substrate thermal conductivity and the ability to process, test and package 300 mm wafers. However, there are also drawbacks associated with this technique, the most important one being the lattice and thermal expansion mismatch. The difference in the lattice constants between the III-V and the Si substrate above a certain thickness ("the critical thickness") results in the formation of lines of missing atoms called "dislocations". These dislocations in the active area can in turn cause degradation in the laser performance, as they act as non-radiative recombination centres.

In addition, due to the different thermal expansion coefficient, the III-V epilayer can experience a large tensile or compressive stress during crystal growth (typically performed in the 350–1200 °C range for most III–V semiconductors), causing crack formation or delamination.

### 2.3.6 Conclusion

In this chapter, several approaches for the development of an integrated laser that have been demonstrated in the last 20 years, have been reviewed and analysed. The first conclusion that can be drawn is that at present, no single technological approach for integrated laser sources on-chip exists as a panacea, but some approaches offer advantages over the others. One of the reasons to explain the uncertainty about the mainstream technological solution that will be chosen is also that it strongly depends on the PIC architecture considered. For instance, one option could be the integration of several low-power small-footprint lasers on-chip while another option could be the integration of only few lasers with higher output powers, feeding the entire PIC. Constraints on laser device performances depend on the integration approach.

Bonding of III–V materials is currently the most developed technique for fabricating III-V light sources on Si. However, aspects of this technology including the reliability,

performance, uniformity and the cost of the aforementioned approaches targeting high-volume, large-scale integration on chip interconnects, are still unknown [123]. Moreover, significantly improving the WPE could render this as the dominant technology. In a long-term perspective, the direct monolithic integration of both group-IV or group-III–V semiconductor lasers may provide ultimate integration opportunities, through full wafer or localised epitaxy. However, significant improvements in material research have to be carried out in order to reach efficient lasing properties.

# Chapter 3

# Suspended Ge waveguides

## 3.1 Introduction

Ge has become a material of high interest for MIR integrated photonics due to the reasons described in 2.2.1. Using suspended Ge has the principal advantage of avoiding material losses from any cladding so that Ge's entire transparency range can be exploited. A further advantage of suspended Ge compared to the GOS platform is that it has a high and symmetrical refractive index contrast between the core and upper and lower air claddings. In the case of GOS, there is a high index contrast between the Ge core ($\Delta$n $\approx$ 3.0 at 7.67 $\mu$m) and upper air cladding, but low contrast with the Si lower cladding ($\Delta$n $\approx$ 0.6 at 7.67 $\mu$m). This results in the need for thicker rib waveguides, which in turn will result in a weak mode overlap of the evanescent field with the upper air cladding. Therefore, suspended Ge enables the development of thinner waveguides that exhibit larger evanescent field. This is a great advantage for sensing applications, in terms of sensitivity, where high mode overlap with an analyte surrounding the waveguide is desirable.

This chapter describes the development of suspended Ge waveguides for 3.8, 7.67 and 9.5 $\mu$m. Four Ge thicknesses $t_{Ge}$ were used for the different wavelengths: $t_{Ge}$ = 400 nm and 500 nm for $\lambda$ = 3.8 $\mu$m, $t_{Ge}$ = 1 $\mu$m for $\lambda$ = 7.67 and lastly $t_{Ge}$ = 2 $\mu$m for $\lambda$ =9.5 $\mu$m. The chapter includes the simulations carried out as well as the fabrication process and the characterisation of the final devices.

## 3.2 Design and simulation

This section includes the simulations carried out for all the components comprising the final device as well as the mask layout. Numerous simulation tools are used to simulate active and passive photonic devices with the most common ones being *Comsol*, *Rsoft*,

*Fimmwave* and *Lumerical*. The software that is widely used in the group and therefore chosen for the simulation of the devices in this work is *Lumerical*.

*Lumerical* [167] is a photonic simulation software that includes a comprehensive waveguide design environment for the analysis and optimisation of integrated optical waveguides, components and fibres. It includes various tools but the ones used in this work are Mode solutions and FDTD Solutions. Both tools can operate in 1D, 2D and 3D mode. Mode solutions can perform modal analysis, bidirectional eigenmode expansion and a Variational Finite-Difference Time-Domain (varFDTD) which is an approximation of a full 3D FDTD. This method is faster than the full 3D FDTD. It reduces the 3D problem into an effective 2D problem but for this to be valid the assumption is that the coupling between the slab modes supported by the vertical waveguide structure is negligible. FDTD solutions is a fully vectorial 3D Maxwell solver but the simulations times are significantly longer, especially for devices of larger dimensions. This is because the number of grid cells covering the device needed for the calculation is proportional to the device's size.

Another solver used in this work is the Eigenmode Expansion (EME) in *Mode Solutions*. This solver considers the propagation of light by decomposing the local field into the modes at that position (known as "supermodes"). While travelling in a uniform medium (e.g. a section of waveguide, a directional coupler or the rectangle in an Multi-Mode Interferometer (MMI)), each mode is propagated individually simply by multiplying by the complex propagation constant. To connect to the next section of the device, scattering parameters are used. The use of S-parameters is inherently bi-directional hence it includes both forward and backwards propagation. This technique is accurate for an infinite number of modes and is well suited for long structures such as MMI couplers, tapers, etc.

### 3.2.1 Waveguides

In this section, the various simulations carried out to investigate the behaviour of the waveguides, are described. Waveguides for three wavelengths were developed: 3.8, 7.67 and finally 9.5 $\mu$m, since sources at these wavelengths are available in the Optoelectronics Research Centre (ORC).

#### 3.2.1.1 Straight waveguides

The guiding structure is a rib waveguide, based on a Ge-on-SOI platform. The wafers were fabricated using Ge-on-SOI with a Ge layer grown by RPCVD on SOI. The Ge layer thickness was varying from 400 nm to 2 $\mu$m depending on the desired wavelength. In order to ease the subsequent removal of the underlying Si layer in the waveguides

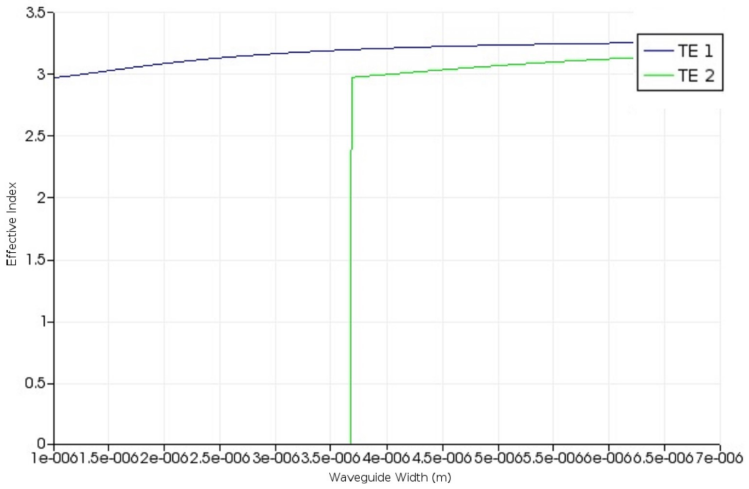


FIGURE 3.1: Effective index as a function of the waveguide width for the 1 $\mu$m thick Ge at $\lambda$ = 7.67 $\mu$m.

designed for $\lambda$=7.67 and 9.5 $\mu$m as described in 3.3, this layer was thinned from 220 nm down to 60 nm using a combination of oxidation and etching steps.

To simulate the waveguides a script had to be developed which was used to change various parameters of the design such as the materials used and their dimensions. The critical dimensions which defined the performance of the waveguide are the Ge layer thickness, the BOX layer thickness, the waveguide's width and the etch depth. The simulation's outcome determined the dimensions that the waveguides need to have to ensure propagation of either single TE or single TM mode. In addition, mode confinement in the waveguide is determined by the etch depth which is important when designing tight bends. However, deeply etched waveguides exhibit higher loss since the main loss mechanism is scattering of light due to surface roughness at the waveguide's sidewalls which scales inversely with the fourth power of the wavelength ($\lambda^{-4}$) [168]. Therefore, there is a trade-off between the mode confinement and the propagation that has to be taken into account when determining the etch depth. Upon carrying out simulations to ensure single mode operation, the optimal values for the width and the etch depth were chosen for each platform. Figure 3.1 shows the simulation results for the 1 $\mu$m thick Ge for $\lambda$ = 7.67 $\mu$m. Similarly, the single mode condition for the other waveguide thicknesses and wavelengths was obtained.

The dimensions as well as the theoretical loss value obtained for each platform are shown in Table 3.1. Figure 3.2(a) and Figure 3.2(b) for example the simulated simulated waveguide design and the fundamental TE mode at 7.67 $\mu$m for the 1 $\mu$m thick Ge. The simulated optical mode confinement of the fundamental TE mode at 7.67 $\mu$m in air, using the dimensions in Table 3.1, is ≈15% as opposed to ≈2.5% in GOS in the waveguides presented in [86].

TABLE 3.1: Rib waveguide dimensions and theoretical propagation loss values obtained for the fundamental TE mode.

| Wavelength | 3.8 $\mu$m | | 7.67 $\mu$m | 9.5 $\mu$m |
|---|---|---|---|---|
| Ge thickness | 400 nm | 500 nm | 1 $\mu$m | 2 $\mu$m |
| Si thickness | 220 nm | | 60 nm | 50 nm |
| BOX thickness | 3 $\mu$m | | | |
| Etch depth | 250 nm | 200 nm | 300 nm | 500 nm |
| Waveguide width | 1.1 $\mu$m | 1.5 $\mu$m | 3.5 $\mu$m | 5.5 $\mu$m |
| Simulated loss | 0.109 dB/cm | 0.084 dB/cm | 0.064 dB/cm | negligible |

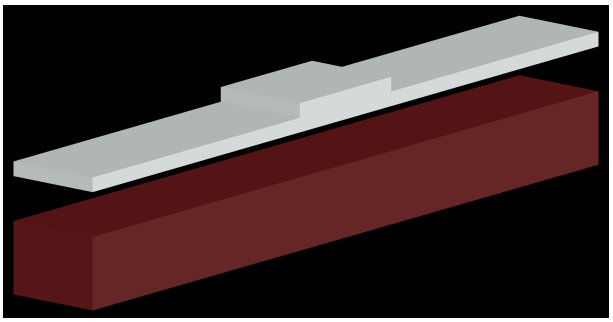

(a)

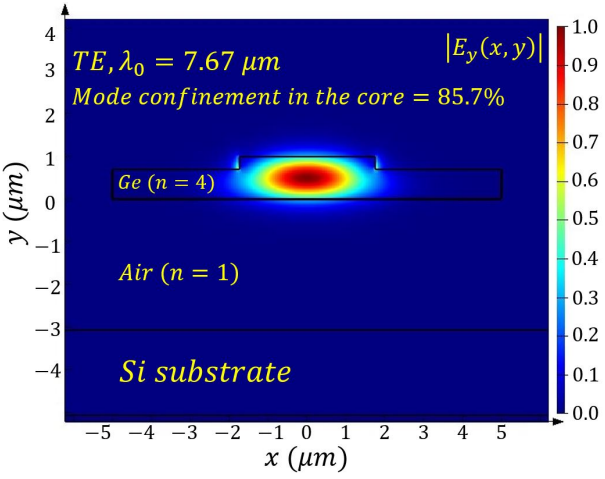


(b)

FIGURE 3.2: (a) Schematic of the simulated 1 $\mu$m Ge waveguide for $\lambda = 7.67$ $\mu$m. The grey layer and the red layer correspond to the Ge layer the Si substrate respectively. (b) Cross section of the simulated fundamental TE mode at $\lambda = 7.67$ $\mu$m.

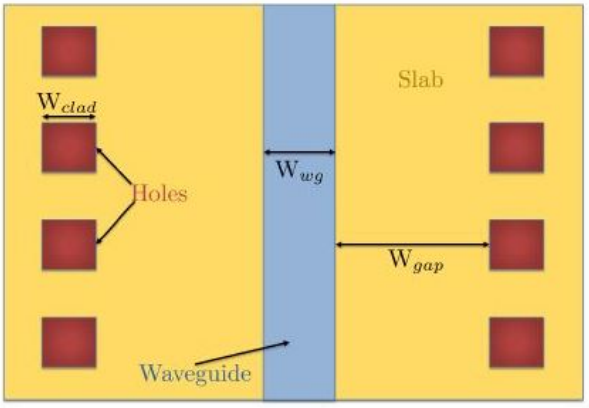


FIGURE 3.3: Diagram showing the structure of the suspended Ge waveguides fabricated with a two dry etch step process.

In order to suspend the waveguides, holes were designed on each side of the waveguides in order to gain access to the BOX and remove it. The lateral distance of the holes from the waveguides was determined using the power and impedance integration tool in the eigensolver analysis window of MODE solutions, such that the fraction of the optical power propagating through the holes does not exceed 0.1%. However, by increasing this distance, the etching time in HF to locally remove the BOX is also increased which compromises the mechanical robustness of the waveguides. Therefore, there is an apparent trade-off of propagation loss due to reflections from the holes and mechanical stability. Figure 3.3 shows a schematic of the top-view of the suspended Ge waveguides.

In the case of the 2 $\mu$m Ge for $\lambda = 9.5$ $\mu$m, the effect of the holes on the propagation loss was investigated by carrying out FDTD simulations for higher accuracy due to the fact that FDTD is a direct solution of *Maxwell*'s equations.

First, by sweeping the the period and the duty cycle of the lateral holes, the dimensions at which the highest reflections were obtained were for a period of $\Lambda = 4$ and DC $=$ 0.35. The duty cycle is defined as the air to Ge ratio. Figure 3.4 shows the reflection spectrum corresponding to a gap between the holes and the waveguide core of 1 $\mu$m.

To ensure minimal reflections from the holes, a simulation was carried out to obtain a figure for the reflection as a function of the distance of the holes from the waveguide core. Figure 3.5 shows the result for a simulation carried out for a 160 $\mu$m long waveguide.

As observed from the simulation result, for a gap of $<3$ $\mu$m the reflection drops below 1%

At such long wavelengths (7.67 and 9.5 $\mu$m), the loss due to the Si substrate leakage becomes a limiting factor. Therefore, having a sufficient air gap thickness between the waveguide and the substrate is crucial for operation at longer wavelengths. Figure 3.6 shows the loss of 1-$\mu$m-thick Ge, due to leakage to the substrate as a function of the air gap thickness. The graph was created by sweeping the position of the lower z boundary

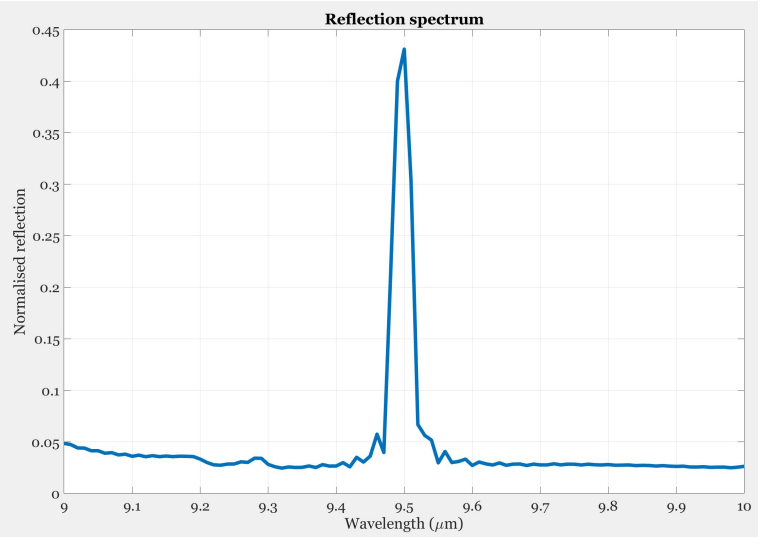


FIGURE 3.4: Reflection spectrum of a 400 $\mu$m long waveguide, for a hole period and duty cycle of $\Lambda = 4$ $\mu$m and DC $= 0.35$ respectively. The distance between the holes and the waveguide core was selected to be 1 $\mu$m.

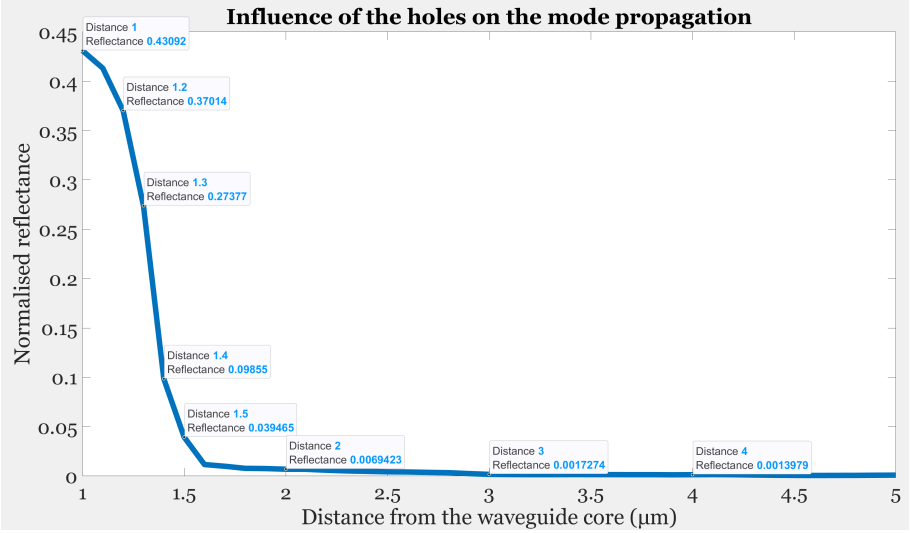


FIGURE 3.5: Reflection due to the lateral holes as a function of the distance between the holes and the waveguide core.

in the Finite Difference Eigenmode (FDE) solver, upon setting it to perfectly matched layer and obtaining the corresponding loss values. It is apparent that at wavelengths longer than 12 $\mu$m, the 3 $\mu$m air gap becomes insufficient for the mode confinement in the waveguide.

#### 3.2.1.2 Bends

Apart from the straight waveguides, simulations have also been carried out for bent waveguides. The solver used to simulate the bends was the 2.5D variational FDTD solver, also called the varFDTD solver. This solver works by collapsing a 3D geometry

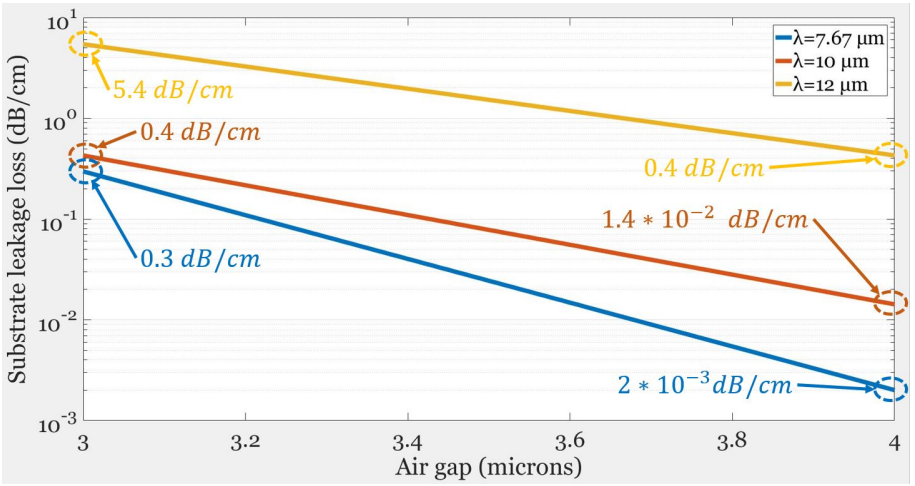


FIGURE 3.6: Substrate leakage loss as a function of the air gap for the waveguide dimensions in Table 3.1

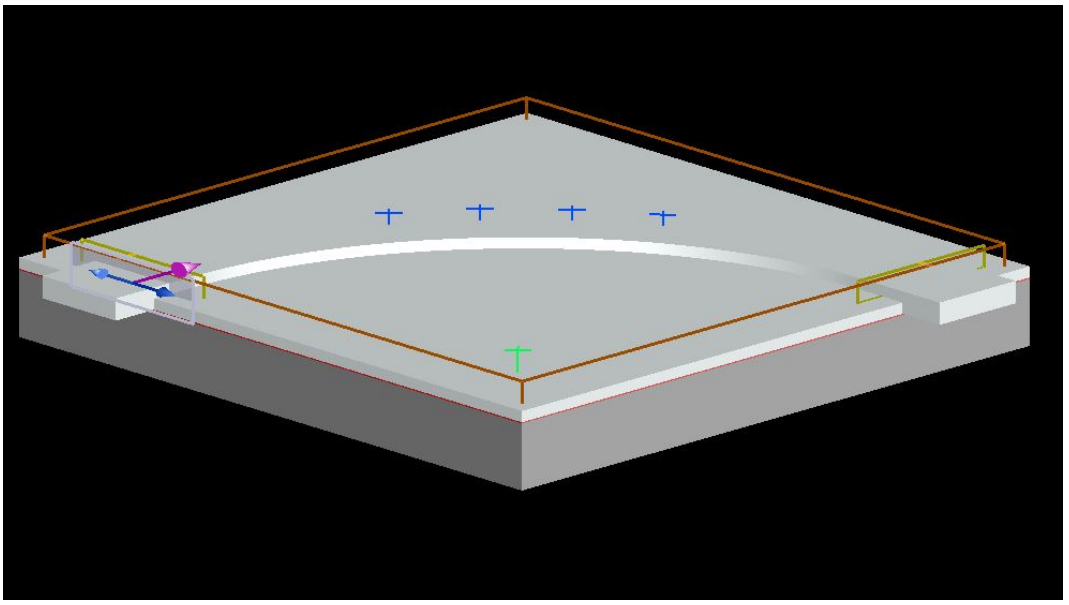

FIGURE 3.7: Schematic of the simulated Ge bend structure. The orange rectangle indicates the simulation region while the yellow rectangles represent the frequency domain power monitors used in order to obtain the transmission. The purple arrow indicates the direction in which the source is emitting while the crosses (green and blue) indicate the x,y coordinates of the test points used to study the materials created in those regions.

into a 2D set of indices, and runs a 2D FDTD simulation which is much faster and uses less memory compared to a 3D FDTD simulation. This works best with waveguides made from planar structures, as the main assumption of this method is that there is little coupling between different supported slab modes. The schematic of the simulated structure is illustrated in Figure 3.7.

The transmission values were obtained using a frequency domain power monitor upon propagating a beam at 7.67 $\mu$m from a light source. There is a trade-off between the etch

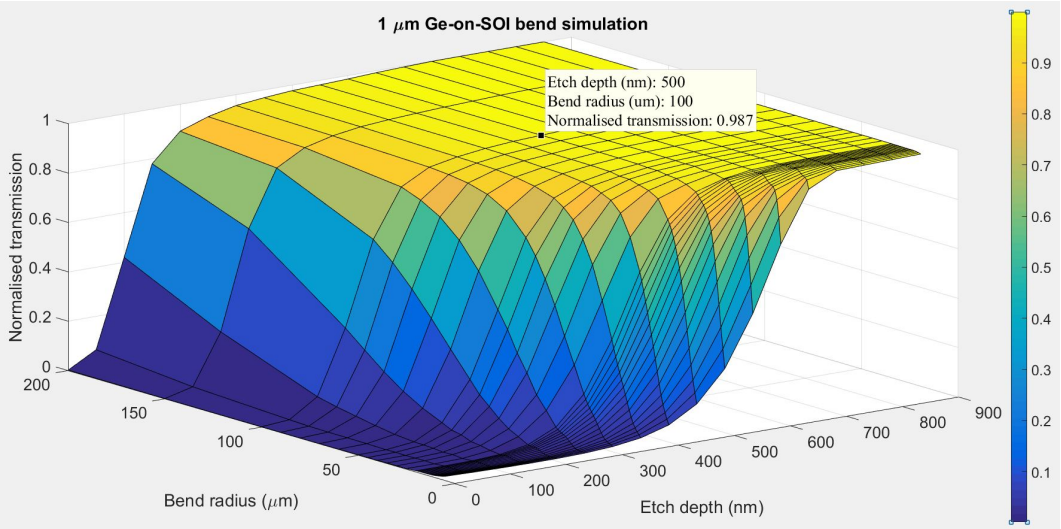


FIGURE 3.8: The graph showing the normalised transmission (z-axis) as a function of the etch depth from 0-1 $\mu$m (y-axis) and the bend radius from 0-200 $\mu$m (x-axis).

depth and the bend radius. Increasing the etch depth will result in a higher confinement of the optical mode inside the waveguide allowing for smaller bend radii. However, it will induce an increase in the propagation loss. Therefore, a sweep was carried out in order to obtain the optimum match for the etch depth and the bend radius such that low propagation losses are achieved using acceptable bend radius values. The results are presented in the form of a three dimensional graph shown in Figure 3.8.

From the simulations the bend radius for which the mode is well-confined in a 3 $\mu$m wide waveguide for an etch depth of 500 nm, is 100 $\mu$m.

### 3.2.2 Grating couplers

The design and simulation of the grating couplers were carried out using the FDTD solving technique, an "exact" numerical calculation of Maxwell's equations, where the accuracy converges to the exact solution as the spatial discretisation of the volume is reduced, i.e. smaller mesh size.

The grating couplers designed are 2D structures. This means that the refractive index changes not only along the x axis but along the y axis as well, as shown in Figure 3.9.

The duty cycles in both axes are defined below:

$$DC_x = \frac{\Lambda_{gr,x} - l_{air,x}}{\Lambda_{gr,x}} \tag{3.1}$$

$$DC_y = \frac{\Lambda_{gr,y} - l_{air,y}}{\Lambda_{gr,y}} \tag{3.2}$$

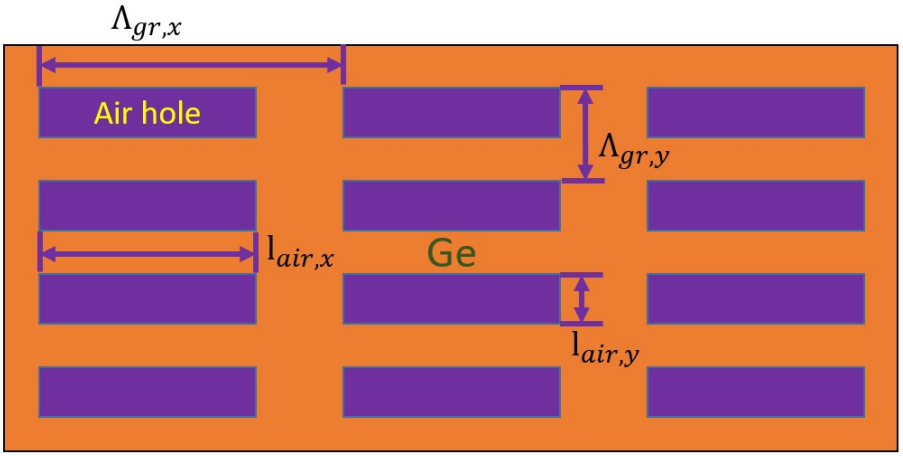


FIGURE 3.9: Schematic of the subwavelength grating coupler.

where $\Lambda_{gr}$, $l_{air}$ and $DC$ are the period, air gap and duty cycle respectively. The subscript indicates the axis.

The 2D FDTD solver in *Mode solutions* was used to simulate the grating couplers because it takes much less computational memory and simulation time compared to the 3D without compromising the accuracy of the results. The illustration in Figure 3.10 depicts a grating coupler structure: the Si wafer on the bottom, a functional Ge layer on top of a 3 $\mu$m BOX. The green parts resemble the holes. Due to the fact that the grating coupler is a 2D structure as explained above, these parts have an effective refractive index value between 1 (air) – 4.02 (Ge) depending on $DC_y$. In this case the lateral duty cycle was 0.8 which corresponded to an effective refractive of $n_{eff} = 3.42$ wich was calculated using Equation 3.2.

$$n_{eff} = DC * n_{effGe} - (1 - DC) * n_{Air} \tag{3.3}$$

The orange rectangle defines the simulation region. Using Perfectly Matched Layer (PML) boundary conditions the radiation appears to propagate out of the computational area and, therefore, does not interfere with the fields inside. The yellow lines shown represent frequency-domain power monitors which collect power flow information in the frequency domain from simulation results across spatial regions within the simulation. Figure 3.10(a) is used to simulate the input grating coupler and Figure 3.10(b) is used to simulate the output grating coupler.

For an input grating coupler, a fundamental TE mode is launched from the top of the grating coupler at an angle (in the case of the lab setup described in Section 3.4.1 the angle of the fibre is 20°) and coupled into the waveguide by the grating. Power monitors are used to record the insertion loss and reflection of the grating coupler. For an output grating coupler, a fundamental TE mode is launched from the waveguide and out-coupled.

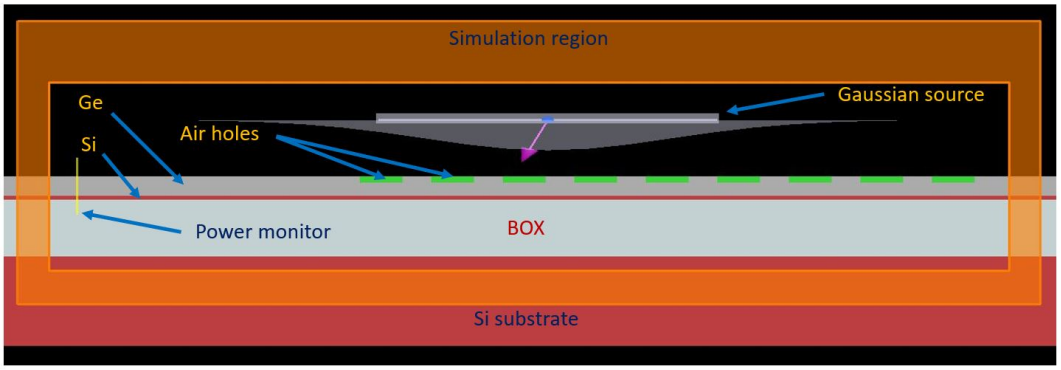


(a) Simulation configuration for an input grating coupler

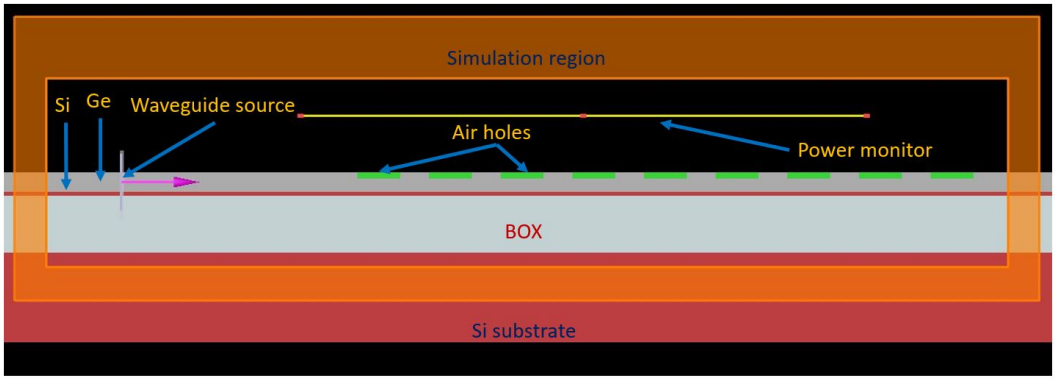


(b) Simulation configuration for an output grating coupler

FIGURE 3.10: 2D FDTD simulation configuration for the grating coupler. Mode sources are used to inject light into the simulation either from above the grating coupler (a) or from the waveguide (b). Frequency domain power monitors are used to measure the transmission.

By running sweeps for the period and the duty cycle, the optimal parameters were obtained taking into account the coupling efficiency as well as the back reflections. The results are presented in a form of graph in which the x-axis is the period and the y-axis in the normalised transmission for a given value of duty cycle as shown in Figure 3.11.

To simulate the grating coupler for $\lambda = 9.5$ $\mu$m the 3D FDTD solver was used for higher accuracy. The 3D schematic of the simulated structure as well as the simulation results are shown in Figure 3.12.

The optimal grating coupler parameters for $\lambda = 3.8$, 7.67 and 9.5 $\mu$m are summarised in Table 3.2.

In terms of the characterisation of the device, the most important part is to keep the back reflections as low as possible. Otherwise, a cavity is formed between the grating couplers and Fresnel reflections are observed, resulting in fringes in the spectrum causing variations in the transmission that make propagation loss measurements using the method described in Section 3.4.3, unreliable.

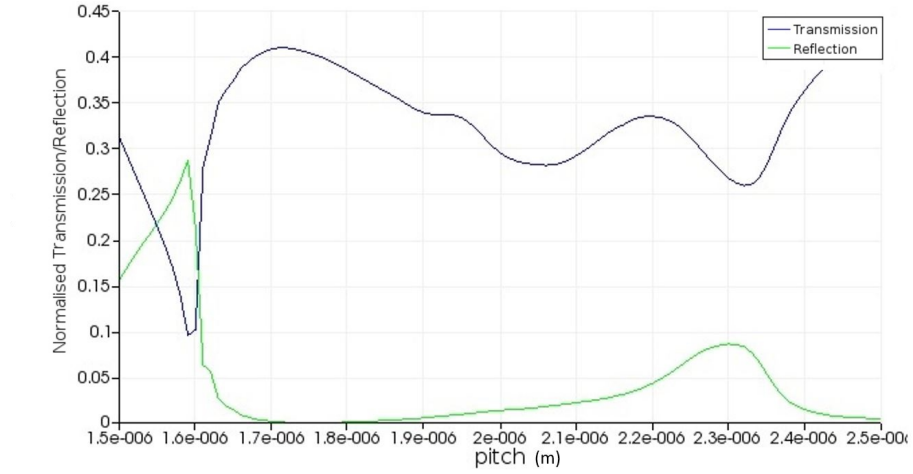


(a)

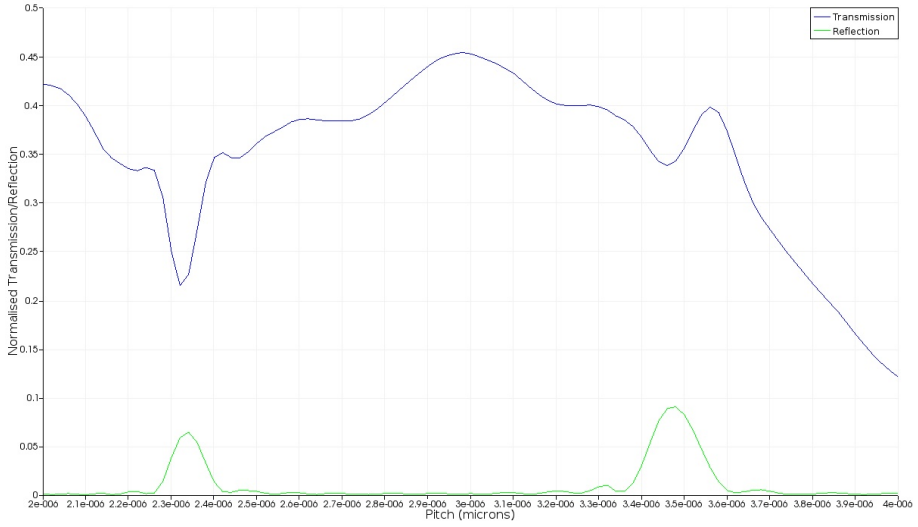


(b)

FIGURE 3.11: Transmission and reflection spectra of the simulated grating coupler designed for (a) $\lambda = 3.8$ $\mu$m and (b) $\lambda = 7.67$ $\mu$m. The blue line shows the transmission while green red one shows the reflection.

TABLE 3.2: Grating coupler properties for 3.8, 7.67 $\mu$m and 9.5 $\mu$m.

| Grating coupler properties | | | |
|---|---|---|---|
| Wavelength | 3.8 $\mu$m | 7.67 $\mu$m | 9.5 $\mu$m |
| Ge thickness | 500 nm | 1 $\mu$m | 2 $\mu$m |
| Etch depth | 200 nm | 300 nm | 1 $\mu$m |
| $T_x$ | 1.71 $\mu$m | 2.98 $\mu$m | 3 $\mu$m |
| $T_y$ | 1 $\mu$m | 1 $\mu$m | NA |
| $DC_x$ | 0.6 | 0.5 | 0.7 |
| $DC_y$ | 0.8 | 0.8 | NA |
| Simulated transmission | 46.18% | 45.43% | 48.48% |
| Simulated reflection | 0.01% | 0.14% | 16.24% |

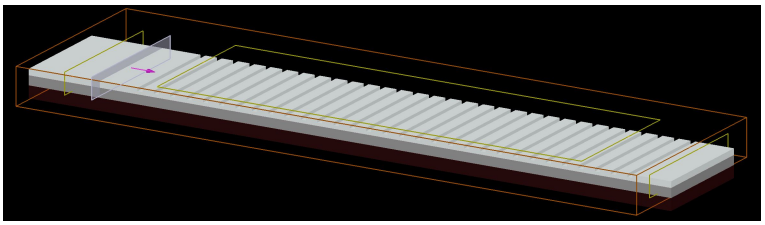

(a) 3D schematic of the simulated grating coupler showing the grating coupler structure and the various monitors used to evaluate the performance of the grating coupler.

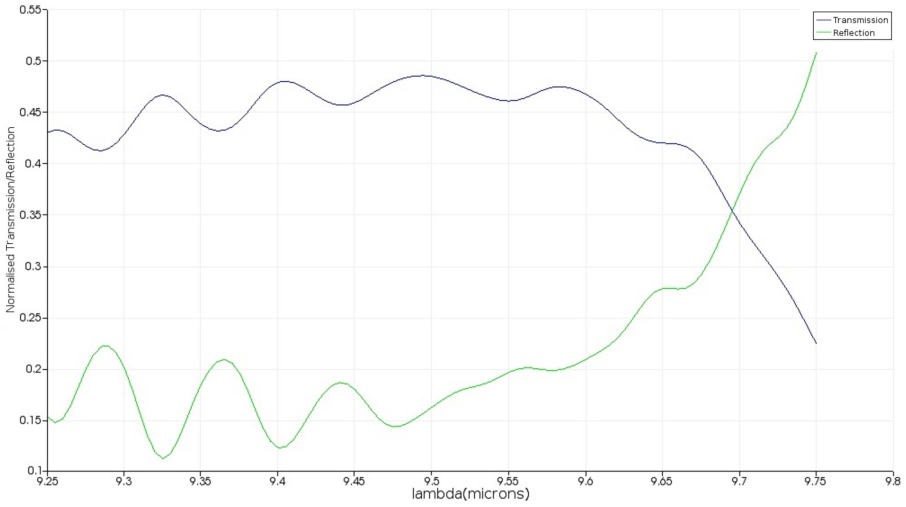


(b) Normalised transmission and reflection spectra.

FIGURE 3.12: Simulated grating coupler for $\lambda = 9.5$ $\mu$m.

## 3.3 Fabrication

Upon simulating the desired devices, producing their layout followed. This was achieved using a combination of the $L-edit$ layout software by *MentorGraphics* [169] and a series of C++ functions which were first written and then called as macros in $L-edit$. First the fundamental blocks of the devices were developed in a form of a library of C++ functions. Then different component parts are aligned so they form different sets of devices. This way the design of multiple components were parameters were changed frequently was made easier and more time efficient. Examples of this include waveguides with different lengths which were used to calculate the propagation loss using the cut-back method (explained in 3.4 and grating couplers with different period and duty cycle for the optimisation of the coupling efficiency from the optical fibres into the waveguides and vice versa.

Once the device dimensions and parameters have been determined, fabrication followed. The initial platform was Ge-on-SOI in which the Ge layer was grown by RPCVD at *IQE* [170] on an SOI wafer with 220 nm top Si and 3 $\mu$m BOX provided by *Simgui* [171]. This fabrication run was carried out using 400 nm and 1 $\mu$m thick Ge. Once the wafer was prepared, the first e-beam step was carried out to define the waveguides and

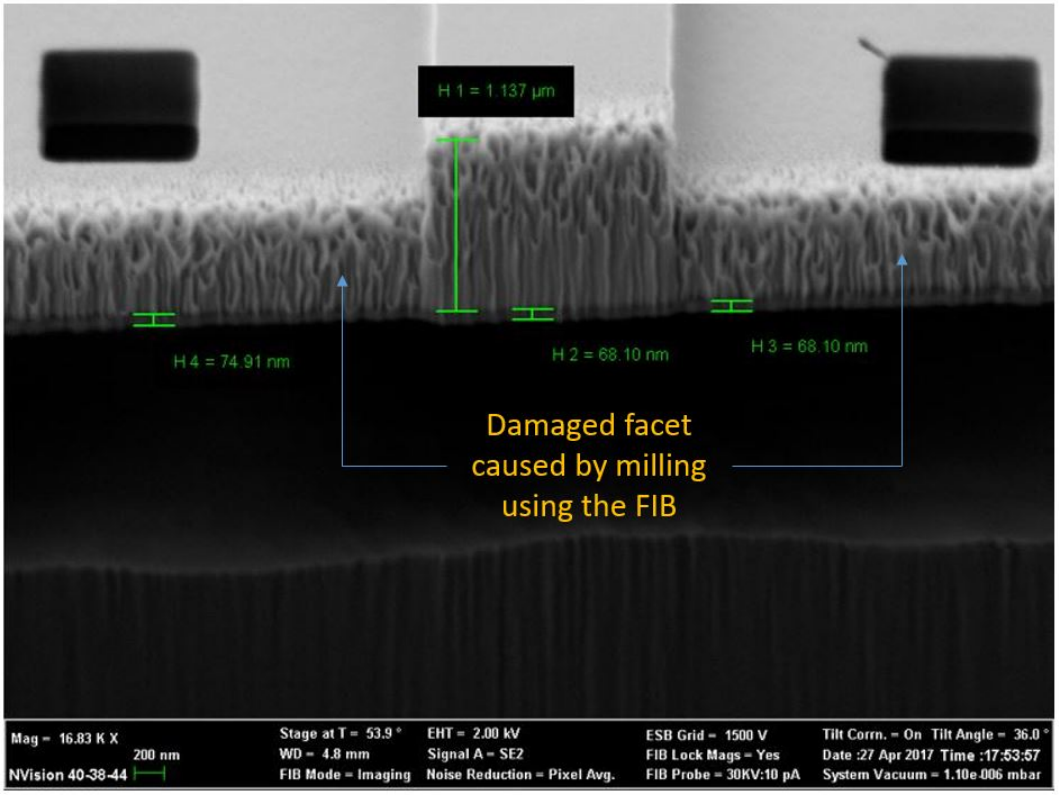


FIGURE 3.13: SEM image of the 1 $\mu$m thick Ge-on-SOI.

the grating couplers. Then, in order to suspend the waveguides, the BOX and the Si had to be removed. This was achieved by patterning holes with a second e-beam step alongside the waveguide core far enough so they do not interact with the guided mode. Using ICP the remaining Ge slab and the Si layer were etched exposing the BOX which was then removed by immersing it in 7:1 HF for 10 minutes. Next, the Si was removed by carrying out a second wet etch using a 25% aqueous solution of TMAH for 2 hours at room temperature. Figure 3.14 shows the overall process flow of the first fabrication run.

As seen from the SEM image taken (Figure 3.13), out of 220 nm of the initial thickness, approximately 70 nm were left.

Due to the 4.2% lattice mismatch between Ge and Si, Ge epitaxial layers on Si substrates have high TDD (in the order of $10^8$ cm$^{-2}$) and surface roughness. The removal of the Si layer causes increased confinement of the optical mode within the Ge waveguide. This results in less mode interaction with the Ge-Si interface reducing the propagation loss due to scattering.

However, it was observed from the results discussed in Section 3.4 that this fabrication process flow was unsuitable for processing Ge resulting in high propagation loss. In particular the main issue was the oxidation of Ge. The asher, which is used to strip the photoresist after every dry etch step, uses an $O_2$ plasma which results in the formation

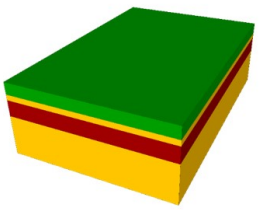

(a) Initial platform.

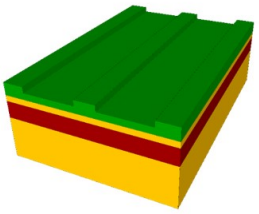

(b) Waveguide patterning

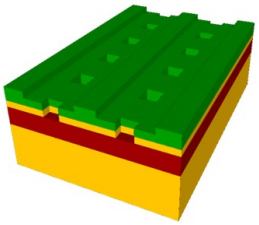

(c) Holes patterning

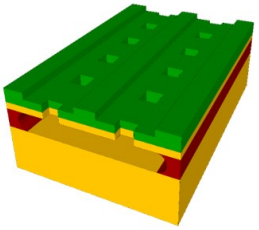

(d) Removal of the BOX

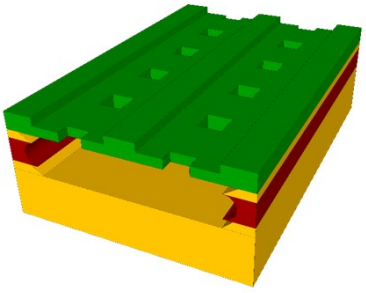

(e) Removal of the Si layer

FIGURE 3.14: Process flow of the first fabrication run. The green, yellow and red parts represent the layers of Ge, Si and BOX respectively.

of Germanium Dioxide ($GeO_2$). This oxide layer has a solubility in water of 0.447 g in 100 mL at 25 °C and 1.07 g in 100 mL at 100 °C [172] . It is also soluble in HF since it contains water. This means that every process step that includes water, defects are created on the Ge layer resulting in high propagation loss. Moreover, it appeared that the BOX was of an inferior quality resulting in a non-uniform etching profile as shown in the SEM image of the waveguide cross section taken in Figure 3.15.

As observed from the SEM image, approximately 52 $\mu$m of the BOX was removed laterally giving an etch rate of 5.2 $\mu$m/minute. However, in the y-direction, the BOX was not completely removed due to the anisotropic etch. This means that the density of the BOX in the y-axis varied.

To overcome the issue of the Ge oxidation, a new fabrication process flow had to be implemented. The exposed Ge was protected by a thin layer of $SiO_2$ (100 nm thick) that

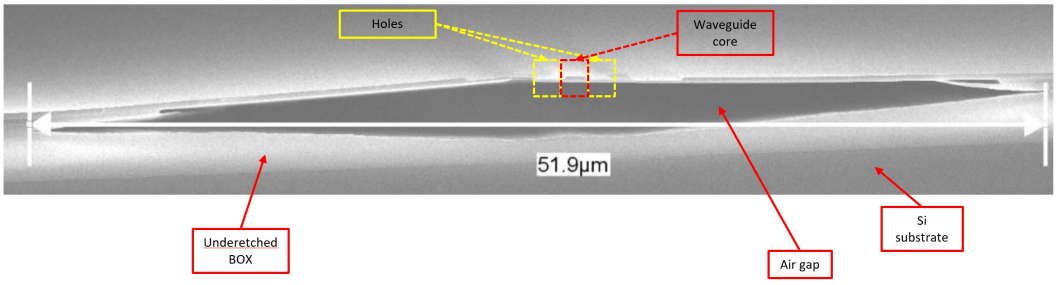


FIGURE 3.15: SEM image of the 1 $\mu$m thick Ge-on-SOI after the first fabrication run.

was deposited using the PECVD tool, before every e-beam step as shown in Figure 3.16.

For the second fabrication run 500 nm and 1 $\mu$m thick Ge layers were used for $\lambda = 3.8$ $\mu$m and 7.6 $\mu$m respectively. The SOI wafer used was provided by *Soitec* [173] having a BOX of a better quality. Also, to decrease the etching time of Si in TMAH, before the growth of Ge, the Si layer was thinned down to 60 nm by performing a dry oxidation step for 26 hours at 1000 °C. This caused the formation of 430 nm of $SiO_2$ which was then removed by wet etching with (7:1) HF for 4 minutes and 45 seconds, given that the etch rate of $SiO_2$ in (7:1) HF is 88 nm/min. The wafer was mapped using the ellipsometer after thinning to obtain the thicknesses and uniformities of the layers as shown in Figure 3.17. According to the mapped graph, the thickness is uniform across a high percentage of the wafer surface.

The wet etching times in HF and TMAH were 80 min and 1 hour respectively. After fabrication SEM images of a waveguide cross section were taken as shown in Figure 3.18.

From Figure 3.18(a) it can be observed that the etching profile is significantly more uniform compared to the first fabrication run resulting in the complete removal of the BOX. Also, because the substrate was exposed this time, it was etched as well resulting in an increase of the air gap by 440 nm. This in turn decreases the loss due to the reduced leakage of the optical mode to the Si substrate. It also shows a route towards fabrication of waveguides suitable for longer wavelengths since the separation between the Ge waveguide and Si substrate can be increased even further.

The fabrication of all the components presented in this work was carried out in the Southampton Nanofabrication Centre (SNC). The size of the samples used was 30×40 mm. Samples were used instead of a whole wafer due to fact that the devices designed were small enough such that a sufficient number of component variations can fit.

The first step includes an e-beam lithography to pattern the samples. In this method of lithography the custom layouts are written by scanning a focused beam of electrons on a surface covered with an electron-sensitive film called resist (exposing). The solubility of the resist is changed by the electron beam, enabling selective removal of either the exposed or non-exposed regions of the resist depending on the type of resist used (positive or negative respectively). The main advantage of e-beam lithography is its

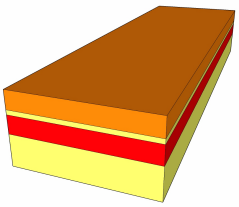

(a) Initial Ge-on-SOI platform.

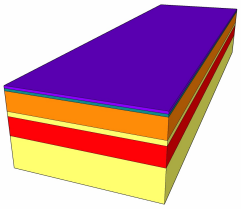

(b) Deposition of $SiO_2$ and spinning of photoresist

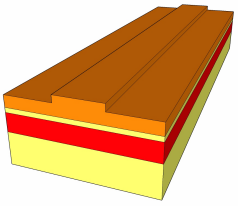

(c) Waveguide patterning.

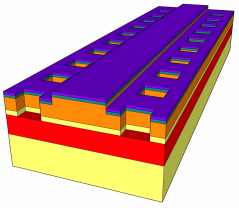

(d) Holes patterning and dry etching.

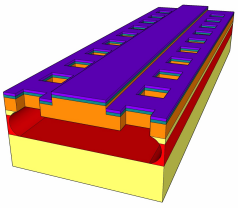

(e) Removal of the BOX and the Si layer by wet etching using HF and TMAH.

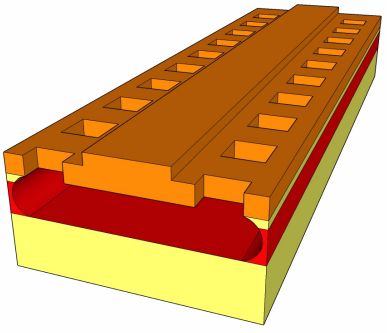

(f) Final structure.

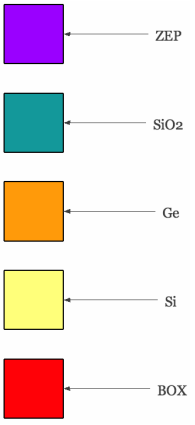


(g) Material colour code.

FIGURE 3.16: Process flow of the second fabrication run.

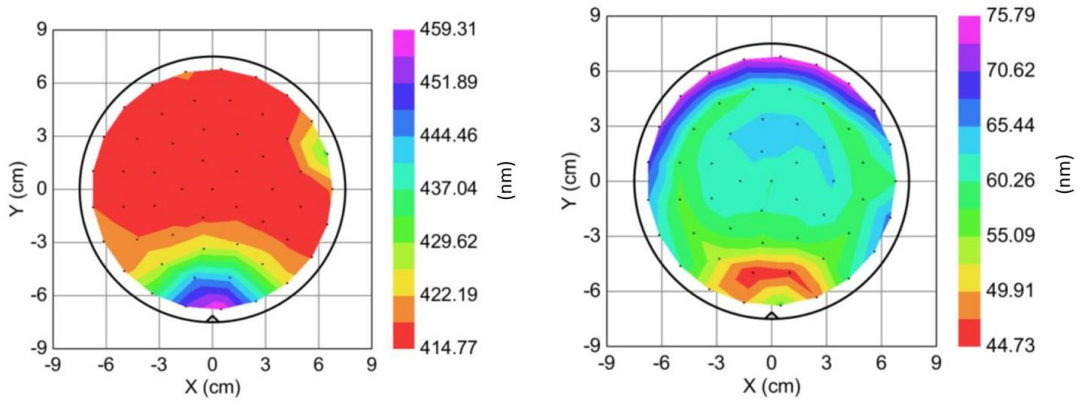


(a) Thermal $SiO_2$ uniformity (b) Thinned Si uniformity

FIGURE 3.17: Mapped SOI wafer after oxidation

capability of drawing custom patterns (direct-write) with sub-10 nm resolution. This form of maskless lithography has high resolution but low throughput due to the long writing times required, limiting its usage to low-volume production of semiconductor devices, and research and development. An important limitation that has to be taken into account when writing on insulating materials (e.g. $SiO_2$) with e-beam, is that negative charge build-up can occur on the surface causing beam deflection and hence pattern distortion. Therefore, the samples have to be spin-coated with *Espacer* $300Z$, a commercially available conductive polymer which can be simply removed by rinsing with water.

In the case where more that one e-beam step are required (in case where the etch depths of various components are different), alignment marks of rectangular shapes (shown in Figure 3.19) had to be written on the wafer so that both beams were well aligned to each other. The alignment marks are a set of predefined marks written at the edges of a chip or wafer, which are then located by the e-beam in order to align between multiple e-beam steps.

Once the mask layout was completed it was then handed to Dr. Ali Khokhar in GDS-II format who converted in to an e-beam file type (.V30 file type) using the *Beamer* software by *GenISys* [174]. GDS-II stream format is a database file format which is the industry standard for data exchange of integrated circuit or Integrated Circuit (IC) layout artwork. It is a binary file format representing planar geometric shapes, text labels, and other information about the layout in hierarchical form. The data can be used to reconstruct all or part of the artwork to be used in sharing layouts, transferring artwork between different tools, or creating photomasks. Apart from the mask layout, parameters for the e-beam operation such as the spot size and the beam's dose are contained in this file. The next step was to spin coat a photoresist layer, which was then baked for 3 minutes at 180 °C. The resist used was ZEP-520A. The etching rate selectivity of this resist to either Si or Ge is approximately 3 to 1. However, there

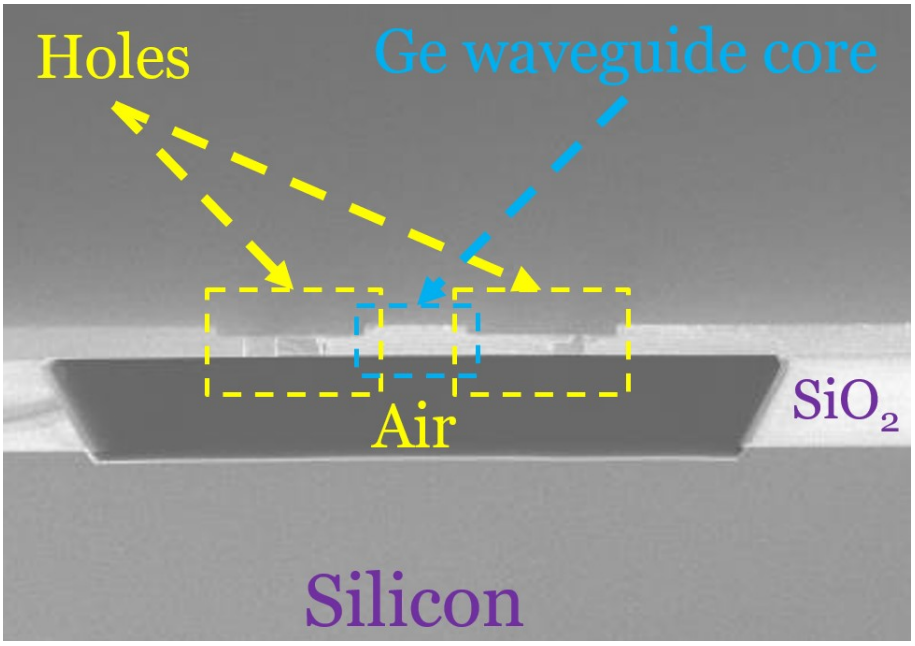


(a)

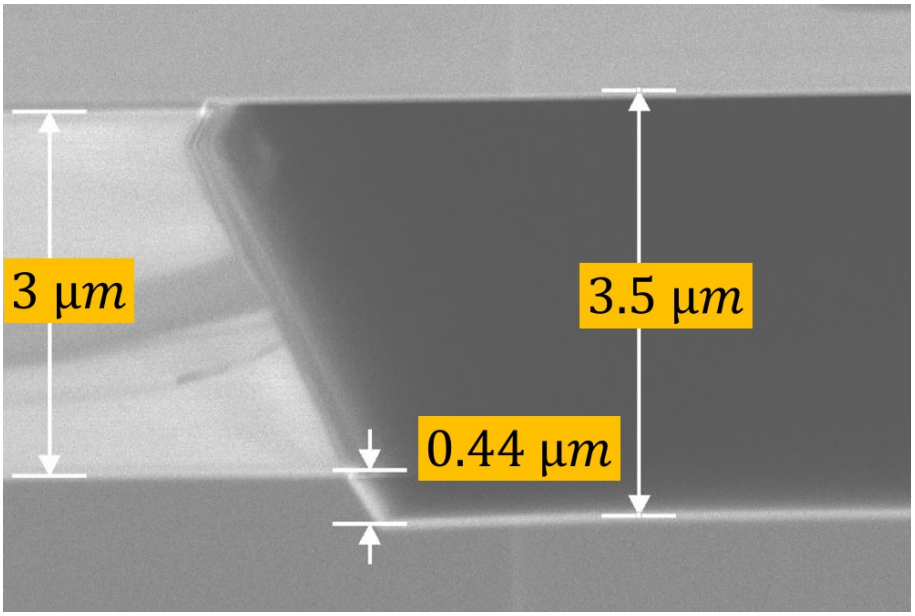


(b)

FIGURE 3.18: SEM images of a waveguide cross section after the second fabrication run.

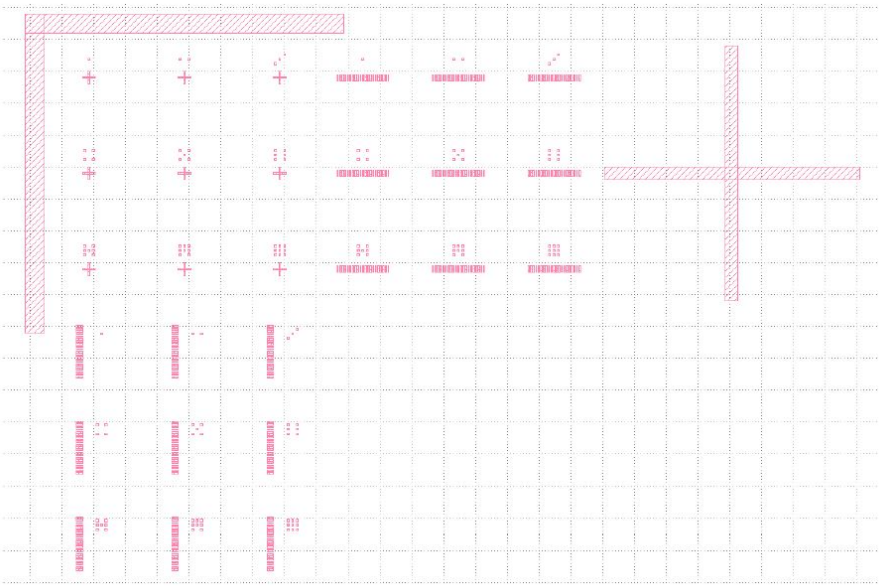

FIGURE 3.19: GDS of alignment marks at the corner of a chip.

is a limitation when determining the thickness of resist. The thicker the resist layer, the bigger the minimum feature size that can be written and this is due to electrons scattering in the resist [175]. The tool used to write the pattern is the *JEOL* JBX-9300 e-beam machine. Upon patterning, the next step was to develop the samples using the ZED-N50 developer after removing the Espacer by rinsing with water.

Having patterned the devices, etching followed. The samples were etched using the *Oxford Instruments* ICP 380 system [176]. The ICP etches the samples by creating a plasma from the gasses injected into its main chamber (Figure 3.20). This is achieved by applying a strong Radio Frequency (RF) power to a coil antenna generating a magnetic field that ionises the gas molecules by stripping them of electrons and, thus creating a plasma. This results in a voltage difference built into the chamber due to the collision of electrons with the wafer caused by of the oscillating RF power (charging the wafer). in order to accelerate the gas ions from the plasma towards the wafer, an additional DC power is created into the chamber. The collision of the gas ions with the sample results in a reaction with the surface etching material.

Inserting the samples in the ICP tool, a plain silicon wafer was used as carrier with the samples resting on top. The gases used for the creation of the plasma were Sulfur hexafluoride ($SF_6$) and Octafluorocyclobutane ($C_4F_8$). The parameters of the etching recipe used are shown in Table 3.3.

This was the standard Si etching recipe utilised by the group, which was used to etch Ge as well. The etch time was calculated according to the desired etch depth and the material being etched. In order to monitor the etching progress, the samples were removed from the ICP and then the remaining layer thickness was checked using an

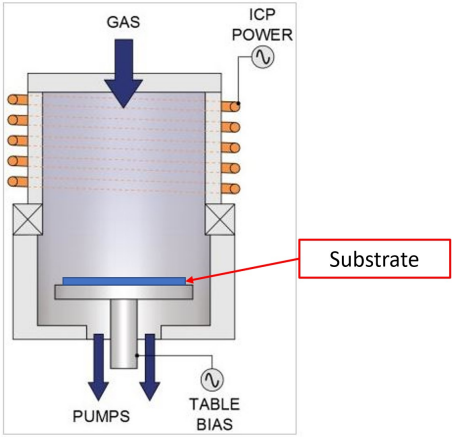


FIGURE 3.20: ICP diagram [176].

TABLE 3.3: ICP etching recipe parameters.

| ICP etching recipe | | |
|---|---|---|
| Parameter | Value | Unit |
| Pressure | 15 | mT |
| RF Power | 50 | W |
| ICP Power | 80 | W |
| Temperature | 15 | degrees |
| $SF_6$ Flow | 25 | sccm |
| $C_4F_8$ Flow | 45 | sccm |

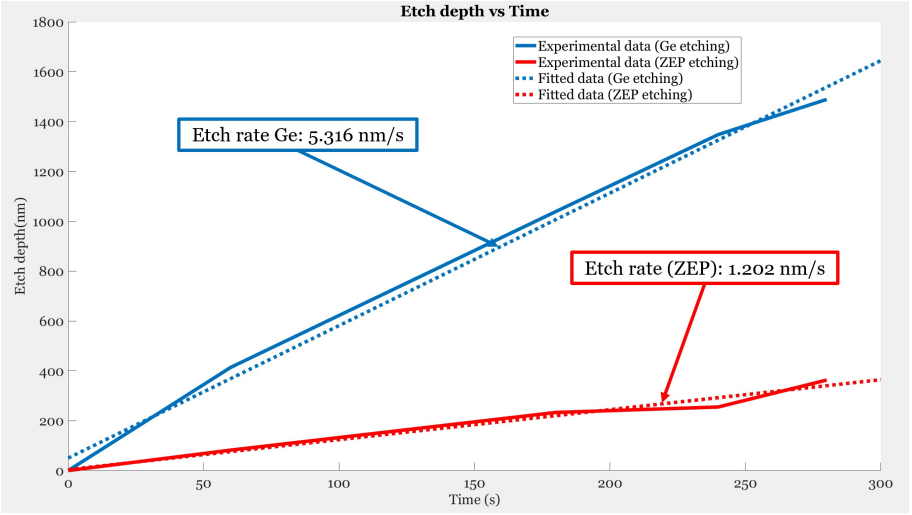


FIGURE 3.21: Etch depth of Ge and ZEP resist as a function of time.

elipsometer. A 1×1 mm metrology box was initially defined in the mask for this purpose. Figure 3.21 shows the etch depth of both Ge and ZEP resist as a function of time. Once etching was completed, the remaining photoresist was removed using an $O_2$ plasma asher.

## 3.4 Characterisation

This section presents the propagation loss measurements taken for the fabricated devices. The various techniques as well as the equipment used for their characterisation are also presented.

### 3.4.1 3.8 $\mu$m setup

In this section the various parts composing the 3.8 $\mu$m setup are described. The beam is initially generated by a tunable QCL provided by *Daylight Solutions* [177] ranging from 3.71 $\mu$m to 3.89 $\mu$m with a peak output power of ~150 mW at 3.8 $\mu$m operating in CW mode. The tuning accuracy is $\pm 0.5$ cm$^{-1}$ and the linewidth is $\pm 0{:}003$ cm$^{-1}$. The beam emitted is TM polarised (>100:1, TM:TE) relative to the plane of the sample when placed flat on a surface. The laser temperature is constantly maintained at 21 °C using a chiller circulating a coolant that consists of a $H_2O$/Isopropyl Alcohol (IPA) mixture. Controlling the laser parameters (wavelength and laser current which in turn controls the optical power) is achieved by a laser controller, supplied by the manufacturer, connected to a PC via the General Purpose Interface Bus (GPIB) and run using the *LabVIEW* software by [178]. The beam is directed to a half-wave plate, using a set of reflectors, in order to control its polarisation. Then, using a ZnSe lens (transmission range 0.5-20 $\mu$m), the beam is coupled to a Fluoride ($F^-$) based MIR single mode fibre (provided by *IRPhotonics* now part of *Thorlabs* [179]) , capable of guiding light from 300 to 4100 nm. The core and cladding dimensions are 9 $\mu$m and 125 $\mu$m respectively. With the help of grating couplers, the beam is coupled into and out of the device fabricated. The sample is placed on a stage, and the input and output optical fibres are supported by three-axis stages which can be aligned manually using piezo-controllers. Navigating the fibres on the chip is achieved with the help of a visible light camera with a magnifying lens tube placed above the sample stage. The camera output is displayed on a screen, showing a top view of the sample. Using the output fibre, the beam is guided to a Mercury Cadmium Telluride (HgCdTe) photodetector with a detectivity of $6\times10^{10}$ Jones provided by *Vigo System* [180]. This detector has the advantage of not requiring liquid nitrogen for its cooling. The detector is connected to a lock-in amplifier which was in turn connected to the PC via another GPIB providing the *LabView* program with the measured transmission which is plotted against the laser output wavelength. The lock-in amplifier locks the signal from the detector onto the modulated laser output from a chopper wheel controller, increasing the Signal-to-Noise Ratio (SNR). The setup is illustrated in the form of a block diagram in Figure 3.22.

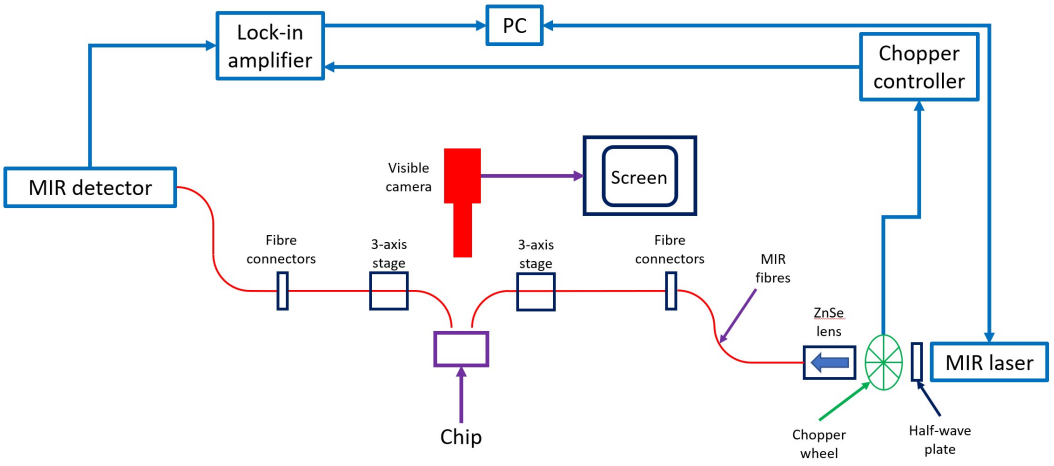


FIGURE 3.22: Block diagram of the 3.8 $\mu$m setup.

### 3.4.2 7.67 and 9.5 $\mu$m setup

The long-wavelength experimental setup utilised to characterise the fabricated waveguides comprises a single-mode CW DFB QCL ([179] QD7500CM1) capable of emitting light with a maximum output power of 106 mW at $\lambda = 7.67$ $\mu$m. It also includes a tunable QCL provided by *Daylight Solutions* [177] ranging from 9.25 $\mu$m to 10 $\mu$m with a peak output power of <100 mW operating in CW mode. The beam of both lasers are then collimated using a black diamond-2 lens with a focal length of 1.9 mm, modulated using a chopper wheel and then coupled into a single-mode Arsenic Triselenide ($As_2Se_3$) fibre (Coractive IRT-SE-28/170) using another black diamond-2 lens with a focal length of 6.0 mm. Light from the output grating couplers was collected via another single-mode fibre and coupled to a liquid-nitrogen-cooled HgCdTe detector ([181] MCT-13-1.00). The signal from the detector was amplified using a pre-amplifier before being guided to a lock-in amplifier to improve the signal-to-noise ratio.

### 3.4.3 The cut-back method

The method utilised to calculate the propagation loss of all the waveguides presented in this work, is the cut-back [182]. In this method the propagation loss is measured using waveguides of different lengths as shown in Figure 3.23. Its main advantage over other methods is that all the other loss mechanisms, including the insertion loss of the grating couplers and the losses induced by the optical fibres, are eliminated and only the propagation loss is extracted.

Another method is to include waveguides of the same length and by progressively reducing it by polishing the chip, the propagation loss is extracted. This method can be considered simpler due to the fact that no grating couplers have to be designed, however, it requires a very good facet every time the sample is polished.

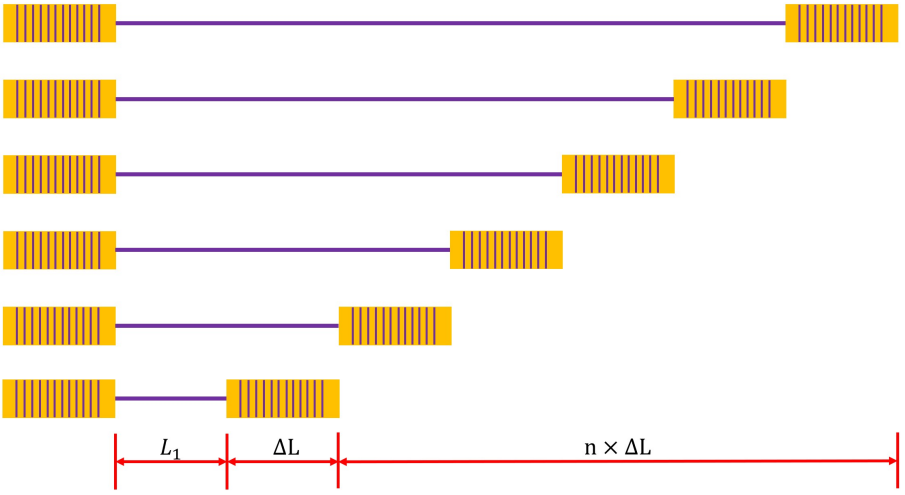


FIGURE 3.23: Effective cut-back method diagram.

Alternatively, there is the Fabry-Pèrot (FP) method. The main drawback of this method is that its accuracy depends on having a precise value of the facet reflectivity. This reflectivity is difficult to determine, because optical facets defining the cavity may have rough texture and profile, which introduces unpredictable reflection losses [183]. Furthermore, the facet reflectivity for small waveguides may differ significantly from the Fresnel formulae, which are based on a single plane wave calculation. For instance, the calculated facet reflectivity of III-V cavity lasers can vary from 20% to 40% depending on waveguide thickness, index contrast and optical polarisation [184]. Apart from the uncertainty in the reflectivity value, interference from leaky modes and stray light can cause variations in the peak height of the FP fringes and imposes difficulty in determining an accurate fringe contrast [185].

Initially, the input power ($I_{In}$) and the output power ($I_{Out1}$) of a waveguide of length $L_1$ are recorded upon launching light using the grating couplers into the waveguide. The same procedure is carried out for the next waveguide, which is longer than the first waveguide by $\Delta L$, to determine $I_{Out2}$ while keeping $I_{In}$ constant. The propagation loss of the length variation ($\Delta L$) is therefore related to the difference in the output power from each measurement. By repeating the process multiple times using many waveguides, an accurate value for the propagation loss is determined. The output power $I$ of a mode propagating in the $z$ direction for a given input power $I_0$ is dependent on the *loss coefficient* ($\alpha$) as the Figure 3.4 shows.

$$I = I_0 e^{-\alpha z} \tag{3.4}$$

Therefore, the propagation loss of a waveguide of length $\Delta L = L_1$-$L_2$ is expressed by 3.5

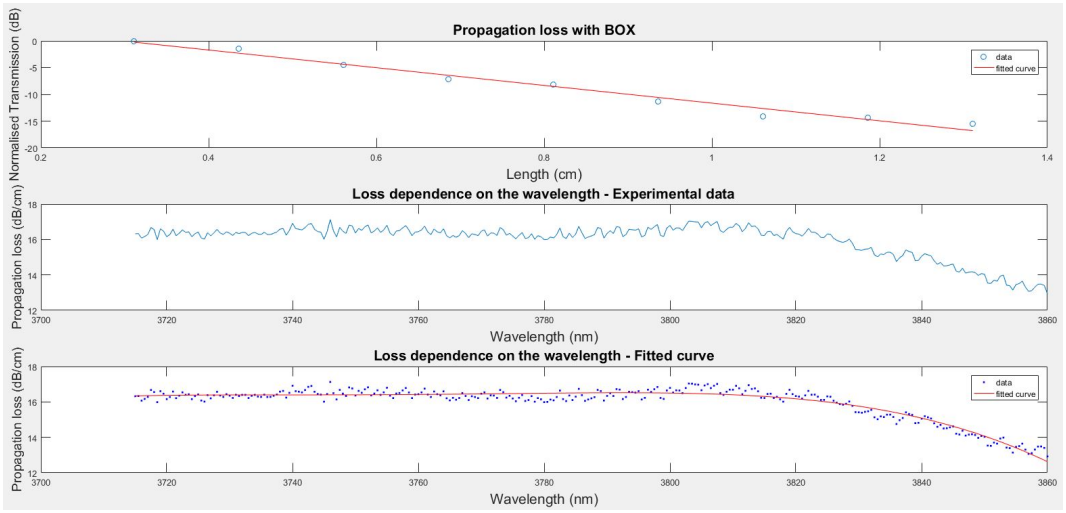


FIGURE 3.24: Measured propagation loss before the removal of the BOX for different wavelengths.

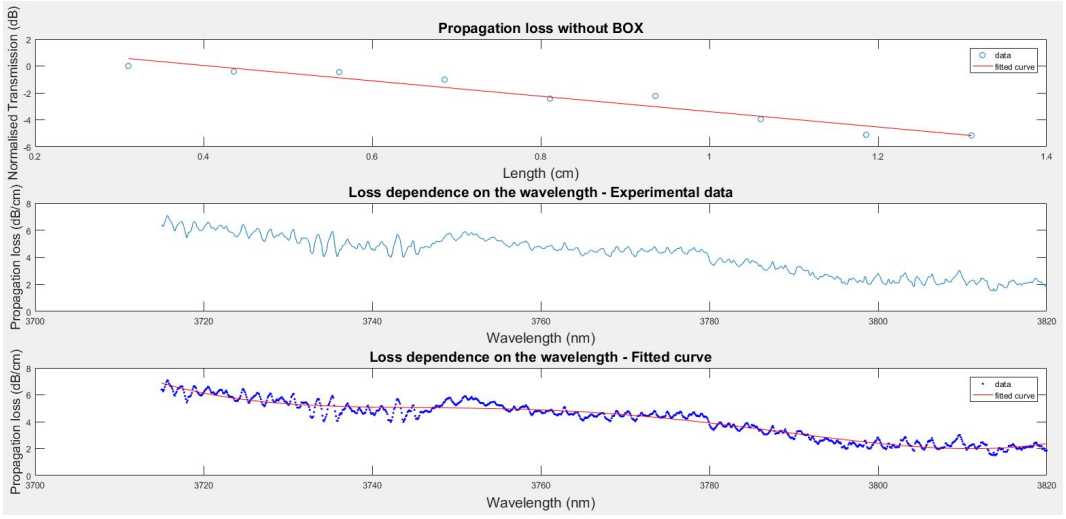


FIGURE 3.25: Measured propagation loss after the removal of the BOX for different wavelengths.

$$\alpha = \left(\frac{1}{\Delta L}\right) ln \left(\frac{I_2}{I_1}\right) \tag{3.5}$$

where $I_1$ and $I_2$ are the output powers of two adjacent waveguides.

### 3.4.4 Experimental results

Measurements have been taken for the 400 nm thick Ge sample developed in the first fabrication run. The transmission was measured and the propagation loss was calculated for the same sample before and after removing the BOX. The results are shown in Figure 3.24 and Figure 3.25.

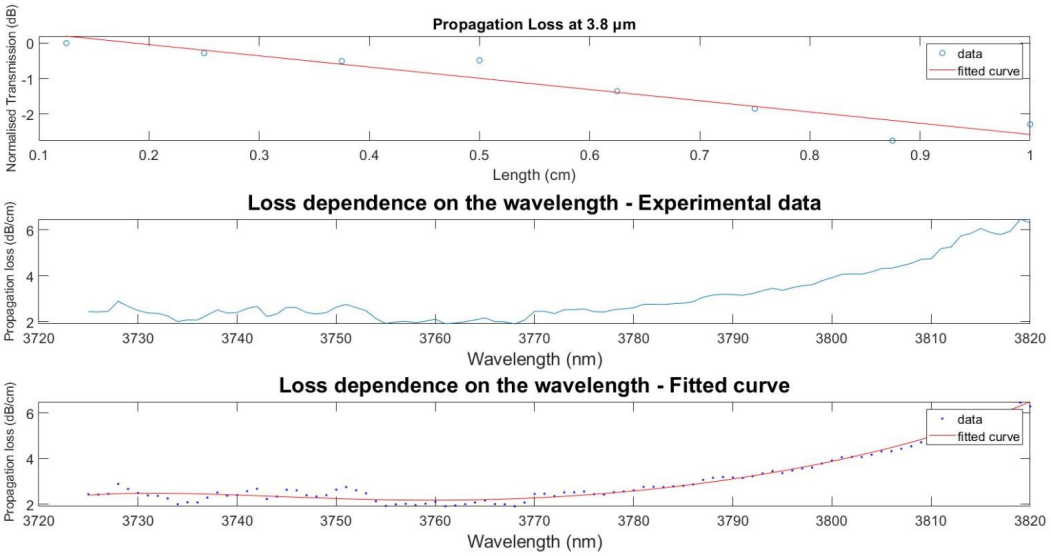


FIGURE 3.26: Measured propagation loss of the 500 nm suspended Ge at $\lambda$=3.8 $\mu$m.

Before removing the BOX the measured propagation loss was approximately 16 dB/cm at 3.8 $\mu$m whereas the one measured after suspending the waveguides was significantly reduced reaching a value of approximately 2.9 dB/cm at the same wavelength.

Similarly, using the same method, the bend loss was calculated to be 0.13 dB/90° bend at 3.8 $\mu$m before removing the BOX. After suspending, the bends collapsed due to the fact that the slab was not thick enough to provide mechanical stability. Therefore no measurements were taken.

Measurements for the 500 nm and 1 $\mu$m thick Ge were also obtained (Figure 3.26).

The measured propagation loss was 3.91 dB/cm. As seen from Figure 3.26, the loss is increasing for wavelengths longer than 3.77 $\mu$m. A potential reason for this is that as the wavelength increases, the size of the optical mode increases resulting in higher interaction with the holes causing higher reflections thus, higher propagation loss.

The 1 $\mu$m thick Ge was measured at $\lambda$=7.67 $\mu$m. The laser at this wavelength is not tunable, therefore the loss could be only measured at the central wavelength. The propagation loss obtained was 2.65 $\pm$ 0.27 dB/cm as shown in Figure 3.27. This propagation loss can be compared to the one reported in [105] in which suspended Ge waveguides have been demonstrated for the the same wavelength exhibiting a propagation loss of 5.3 dB/cm.

The absorption coefficient of Ge at $\lambda = 7.67$ $\mu$m is negligible [186]. In addition, according to simulations, leakage losses are 0.3 dB/cm for an air gap of 3 $\mu$m, decreasing to $2.4\times10^{-2}$ for an air gap of 3.5 $\mu$m. Therefore, the propagation loss is likely caused by scattering at the waveguide side-walls and by defects due to threading dislocations in the Ge at the Ge–Si interface emanating from the 4.2% lattice mismatch between Ge and

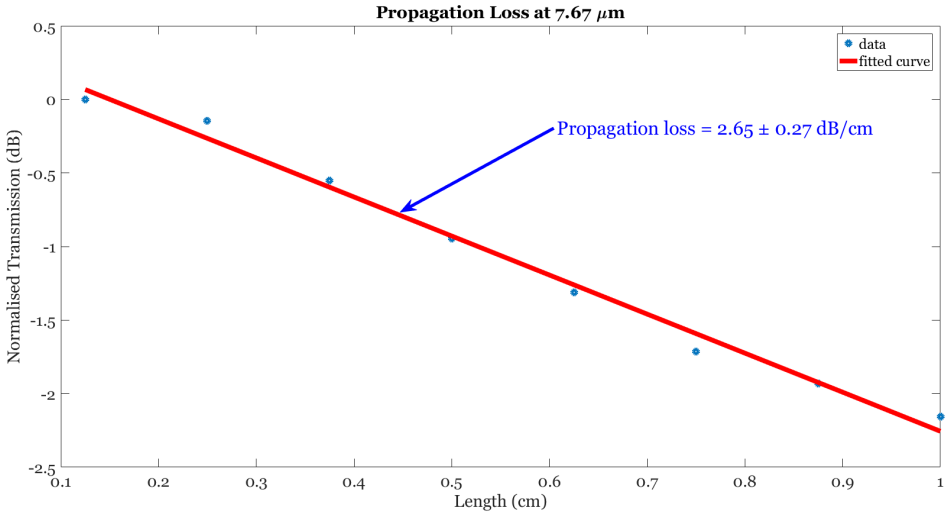


FIGURE 3.27: Measured propagation loss of the 1 $\mu$m suspended Ge at $\lambda = 7.67$ $\mu$m.

Si. Using the model for the calculation of the scattering loss due to side-wall roughness in [168], the standard deviation of the roughness $\sigma$ corresponding to the propagation loss measured in this work for a correlation length of $L_c = 50$ nm would be $\sigma = 15$ nm. The source of propagation loss cannot be accurately defined, as no Atomic Force Microscopy (AFM) measurement of the sidewall roughness was taken. However, the sidewall roughness of 15 nm is believed to be very unlikely in the fabrication process used to develop these waveguides. A typical sidewall roughness of $\sigma = 5$ nm would result in a propagation loss of 0.3 dB/cm. The rest (2.3 dB/cm) would then emanate mostly from the threading dislocations.

## 3.5 Conclusion

A set of suspended MIR Ge devices, such as waveguides, bends and grating couplers has been demonstrated in this chapter. The lowest measured waveguide propagation loss at $\lambda = 3.8$ $\mu$m was 2.9 dB/cm using a 400 nm thick Ge layer. The bend loss after suspending the waveguides could not be measured due the collapse of the bent waveguides due to mechanical instability. At $\lambda = 7.67$ $\mu$m the lowest measured propagation was 2.65 dB/cm. This was the first demonstration of low-loss suspended Ge waveguides at such a long wavelength. Waveguides for a wavelength of $\lambda = 9.5$ $\mu$m have also been designed but not yet fabricated. Initial simulations were performed considering an air gap of 3 $\mu$m to investigate the substrate leakage of the fundamental mode. These simulations suggest that in order to keep the substrate leakage losses in the sub-dB range, the 3 $\mu$m air gap becomes insufficient for wavelengths longer than 10 $\mu$m. Such waveguides are of fundamental importance for building MIR PICs. Moreover, the fabrication technique provides the ability to locally remove a portion of the Si substrate precisely, increasing

the air gap underneath the waveguide, enabling operation at longer wavelengths with reduced substrate leakage losses using wafers with a conventional 3 $\mu$m thick BOX. These results show that suspended Ge waveguides fabricated using Ge-on-SOI wafers have the potential to be used throughout the MIR transparency window of Ge and for sensing applications above 8 $\mu$m. The next step to extend this work would be to fabricate the designed waveguides for $\lambda = 9.5$ $\mu$m. In addition, since suspended waveguides have been optimised for the wavelength of $\lambda = 7.67$ $\mu$m at which $CH_4$ exhibits strong absorption as shown in Figure 1.3, it would be an excellent opportunity to characterise the performance of this waveguide design in sensing experiments and compare them to results obtained using alternative platforms at different wavelengths such as the work reported in [27]. As a final remark, the results obtained in this chapter, in particular the low waveguide propagation loss of 2.65 dB/cm, along with the successful increase of the air gap, constitute very good indications of the validity of the suspended waveguide design to extend the range at which Ge can be used in the MIR.

# Chapter 4

# QCL integration on GOS platform using flip-chip bonding

In this chapter the process of integrating QCLs on a GOS platform using flip-chip bonding is described. First, the main idea is presented along with the various simulations carried out to investigate the influence of the laser misalignment of the coupling efficiency. Finally, the fabrication process as well as the experimental results are presented.

## 4.1 Design and simulation

In this section, the design of the device is presented along with the various simulations carried out to investigate the influence of the laser misalignment of the coupling efficiency.

As discussed in 2.3.4.1, flip-chip bonding has been previously used to integrate light sources with group-IV-based platforms. However, these demonstrations were operating at telecom wavelengths, hence, the main idea of the work presented here is to integrate QCLs emitting in the MIR. This is of particular interest for sensing applications as described in 1.2. In this work, QCLs operating at a wavelength of 5.5 $\mu$m are flip-chipped on a 3 $\mu$m processed GOS wafer as shown in Figure 4.1. Light is then butt-coupled to a rib waveguide and then to an optical fibre via a grating coupler. The light sources are in a form of bars each one containing 24 lasers and were provided by the university of Sheffield.

To evaluate the influence of misalignment on the coupling efficiency between the laser and the waveguide, simulations were carried out using Photon Design Fimmwave [187]. First, the cross-section of the QCL structure was drawn by constructing the rectangular waveguide by a series of slices. It is within these slices that the epitaxial layer structure is defined. Then the thickness and refractive index of each slice are defined

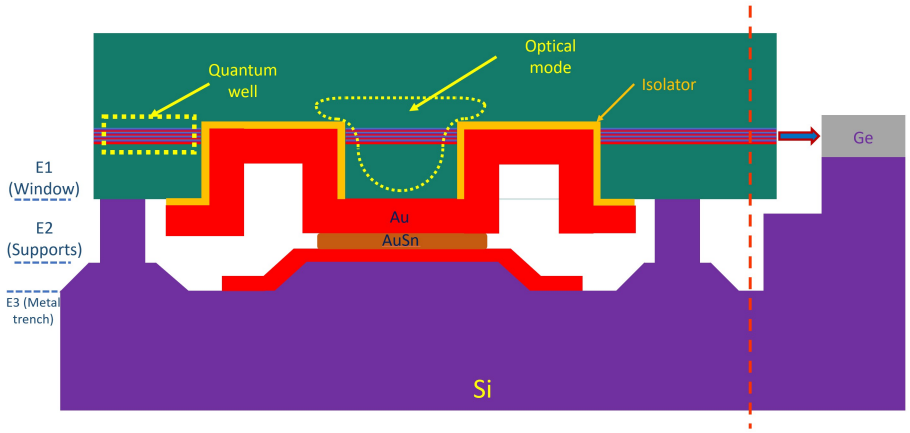


FIGURE 4.1: Cross-sectional schematic of the integrated QCL with the GOS platform presented in this thesis. The red dashed line separates the front-view (left side) from the side-view (right side).

to finally obtain the QCL structure as shown in (Figure 4.2(a)). The model for the QCL structure was provided by the university of Sheffield. Having completed the QCL structure, a simulation was carried out to locate the modes of the waveguide using the Film Mode Matching (FMM) solver. This solver was used because of its higher accuracy compared to the other methods available in the simulator for rectangular structures that can be described in a relatively low number of uniform refractive index regions, since FMM is a semi-analytical algorithm. The simulated fundamental TM mode is shown in Figure 4.2(b).

Once the fundamental mode was found, a 3D version of the full structure, including the QCL, the input and output waveguides as well as the taper connecting them, was constructed in a FIMMPROP model. This is very useful to simulate structures that have a low number of distinct cross sections along the propagating direction (such as MMIs), or continuously varying structures like tapers and Y-junctions. It uses an eigenmode expansion algorithm calculating the local modes at different points in the structure and coupling matrices between those modes. Once the structure was drawn, the simulation was carried out to calculate the field at every y-position and then plot the average value. The simulated structure and the plotted field are shown in Figure 4.3. In this case, the etch depth and the lateral offset as well as the gap between the laser and the output waveguide were set to 0. For these conditions, the mode overlap was calculated to be 88%.

To investigate the transmission dependence on the lateral and etch depth misalignment as well as the gap between the two facets, a parameter sweep was performed. This was performed using a FIMMPROP Scanner that was controlled via a MATLAB script. The sweep results are summarised in Figure 4.4.

From the simulation results, it is observed that the coupling efficiency is more affected by misalignment in the z-axis due to etch depth error than in the y-axis due to lateral

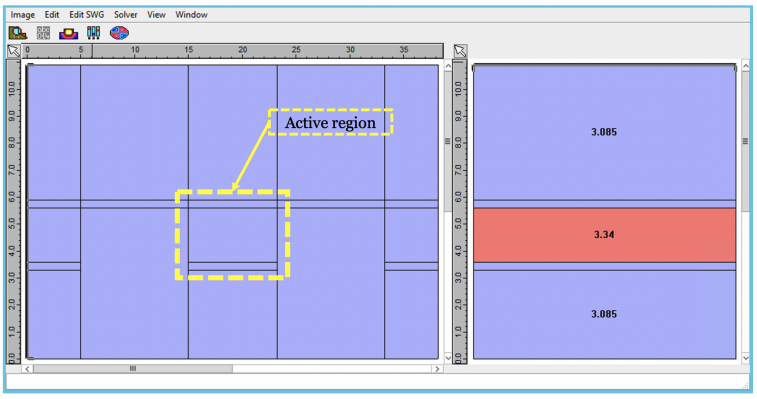


(a) Cross-section and material stack of the simulated QCL showing the waveguide core and the etched trenches along with the refractive index of each material

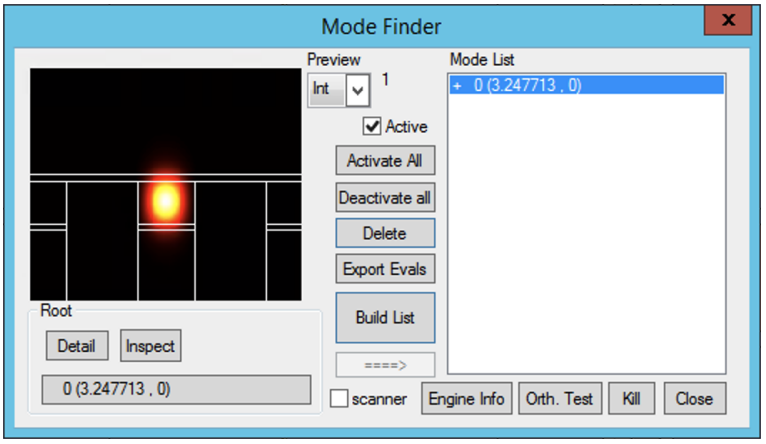


(b) Cross-section of the QCL fundamental TM mode

FIGURE 4.2: Simulated QCL

misalignment. In fact, an etch depth error of 2.4 $\mu$m results in a reduction in the coupling efficiency by 50%. On the other hand, the same reduction in the coupling efficiency is caused by 6 $\mu$m of lateral misalignment. The simulation results also show that due to the beam divergence of the laser mode, the gap between the laser and the taper should be minimised in order to maximise coupling efficiency. In fact, from the plot in Figure 4.4(c), 1 $\mu$m of gap results in a reduction in the coupling efficiency by 77%. In addition, due to the cavity that is formed between the two facets, the plot reveals the existence of Fresnel reflections. A similar plot is presented in [188] verifying the behaviour of the system without using an anti-reflective coating.

To minimise reflections from the taper back to the QCL the first was designed to have an angle ranging from 5° to 17°. Light from the QCL is coupled to the taper that is 10 $\mu$m wide adiabatically reduced to match the single TM mode waveguide of 3.1 $\mu$m. In order to ensure that the transmission measured during characterisation of the device is light coupled to the waveguide rather than mode coupled through the slab directly from the QCL, bends are used after the taper guiding the coupled mode away from the emission

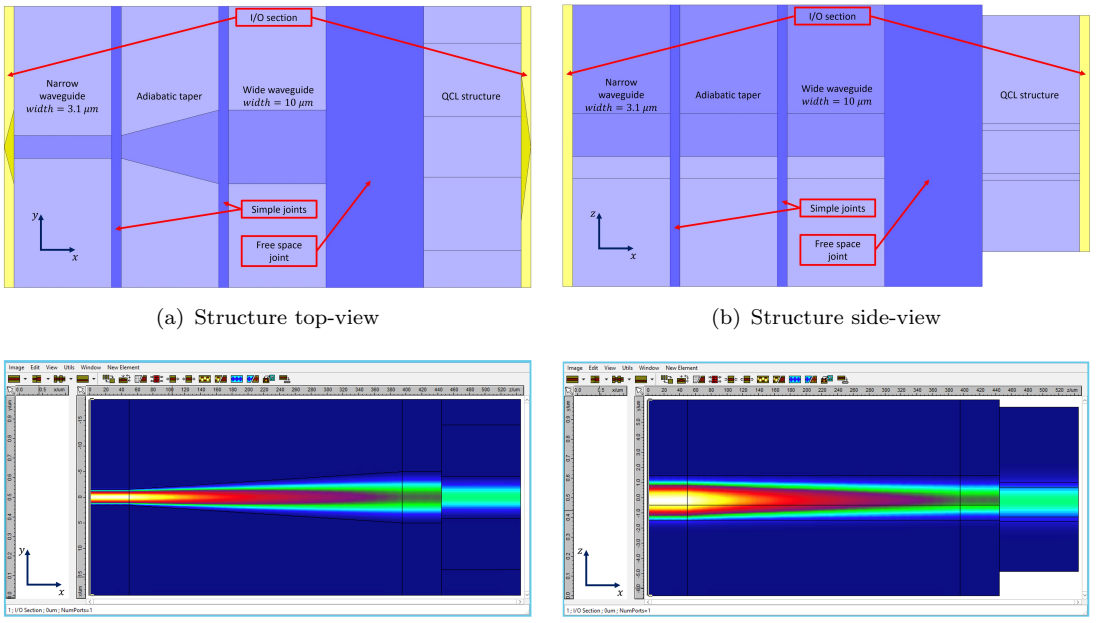


(a) Structure top-view

(b) Structure side-view

(c) Calculated field top-view

(d) Calculated field side-view

FIGURE 4.3: Simulated structure and field view of the QCL-waveguide system used to investigate the overlap of the two modes.

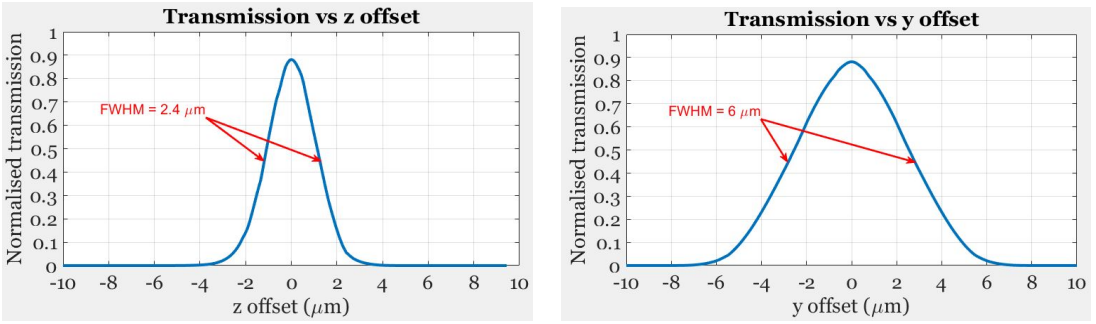


(a)

(b)

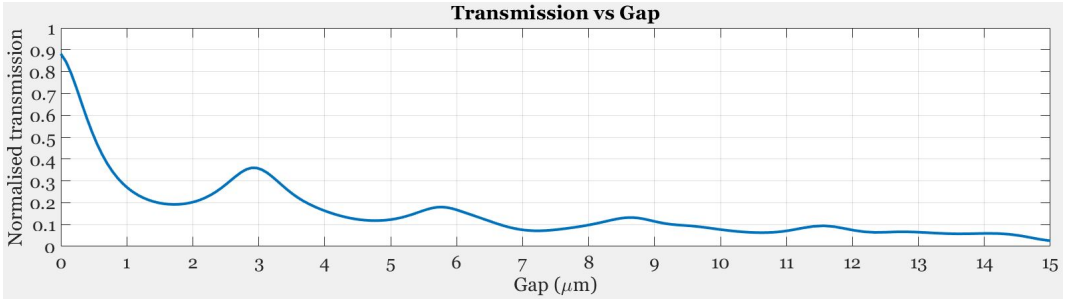


(c)

FIGURE 4.4: Simulation of the impact of misalignment along the slow (a) and fast axis (b) between the QCL ridge waveguide and the GOS input waveguide on the coupling efficiency. (c) Coupling efficiency as a function of the gap between the waveguides for optimally aligned waveguides.

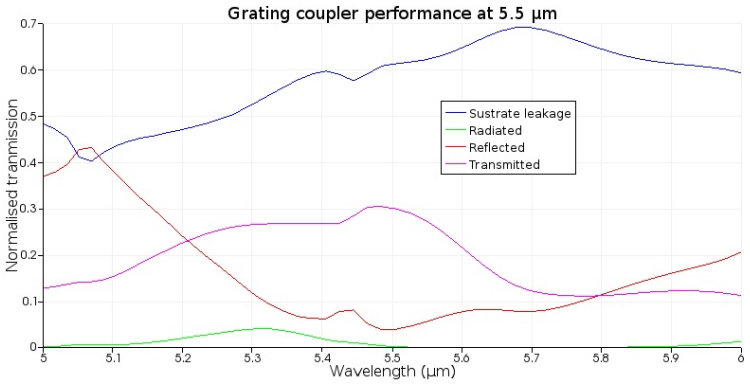


FIGURE 4.5: Simulated performance of the grating coupler for $\lambda = 5.5$ $\mu$m, used to couple light from the integrated QCL to the optical fibre. The grating coupler parameters were: Periods of $\Lambda_{Gr} = 7.3$ $\mu$m with a DC of 0.5 and $\Lambda_{AR} = 1.18$ $\mu$m with a DC of 0.7 for the diffractive and antireflective elements respectively.

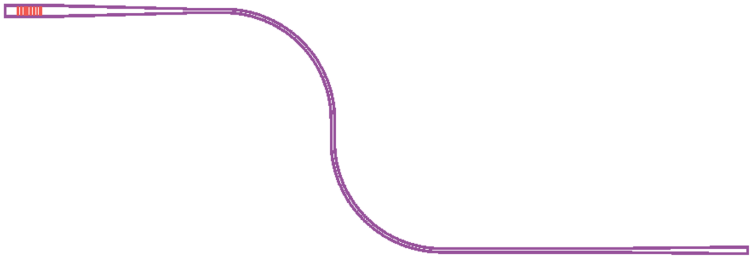

FIGURE 4.6: Schematic of the passive circuitry in which light from the integrated QCL is coupled showing the input and output tapers, the waveguide bends and the grating coupler.

axis of the QCL. To ensure minimal bend loss, the bending radius was selected to be 250 $\mu$m. After the bends, the mode enters another taper to match the width of the grating coupler that was used to couple light in an optical fibre for the characterisation of the device. A novel grating coupler design was used, that was proposed in [115], that is comprised of a few diffractive elements with and an antireflective element. This type of grating coupler was used because of its higher coupling efficiency, broader bandwidth as well as lower back-reflections compared to a conventional grating coupler. The grating coupler was optimised for the QCL emission wavelength (5.5 $\mu$m) and had periods of $\Lambda_{Gr}$ = 7.3 $\mu$m with a DC of 0.5 and $\Lambda_{AR} = 1.18$ $\mu$m with a DC of 0.7 for the diffractive and antireflective elements respectively. The simulated performance of the grating coupler is shown in Figure 4.5. At $\lambda = 5.5$ $\mu$m the grating coupler exhibits: a coupling efficiency of 30%, a radiation of 0.01%, a substrate leakage of 61.3% and a low reflection of 0.04%.

The simulations carried out to obtain the optimum parameters for the passive circuitry were carried out by Dr Jordi Soler Penadés. A schematic showing the design of the passive circuitry is shown in Figure 4.6.

Once the simulations were completed, the mask layout was developed. The layout included 6 layers: 4 for etching and 2 for metal deposition. The dimensions of each layer

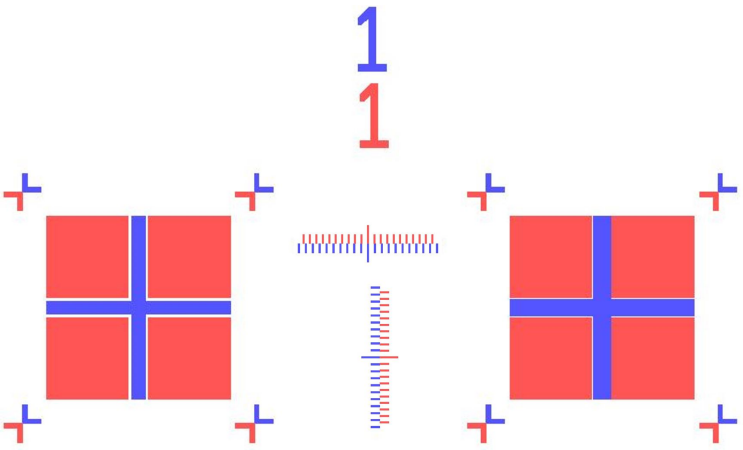


FIGURE 4.7: Mask layout of the alignment marks showing the *Vernier* scale and the number corresponding to each layer.

were chosen with respect to the dimensions of the laser. To understand the purpose of each layer, the laser structure is described with the aid of the schematic shown in Figure 4.1. To fabricate the laser, the waveguide is initially defined by etching 2 trenches on both sides of the waveguide core. Lasers with waveguides of 5 and 8 $\mu$m width were provided. After defining the waveguide, a thin film of $SiO_2$ was deposited in the trenches for isolation (orange layer), leaving the waveguide core exposed for the contact deposition. The next step was to deposit a thick (~750 nm) Au layer which acted as the top contact of the laser (red layer). The thickness of the bottom contact was ~3 $\mu$m. Such thick metal layer was chosen to ensure sufficient heat dissipation, thus enabling CW operation. The first layer was for the defining the passive circuitry (tapers, waveguides, bends and grating couplers) in which light from the laser will be coupled into. This layer was designed to be exposed using e-beam lithography due to the small features contained such as the grating couplers in which the smallest dimension was 354 nm that would not be possible to write with optical lithography in which the highest resolution is in the micrometer scale. The same layer also included the alignment marks of the wafer that consisted of 2 crosses in which the lines where 14 and 18 $\mu$m wide for an initial approximate alignment and a *Vernier* scale in which the lines where 2 $\mu$m for higher accuracy alignment as shown in Figure 4.7.

The next layer was for etching a window that will house the whole laser bar and define the top part of the supports on which the laser bar will be placed. The laser bars provided had a length of 13.4 mm and widths of 1.45, 2, 2.5 and 3 $\mu$m emitting different output powers. Therefore, to be able to house all the laser bars and have sufficient space for the subsequent bottom contact deposition, the window was designed to have a length of 13.5 mm and a width of 4.15 mm. The mask layout showing the window is shown in Figure 4.8.

After designing the etching window, the next step was to design the mask layout for the supports which were strips onto which the laser bar will be placed. In order for the

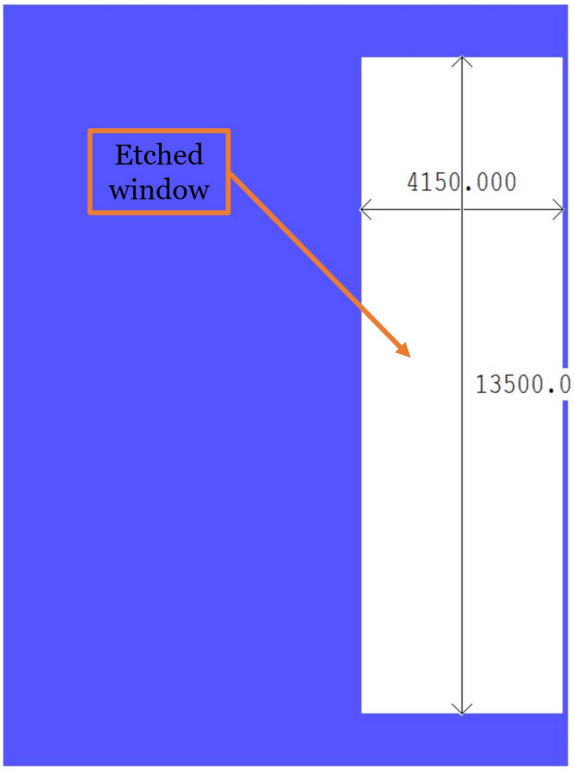


FIGURE 4.8: Mask layout of the layer defining the window.

design to be compatible with all laser bar lengths, the strips have a 200 $\mu$m gap in the x-axis between them providing addition space for potential residues at the laser facet that may be formed due to cleaving, thus preventing tilting of the laser bar causing misalignment. The gap between the supports in the y-axis was 350 $\mu$m. The same layer also defines the taper angled facets as shown in Figure 4.9. To be able to minimise the distance between the laser and the taper facet, the top part of the taper has been flattened to avoid protruding edges.

The next step was to design the mask layout for the trench as shown in Figure 4.10. This trench was included to provide an additional safety measure to prevent liquid AuSn solder, that will be deposited in following steps, to flow during flip-chip bonding until it reaches the space between the laser and taper facet thus preventing coupling. The trench is etched using HF achieving an angled etching profile.

The next mask layout was to define the Au bottom contact of the laser. Since the laser characteristics allowed for a shorter contact, tracks having a different distance (100 and 500 $\mu$m) from the laser facet were designed. Having the track more far away from the laser facet would aid the lift-off process with which the Au contacts are formed. The mask layout is shown in Figure 4.11.

The final layer was for the definition of the AuSn solder-tracks for contacting the bottom contact on the substrate with the contact of the laser. Similarly to the mask layout defining the laser supports, the AuSn strips are separated from each other with 150

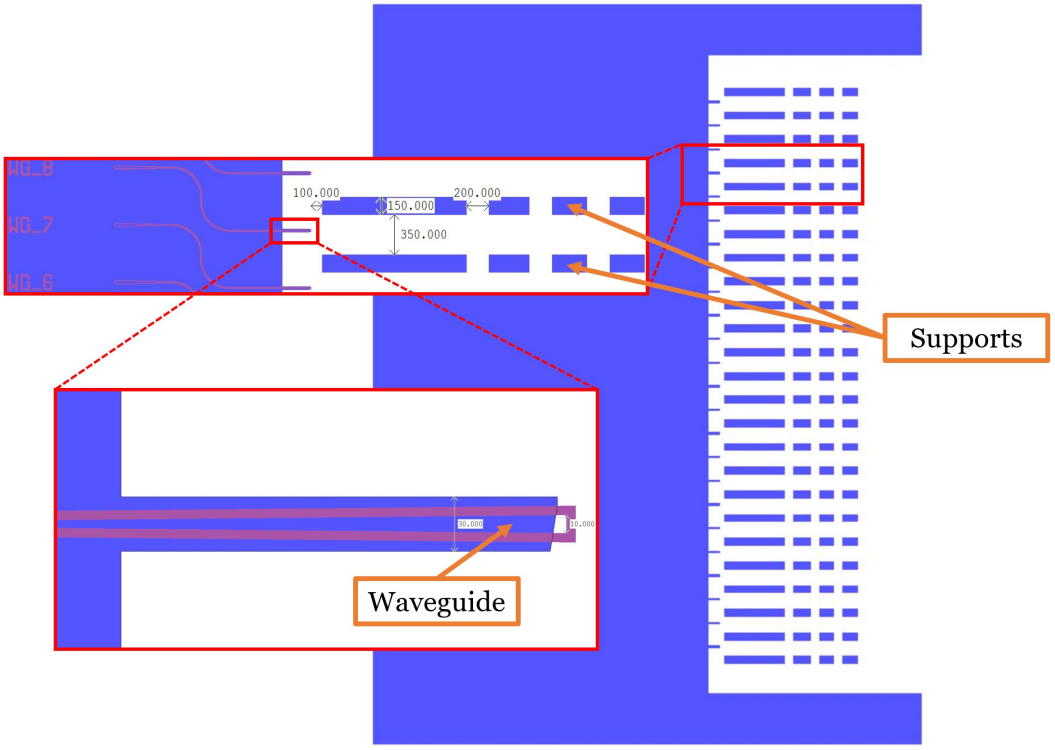


FIGURE 4.9: Mask layout of the layer defining the supports and taper angled facets.

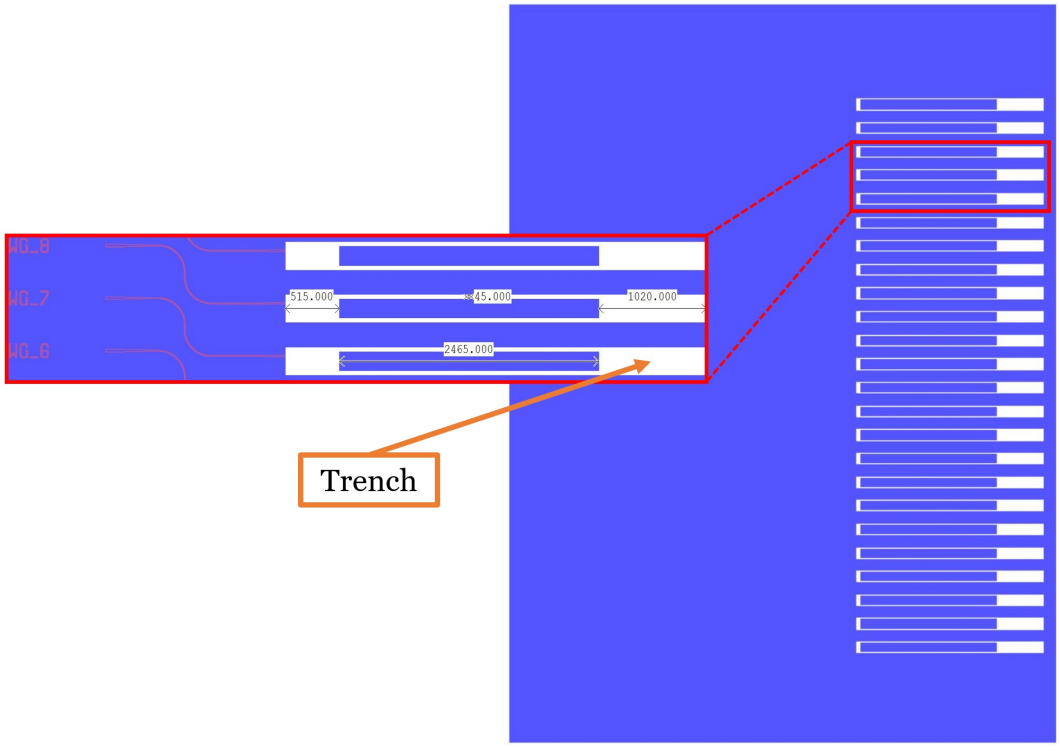


FIGURE 4.10: Mask layout of the layer defining the trench.

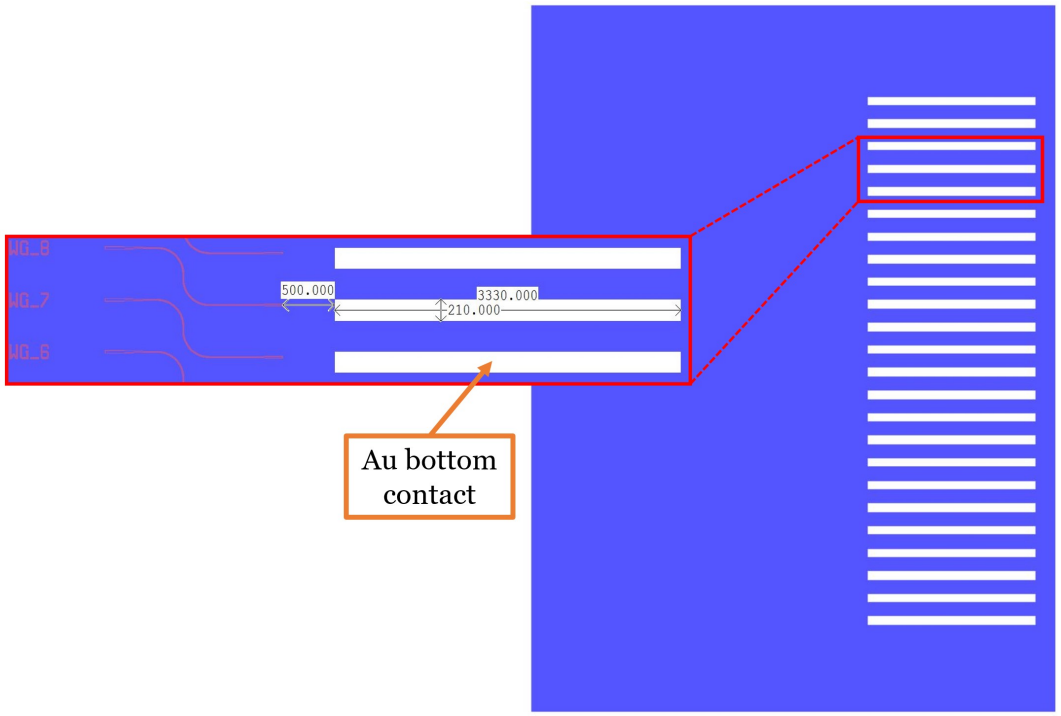


FIGURE 4.11: Mask layout of the layer defining the Au bottom contact.

$\mu$m gaps providing addition space for potential residues at the laser facet that may be formed due to cleaving. To aid fabrication, the dimensions of the mask layouts were designed taking into account the requirements for the lithography and lift-off processes for the various metal depositions. Therefore, the mask layouts were designed with a 15 $\mu$m gap between the various layers. The mask layout for the AuSn deposition is shown in Figure 4.12.

To verify that the dimensions of all the layers are in accordance to the dimensions of the laser-bar, the mask layout of the latter is added as an instance to the mask layout of the substrate as shown in Figure 4.13.

## 4.2 Fabrication

Once the mask layouts for all the layers were carried out, fabrication followed. The first step was to etch the window that will house the whole laser bar and define the top part of the supports on which the laser bar will be placed. This etch depth is crucial for maximising the coupling efficiency as it controls the alignment in the z-axis. The targeted etch depth for optimal coupling efficiency according to simulations was 6.5 $\mu$m. To achieve such a deep etch, thick resist was used to carry out the lithography. For cost-saving purposes, to test the deep etch, a bulk Si wafer instead of a GOS wafer was used since the behaviour of both materials under the same etching conditions is similar. First, the wafer was placed in an oven for 2 hours at 210 °C to eliminate any

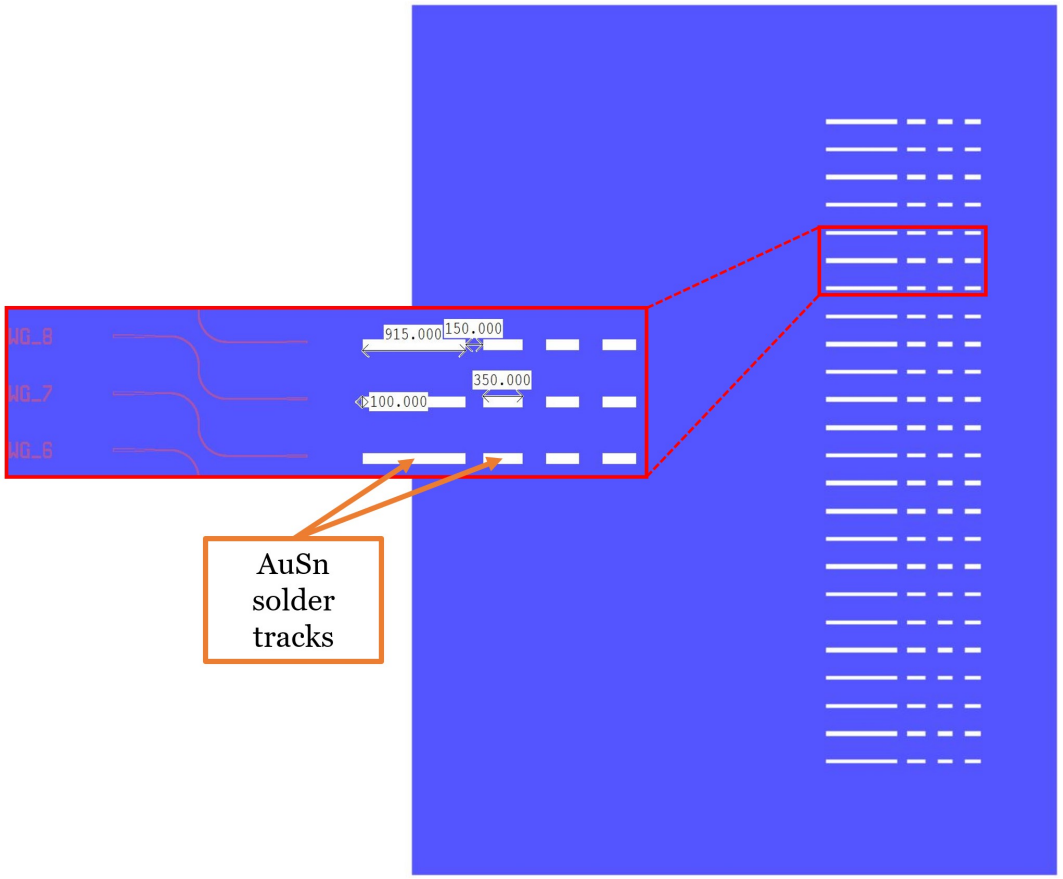


FIGURE 4.12: Mask layout of the layer defining the AuSn solder track.

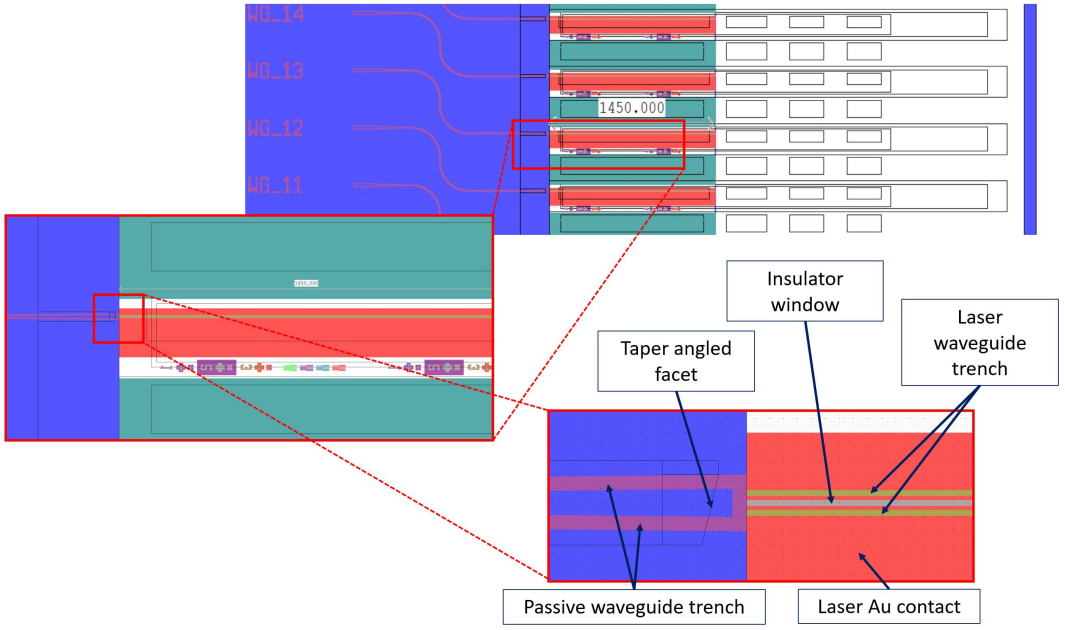


FIGURE 4.13: Mask layout showing the laser and the substrate.

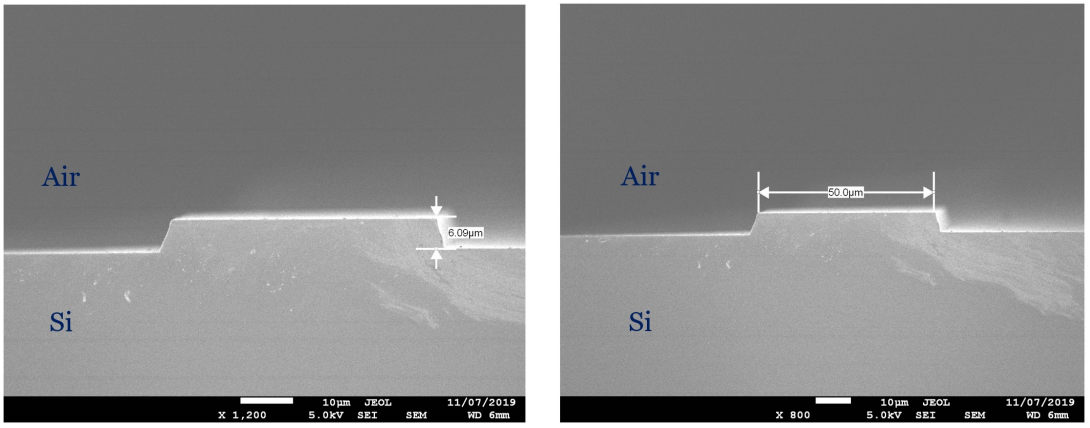


(a) (b)

FIGURE 4.14: SEM images showing the cross section of a 50 $\mu$m wide etched area on a test wafer .

moisture on the wafer that would potentially compromise the adhesion of the resist on the wafer. Upon letting the wafer reach room temperature, the resist was spun. In this case, the resist used was the AZ 9260 with a thickness of 7 microns. Once the resist was spun, it was baked for 180 seconds at 110 °C and then left to cool down for 30 before exposure. To expose the layer, contact lithography was used using hard contact for optimal alignment accuracy. Once the mask was aligned with the wafer, the latter was exposed for 12 seconds. To develop the layer after exposure, development followed using the AZ400K developer that was diluted with a 1:4 water to developer ratio for 3 minutes and 30 seconds. Once the wafer was developed, it was cleaned using DI water before hard baking the resist for 60 seconds at 170 °C. After lithography, testing of the etching recipe followed. The etching time required to etch 6 $\mu$m of Si was 24 minutes, however the initial test which involved a 5-minute etch step resulted in burning of the resist due to the high temperature developed during etching. To tackle this issue, the recipe was modified by limiting the etch time to a maximum of 90 seconds and by adding 2-minute cooling steps in between the etch steps in order to prevent burning of the resist. The modified recipe was tested using a test wafer in which a 50 $\mu$m wide area was defined. The result revealed an etching profile with a slight angle as shown in the SEM pictures in Figure 4.14.

Once the process was tested, the device wafer was etched. According to the simulations described in Figure 4.4 the etch depth for which the optimum coupling efficiency is achieved was 6.5 $\mu$m. However, the thickness of the resist could not be measured during processing using conventional ellipsometry due to its large thickness. An alternative method was used in which a small part of the resist at the edge of the wafer was locally removed using acetone. Figure 4.15 shows the etch depth of Ge and Si as a function of time.

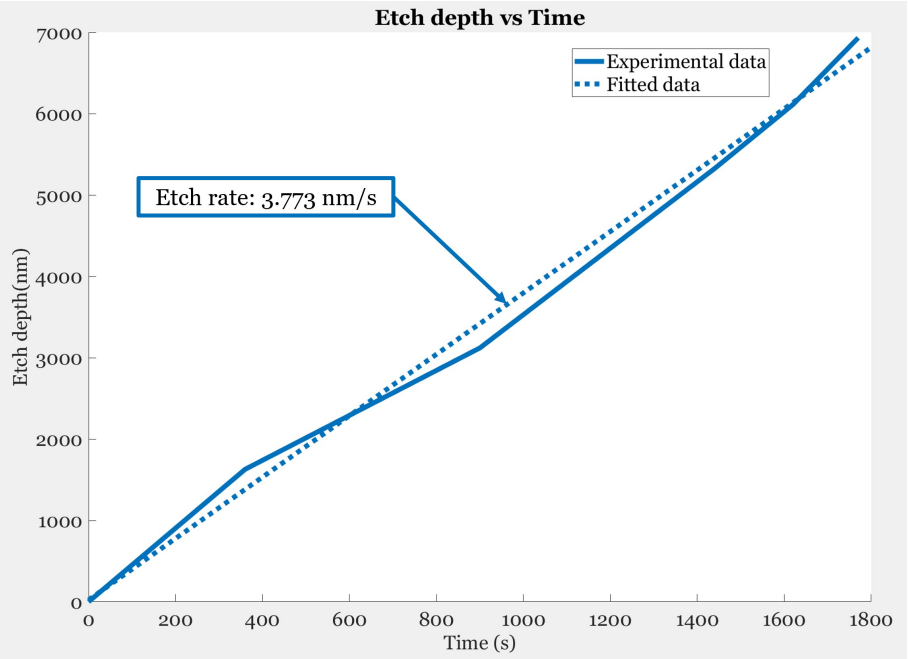


FIGURE 4.15: Etch depth of Ge as a function of time.

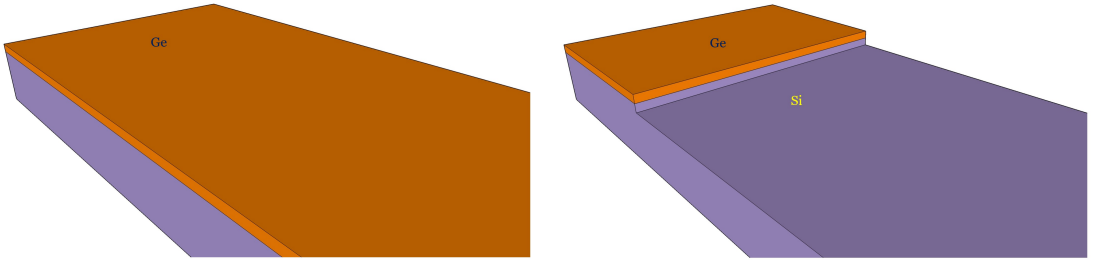


(a) Initial platform (b) Etched window

FIGURE 4.16: 3D schematic of the first etch step.

However, this method was not accurate due to the difference of the etch rate and the thickness of the resist between the edge and the middle of the wafer. As a result, the layer was overetched by $\sim 400$ nm. A 3D schematic illustrating the etching of the window layer is shown in Figure 4.16.

The second etch step defined the supports onto which the laser bar will be placed as well as the input taper facet as shown in the 3D schematic in Figure 4.17. The etch depth had to be equal or bigger that the first etch otherwise a protruding edge at the bottom of the input taper would be formed thus tilting the laser bar. However, this can be avoided even with a smaller etch depth as the etch rate of Ge is higher than that of Si. The etch depth of the second etch was 6.25 $\mu$m.

At this point, it was decided that the wet etch step defining the safety trench was redundant due to the second etch step being deep enough such that sufficient space is ensured for the solder track given its volume. Given that the bottom contact of the

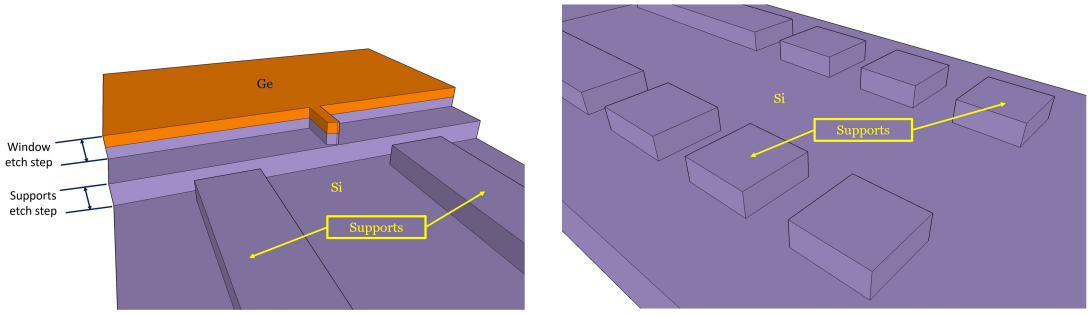


(a) Laser supports and input taper facet (b) Segmented supports

FIGURE 4.17: 3D schematic of the second etch step.

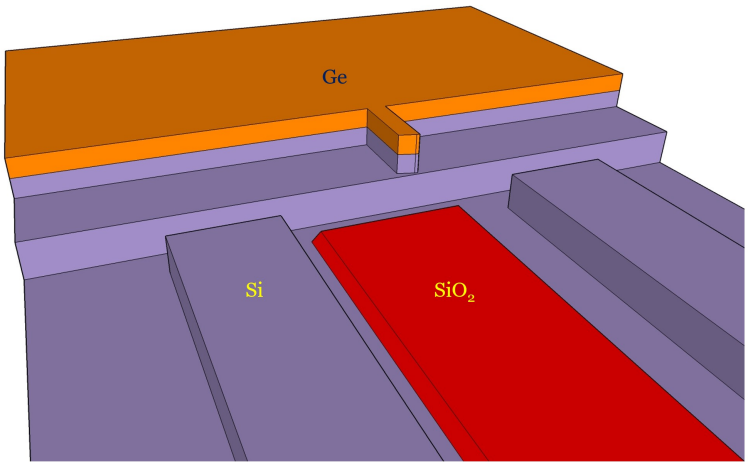


FIGURE 4.18: 3D schematic showing the $SiO_2$ deposition.

laser bar is ∼3 $\mu$m, in order to ensure contact between the laser bar bottom contact and the contact on the substrate, the combined thickness of Au and AuSn that has to be deposited must be ≥3.25 $\mu$m. However, this would not be viable as such thickness would increase the cost dramatically. In order to overcome this issue, a ∼2 $\mu$m $SiO_2$ was deposited to decrease the metal thickness needed. This step was carried out using using the mask layout of the bottom contact with a negative resist. The resist used was the AZ2070 that was spun at 4 thousand rounds per minute to obtain a thickness of 5.5 $\mu$m. Once the layer was exposed, development followed using the AZ726 metal ion free developer for 60 seconds. In order to facilitate lift-off of the subsequent Au layer, the dry etch was performed using an angled etching profile. A 3D schematic illustrating the $SiO_2$ deposition is shown in Figure 4.18.

Once the $SiO_2$ layer was deposited, deposition of the bottom Au contact followed using evaporation as shown in the 3D schematic in Figure 4.19. To ensure efficient adhesion of the Au films on the substrate, a thin Ti film of 20 nm was initially deposited. In this first attempt, a single-layer lift-off process was used. The thickness of the deposited layer was ∼750 nm.

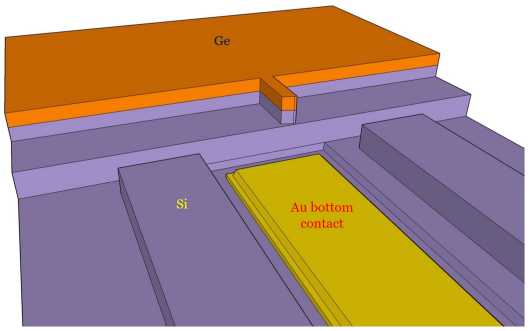


FIGURE 4.19: 3D schematic showing the bottom Au contact deposition.

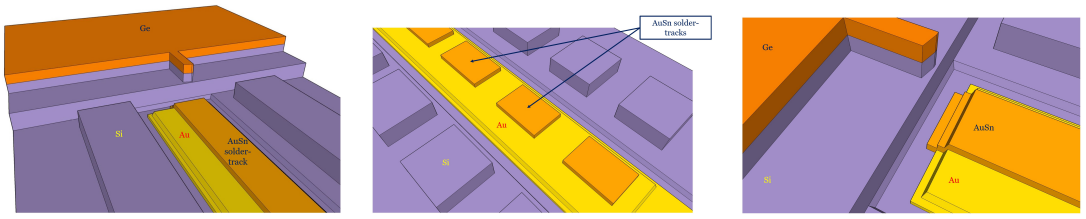


(a) (b) (c)

FIGURE 4.20: 3D schematic showing the AuSn solder-tracks deposition.

Once the Au film was deposited, the final step was to deposit the AuSn solder-tracks. In order ensure that a good contact between the two Au contacts, the thickness variation of the Au contacts of the laser-bars have to be taken into account. Therefore, the thickness of the AuSn deposited layer was ∼770 nm which ensures contact for a minimum laser-bar contact thickness of 2.7 $\mu$m. A 3D schematic showing the deposition of the AuSn solder-tracks is shown in Figure 4.20.

However, the single-layer lift-off process proved unsuitable as the AuSn layer stuck on the substrate. To assist lift-off, ultrasonic bath was employed which resulted in the delamination of a big part of the AuSn film leaving tiny chunks unsuitable for soldering. A microscope image showing the failed lift-off of AuSn is shown in Figure 4.21.

To tackle the issue of the metal delamination and to ensure a lift-off of high quality with clean metal sidewalls, a bi-layer lift-off process was employed. This was carried out using LOR 5A lift-off resist that is based on the Polydimethylglutarimide (PMGI) platform. This type of resist is well suited for a variety of critical lift-off processes. It was used in combination with a conventional positive resist (in this case AZ 9260). First, LOR 5A was spun at 1000 rounds per minute to obtain a 1 $\mu$m thick layer and then baked at 180 °C for 3 minutes. Then AZ9260 was spun using the same process as used in the exposure of the previous layers, to obtain a combined resist thickness of 8 $\mu$m. A schematic describing the lift-off using a bi-layer resist stack is shown in Figure 4.22.

The recipe was first tested using a test wafer where a 1 $\mu$m thick layer of Al was deposited and lifted-off before processing the expensive Au. An SEM image showing the cross-section of a 1 $\mu$m thick Al layer is shown in Figure 4.23.

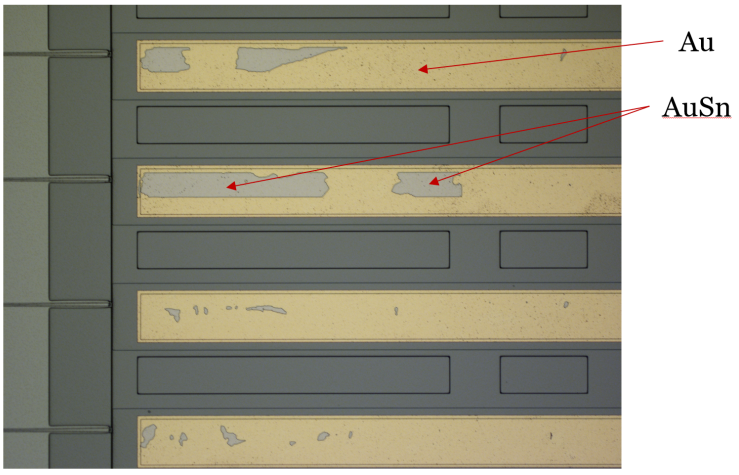


FIGURE 4.21: Microscope image of the substrate showing parts of the delaminated AuSn film.

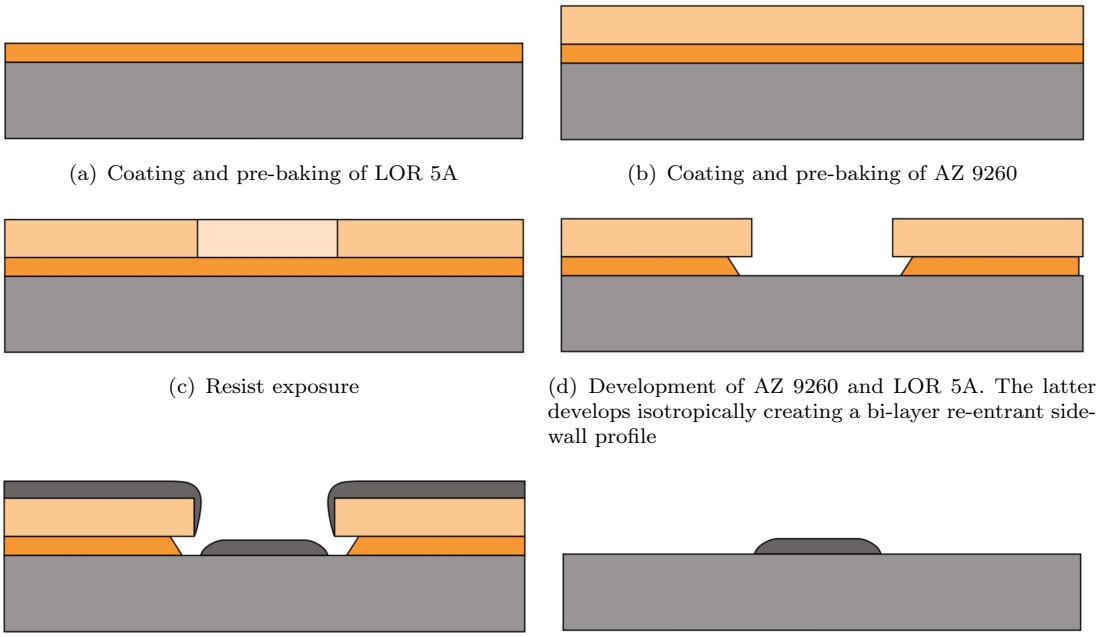

(a) Coating and pre-baking of LOR 5A

(b) Coating and pre-baking of AZ 9260

(c) Resist exposure

(d) Development of AZ 9260 and LOR 5A. The latter develops isotropically creating a bi-layer re-entrant side-wall profile

(e) Metal film deposition. The re-entrant profile ensures discontinuous film deposition

(f) Lift-off bi-layer resist stack, leaving only desired film

FIGURE 4.22: Lift-off process using a bi-layer resist stack [189]

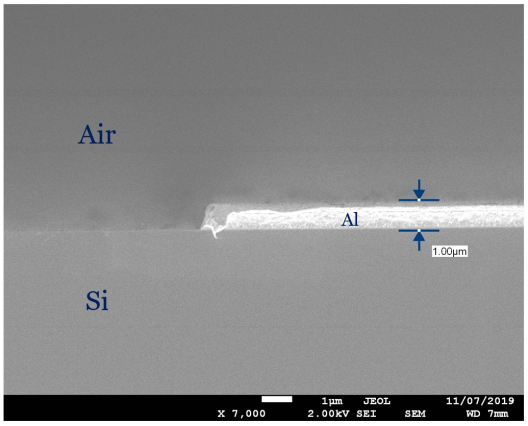


FIGURE 4.23: SEM image of the cross-section of a 1 $\mu$m thick Al layer using bi-layer resist stack.


FIGURE 4.24: The FINEPLACER lambda sub-micron die-bonder used for precision die attach and advanced chip packaging [190].

Once the recipe was verified, fabrication of a new wafer was carried out in which the deposition of the Au bottom contacts and and AuSn solder tracks was carried out using the new lift-off process.

## 4.3 Flip-chip bonding

Once fabrication of the substrate was carried out, flip-chip bonding of the laser-bars followed. The tool used was the FINEPLACER lambda flip-chip bonder by Finetech [190] (Figure 4.24). It is a die-bonder that exhibits a sub-micron placement accuracy for precision die attach and advanced chip packaging.

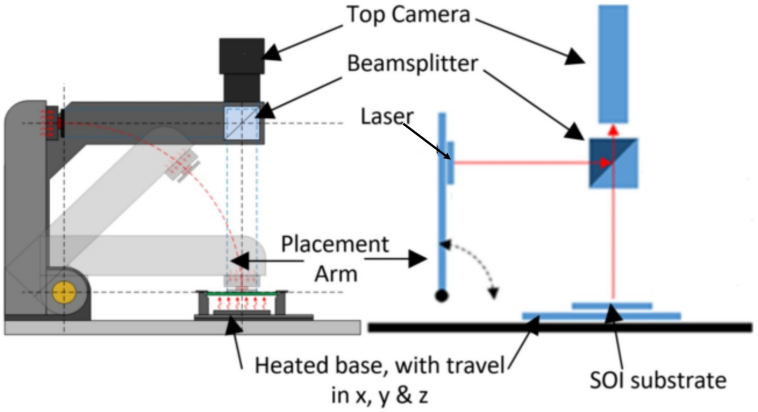


FIGURE 4.25: Schematic of the flip-chip bonder showing its principle of operation.

The process begins by placing the laser-bar face-down on top of the pre-fabricated substrate that is face-up. A placement arm is used to pick the laser-bar so it can be optically aligned with the substrate. A beam-splitter is used to obtain images of both the substrate and the laser-bar and then superimpose them. A schematic describing the principle of operation is illustrated in Figure 4.25. This image shows the relative location of the components upon physically contacting them.

Calibration of the beam-splitter is initially carried out that will determine the placement accuracy. This is achieved by using two transparent quartz slides each with markings to allow a *Vernier* scale measurement when in contact with each other. The slides are aligned using the beam-splitter and placed upon each other as if they were to be bonded. The *Vernier* scales, visible through the quartz, then provide a direct measurement of alignment as shown in Figure 4.26. Adjusting the beam-splitter is carried out by repetitively aligning, placing, measuring and adjusting until optimal alignment is achieved. Depending upon the tool and type of alignment optics utilised, accuracies down to 0.3 $\mu$m with three-$\sigma$ conformity (>99.7%) have been demonstrated as a standard specification by Finetech in an automated version of the tool, demonstrating the ability to scale this laser integration technique for automated manufacturing.

To fully compensate for any roll error in placement from the rigid flip-chip mechanism a single-axis gimballed placement head was used as shown in Figure 4.27. This ensures the absolutely flat placement of the the laser-bar along the long dimension of the laser bar. Precise alignment of the pitch is achieved by adjusting a screw on the placement head and inspected by the side camera as shown in Figure 4.24. This does not eliminate pitch error completely, but does reduce it to acceptable levels.

Visual inspection through the side camera on high magnification clearly shows a submicrometre error across the width, allowing accurate alignment as shown in the overlay image of the substrate and the laser-bar in Figure 4.28.

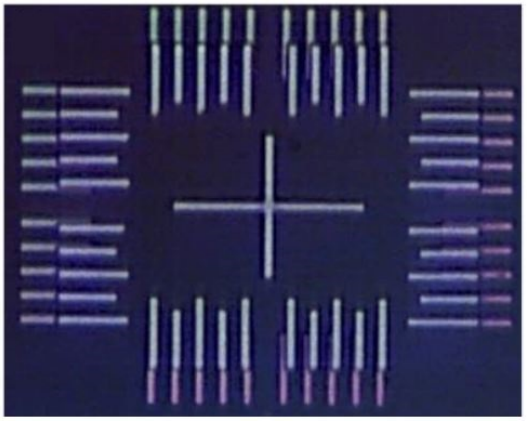

FIGURE 4.26: Calibration glasses used for the calibration of the beam-splitter at high magnification showing the *Vernier* scaled used for alignment.

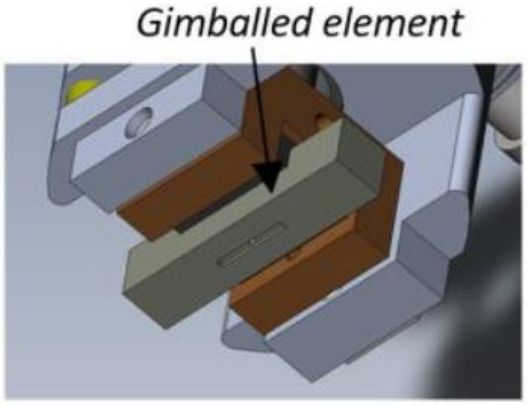


FIGURE 4.27: Schematic of the single-axis gimbal laser placement tool (rotating element is illustrated in grey).

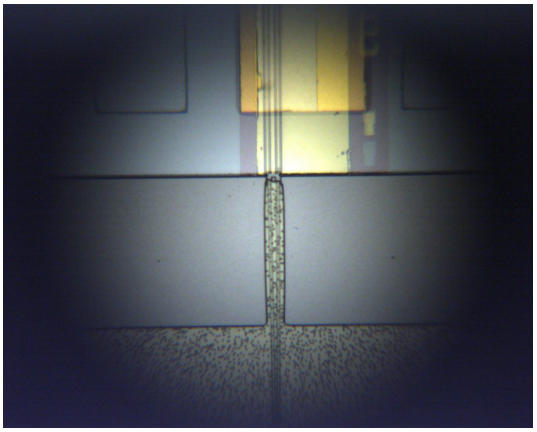

FIGURE 4.28: Overlay image of the substrate and the laser-bar showing sub-micron alignment.

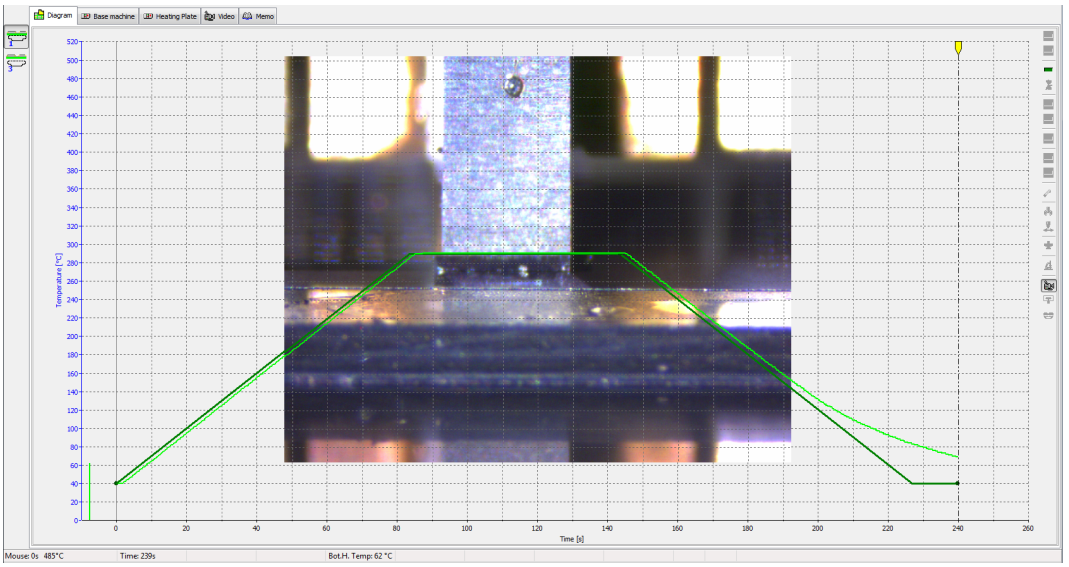


FIGURE 4.29: Overlay image showing the bonded laser bar and a graph of the temperature of the heated base as a function of time.

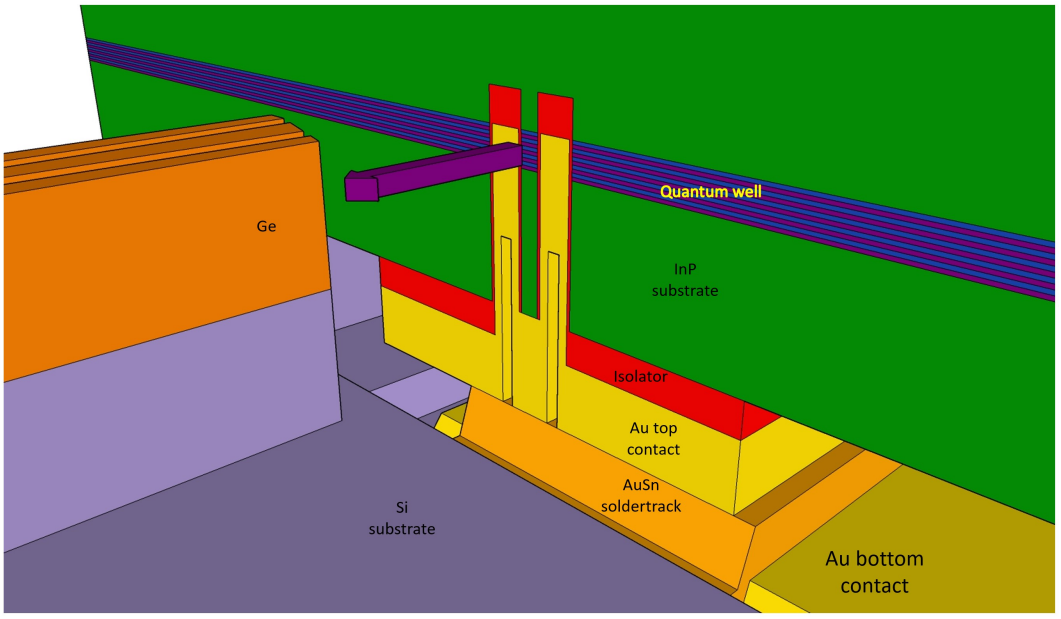


FIGURE 4.30: 3D schematic showing an integrated laser-bar.

Once the the laser-bar and the substrate were aligned, they were brought to physical contact using the placement-arm. Then, using the heated base of the flip-chip bonder the AuSn solder between the Au metal contacts on the laser-bar and the substrate was heated to reach its melting point at 280°C as shown in Figure 4.29. The bond achieved exhibits low thermal budget, mechanical strength and excellent Ohmic properties between the gold pads on the laser-bar and the substrate.

A schematic illustrating the final device is shown in Figure 4.30.

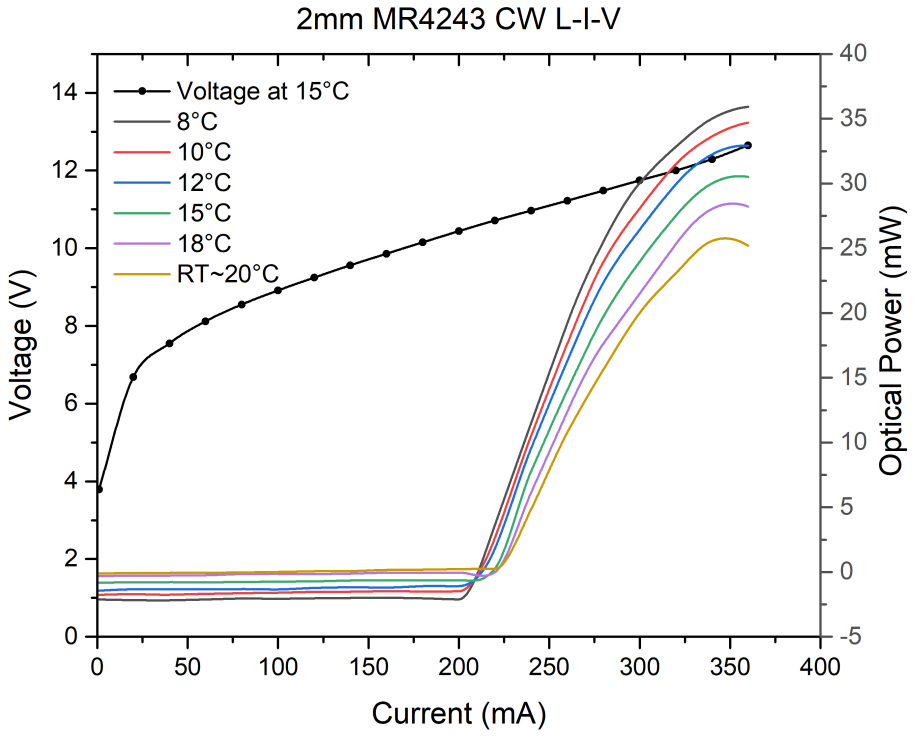


FIGURE 4.31: L-I-V curve of a 2 mm long laser-bar measured before bonding (Data provided by the university of Sheffield).

## 4.4 Experimental results and discussion

Laser-bars where pre-characterised prior to bonding in order for performance comparison before and after bonding. This included both electrical and optical measurements from which the L-I-V curve of the laser-bars was obtained as shown in Figure 4.31.

The voltage of the laser-bar was measured at 15 °C whereas the optical power was measured at temperatures raising from 8 °C to room temperature ∼20 °C. As observed from the graph, the laser turn-or current was between 200 and 225 mA. The emitted optical power was ranging from a minimum of ∼25 to a maximum of ∼ 35 mW.

Laser-bars of the same material were characterised once they were flip-chip bonded. The results are shown Figure 4.32.

To investigate the yield of the electrical contacts, all of the lasers were measured across the entire laser-bar. Figure 4.32 is showing the I-V curves for three lasers located at different points on the laser-bar. From the graphs it can be seen that the electrical contacts to the laser-bar demonstrated uniform current-voltage characteristics which exhibited a yield for the electrical contacts of 100%.

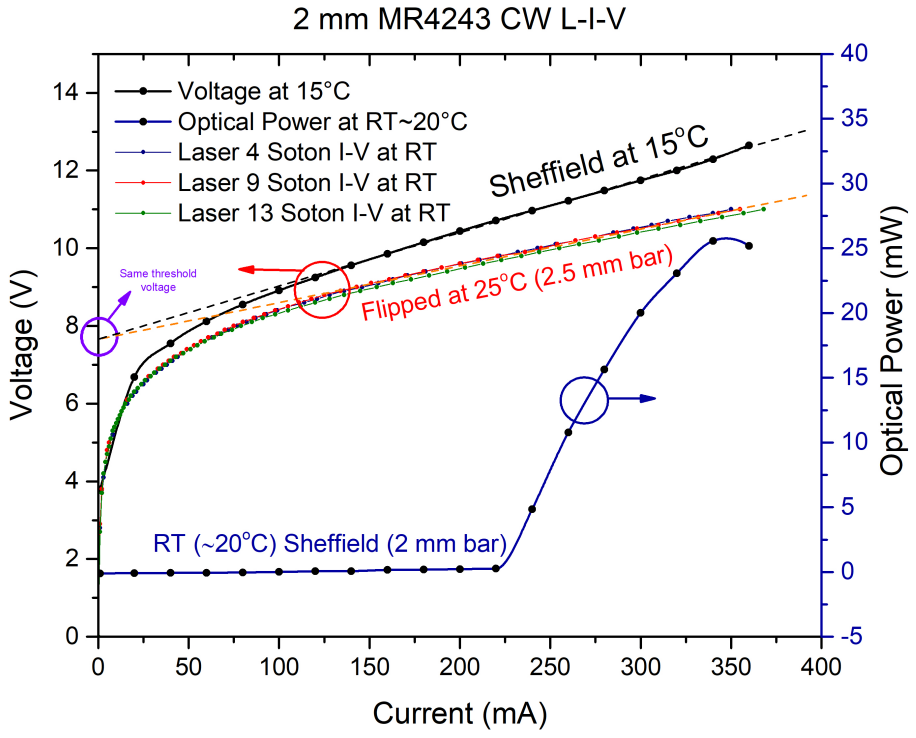


FIGURE 4.32: L-I-V curve of a laser-bar measured after bonding. Note the the optical power curve corresponds to a laser-bar before bonding.

This high yield also demonstrated the accurate control of the deposited metal thicknesses and placement considering the tolerances regarding the required the excess solder for good quality contact and the deposited metal thickness variation across the wafer. Moreover, the I-V curves before and after bonding show an identical behaviour. The difference in the graph shown in Figure 4.32 are due to the fact that the laser-bars measured before and after bonding were of different length (1.45 and 2.5 mm before and after bonding respectively). The identical threshold voltage in both cases verifies the identical electrical characteristics of the contacts. This indicates that no loss of electrical power occurred due to the integration of the device.

The optical power measured through the grating coupler was measured to obtain the optical characteristics of the integrated device. The measurements were carried out in pulsed mode where pulses of f = 980 Hz and DC = 10% (up to 350mA, with 400 mA shown) where used. Pulse generation was achieved using a QCL controller by Thorlabs [179], that also has a Thermoelectric Cooler (TEC) for temperature control. A cooling stage was used to cool the laser-bars down to a temperature of 20 °C.

The coupled optical power from the GOS waveguides was collected through a multimode optical fibre via the grating coupler. The optical power was measured using the detector and the lock-in amplifier described in to acquire the measured data. Light coupling from the QCL was verified as power decreased by misaligning the fibre in respect to

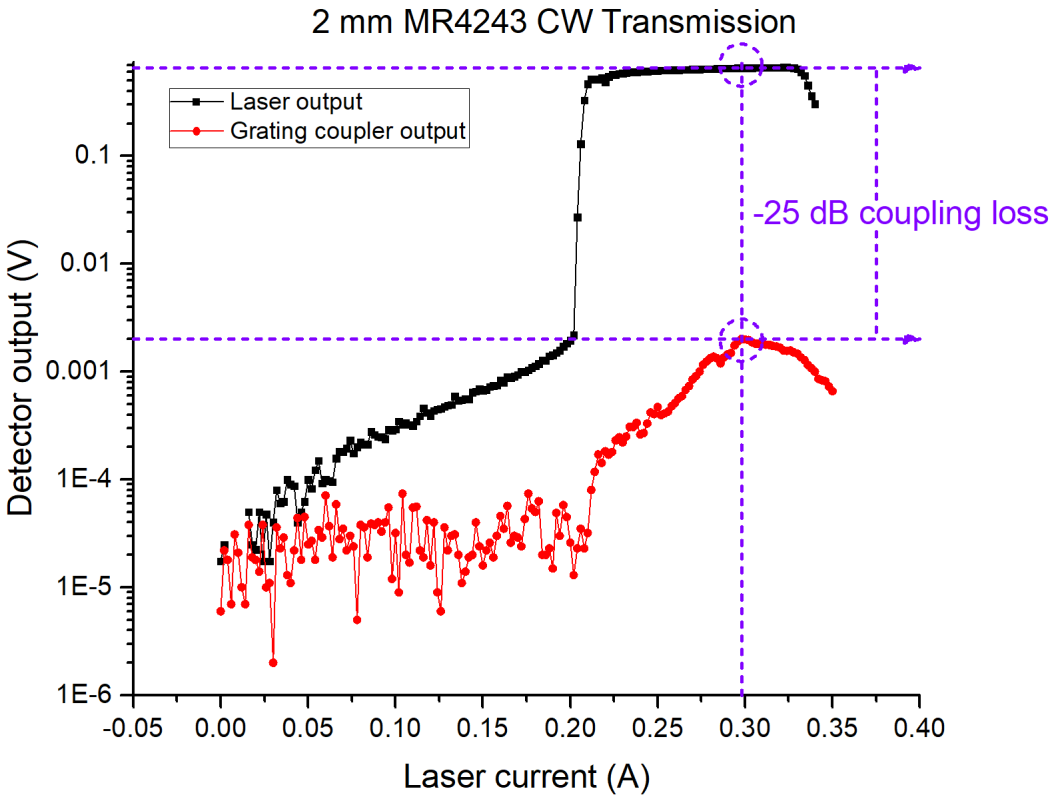


FIGURE 4.33: Measured optical power as a function of the laser current.

the grating coupler. To obtain a figure of the coupling loss, the optical power from a QCL on a diced sample, where the GOS waveguides were removed, was measured as a reference. The graphs for the coupled and the optical power emitted from the QCL are shown in Figure 4.33.

The measured coupling loss was 25 dB at the point where the maximum coupled optical power was obtained which corresponded to a laser current of ∼300 mA. This coupling loss is attributed to various mechanisms. As already mentioned in 4.2 the window layer that defined the top of the supports and thus the z position of the laser, was overetched by ∼400 nm. According to simulations, this corresponds to a ∼1 dB loss. The gap between the laser and the taper facet as well as the placement misalignment of the laser-bar laterally could not be determined as no alignment marks where designed for that purpose. Taking into account that the placement accuracy of the flip-chip bonder used is ∼500 nm, this, according to simulations, corresponds to a coupling loss of ∼0.7 dB. The laser-bar was placed such that the gap was minimised, however, a gap of 1 $\mu$m would result in a a further loss of ∼6 dB. Therefore, approximately 8 dB of coupling loss emanate from the misalignment of the laser-bar with respect to the taper in all 3 axes. Once light was coupled to the passive GOS circuitry, it experienced propagation loss and bend loss in the waveguide before reaching the grating coupler. However, due to the lack of a light source emitting at 5.5 $\mu$m, the propagation loss and bend loss of the waveguides could not be characterised. The next loss mechanism is associated with

the grating coupler which had a simulated coupling efficiency of ∼5.5 dB at 5.5 $\mu$m. Finally, an additional loss mechanism originates from the optical fibre that was used to guide the optical beam to the detector to be measured. As the bending loss of the type of fibre used varies substantially, the fibre could not be characterised. Therefore, this 12 dB loss is attributed to the uncharacterised components of the system.

## 4.5 Conclusion

QCL integration on GOS platform using flip-chip bonding at a wavelength of $\lambda = 5.5$ $\mu$m has been demonstrated in this chapter. Initially, simulations were carried out to evaluate the influence of misalignment on the coupling efficiency between the laser and the waveguide, revealing that the coupling efficiency is more affected by misalignment in the z-axis due to etch depth error than in the y-axis due to lateral misalignment. From these simulation it was also observed that the gap between the laser and the waveguide has a significant influence on the coupling efficiency.

Fabrication included multiple etch steps as well as metal deposition steps. The main issue was to control the etch depth since it could not be monitored using conventional elipsometry. Instead, the technique that was used was to manually remove portions of the resist and then measure the thickness of the resist using profilometry. However, this method was inaccurate, resulting in the final etch depth having an offset from the initially desired value. An additional fabrication issue regarding the deposition of the AuSn solder-tracks was the lift-off process. The first set of devices was fabricated using a single-layer lift-off process that proved to be unsuitable. To overcome this issue, a bi-layer lift-off process was employed resulting in a final layer of AuSn of good quality without residues. Subsequent measurements showed that the electrical contacts to the laser-bar demonstrated uniform current-voltage characteristics, which exhibited a yield for the electrical contacts of 100%.

Flip-chip bonding of the laser-bars was carried out once the fabrication of the of the substrate was completed. The main issue of this process was aligning the laser-bars with the substrate in order to achieve the highest coupling efficiency possible. Optimal alignment was ensured by carrying out a fine calibration of the beam-splitter that determines the placement accuracy, which can be down to 0.3 $\mu$m according to the standard specification from the manufacturer.

Although the coupling efficiency achieved was not the optimal due to the issues described in this chapter, these results are of great importance as they were obtained from the first attempt. Coupling can be improved upon optimising the various fabrication processes used to realise laser integration. Such a system is of fundamental importance for building MIR sensors using an integrated light source at various wavelengths as this method allows the use of various light sources that can be integrated with various passive platforms.

# Chapter 5

# Conclusions and future work

## 5.1 Conclusions

In this thesis suspended Ge waveguides, using Ge-on-SOI as the initial platform, have been demonstrated. The first designs were carried out using a Ge thickness of 400 nm. Waveguides with a width of 1.1 $\mu$m and an etch depth of 250 nm were fabricated and characterised at $\lambda = 3.8$ $\mu$m. The propagation loss was measured before and after the BOX removal to investigate how it is affected by the absorption of $SiO_2$. The propagation loss measured initially was 16 dB/cm, which decreased to 2.7 dB/cm once the BOX was etched. Structures for the calculation of the bend loss were also included. The initial bend loss was measured to be 0.13 dB. However, by removing the BOX, the mechanical stability of the structure was reduced, which resulted in the bends to collapse. Therefore, the bend loss of the suspended structures could not be measured. The next designs that were carried out used a Ge thickness of 500 nm. Waveguides with a width of 1.5 $\mu$m and an etch depth of 200 nm were fabricated and characterised at the same wavelength. The measured propagation loss was 3.91 dB/cm. Based on these results, the next step was to extend the operation wavelength to longer ones. The final design was carried out using a thicker Ge thickness (1 $\mu$m). Waveguides with a width of 3.5 $\mu$m and an etch depth of 300 nm were fabricated for $\lambda = 7.67$ $\mu$m. To demonstrate an all-Ge waveguide the underlying Si had to be removed. To reduce etching time, the Si layer of the SOI wafer, onto which the Ge layer was grown, was thinned down to 60 nm from the initial thickness of 220 nm. The first fabrication run was carried out using SOI wafers provided by Simgui [171]. The BOX in these wafers was of inferior quality resulting in a non-uniform etching profile which in turn caused many of the waveguides to collapse due to reduced mechanical stability. In addition, this fabrication process was proven to be unsuitable for processing Ge as it included a step for removing the resist after every lithography step, that caused the oxidation of Ge. The oxidised Ge is soluble in water resulting in defects that increase the propagation loss. To overcome both issues, wafers with a superior BOX quality provided by Soitec [173] were used that exhibited a

more uniform etching profile. Moreover, an additional fabrication step, that included the deposition of a thin $SiO_2$ layer before spinning resist, was implemented. This resulted in the protection of the Ge layer thus preventing the formation of defects. The propagation loss measured for these waveguides was 2.6±0.3 dB/cm. The simulated optical mode confinement of the fundamental TE mode at 7.67 $\mu$m in air was ∼15% as opposed to ∼2.5% in the GOS waveguides presented in [86]. In addition, by tailoring the air-gap underneath the Ge layer by precisely controlling the etch time of Si, it was shown that the standard SOI wafer with the 3 $\mu$m thick BOX can be utilised at longer wavelengths. These results showed that suspended Ge waveguides fabricated using Ge-on-SOI wafers have the potential to be exploited throughout the entire MIR transparency window of Ge and for sensing applications above 8 $\mu$m that is the transparency limit of Si. To the best of my knowledge, at the time this was work was carried out, this was the first demonstration of low-loss suspended Ge waveguides at such a long wavelength. The next demonstration at such a long wavelength involved suspended Ge waveguides with a subwavelength metamaterial lateral cladding that simultaneously provides optical confinement and allows structural suspension [105]. Nevertheless, the propagation loss reported is approximately twice as high than what is reported in this thesis (5.3 compared to 2.6 dB/cm). Lastly, waveguides using a 2 $\mu$m thick Ge layer with a thinned Si layer of 50 nm were designed for $\lambda = 9.5$ $\mu$m. However, due to fabrication issues they were not characterised.

Finally, in chapter 4, the process of integrating QCLs on a GOS platform using flip-chip bonding was demonstrated. Laser integration can be realised using various approaches as described in 2.3.4, each one exhibiting benefits and challenges. In this thesis, a more conventional approach of bonding pre-fabricated lasers directly on a PIC with the emitted light being butt-coupled into a waveguide was implemented. This so-called hybrid integration approach where III-V lasers are integrated with group IV PICs enables the use of optimal materials for the development of each component. Coupling these as a back-end process enables the fabrication of these devices in existing dedicated production facilities separately. This allows for the independent characterisation of each component, increasing final yield. The light source and PIC can subsequently be integrated at an isolated location thus eliminating any contamination to the main fabrication facilities such as between group IV and III-V elements which are dopants to each other. The work presented in this thesis demonstrates the integration of QCLs operating at a wavelength of 5.5 $\mu$m, that were provided by the university of Sheffield, using flip-chip bonding on 3 $\mu$m pre-processed GOS samples. Light from the QCLs was butt-coupled to rib waveguides and subsequently to an optical fibre using grating couplers. Simulations have been carried out to evaluate the effect of lateral and vertical misalignment on the coupling efficiency. It was observed that the coupling efficiency was more affected by misalignment in the vertical direction due to etch depth error than due to lateral misalignment. In fact, an etch depth error of 2.4 $\mu$m resulted in a reduction in the coupling efficiency by 50%. On the other hand, the same reduction in the coupling

efficiency was caused by a 6 $\mu$m lateral misalignment. The simulation results also showed that due to the beam divergence of the laser mode, the gap between the laser and the taper should be minimised in order to maximise coupling efficiency. In fact, 1 $\mu$m of gap resulted in a reduction in the coupling efficiency of 77%. To couple light out of the waveguide and into the optical fibre, a novel grating coupler design with a high coupling efficiency was utilised that was comprised of a few diffractive elements with and an antireflective element for minimised back-reflections. The simulated grating coupler was optimised for $\lambda = 5.5$ $\mu$m and exhibited a coupling efficiency of 30%, a radiation of 0.01%, a substrate leakage of 61.3% and a low reflection of 0.04%. However, due to the lack of a light source at this wavelength, the grating couplers were not experimentally tested prior to implementation in the final device. To ensure that the transmission measured during characterisation of the device is light coupled to the waveguide rather than mode coupled through the slab directly from the QCL, bends were used after the taper, guiding the coupled mode away from the emission axis of the QCL. The bending radius was selected to be 250 $\mu$m to ensure minimal bend loss. Once the modelling of the device was completed fabrication followed, which included three etch steps and two metal depositions. The etch steps were of large depth ($\geq$6 $\mu$m), therefore they had to be initially tested using test wafers. The results showed a vertical etching profile and a good material to resist ratio. Upon developing the fabrication processes for the deep etching of Si, the wafer underwent the first etch step that defined the window that would house the whole laser bar and define the top part of the supports, onto which the laser bar will be placed. Due to the lack of another layer underneath the Si substrate, the etch depth could not be evaluated using ellipsometry. Instead, small areas of the resist were manually stripped using acetone and then the profile was measured using profilometry. This however was an inaccurate method of measuring the etch depth leading to overetching the substrate resulting in vertical misalignment between the laser-bar and the waveguide. The second etch step defined the supports, onto which the laser bar will subsequently be placed. The supports are strips, onto which the substrate of the laser is supported. The etch step defining the trench was eliminated as it was decided to be redundant due to the already high volume of free space formed by the previous etch steps. Once all the etch steps were carried out, the deposition of the Au bottom contacts followed. Since the metal thickness was high, the lift-off recipe was developed using test wafers where Al was deposited instead of Au to reduce cost. Once the bottom contacts were deposited, the final step was to deposit the AuSn solder-tracks for contacting the bottom contacts on the substrate with the contacts on the laser-bar. However, the lift-off process did not perform as planned, which resulted in chunks of AuSn to stick on the substrate. To remove these chunks, the wafer was placed in a bath and ultrasonication was used to enhance lift-off. However, this resulted in the removal of most AuSn solder-tracks as well. To prevent this from happening in a subsequent fabrication run, a bi-layer lift-off process was implemented, which resulted in very high yield. A new fabrication run was used by implementing the new lift-off process. However, the window layer was

overetched by ∼400 nm. In this fabrication run, the combined thickness of the Au and the AuSn to ensure contact, had to be ≥3.25 $\mu$m. Having to deposit such a thick metal layer would increase the cost dramatically. Therefore, a ∼2 $\mu$m thick $SiO_2$ was deposited on the Si substrate prior to metal deposition. Once fabrication was completed, the wafer was diced into 15×20 $mm^2$ samples and were prepared for bonding. This was carried out upon aligning the laser-bars to the PIC and then by heating the substrate to the melting point of AuSn (280°C), a strong bond between the two Au contacts was formed. Laser-bars were characterised prior to bonding to investigate bonding quality. From the obtained I-V curves it was observed that the electrical contacts to the laser-bar demonstrated uniform current-voltage characteristics, which exhibited a yield for the electrical contacts of 100%. The emitted optical power was ranging from a minimum of ∼25 to a maximum of ∼35 mW. Laser-bars of the same material were characterised once they were flip-chip bonded and the measured coupling loss was 25 dB at the point where the maximum coupled optical power was obtained, which corresponded to a laser current of ∼300 mA. This coupling loss is attributed to various mechanisms. The window layer that defined the top of the supports and thus the z position of the laser, was overetched by ∼400 nm. According to simulations, this corresponds to a ∼1 dB loss. The gap between the laser and the taper facet as well as the placement misalignment of the laser-bar laterally could not be determined as no alignment marks where designed for that purpose. Taking into account that the placement accuracy of the flip-chip bonder used is ∼500 nm, this, according to simulations, corresponds to a coupling loss of ∼0.7 dB. The laser-bar was placed such that the gap was minimised, however, a gap of 1 $\mu$m would result in a a further loss of ∼6 dB. Therefore, approximately 8 dB of coupling loss emanate from the misalignment of the laser-bar with respect to the taper in all 3 axes. Once light was coupled to the passive GOS circuitry, it experienced propagation loss and bend loss in the waveguide before reaching the grating coupler. However, due to the lack of a light source emitting at 5.5 $\mu$m, the propagation loss and bend loss of the waveguides could not be characterised. The next loss mechanism is associated with the grating coupler which had a simulated coupling efficiency of ∼5.5 dB at 5.5 $\mu$m. Finally, an additional loss mechanism originates from the optical fibre that was used to guide the optical beam to the detector to be measured. As the bending loss of the type of fibre used varies substantially, the fibre could not be characterised. Therefore, this 12 dB loss is attributed to the uncharacterised components of the system. Despite the fact that the coupling efficiency is low, to the best of my knowledge, this is the first demonstration of laser integration on a Ge-based platform in the MIR.

## 5.2 Future work

In chapter 3 the suspended waveguides presented were all based on the rib waveguide geometry. This is favourable in terms of achieving a low propagation loss as the main

loss mechanism is the roughness at the waveguide sidewalls. However, at such long wavelengths, scattering becomes negligible, as it is proportional to $\sim \lambda^4$. Therefore, in order to make fabrication simpler, a new design based on the subwavelength cladding (as described in [74]) can be implemented. In addition, to be able to characterise these waveguides at wavelengths as long as 9.5 $\mu$m, the grating couplers should also be suspended as the absorption due to the underlying Si and especially $SiO_2$ becomes very high. New grating couplers will have to be designed in order for these waveguides to be characterised. Moreover, to fully exploit the entire transparency window of Ge, this approach can potentially be followed to design waveguides for even higher wavelengths up to 14 $\mu$m by creating a sufficient air-gap to minimise losses due to substrate leakage.

As for the integration using flip-chip bonding, the GOS samples will have to be refabricated using wafers of higher quality, to ensure low propagation loss. Moreover, a new process for the more precise control of the etch depth will have to be implemented in order to minimise misalignment thus achieving optimum coupling efficiency. In addition, due to the high refractive index contrast between Ge and air ($\Delta$n$\sim$3), high reflections are caused at the Ge-air interface. To tackle this issue, an antireflective coating with a refractive index between that of Ge and air can be used in a similar manner to what has been demonstrated in [188]. Furthermore, wavelength tunability is very desirable for increasing the functionality and the flexibility of an integrated laser. To enable this, a *Vernier* racetrack resonator tunable filter can be used as demonstrated in [191].

To evaluate how an integrated laser source can be employed for MIR absorption spectroscopy, it can be used to develop a PIC for trace-gas sensing applications in which MIR radiation directly interacts with the targeted analyte. A potential gas that can be targeted is $CH_4$, which exhibits high absorption in the 7-8 $\mu$m wavelength region. Since that QCLs can be developed to emit light in that wavelength region, they can be integrated with the suspended Ge platform in order to realise an integrated MIR optical $CH_4$ sensor in a similar fashion with the gas sensor demonstrated in [40].

# Bibliography


[1] M. B. Ritter, Y. Vlasov, J. A. Kash, and A. Benner, "Optical technologies for data communication in large parallel systems," *Journal of Instrumentation*, vol. 6, no. 01, p. C01012, 2011.

[2] Y. Arakawa, T. Nakamura, Y. Urino, and T. Fujita, "Silicon photonics for next generation system integration platform," *IEEE Communications Magazine*, vol. 51, no. 3, pp. 72–77, 2013.

[3] B. R. Koch, E. J. Norberg, B. Kim, J. Hutchinson, J.-H. Shin, G. Fish, and A. Fang, "Integrated silicon photonic laser sources for telecom and datacom," in *National Fiber Optic Engineers Conference*. Optical Society of America, 2013, pp. PDP5C–8.

[4] H. Sasaki, "Development of silicon photonics integrated circuits for next generation optical access networks," in *2019 2nd International Symposium on Devices, Circuits and Systems (ISDCS)*. IEEE, 2019, pp. 1–4.

[5] A. V. Krishnamoorthy, R. Ho, X. Zheng, H. Schwetman, J. Lexau, P. Koka, G. Li, I. Shubin, and J. E. Cunningham, "Computer systems based on silicon photonic interconnects," *Proceedings of the IEEE*, vol. 97, no. 7, pp. 1337–1361, 2009.

[6] T. Tekin, N. Pleros, R. Pitwon, and A. Hakansson, *Optical interconnects for data centers*. Woodhead Publishing, 2016.

[7] R. Soref and J. Lorenzo, "Single-crystal silicon: a new material for 1.3 and 1.6 $\mu$m integrated-optical components," *Electronics Letters*, vol. 21, no. 21, pp. 953–954, 1985.

[8] A. Rickman, "The commercialization of silicon photonics," *Nature Photonics*, vol. 8, no. 8, p. 579, 2014.

[9] G. T. Reed, W. R. Headley, and C. J. Png, "Silicon photonics: The early years," in *Optoelectronic Integration on Silicon II*, vol. 5730. International Society for Optics and Photonics, 2005, pp. 1–18.

[10] J. Liu, D. D. Cannon, K. Wada, Y. Ishikawa, S. Jongthammanurak, D. T. Danielson, J. Michel, and L. C. Kimerling, "Tensile strained Ge p-i-n photodetectors

on Si platform for C and L band telecommunications," *Applied Physics Letters*, vol. 87, no. 1, p. 011110, 2005.

[11] Y. Kim, J. Fujikata, S. Takahashi, M. Takenaka, and S. Takagi, "First demonstration of SiGe-based carrier-injection Mach–Zehnder modulator with enhanced plasma dispersion effect," *Optics express*, vol. 24, no. 3, pp. 1979–1985, 2016.

[12] B. A. Dorin and N. Y. Winnie, "Two-mode division multiplexing in a silicon-on-insulator ring resonator," *Optics express*, vol. 22, no. 4, pp. 4547–4558, 2014.

[13] P. Dong, "Silicon photonic integrated circuits for wavelength-division multiplexing applications," *IEEE Journal of Selected Topics in Quantum Electronics*, vol. 22, no. 6, pp. 370–378, 2016.

[14] D. Dodane, J. Bourderionnet, S. Combrié, and A. de Rossi, "Fully embedded photonic crystal cavity with Q= 0.6 million fabricated within a full-process CMOS multiproject wafer," *Optics express*, vol. 26, no. 16, pp. 20 868–20 877, 2018.

[15] C. G. Littlejohns, Y. Hu, F. Y. Gardes, D. J. Thomson, S. A. Reynolds, G. Z. Mashanovich, and G. T. Reed, "50 Gb/s silicon photonics receiver with low insertion loss," *IEEE Photonics Technology Letters*, vol. 26, no. 7, pp. 714–717, 2014.

[16] X. Chen and H. K. Tsang, "Polarization-independent grating couplers for silicon-on-insulator nanophotonic waveguides," *Optics letters*, vol. 36, no. 6, pp. 796–798, 2011.

[17] O. Katz and D. Malka, "Design of novel SOI 1×4 optical power splitter using seven horizontally slotted waveguides," *Photonics and Nanostructures-Fundamentals and Applications*, vol. 25, pp. 9–13, 2017.

[18] H. Guan, Q. Fang, G.-Q. Lo, and K. Bergman, "High-efficiency biwavelength polarization splitter-rotator on the SOI platform," *IEEE Photonics Technology Letters*, vol. 27, no. 5, pp. 518–521, 2014.

[19] C. A. Barrios, "Optical slot-waveguide based biochemical sensors," *sensors*, vol. 9, no. 6, pp. 4751–4765, 2009.

[20] B. Jalali, "Silicon photonics: Nonlinear optics in the mid-infrared," *Nature Photonics*, vol. 4, no. 8, p. 506, 2010.

[21] J. Doylend and S. Gupta, "An overview of silicon photonics for LIDAR," in *Silicon Photonics XV*, vol. 11285. International Society for Optics and Photonics, 2020, p. 112850J.

[22] M. Sieger and B. Mizaikoff, "Toward on-chip mid-infrared sensors," 2016.

[23] M. Sieger, J. Haas, M. Jetter, P. Michler, M. Godejohann, and B. Mizaikoff, "Mid-infrared spectroscopy platform based on GaAs/AlGaAs thin-film waveguides and quantum cascade lasers," *Analytical chemistry*, vol. 88, no. 5, pp. 2558–2562, 2016.

[24] R. Lu, W.-W. Li, B. Mizaikoff, A. Katzir, Y. Raichlin, G.-P. Sheng, and H.-Q. Yu, "High-sensitivity infrared attenuated total reflectance sensors for in situ multicomponent detection of volatile organic compounds in water," *Nature protocols*, vol. 11, no. 2, p. 377, 2016.

[25] "NIST standard reference data program," http://webbook.nist.gov/cgi/cbook.cgi?ID=C7446095&Type=IR-SPEC&Index=0#.

[26] D. Caffey, M. B. Radunsky, V. Cook, M. Weida, P. R. Buerki, S. Crivello, and T. Day, "Recent results from broadly tunable external cavity quantum cascade lasers," in *Novel In-Plane Semiconductor Lasers X*, vol. 7953. International Society for Optics and Photonics, 2011, p. 79531K.

[27] L. Tombez, E. Zhang, J. Orcutt, S. Kamlapurkar, and W. Green, "Methane absorption spectroscopy on a silicon photonic chip," *Optica*, vol. 4, no. 11, pp. 1322–1325, 2017.

[28] "NIST chemistry webbook." [Online]. Available: https://webbook.nist.gov/cgi/cbook.cgi?ID=C74828&Units=SI&Type=IR-SPEC&Index=1#IR-SPEC

[29] F. Ottonello-Briano, C. Errando-Herranz, H. Rödjegård, H. Martin, H. Sohlström, and K. B. Gylfason, "Carbon dioxide absorption spectroscopy with a mid-infrared silicon photonic waveguide," *Optics Letters*, vol. 45, no. 1, pp. 109–112, 2020.

[30] S. A. Miller, M. Yu, X. Ji, A. G. Griffith, J. Cardenas, A. L. Gaeta, and M. Lipson, "Low-loss silicon platform for broadband mid-infrared photonics," *Optica*, vol. 4, no. 7, pp. 707–712, 2017.

[31] M. S. Luchansky and R. C. Bailey, "High-Q optical sensors for chemical and biological analysis," *Analytical chemistry*, vol. 84, no. 2, pp. 793–821, 2012.

[32] J. Wang, Z. Yao, T. Lei, and A. W. Poon, "Silicon coupled-resonator optical-waveguide-based biosensors using light-scattering pattern recognition with pixelized mode-field-intensity distributions," *Scientific reports*, vol. 4, p. 7528, 2014.

[33] S. M. Grist, S. A. Schmidt, J. Flueckiger, V. Donzella, W. Shi, S. T. Fard, J. T. Kirk, D. M. Ratner, K. C. Cheung, and L. Chrostowski, "Silicon photonic microdisk resonators for label-free biosensing," *Optics express*, vol. 21, no. 7, pp. 7994–8006, 2013.

[34] M. La Notte and V. M. Passaro, "Ultra high sensitivity chemical photonic sensing by Mach-Zehnder interferometer enhanced Vernier-effect," *Sensors and Actuators B: Chemical*, vol. 176, pp. 994–1007, 2013.

[35] T. Claes, W. Bogaerts, and P. Bienstman, "Experimental characterization of a silicon photonic biosensor consisting of two cascaded ring resonators based on the Vernier-effect and introduction of a curve fitting method for an improved detection limit," *Optics express*, vol. 18, no. 22, pp. 22 747–22 761, 2010.

[36] L. Qin, L. Wang, M. Li, and J.-J. He, "Optical sensor based on Vernier-cascade of ring resonator and Echelle diffraction grating," *IEEE Photonics Technology Letters*, vol. 24, no. 11, pp. 954–956, 2012.

[37] X. Jiang, Y. Chen, F. Yu, L. Tang, M. Li, and J.-J. He, "High-sensitivity optical biosensor based on cascaded Mach-Zehnder interferometer and ring resonator using Vernier effect," *Optics letters*, vol. 39, no. 22, pp. 6363–6366, 2014.

[38] B. Troia, A. Z. Khokhar, M. Nedeljkovic, J. S. Penades, V. M. Passaro, and G. Z. Mashanovich, "Cascade-coupled racetrack resonators based on the Vernier effect in the mid-infrared," *Optics express*, vol. 22, no. 20, pp. 23 990–24 003, 2014.

[39] B. Troia, J. S. Penades, A. Z. Khokhar, M. Nedeljkovic, C. Alonso-Ramos, V. M. Passaro, and G. Z. Mashanovich, "Germanium-on-silicon Vernier-effect photonic microcavities for the mid-infrared," *Optics letters*, vol. 41, no. 3, pp. 610–613, 2016.

[40] K. M. Yoo, J. Midkiff, A. Rostamian, C.-j. Chung, H. Dalir, and R. T. Chen, "InGaAs membrane waveguide: a promising platform for monolithic integrated mid-infrared optical gas sensor," *ACS sensors*, vol. 5, no. 3, pp. 861–869, 2020.

[41] P. Wägli, Y.-C. Chang, A. Homsy, L. Hvozdara, H. P. Herzig, and N. F. de Rooij, "Microfluidic droplet-based liquid–liquid extraction and on-chip IR spectroscopy detection of cocaine in human saliva," *Analytical chemistry*, vol. 85, no. 15, pp. 7558–7565, 2013.

[42] Y.-C. Chang, P. Wägli, V. Paeder, A. Homsy, L. Hvozdara, P. van der Wal, J. Di Francesco, N. F. de Rooij, and H. P. Herzig, "Cocaine detection by a mid-infrared waveguide integrated with a microfluidic chip," *Lab on a Chip*, vol. 12, no. 17, pp. 3020–3023, 2012.

[43] C. Bauer, A. Sharma, U. Willer, J. Burgmeier, B. Braunschweig, W. Schade, S. Blaser, L. Hvozdara, A. Müller, and G. Holl, "Potentials and limits of mid-infrared laser spectroscopy for the detection of explosives," *Applied Physics B*, vol. 92, no. 3, pp. 327–333, 2008.

[44] R. Rehm, M. Walther, J. Schmitz, J. Fleissner, J. Ziegler, W. Cabanski, and R. Breiter, "Dual-colour thermal imaging with InAs/GaSb superlattices in mid-wavelength infrared spectral range," *Electronics Letters*, vol. 42, no. 10, pp. 577–578, 2006.

[45] R. Martini, C. Bethea, F. Capasso, C. Gmachl, R. Paiella, E. Whittaker, H. Hwang, D. Sivco, J. Baillargeon, and A. Cho, "Free-space optical transmission of multimedia satellite data streams using mid-infrared quantum cascade lasers," *Electronics Letters*, vol. 38, no. 4, pp. 181–183, 2002.

[46] M. Pfennigbauer and A. Ullrich, "Multi-wavelength airborne laser scanning," in *Proceedings of the International Lidar Mapping Forum, ILMF, New Orleans*, 2011.

[47] Wikipedia, "Infrared window — wikipedia, the free encyclopedia," 2017, [Online; accessed 14-May-2017]. [Online]. Available: https://en.wikipedia.org/w/index.php?title=Infrared_window&oldid=776519003

[48] B. Kuyken, P. Verheyen, P. Tannouri, X. Liu, J. Van Campenhout, R. Baets, W. Green, and G. Roelkens, "Generation of 3.6 $\mu$m radiation and telecom-band amplification by four-wave mixing in a silicon waveguide with normal group velocity dispersion," *Optics letters*, vol. 39, no. 6, pp. 1349–1352, 2014.

[49] X. Liu, R. M. Osgood Jr, Y. A. Vlasov, and W. M. Green, "Mid-infrared optical parametric amplifier using silicon nanophotonic waveguides," *Nature Photonics*, vol. 4, no. 8, p. 557, 2010.

[50] A. G. Griffith, R. K. Lau, J. Cardenas, Y. Okawachi, A. Mohanty, R. Fain, Y. H. D. Lee, M. Yu, C. T. Phare, C. B. Poitras *et al.*, "Silicon-chip mid-infrared frequency comb generation," *Nature communications*, vol. 6, p. 6299, 2015.

[51] M.-S. Rouifed, C. G. Littlejohns, G. X. Tina, Q. Haodong, T. Hu, Z. Zhang, C. Liu, G. T. Reed, and H. Wang, "Low loss SOI waveguides and MMIs at the MIR wavelength of 2 $\mu$m," *IEEE Photonics Technology Letters*, vol. 28, no. 24, pp. 2827–2829, 2016.

[52] G. Z. Mashanovich, M. M. Milošević, M. Nedeljkovic, N. Owens, B. Xiong, E. J. Teo, and Y. Hu, "Low loss silicon waveguides for the mid-infrared," *Optics Express*, vol. 19, no. 8, pp. 7112–7119, 2011.

[53] M. M. Milošević, M. Nedeljkovic, T. M. Ben Masaud, E. Jaberansary, H. M. Chong, N. G. Emerson, G. T. Reed, and G. Z. Mashanovich, "Silicon waveguides and devices for the mid-infrared," *Applied Physics Letters*, vol. 101, no. 12, p. 121105, 2012.

[54] M. Muneeb, X. Chen, P. Verheyen, G. Lepage, S. Pathak, E. Ryckeboer, A. Malik, B. Kuyken, M. Nedeljkovic, J. Van Campenhout *et al.*, "Demonstration of silicon-on-insulator mid-infrared spectrometers operating at 3.8 $\mu$m," *Optics Express*, vol. 21, no. 10, pp. 11 659–11 669, 2013.

[55] J. S. Penadés, A. Z. Khokhar, M. Nedeljkovic, and G. Z. Mashanovich, "Low-loss mid-infrared SOI slot waveguides," *IEEE Photonics Technology Letters*, vol. 27, no. 11, pp. 1197–1199, 2015.

[56] P. Ma, D.-Y. Choi, Y. Yu, Z. Yang, K. Vu, T. Nguyen, A. Mitchell, B. Luther-Davies, and S. Madden, "High q factor chalcogenide ring resonators for cavity-enhanced mir spectroscopic sensing," *Optics express*, vol. 23, no. 15, pp. 19 969–19 979, 2015.

[57] V. Mittal, N. P. Sessions, J. S. Wilkinson, and G. S. Murugan, "Optical quality znse films and low loss waveguides on si substrates for mid-infrared applications," *Optical Materials Express*, vol. 7, no. 3, pp. 712–725, 2017.

[58] R. Kitamura, L. Pilon, and M. Jonasz, "Optical constants of silica glass from extreme ultraviolet to far infrared at near room temperature," *Applied optics*, vol. 46, no. 33, pp. 8118–8133, 2007.

[59] R. A. Soref, S. J. Emelett, and W. R. Buchwald, "Silicon waveguided components for the long-wave infrared region," *Journal of Optics A: Pure and Applied Optics*, vol. 8, no. 10, p. 840, 2006.

[60] M. A. Green, "Self-consistent optical parameters of intrinsic silicon at 300 K including temperature coefficients," *Solar Energy Materials and Solar Cells*, vol. 92, no. 11, pp. 1305–1310, 2008.

[61] M. Nedeljković, "Silicon photonic modulators for the mid-infrared," Ph.D. dissertation, University of Southampton, 2013.

[62] R. Soref, "Mid-infrared photonics in silicon and germanium," *Nature photonics*, vol. 4, no. 8, p. 495, 2010.

[63] J. S. Penadés, A. Sánchez-Postigo, M. Nedeljkovic, A. Ortega-Moñux, J. Wangüemert-Pérez, Y. Xu, R. Halir, Z. Qu, A. Khokhar, A. Osman *et al.*, "Suspended silicon waveguides for long-wave infrared wavelengths," *Optics letters*, vol. 43, no. 4, pp. 795–798, 2018.

[64] G. Roelkens, A. Abassi, P. Cardile, U. Dave, A. De Groote, Y. De Koninck, S. Dhoore, X. Fu, A. Gassenq, N. Hattasan *et al.*, "III-V-on-silicon photonic devices for optical communication and sensing," in *Photonics*, vol. 2, no. 3. Multidisciplinary Digital Publishing Institute, 2015, pp. 969–1004.

[65] D. Jung, J. Faucher, S. Mukherjee, A. Akey, D. J. Ironside, M. Cabral, X. Sang, J. Lebeau, S. R. Bank, T. Buonassisi *et al.*, "Highly tensile-strained Ge/InAlAs nanocomposites," *Nature communications*, vol. 8, no. 1, pp. 1–7, 2017.

[66] H. Hu, R. Ricken, and W. Sohler, "Low-loss ridge waveguides on lithium niobate fabricated by local diffusion doping with titanium," *Applied Physics B*, vol. 98, no. 4, pp. 677–679, 2010.

[67] P. Lenzo, E. Spencer, and K. Nassau, "Electro-optic coefficients in single-domain ferroelectric lithium niobate," *JOSA*, vol. 56, no. 5, pp. 633–635, 1966.

[68] X. Chen, M. M. Milosevic, A. F. Runge, X. Yu, A. Z. Khokhar, S. Mailis, D. J. Thomson, A. C. Peacock, S. Saito, and G. T. Reed, "Silicon erasable waveguides and directional couplers by germanium ion implantation for configurable photonic circuits," *Optics Express*, vol. 28, no. 12, pp. 17 630–17 642, 2020.

[69] G. T. Reed, *Silicon Photonics: The State of the Art*. John Wiley & Sons, 2008.

[70] R. A. Soref, J. Schmidtchen, and K. Petermann, "Large single-mode rib waveguides in GeSi-Si and Si-on-$SiO_2$," *IEEE Journal of Quantum Electronics*, vol. 27, no. 8, pp. 1971–1974, 1991.

[71] M. Nedeljkovic, A. Khokhar, Y. Hu, X. Chen, J. S. Penades, S. Stankovic, H. Chong, D. Thomson, F. Gardes, G. Reed *et al.*, "Silicon photonic devices and platforms for the mid-infrared," *Optical Materials Express*, vol. 3, no. 9, pp. 1205–1214, 2013.

[72] N. Hattasan, B. Kuyken, F. Leo, E. M. Ryckeboer, D. Vermeulen, and G. Roelkens, "High-efficiency SOI fiber-to-chip grating couplers and low-loss waveguides for the short-wave infrared," *IEEE Photonics Technology Letters*, vol. 24, no. 17, pp. 1536–1538, 2012.

[73] Z. Cheng, X. Chen, C. Y. Wong, K. Xu, and H. K. Tsang, "Mid-infrared suspended membrane waveguide and ring resonator on silicon-on-insulator," *IEEE photonics journal*, vol. 4, no. 5, pp. 1510–1519, 2012.

[74] J. S. Penadés, C. Alonso-Ramos, A. Khokhar, M. Nedeljkovic, L. Boodhoo, A. Ortega-Moñux, I. Molina-Fernández, P. Cheben, and G. Mashanovich, "Suspended SOI waveguide with sub-wavelength grating cladding for mid-infrared," *Optics letters*, vol. 39, no. 19, pp. 5661–5664, 2014.

[75] J. S. Penades, A. Ortega-Moñux, M. Nedeljkovic, J. Wangüemert-Pérez, R. Halir, A. Khokhar, C. Alonso-Ramos, Z. Qu, I. Molina-Fernández, P. Cheben *et al.*, "Suspended silicon mid-infrared waveguide devices with subwavelength grating metamaterial cladding," *Optics express*, vol. 24, no. 20, pp. 22 908–22 916, 2016.

[76] N. Nader, A. Kowligy, J. Chiles, E. J. Stanton, H. Timmers, A. J. Lind, F. C. Cruz, D. M. Lesko, K. A. Briggman, S. W. Nam *et al.*, "Infrared frequency comb generation and spectroscopy with suspended silicon nanophotonic waveguides," *Optica*, vol. 6, no. 10, pp. 1269–1276, 2019.

[77] P. T. Lin, V. Singh, H.-Y. G. Lin, T. Tiwald, L. C. Kimerling, and A. M. Agarwal, "Low-stress silicon nitride platform for mid-infrared broadband and monolithically integrated microphotonics," *Advanced Optical Materials*, vol. 1, no. 10, pp. 732–739, 2013.

[78] S. Khan, J. Chiles, J. Ma, and S. Fathpour, "Silicon-on-nitride waveguides for mid- and near-infrared integrated photonics," *Applied physics letters*, vol. 102, no. 12, p. 121104, 2013.

[79] R. A. Johnson, P. De La Houssaye, C. E. Chang, P.-F. Chen, M. E. Wood, G. A. Garcia, I. Lagnado, and P. M. Asbeck, "Advanced thin-film silicon-on-sapphire technology: Microwave circuit applications," *IEEE Transactions on electron devices*, vol. 45, no. 5, pp. 1047–1054, 1998.

[80] G. Imthurn, "The history of silicon-on-sapphire," *Peregrine Semiconductor Corporation*, 2007.

[81] T. Baehr-Jones, A. Spott, R. Ilic, A. Spott, B. Penkov, W. Asher, and M. Hochberg, "Silicon-on-sapphire integrated waveguides for the mid-infrared," *Optics express*, vol. 18, no. 12, pp. 12 127–12 135, 2010.

[82] F. Li, S. D. Jackson, C. Grillet, E. Magi, D. Hudson, S. J. Madden, Y. Moghe, C. O'Brien, A. Read, S. G. Duvall *et al.*, "Low propagation loss silicon-on-sapphire waveguides for the mid-infrared," *Optics express*, vol. 19, no. 16, pp. 15 212–15 220, 2011.

[83] K. W. Carey, F. A. Ponce, J. Amano, and J. Aranovich, "Structural characterization of low-defect-density silicon on sapphire," *Journal of applied physics*, vol. 54, no. 8, pp. 4414–4420, 1983.

[84] D. Chandler-Horowitz and P. M. Amirtharaj, "High-accuracy, mid-infrared (450 $\text{cm}^{-1} \leq \omega \leq 4000\ \text{cm}^{-1}$) refractive index values of silicon," *Journal of Applied physics*, vol. 97, no. 12, p. 123526, 2005.

[85] Y.-C. Chang, V. Paeder, L. Hvozdara, J.-M. Hartmann, and H. P. Herzig, "Low-loss germanium strip waveguides on silicon for the mid-infrared," *Optics letters*, vol. 37, no. 14, pp. 2883–2885, 2012.

[86] M. Nedeljkovic, J. S. Penades, V. Mittal, G. S. Murugan, A. Z. Khokhar, C. Littlejohns, L. G. Carpenter, C. B. Gawith, J. S. Wilkinson, and G. Z. Mashanovich, "Germanium-on-silicon waveguides operating at mid-infrared wavelengths up to 8.5 $\mu$m," *Optics express*, vol. 25, no. 22, pp. 27 431–27 441, 2017.

[87] M. Nedeljkovic, J. S. Penadés, C. J. Mitchell, A. Z. Khokhar, S. Stanković, T. D. Bucio, C. G. Littlejohns, F. Y. Gardes, and G. Z. Mashanovich, "Surface-grating-coupled low-loss Ge-on-Si rib waveguides and multimode interferometers," *IEEE Photonics Technology Letters*, vol. 27, no. 10, pp. 1040–1043, 2015.

[88] K. Gallacher, R. Millar, U. Griškevičiūte, L. Baldassarre, M. Sorel, M. Ortolani, and D. Paul, "Low loss Ge-on-Si waveguides operating in the 8-14 $\mu$m atmospheric transmission window," *Optics express*, vol. 26, no. 20, pp. 25 667–25 675, 2018.

[89] A. Malik, S. Dwivedi, L. Van Landschoot, M. Muneeb, Y. Shimura, G. Lepage, J. Van Campenhout, W. Vanherle, T. Van Opstal, R. Loo *et al.*, "Ge-on-Si and Ge-on-SOI thermo-optic phase shifters for the mid-infrared," *Optics express*, vol. 22, no. 23, pp. 28 479–28 488, 2014.

[90] U. Younis, S. K. Vanga, A. E.-J. Lim, P. G.-Q. Lo, A. A. Bettiol, and K.-W. Ang, "Germanium-on-SOI waveguides for mid-infrared wavelengths," *Optics express*, vol. 24, no. 11, pp. 11 987–11 993, 2016.

[91] H. Icenogle, B. C. Platt, and W. L. Wolfe, "Refractive indexes and temperature coefficients of germanium and silicon," *Applied optics*, vol. 15, no. 10, pp. 2348–2351, 1976.

[92] J. Kang, M. Takenaka, and S. Takagi, "Novel Ge waveguide platform on Ge-on-insulator wafer for mid-infrared photonic integrated circuits," *Optics express*, vol. 24, no. 11, pp. 11 855–11 864, 2016.

[93] G. Mashanovich, M. Nedeljkovic, J. Soler-Penades, Z. Qu, W. Cao, A. Osman, Y. Wu, C. Stirling, Y. Qi, Y. Cheng *et al.*, "Group IV mid-infrared photonics," *Optical Materials Express*, vol. 8, no. 8, pp. 2276–2286, 2018.

[94] S. Kim, J.-H. Han, J.-P. Shim, H.-j. Kim, and W. J. Choi, "Verification of Ge-on-insulator structure for a mid-infrared photonics platform," *Optical Materials Express*, vol. 8, no. 2, pp. 440–451, 2018.

[95] W. Li, P. Anantha, S. Bao, K. H. Lee, X. Guo, T. Hu, L. Zhang, H. Wang, R. Soref, and C. S. Tan, "Germanium-on-silicon nitride waveguides for mid-infrared integrated photonics," *Applied physics letters*, vol. 109, no. 24, p. 241101, 2016.

[96] R. A. Soref, S. J. Emelett, and W. R. Buchwald, "Silicon waveguided components for the long-wave infrared region," *Journal of Optics A: Pure and Applied Optics*, vol. 8, no. 10, p. 840, 2006.

[97] P. Barritault, M. Brun, P. Labeye, O. Lartigue, J.-M. Hartmann, and S. Nicoletti, "Mlines characterization of the refractive index profile of SiGe gradient waveguides at 2.15 $\mu$m," *Optics express*, vol. 21, no. 9, pp. 11 506–11 515, 2013.

[98] N. K. Hon, R. Soref, and B. Jalali, "The third-order nonlinear optical coefficients of Si, Ge, and $Si_{1-x}$ $Ge_x$ in the midwave and longwave infrared," *Journal of Applied Physics*, vol. 110, no. 1, p. 9, 2011.

[99] M. A. Ettabib, K. Hammani, F. Parmigiani, L. Jones, A. Kapsalis, A. Bogris, D. Syvridis, M. Brun, P. Labeye, S. Nicoletti *et al.*, "FWM-based wavelength conversion of 40 Gbaud PSK signals in a silicon germanium waveguide," *Optics express*, vol. 21, no. 14, pp. 16 683–16 689, 2013.

[100] A. Baudrant, *Silicon Technologies: Ion Implantation and Thermal Treatment*. John Wiley & Sons, 2013.

[101] M. Brun, P. Labeye, G. Grand, J.-M. Hartmann, F. Boulila, M. Carras, and S. Nicoletti, "Low loss SiGe graded index waveguides for mid-IR applications," *Optics express*, vol. 22, no. 1, pp. 508–518, 2014.

[102] J. Ramirez, Q. Liu, V. Vakarin, J. Frigerio, A. Ballabio, X. Le Roux, D. Bouville, L. Vivien, G. Isella, and D. Marris-Morini, "Graded SiGe waveguides with broadband low-loss propagation in the mid infrared," *Optics express*, vol. 26, no. 2, pp. 870–877, 2018.

[103] M. Montesinos-Ballester, V. Vakarin, Q. Liu, X. Le Roux, J. Frigerio, A. Ballabio, A. Barzaghi, C. Alonso-Ramos, L. Vivien, G. Isella *et al.*, "Ge-rich graded SiGe waveguides and interferometers from 5 to 11 $\mu$m wavelength range," *Optics Express*, vol. 28, no. 9, pp. 12 771–12 779, 2020.

[104] B. Dong, X. Guo, C. P. Ho, B. Li, H. Wang, C. Lee, X. Luo, and G.-Q. Lo, "Silicon-on-insulator waveguide devices for broadband mid-infrared photonics," *IEEE Photonics Journal*, vol. 9, no. 3, pp. 1–10, 2017.

[105] A. Sánchez-Postigo, A. O.-M. nux, J. S. Penadés, A. Osman, M. Nedeljkovic, Z. Qu, Y. Wu, I. nigo Molina-Fernández, P. Cheben, G. Z. Mashanovich, and J. G. Wangüemert-Pérez, "Suspended germanium waveguides with subwavelength-grating metamaterial cladding for the mid-infrared band," *Opt. Express*, vol. 29, no. 11, pp. 16 867–16 878, May 2021. [Online]. Available: http://www.opticsexpress.org/abstract.cfm?URI=oe-29-11-16867

[106] P. Tai Lin, V. Singh, L. Kimerling, and A. Murthy Agarwal, "Planar silicon nitride mid-infrared devices," *Applied physics letters*, vol. 102, no. 25, p. 251121, 2013.

[107] U. Younis, A. E.-J. Lim, P. G.-Q. Lo, A. A. Bettiol, and K.-W. Ang, "Propagation loss improvement in Ge-on-SOI mid-infrared waveguides using rapid thermal annealing," *IEEE Photonics Technology Letters*, vol. 28, no. 21, pp. 2447–2450, 2016.

[108] J. Kang, Z. Cheng, W. Zhou, T.-H. Xiao, K.-L. Gopalakrisna, M. Takenaka, H. K. Tsang, and K. Goda, "Focusing subwavelength grating coupler for mid-infrared suspended membrane germanium waveguides," *Optics letters*, vol. 42, no. 11, pp. 2094–2097, 2017.

[109] T.-H. Xiao, Z. Zhao, W. Zhou, M. Takenaka, H. K. Tsang, Z. Cheng, and K. Goda, "Mid-infrared germanium photonic crystal cavity," *Optics letters*, vol. 42, no. 15, pp. 2882–2885, 2017.

[110] T.-H. Xiao, Z. Zhao, W. Zhou, C.-Y. Chang, S. Y. Set, M. Takenaka, H. K. Tsang, Z. Cheng, and K. Goda, "Mid-infrared high-Q germanium microring resonator," *Optics letters*, vol. 43, no. 12, pp. 2885–2888, 2018.

[111] J. Yuan, Z. Kang, F. Li, X. Zhang, X. Sang, Q. Wu, B. Yan, K. Wang, X. Zhou, K. Zhong *et al.*, "Mid-infrared octave-spanning supercontinuum and frequency comb generation in a suspended germanium-membrane ridge waveguide," *Journal of Lightwave Technology*, vol. 35, no. 14, pp. 2994–3002, 2017.

[112] G. T. Reed and A. P. Knights, *Silicon photonics: an introduction*. John Wiley & Sons, 2004.

[113] F. Van Laere, G. Roelkens, M. Ayre, J. Schrauwen, D. Taillaert, D. Van Thourhout, T. F. Krauss, and R. Baets, "Compact and highly efficient grating couplers between optical fiber and nanophotonic waveguides," *Journal of lightwave technology*, vol. 25, no. 1, pp. 151–156, 2007.

[114] C. Alonso-Ramos, M. Nedeljkovic, D. Benedikovic, J. S. Penadés, C. G. Littlejohns, A. Z. Khokhar, D. Pérez-Galacho, L. Vivien, P. Cheben, and G. Z. Mashanovich, "Germanium-on-silicon mid-infrared grating couplers with low-reflectivity inverse taper excitation," *Optics letters*, vol. 41, no. 18, pp. 4324–4327, 2016.

[115] A. Sánchez-Postigo, A. Ortega-Moñux, D. Pereira-Martín, Í. Molina-Fernández, R. Halir, P. Cheben, J. S. Penadés, M. Nedeljkovic, G. Mashanovich, and J. Wangüemert-Pérez, "Design of a suspended germanium micro-antenna for efficient fiber-chip coupling in the long-wavelength mid-infrared range," *Optics express*, vol. 27, no. 16, pp. 22 302–22 315, 2019.

[116] D. Taillaert, F. Van Laere, M. Ayre, W. Bogaerts, D. Van Thourhout, P. Bienstman, and R. Baets, "Grating couplers for coupling between optical fibers and nanophotonic waveguides," *Japanese Journal of Applied Physics*, vol. 45, no. 8R, p. 6071, 2006.

[117] C.-H. Chen and C.-H. Chiu, "Taper-integrated multimode-interference based waveguide crossing design," *IEEE Journal of Quantum Electronics*, vol. 46, no. 11, pp. 1656–1661, 2010.

[118] J. Wu, B. Shi, and M. Kong, "Exponentially tapered multi-mode interference couplers," *Chinese Optics Letters*, vol. 4, no. 3, pp. 167–169, 2006.

[119] W. Bogaerts, P. Dumon, D. Van Thourhout, and R. Baets, "Low-loss, low-cross-talk crossings for silicon-on-insulator nanophotonic waveguides," *Optics letters*, vol. 32, no. 19, pp. 2801–2803, 2007.

[120] Y. Fu, T. Ye, W. Tang, and T. Chu, "Efficient adiabatic silicon-on-insulator waveguide taper," *Photonics Research*, vol. 2, no. 3, pp. A41–A44, 2014.

[121] Y. Yao, A. J. Hoffman, and C. F. Gmachl, "Mid-infrared quantum cascade lasers," *Nature Photonics*, vol. 6, no. 7, pp. 432–439, 2012.

[122] Y. Bai, N. Bandyopadhyay, S. Tsao, S. Slivken, and M. Razeghi, "Room temperature quantum cascade lasers with 27% wall plug efficiency," *Applied Physics Letters*, vol. 98, no. 18, p. 181102, 2011.

[123] D. Liang and J. E. Bowers, "Recent progress in lasers on silicon," *Nature photonics*, vol. 4, no. 8, p. 511, 2010.

[124] M. A. Green, J. Zhao, A. Wang, P. J. Reece, and M. Gal, "Efficient silicon light-emitting diodes," *Nature*, vol. 412, no. 6849, pp. 805–808, 2001.

[125] L. T. Canham, "Silicon quantum wire array fabrication by electrochemical and chemical dissolution of wafers," *Applied physics letters*, vol. 57, no. 10, pp. 1046–1048, 1990.

[126] J. Liu, "Monolithically integrated Ge-on-Si active photonics," in *Photonics*, vol. 1, no. 3. Multidisciplinary Digital Publishing Institute, 2014, pp. 162–197.

[127] Y.-Y. Fang, J. Tolle, R. Roucka, A. Chizmeshya, J. Kouvetakis, V. D'Costa, and J. Menéndez, "Perfectly tetragonal, tensile-strained Ge on $Ge_{1-y}$ $Sn_y$ buffered Si (100)," *Applied physics letters*, vol. 90, no. 6, p. 061915, 2007.

[128] J. R. Jain, A. Hryciw, T. M. Baer, D. A. Miller, M. L. Brongersma, and R. T. Howe, "A micromachining-based technology for enhancing germanium light emission via tensile strain," *Nature Photonics*, vol. 6, no. 6, p. 398, 2012.

[129] D. S. Sukhdeo, D. Nam, J.-H. Kang, M. L. Brongersma, and K. C. Saraswat, "Direct bandgap germanium-on-silicon inferred from 5.7% <100> uniaxial tensile strain," *Photonics Research*, vol. 2, no. 3, pp. A8–A13, 2014.

[130] E. M. Fadaly, A. Dijkstra, J. R. Suckert, D. Ziss, M. A. van Tilburg, C. Mao, Y. Ren, V. T. van Lange, K. Korzun, S. Kölling *et al.*, "Direct-bandgap emission from hexagonal Ge and SiGe alloys," *Nature*, vol. 580, no. 7802, pp. 205–209, 2020.

[131] S. A. Ghetmiri, W. Du, J. Margetis, A. Mosleh, L. Cousar, B. R. Conley, L. Domulevicz, A. Nazzal, G. Sun, R. A. Soref *et al.*, "Direct-bandgap GeSn grown on silicon with 2230 nm photoluminescence," *Applied Physics Letters*, vol. 105, no. 15, p. 151109, 2014.

[132] S. Wirths, Z. Ikonic, A. Tiedemann, B. Holländer, T. Stoica, G. Mussler, U. Breuer, J. Hartmann, A. Benedetti, S. Chiussi *et al.*, "Tensely strained GeSn alloys as optical gain media," *Applied physics letters*, vol. 103, no. 19, p. 192110, 2013.

[133] S. Wirths, R. Geiger, N. von den Driesch, G. Mussler, T. Stoica, S. Mantl, Z. Ikonic, M. Luysberg, S. Chiussi, J.-M. Hartmann *et al.*, "Lasing in direct-bandgap GeSn alloy grown on Si," *Nature photonics*, vol. 9, no. 2, pp. 88–92, 2015.

[134] L. F. Miller, "Controlled collapse reflow chip joining," *IBM Journal of Research and Development*, vol. 13, no. 3, pp. 239–250, 1969.

[135] W. R. Imler, K. D. Scholz, M. Cobarruviaz, V. Nagesh, C. C. Chao, and R. Haitz, "Precision flip-chip solder bump interconnects for optical packaging," *IEEE transactions on components, hybrids, and manufacturing technology*, vol. 15, no. 6, pp. 977–982, 1992.

[136] K. Jackson, E. Flint, M. Cina, D. Lacey, Y. Kwark, J. Trewhella, T. Caulfield, P. Buchmann, C. Harder, and P. Vettiger, "A high-density, four-channel, OEIC transceiver module utilizing planar-processed optical waveguides and flip-chip, solder-bump technology," *Journal of lightwave technology*, vol. 12, no. 7, pp. 1185–1191, 1994.

[137] C. Cornet, Y. Léger, and C. Robert, *Integrated lasers on silicon.* Elsevier, 2016.

[138] B. T. Tung, N. Watanabe, F. Kato, K. Kikuchi, and M. Aoyagi, "Flip-chip bonding alignment accuracy enhancement using self-aligned interconnection elements to realize low-temperature construction of ultrafine-pitch copper bump interconnections," in *2014 IEEE 64th Electronic Components and Technology Conference (ECTC).* IEEE, 2014, pp. 62–67.

[139] Y. Martin, S. Kamlapurkar, N. Marchack, J.-W. Nah, and T. Barwicz, "Novel solder pads for self-aligned flip-chip assembly," in *2019 IEEE 69th Electronic Components and Technology Conference (ECTC).* IEEE, 2019, pp. 528–534.

[140] S. Lindgren, H. Ahlfeldt, L. Backlin, L. Forssén, C. Vieider, H. Elderstig, M. Svensson, L. Granlund, L. Andersson, B. Kerzar *et al.*, "24-GHz modulation bandwidth and passive alignment of flip-chip mounted DFB laser diodes," *IEEE Photonics Technology Letters*, vol. 9, no. 3, pp. 306–308, 1997.

[141] A. Moscoso-Mártir, F. Merget, J. Mueller, J. Hauck, S. Romero-García, B. Shen, F. Lelarge, R. Brenot, A. Garreau, E. Mentovich *et al.*, "Hybrid silicon photonics flip-chip laser integration with vertical self-alignment," in *Conference on Lasers and Electro-Optics/Pacific Rim.* Optical Society of America, 2017, p. s2069.

[142] H. Lu, J. S. Lee, Y. Zhao, C. Scarcella, P. Cardile, A. Daly, M. Ortsiefer, L. Carroll, and P. O'Brien, "Flip-chip integration of tilted VCSELs onto a silicon photonic integrated circuit," *Optics express*, vol. 24, no. 15, pp. 16 258–16 266, 2016.

[143] A. Spott, J. Peters, M. L. Davenport, E. J. Stanton, C. D. Merritt, W. W. Bewley, I. Vurgaftman, C. S. Kim, J. R. Meyer, J. Kirch *et al.*, "Quantum cascade laser on silicon," *Optica*, vol. 3, no. 5, pp. 545–551, 2016.

[144] A. W. Fang, H. Park, O. Cohen, R. Jones, M. J. Paniccia, and J. E. Bowers, "Electrically pumped hybrid AlGaInAs-silicon evanescent laser," *Optics express*, vol. 14, no. 20, pp. 9203–9210, 2006.

[145] A. W. Fang, B. R. Koch, R. Jones, E. Lively, D. Liang, Y.-H. Kuo, and J. E. Bowers, "A distributed Bragg reflector silicon evanescent laser," *IEEE Photonics Technology Letters*, vol. 20, no. 20, pp. 1667–1669, 2008.

[146] C. Zhang, S. Srinivasan, Y. Tang, M. J. Heck, M. L. Davenport, and J. E. Bowers, "Low threshold and high speed short cavity distributed feedback hybrid silicon lasers," *Optics express*, vol. 22, no. 9, pp. 10 202–10 209, 2014.

[147] D. Liang, M. Fiorentino, S. Srinivasan, J. E. Bowers, and R. G. Beausoleil, "Low threshold electrically-pumped hybrid silicon microring lasers," *IEEE Journal of Selected Topics in Quantum Electronics*, vol. 17, no. 6, pp. 1528–1533, 2011.

[148] G. Roelkens, L. Liu, D. Liang, R. Jones, A. Fang, B. Koch, and J. Bowers, "III-V/silicon photonics for on-chip and intra-chip optical interconnects," *Laser & Photonics Reviews*, vol. 4, no. 6, pp. 751–779, 2010.

[149] G. Roelkens, D. Van Thourhout, R. Baets, R. Nötzel, and M. Smit, "Laser emission and photodetection in an InP/InGaAsP layer integrated on and coupled to a silicon-on-insulator waveguide circuit," *Optics express*, vol. 14, no. 18, pp. 8154–8159, 2006.

[150] S. Stankovic, R. Jones, M. N. Sysak, J. M. Heck, G. Roelkens, and D. Van Thourhout, "1310-nm hybrid III-V/Si Fabry-Pérot laser based on adhesive bonding," *IEEE Photonics Technology Letters*, vol. 23, no. 23, pp. 1781–1783, 2011.

[151] S. Stanković, R. Jones, M. N. Sysak, J. M. Heck, G. Roelkens, and D. Van Thourhout, "Hybrid III-V/Si distributed-feedback laser based on adhesive bonding," *IEEE Photonics Technology Letters*, vol. 24, no. 23, pp. 2155–2158, 2012.

[152] K. Tanabe, D. Guimard, D. Bordel, S. Iwamoto, and Y. Arakawa, "Electrically pumped 1.3 $\mu$m room-temperature InAs/GaAs quantum dot lasers on Si substrates by metal-mediated wafer bonding and layer transfer," *Optics express*, vol. 18, no. 10, pp. 10 604–10 608, 2010.

[153] T. Creazzo, E. Marchena, S. B. Krasulick, K. Paul, D. Van Orden, J. Y. Spann, C. C. Blivin, L. He, H. Cai, J. M. Dallesasse *et al.*, "Integrated tunable CMOS laser," *Optics express*, vol. 21, no. 23, pp. 28 048–28 053, 2013.

[154] T. Hong, G.-Z. Ran, T. Chen, J.-Q. Pan, W.-X. Chen, Y. Wang, Y.-B. Cheng, S. Liang, L.-J. Zhao, L.-Q. Yin *et al.*, "A selective-area metal bonding InGaAsP-Si laser," *IEEE Photonics Technology Letters*, vol. 22, no. 15, pp. 1141–1143, 2010.

[155] M.-S. Park, M. Rezaei, I. Nia, R. Brown, S. Bianconi, C. L. Tan, and H. Mohseni, "InGaAs/InP quantum well infrared photodetector integrated on Si substrate by Mo/Au metal-assisted wafer bonding," *Optical Materials Express*, vol. 8, no. 2, pp. 413–419, 2018.

[156] B. B. Bakir, A. Descos, N. Olivier, D. Bordel, P. Grosse, E. Augendre, L. Fulbert, and J. Fedeli, "Electrically driven hybrid Si/III-V Fabry-Pérot lasers based on adiabatic mode transformers," *Optics express*, vol. 19, no. 11, pp. 10 317–10 325, 2011.

[157] S. Keyvaninia, S. Verstuyft, L. Van Landschoot, F. Lelarge, G.-H. Duan, S. Messaoudene, J. Fedeli, T. De Vries, B. Smalbrugge, E. Geluk *et al.*, "Heterogeneously integrated III-V/silicon distributed feedback lasers," *Optics letters*, vol. 38, no. 24, pp. 5434–5437, 2013.

[158] S. Keyvaninia, G. Roelkens, D. Van Thourhout, C. Jany, M. Lamponi, A. Le Liepvre, F. Lelarge, D. Make, G.-H. Duan, D. Bordel *et al.*, "Demonstration of a heterogeneously integrated III-V/SOI single wavelength tunable laser," *Optics express*, vol. 21, no. 3, pp. 3784–3792, 2013.

[159] Y. De Koninck, G. Roelkens, and R. Baets, "Electrically pumped 1550 nm single mode III-V-on-silicon laser with resonant grating cavity mirrors," *Laser & Photonics Reviews*, vol. 9, no. 2, pp. L6–L10, 2015.

[160] M. A. Meitl, Z.-T. Zhu, V. Kumar, K. J. Lee, X. Feng, Y. Y. Huang, I. Adesida, R. G. Nuzzo, and J. A. Rogers, "Transfer printing by kinetic control of adhesion to an elastomeric stamp," *Nature materials*, vol. 5, no. 1, pp. 33–38, 2006.

[161] A. De Groote, P. Cardile, A. Z. Subramanian, A. M. Fecioru, C. Bower, D. Delbeke, R. Baets, and G. Roelkens, "Transfer-printing-based integration of single-mode waveguide-coupled III-V-on-silicon broadband light emitters," *Optics Express*, vol. 24, no. 13, pp. 13 754–13 762, 2016.

[162] H. Yang, D. Zhao, S. Chuwongin, J.-H. Seo, W. Yang, Y. Shuai, J. Berggren, M. Hammar, Z. Ma, and W. Zhou, "Transfer-printed stacked nanomembrane lasers on silicon," *Nature Photonics*, vol. 6, no. 9, p. 615, 2012.

[163] X. Sheng, C. Robert, S. Wang, G. Pakeltis, B. Corbett, and J. A. Rogers, "Transfer printing of fully formed thin-film microscale GaAs lasers on silicon with a thermally conductive interface material," *Laser & photonics reviews*, vol. 9, no. 4, pp. L17–L22, 2015.

[164] J. Justice, C. Bower, M. Meitl, M. B. Mooney, M. A. Gubbins, and B. Corbett, "Wafer-scale integration of group III-V lasers on silicon using transfer printing of epitaxial layers," *Nature Photonics*, vol. 6, no. 9, pp. 610–614, 2012.

[165] B. Corbett, C. Bower, A. Fecioru, M. Mooney, M. Gubbins, and J. Justice, "Strategies for integration of lasers on silicon," *Semiconductor science and technology*, vol. 28, no. 9, p. 094001, 2013.

[166] A. Lee, H. Liu, and A. Seeds, "Semiconductor III-V lasers monolithically grown on Si substrates," *Semiconductor science and technology*, vol. 28, no. 1, p. 015027, 2012.

[167] "Lumerical." [Online]. Available: https://www.lumerical.com

[168] D. E. Hagan and A. P. Knights, "Mechanisms for optical loss in SOI waveguides for mid-infrared wavelengths around 2 $\mu$m," *Journal of Optics*, vol. 19, no. 2, p. 025801, 2016.

[169] "Mentor Graphics." [Online]. Available: https://www.mentor.com/

[170] "IQE." [Online]. Available: https://www.iqep.com/

[171] "Simgui." [Online]. Available: http://www.simgui.com.cn/en/

[172] "NIST standard reference data program." [Online]. Available: https://pubchem.ncbi.nlm.nih.gov/compound/Germanium-dioxide

[173] "Soitec." [Online]. Available: https://www.soitec.com/en

[174] "GenISys." [Online]. Available: https://www.genisys-gmbh.com/

[175] K. W. Lee, S. Yoon, S. Lee, W. Lee, I. Kim, C. E. Lee, and D. Kim, "Secondary electron generation in electron-beam-irradiated solids: resolution limits to nanolithography," *Journal of the Korean Physical Society*, vol. 55, no. 4, pp. 1720–1723, 2009.

[176] "Oxford Instruments." [Online]. Available: https://www.oxinst.com/

[177] "Daylight Solutions." [Online]. Available: https://daylightsolutions.com/

[178] "National Instruments." [Online]. Available: https://www.ni.com/en-gb.html

[179] "Thorlabs." [Online]. Available: https://www.thorlabs.com/

[180] "Vigo System." [Online]. Available: https://vigo.com.pl/en/home/

[181] "InfraRed Associates." [Online]. Available: http://www.irassociates.com/

[182] R. G. Hunsperger, "Losses in optical waveguides," in *Integrated Optics*. Springer, 2009, pp. 107–128.

[183] S. Chen, Q. Yan, Q. Xu, Z. Fan, and J. Liu, "Optical waveguide propagation loss measurement using multiple reflections method," *Optics communications*, vol. 256, no. 1-3, pp. 68–72, 2005.

[184] T. Ikegami, "Reflectivity of mode at facet and oscillation mode in double-heterostructure injection lasers," *IEEE Journal of quantum electronics*, vol. 8, no. 6, pp. 470–476, 1972.

[185] G. Tittelbach, B. Richter, and W. Karthe, "Comparison of three transmission methods for integrated optical waveguide propagation loss measurement," *Pure and Applied Optics: Journal of the European Optical Society Part A*, vol. 2, no. 6, p. 683, 1993.

[186] "Tydex germanium data sheet." [Online]. Available: http://www.tydexoptics.com/pdf/Germanium.pdf

[187] "Photon design." [Online]. Available: http://www.photondesign.com

[188] S. Radosavljevic, A. Radosavljević, C. Schilling, S. Hugger, R. Ostendorf, B. Kuyken, and G. Roelkens, "Thermally tunable quantum cascade laser with an external germanium-on-SOI distributed Bragg reflector," *IEEE Journal of Selected Topics in Quantum Electronics*, vol. 25, no. 6, pp. 1–7, 2019.

[189] "Lor lift-off resists data sheet." [Online]. Available: https://amolf.nl/wp-content/uploads/2016/09/datasheets_LOR_datasheet.pdf

[190] "Finetech." [Online]. Available: https://www.finetech.de/

[191] S. Radosavljevic, N. T. Beneitez, A. Katumba, M. Muneeb, M. Vanslembrouck, B. Kuyken, and G. Roelkens, "Mid-infrared vernier racetrack resonator tunable filter implemented on a germanium on soi waveguide platform," *Optical Materials Express*, vol. 8, no. 4, pp. 824–835, 2018.